



DISCOVERY OF WNK-SPAK/OSR1 SIGNALLING INHIBITORS AS POTENTIAL THERAPEUTICS

BY

MUBARAK ABDULRAHAMAN M ALAMRI

A thesis submitted to the University of Birmingham

For the degree of

DOCTOR OF PHILOSOPHY

School of Pharmacy

The Institute of Clinical Sciences

College of Medical and Dental Sciences

University of Birmingham

July 2018

UNIVERSITY OF
BIRMINGHAM

University of Birmingham Research Archive

e-theses repository

This unpublished thesis/dissertation is copyright of the author and/or third parties. The intellectual property rights of the author or third parties in respect of this work are as defined by The Copyright Designs and Patents Act 1988 or as modified by any successor legislation.

Any use made of information contained in this thesis/dissertation must be in accordance with that legislation and must be properly acknowledged. Further distribution or reproduction in any format is prohibited without the permission of the copyright holder.

ABSTRACT

Protein kinases are major drug targets for many diseases. Among these are the STE20/SPS1- related proline/alanine-rich kinase (SPAK) and the oxidative- stress-responsive kinase 1 (OSR1), which are two related serine/threonine protein kinases. Both kinases are key components of the WNK-SPAK/OSR1 signaling pathway that has emerged as a key regulator of electrolyte homeostasis, body fluid and blood pressure. SPAK and OSR1 kinases become activated following their phosphorylation by WNK kinases, which are mutated in humans with an inherited form of hypertension known as Gordon's syndrome. Once activated, SPAK and OSR1 kinases phosphorylate a series of sodium, potassium and chloride ion co-transporters leading to either their inhibition or activation.

Various knock-in and knock-out SPAK and OSR1 mouse models exhibited reduced blood pressure. This highlighted SPAK and OSR1 kinases as promising targets in the treatment of hypertension. Encouraged by this, this project was initiated to discover specific WNK-signalling inhibitors by targeting SPAK and OSR1 kinases as potential novel antihypertensive agents. My work led to the identification of an allosteric pocket located in the highly conserved C-terminal domains of SPAK and OSR1, which influences their kinase activities. Also, some known WNK-SPAK/OSR1 signalling inhibitors were shown to bind to this allosteric site. Using *in silico* screening, Rafoxanide, an anti-parasitic agent, was identified as a novel allosteric inhibitor of SPAK and OSR1. Additionally, high throughput screening led to the discovery of the clinically used agent, Verteporfin (Visudyne®), as a novel and potent WNK-signalling inhibitor. Moreover, several fragment-binders to the C-terminal domain of OSR1 kinase were identified using NMR-fragment based screening. In addition, the NMR backbone assignments of the C-terminal domain of OSR1 kinase were determined and used to map the previously unknown binding site of different OSR1 and SPAK inhibitors. Using NMR-chemical shift data, the structural differences between the C-terminal domains of OSR1 and SPAK were shown. Collectively, these findings have significantly advanced the field of SPAK and OSR1 kinase inhibition and provided key tools and observations that will facilitate the future discovery of other SPAK and OSR1 kinase inhibitors.

ACKNOWLEDGMENT

I express my sincere appreciation to those who have contributed to this thesis and supported me in one way or the other during this amazing journey for without any of them, this research work would not have been possible.

First and Foremost, I want to offer this endeavour to our GOD Almighty for the wisdom he bestowed upon me, the strength, peace of my mind and good health in order to finish this thesis.

I would like to express my special gratitude and thanks to my supervisor, Dr Youcef Mehellou for providing me an opportunity to complete my PhD thesis. I appreciate his contributions of time and ideas to make my work productive and stimulating. His valuable suggestions, comments and guidance encourage me to learn more day by day. I am extremely grateful to my joint supervisor, Dr Mark Jeeves for his willingness to be my joint supervisor. He really has been a tremendous mentor and guidance for me

I would like to express my gratitude towards my family for the encouragement which helped me in completion of my PhD. My beloved and supportive wife, BASHAYR, and daughter, NOUR, who served as my inspiration to pursue my academic goals. Words cannot express the feelings I have for my parents for their constant unconditional support both in my study and my career as well. I would not be here if it not for you. A heartfelt thanks to my supportive wonderful brothers and sisters for being as my support in the moments of difficulties during the last three years. I thank God for introducing such people in my life.

My sincere gratitude is reserved for Dr. Hachemi Kadri for his invaluable insights and suggestions. I would like also to express my sincere gratitude to Dr Luke Alderwick, Dr Hannah Batchelor and Prof Nigel Simpkins for their insights, knowledge and guidance.

I would like to thank my sponsor, Prince Sattam bin Abdulaziz University, for granting me a scholarship so I could complete my studies. I also thank all the staff at the Pharmacy School at University of Birmingham for helping me during these years of my study both academically and officially.

TABLE OF CONTENTS

CHAPTER 1: INTRODUCTION	1
1.1 Human protein kinases: An overview	2
1.1.1 Protein kinases	2
1.1.2 Catalytic reaction of eukaryotic protein kinases	6
1.1.3 Protein kinases structure and function	8
1.1.4 Protein kinases in human diseases	13
1.1.5 Structural basis for protein kinase inhibition with small molecules	15
1.2 Regulation of blood pressure by the WNK-SPAK/OSR1 signalling pathway	21
1.2.1 Hypertension	21
1.2.2 WNK-SPAK/OSR1 signalling pathway	22
1.2.2.1 WNK kinases	23
1.2.2.2 SPAK and OSR1 Kinases	26
1.2.2.3 Cation-Chloride Cotransporters (CCCs)	33
1.2.2.4 Regulation of WNK Signalling	34
1.3 Validation of the WNK-SPAK/OSR1 signalling pathway as a novel target for the treatment of hypertension	43
1.4 Strategies for inhibiting WNK-SPAK/OSR1 signalling	46
1.4.1 Targeting WNK kinases	47
1.4.1.1 ATP-competitive inhibitors of WNK kinases	47
1.4.1.2 Non-ATP Competitive (Allosteric) Inhibitors of WNK Kinases	51
1.4.2 Targeting WNK binding to SPAK/OSR1 kinases	54
1.4.3 Targeting SPAK and OSR1 kinases	59
1.4.4 Targeting SPAK/OSR1 binding to MO25	60
1.5 Hypothesis	62
CHAPTERII: MATERIALS AND METHODS.....	63
2.1 Molecular biology	64
2.1.1 Bacterial strains	64
2.1.2 Generation of bacterial competent cells	64
2.1.3 Transformation of bacterial cells	64
2.1.4 DNA Extraction and Purification	65
2.1.5 DNA quantification and purity determination	68
2.1.6 DNA sequencing	68

2.1.7	Protein expression and purification	69
2.1.7.1	Expression and purification of proteins from <i>Escherichia coli</i> (<i>E.coli</i>)	69
2.1.7.2	Expression and purification of ^{15}N and ^{13}C isotopically labelled proteins from <i>Escherichia coli</i> (<i>E.coli</i>) for NMR studies	70
2.1.8	Protein quantification and purity determination	72
2.1.9	Growth media	74
2.1.9.1	LB broth and LB broth agar media.....	74
2.1.9.2	M9 minimal medium	74
2.2	Cell culture	76
2.2.1	Cell line culture.....	76
2.2.2	Transient transfection of mammalian HEK-293 cells	76
2.2.3	Cell treatments and inhibition assay	77
2.2.4	Western blot and immunoblot.....	77
2.3	Binding assay	81
2.3.1	Biotin-RFQV pull-down	81
2.3.2	Fluorescence polarisation assay	82
2.4	Functional assay	83
2.4.1	ADP-Glo kinase assay	83
2.4.2	Screening in-house FDA chemical library using ADP-Glo kinase assay.	85
2.4.2.1	Preparation of in-house FDA Chemical Library	85
2.4.2.2	Library Screening Protocol.....	85
2.4.2.3	Assay performance.	88
2.4.3	Selectivity profiling	89
2.5	Molecular modelling	89
2.5.1	Binding mode assessment.....	89
2.5.2	Structure-based virtual screening (SBVS)	91
2.6	Nuclear magnetic resonance (NMR).....	92
2.6.1	Fragment library	92
2.6.2	Ligand-based NMR screening experiment	92
2.6.3	STD-NMR competition assay for ligand binding specificity	93
2.6.4	^1H - ^{15}N HSQC for studying the suitability of C-terminal domains of SPAK and OSR1 for NMR studies.....	94
2.6.5	Sequence-specific ^1H , ^{13}C and ^{15}N backbone resonance assignments of the C-terminal domain of human OSR1	94

2.6.5.1	HNCO and HN(CA)CO	94
2.6.5.2	HNCA and HN(CO)CA	95
2.6.5.3	HNCACB and HN(CO)CACB.....	95
2.6.6	Chemical shift mapping (chemical shift perturbations (CSPs))	97
2.6.7	Analysis of chemical shift perturbations (CSPs)	97
2.6.8	Secondary structure prediction of OSR1 CCT based on NMR chemical shifts	98
2.6.9	Predication of OSR1 C-terminal domain 3D structures	98
CHAPTER III: DETERMINE THE EFFECT OF THE SECONDARY POCKET OF SPAK AND OSR1 ON THEIR KINASES ACTIVITY		99
3.1	Introduction	100
3.2	Aim.....	101
3.3	Results	103
3.3.1	Evaluation of the effect of secondary pocket mutations on OSR1 T185E catalytic activity.....	103
3.3.2	Evaluation of the effect of secondary pocket mutations on OSR1 CCT domain ability to bind upstream WNK kinase	103
3.3.2.1	Biotin–streptavidin pull down assay	103
3.3.2.2	Fluorescence polarisation (FP) assay	104
3.3.3	Molecular docking of known WNK signalling inhibitors into OSR1 CCT domain	107
3.3.4	Effect of STOCK1S-50699 and Closantel on OSR1 kinase activity <i>in vitro</i>	110
3.3.5	Effect of STOCK1S-50699 and Closantel on OSR1 kinase at different ATP-concentrations.....	111
3.3.6	Structure-based virtual screening of 1,200 FDA-approved compounds.	113
3.3.7	Characterisation of the inhibitory effect of Rafoxanide as a novel SPAK and OSR1 allosteric inhibitor.....	115
3.3.8	Effect of Rafoxanide on hypotonicity-induced WNK-SPAK/OSR1-NKCC1 signalling in HEK293 cells.....	117
3.3.9	Effect of Rafoxanide on OSR1 CCT domain ability to bind to WNK kinase	119
3.3.10	Discussion.....	121
CHAPTER IV: IDENTIFY NEW SPAK AND OSR1 KINASE INHIBITORS USING HIGH-THROUGHPUT SCREENING		126
4.1	Introduction	127

4.2	Aim.....	127
4.3	Results.....	128
4.3.1	Optimisation of OSR1 high-throughput screening (HTS) assay	128
4.3.2	Screening of in-house chemical library	129
4.3.3	Identification of Verteporfin (Visudyne®) as a novel and potent inhibitor of SPAK/OSR1 kinases.....	131
4.3.4	Characterisation of the inhibitory effect of Verteporfin on SPAK and OSR1 kinases <i>in vitro</i>	139
4.3.5	Selectivity of Verteporfin for SPAK and OSR1 across 140 protein kinases	142
4.3.6	Verteporfin inhibited hypotonicity-stimulated WNK-signalling in dose-dependent manner.....	144
4.3.7	Verteporfin analogues have no effect on the kinase activity of OSR1 T185E	146
4.3.8	Verteporfin binds to the activation segment of SPAK and OSR1 <i>in silico</i>	148
4.3.9	Discussion.....	150
CHAPTER V: USE NMR-BASED FRAGMENT SCREENING TO IDENTIFY SPAK AND OSR1 KINASE INHIBITORS		155
5.1	Introduction.....	156
5.2	Aim.....	156
5.3	Results.....	157
5.3.1	Expression and purification of GST-OSR1 CCT domain and GST-tag proteins	157
5.3.2	In-house fragment library screening by STD-NMR and waterLOGSY ..	159
5.3.3	Confirmation of the fragment hits by STD-NMR	163
5.3.4	STD-NMR competition assay for ligand binding specificity	166
5.3.5	The effect of hit fragments on the activity of OSR1 T185E and SPAK T233E <i>in vitro</i>	168
5.3.6	The inhibitory effect of fragment-hybrid ligands on the activity of OSR1 T185E <i>in vitro</i>	170
5.3.7	Expression and purification of ¹⁵ N and/or ¹³ C isotopically labelled OSR1 and SPAK CCT domains.....	172
5.3.8	Suitability of CCT domain of OSR1 and SPAK for NMR studies.....	174
5.3.9	Sequence-specific ¹ H, ¹³ C and ¹⁵ N backbone resonance assignments of the CCT domain of human OSR1	177

5.3.10	Chemical shift resonance of SPAK CCT domain is different than OSR1 CCT domain	181
5.3.11	Chemical shift mapping	183
5.3.12	Assessment of RFQV, STOCK2S-26016 and Rafoxanide binding to OSR1 CCT domain by ^1H - ^{15}N HSQC.....	183
5.3.13	Chemical shift perturbation following the addition of RFQV peptide to ^{15}N -labelled OSR1 CCT domain	184
5.3.14	Chemical shift perturbation following the addition of STOCK2S-26016 and Rafoxanide to ^{15}N -labelled OSR1 CCT domain	188
5.3.15	Assessment of fragment hits binding to OSR1 CCT domain by ^1H - ^{15}N HSQC	192
5.3.16	OSR1 CCT domain secondary structure prediction based on NMR chemical shifts	196
5.3.17	Predication of OSR1 CCT domain 3D structure	199
5.3.18	Discussion.....	202
CHAPTER VI: GENERAL CONCLUSIONS AND FUTURE WORK		209
REFERENCES		214
APPENDICES.....		232

LIST OF ABBREVIATIONS

WNKs	With-no-lysine kinases
SPAK	STE20/SPS1- related proline/alanine-rich kinase
OSR1	Oxidative- stress-responsive kinase 1
MO25	Mouse only protein 25
CUL3	Cullin-3
KLHL3	Kelch-like protein 3
PKA	Protein kinase A
CCT	C-terminal domain
NKCC	Sodium, potassium, and chloride ions cotransporter
RFQV	Arginine-Phenyl aniline-Glutamine-Valine containing peptide
SH3	Src homology 3
GST	Glutathione S-transferase
CATCHtide	Cation chloride co-transporter peptide substrate
GAPDH	Glyceraldehyde 3-phosphate dehydrogenase
ARHGAP12	Rho GTPase-activating protein 12
STRAD	STE20-related kinase adapter protein
c-Abl	Abelson murine leukemia viral oncogene homolog 1
CDK2	Cyclin-Dependent Kinase 2
EGFR	Epidermal growth factor receptor
MEK 1	Mitogen-activated protein kinase kinase 1
VEGFR2	Vascular endothelial growth factor receptor 2

Src	Proto-oncogene tyrosine-protein kinase
VGLUT	Vesicular glutamate transporter
B-RAF	V-raf murine sarcoma viral oncogene homolog B1
FHHt	Familial hyperkalemic hypertension
HEK293	Human embryonic kidney cells 293
MpkDCT	Murine distal convoluted tubule
MOVAS	Primary vascular aortic smooth muscle cells
ADP	Adenosine 5'-diphosphate
ATP	Adenosine 5'-triphosphate
FDA	Food and drug administration
WT	Wild type
FL	Full length
DMSO	Dimethyl sulfoxide
SDS PAGE	Sodium dodecyl sulfate polyacrylamide gel electrophoresis
FP	Fluorescence polarisation
<i>E.coli</i>	Escherichia coli
IPTG	Isopropyl- β -D-1-thiogalactopyranoside
LB	Luria broth
BLAST	Basic alignment search tool
HSQC	Heteronuclear single quantum coherence
TROSY	Transverse relaxation optimised spectroscopy
STD-NMR	Saturation transfer difference-nuclear magnetic resonance
WaterLOGSY	Water-ligand observed gradient spectroscopy
NOE	Nuclear overhauser effect

LIST OF TABELS

Table 1.1: Diseases caused by mutations in particular protein kinases	14
Table 2.2: List of cDNA Clones	67
Table 2.3: Qiagen Plasmid Maxi kit buffers.....	68
Table 2.4: List of buffers used for proteins purification.....	71
Table 2.5: Components of SDS-PAGE resolving gel.....	73
Table 2.6: Components of SDS-PAGE stacking gel.	73
Table 2.7: Components of LB broth and LB broth agar media	74
Table 2.8: Component of M9 salts.....	75
Table 2.9: Composition of nutrient mix.....	75
Table 2.10: List of antibodies used for western blot.....	79
Table 2.11: List of buffers used for cell culture work	80
Table 2.12: Compositions of dialysis buffer.....	83
Table 2.13: Chemical library screening data.	87
Table 2.14: Screening protocol in 384 well-plate.....	88

LIST OF FIGURES

Figure 1.1: Human kinome.	5
Figure 1.2: Reversible protein phosphorylation reactions.	7
Figure 1.3: Anatomy of the eukaryotic catalytic kinase domain.	10
Figure 1.4: Active and inactive conformations of protein kinases.	12
Figure 1.5: ATP binding site of PKA.	16
Figure 1.6: Chemical structures and binding modes of different protein kinase inhibitors.	20
Figure 1.7: Structural analysis of WNK kinases.	25
Figure 1.8: Mammalian Ste20-related kinases.	27
Figure 1.9: Sequence alignment of human OSR1 and SPAK kinases.	29
Figure 1.10: 3D structures of SPAK and OSR1 kinase domains.	32
Figure 1.11: Regulation of the WNK-SPAK/OSR1 signalling pathway.	38
Figure 1.12: Structural analysis of SLC12A cotransporters.	41
Figure 1.13: Discovery of a WNK kinase ATP-competitive inhibitor.	50
Figure 1.14: Discovery of a WNK kinase allosteric inhibitor.	53
Figure 1.15: Discovery of WNK-SPAK/OSR1 binding inhibitors.	56
Figure 1.16: Chemical structures of STOCK2S-26016 and its different analogues.	58
Figure 1.17: Chemical structures of STOCK1S-14279, Closantel and HK01.	59
Figure 2.1: 3D TROSY-based backbone assignment experiments.	96
Figure 3.1: Characterisation of the inhibitory effect of STOCK1S-50699 in <i>in vitro</i> cell-free based assays and in HEK293 cells.	102
Figure 3.2: Characterisation of the effect of secondary pocket on OSR1 kinase.	106
Figure 3.3: Chemical structures and docking results of four WNK-SPAK/OSR1 signalling inhibitors.	109
Figure 3.4: Characterisation of STOCK1S-50699 and Closantel Activity <i>in vitro</i>	112
Figure 3.5: Identification of Rafoxanide using structure-based virtual screening.	114
Figure 3.6: Characterisation of the activity of Rafoxanide as a novel SPAK and OSR1 allosteric inhibitor.	116
Figure 3.7: Inhibitory effect of Closantel and Rafoxanide on WNK-SPAK/OSR1 signalling in HEK293 cells.	118
Figure 3.8: Rafoxanide and Closantel do not compete with the 18-mer RFQV peptide for binding to the primary pocket.	120

Figure 3.9: Graphical conclusion.....	125
Figure 4.1: Scatterplots of the primary screening using the developed assay.	130
Figure 4.2: The secondary screening using the developed assay	130
Figure 4.3: Determination of the IC ₅₀ of Vertepofrin.....	132
Figure 4.4: Determination of the IC ₅₀ of Toremifene.....	133
Figure 4.5: Determination of the IC ₅₀ of Alexidine Dihydrochloride.	134
Figure 4.6: Determination of the IC ₅₀ of β -Escin	135
Figure 4.7: Determination of the IC ₅₀ of Chicago Sky Blue 6B.....	136
Figure 4.8: Determination of the IC ₅₀ of Chlorhexidine Dihydrochloride	137
Figure 4.9: Determination of the IC ₅₀ of Methyl Benzethonium Chloride.....	138
Figure 4.10: <i>In vitro</i> characterization of Verteporfin as OSR1 and OSR1 kinase inhibitor.	141
Figure 4.12: Inhibitory effect of Vetreporfin on WNK-SPAK/OSR1 signalling in HEK293 cells.....	145
Figure 4.13: The inhibitory effect of Verteporfin's derivatives.	147
Figure 4.14: Graphical representation of the predicted binding mode of Verteporfin to OSR1 kinase domain (PDB ID: 2VWI).....	149
Figure 4.15: Graphical conclusion.....	154
Figure 5.1: Expression and purification of proteins from <i>E.coli</i>	158
Table 5.1: List of fragment hits from primary screening of in-house 384 fragments...	161
Figure 5.2: Examples for STD-NMR and waterLogsy spectra for fragment hits.....	162
Table 5.2: Chemical structures of confirmed 19 fragment hits	164
Figure 5.3: Examples for STD-NMR for confirming the binding of fragment number (a) 179 and (b) 330 to GST-OSR1 CCT domain.	165
Figure 5.4: STD-NMR competition assay for ligand binding specificity.....	167
Figure 5.5: Inhibitory effect of fragment hits on the activity of SPAK and OSR1 kinases.....	169
Figure 5.6: The inhibitory effect of fragment-hybrid ligands on the activity of OSR1 T185E <i>in vitro</i>	171
Figure 5.7: Expression and purification of proteins from <i>E.coli</i>	173
Figure 5.8: ¹ H- ¹⁵ N HSQC spectrum of ¹⁵ N-OSR1 CCT domain.....	175
Figure 5.9: ¹ H- ¹⁵ N HSQC spectrum of ¹⁵ N-SPAK CCT domain.	176
Figure 5.10: ¹ H- ¹⁵ N TROSY-HSQC of ¹⁵ N- ¹³ C-labelled OSR1 CCT domain.....	178
Figure 5.11: OSR1 CCT domain assignments.....	179

Figure 5.12: Mapping unassigned residues onto OSR1 CCT domain crystal structure (PDB: 2V3S).....	180
Figure 5.13: Comparison of homology sequence and	182
Figure 5. 14: Chemical shift perturbation following the addition of RFQV peptide to ¹⁵ N-labelled OSR1 CCT domain	185
Figure 5.15: Chemical shift perturbations (CSPs) of human OSR1 CCT domain in presence of 50 µM RFQV peptide.....	186
Figure 5.16: Mapping of spectral changes.....	187
Figure 5.17: Chemical shift perturbation (CSPs) following the addition of STOCK2S-26016 and Rafoxanide.	189
Figure 5.18: Chemical shift perturbations (CSPs) of human OSR1 CCT domain in presence of 200 µM (a) STOCK2S-26016 and (b) Rafoxanide	190
Figure 5.19: Location of Lys517 (K517) residue in the OSR1 structure.	191
Figure 5.20: Chemical shift perturbation (CSPs) following the addition of 156 and 179.	193
Figure 5.21: Chemical shift perturbation (CSPs) following the addition of 234 and 330.	194
Figure 5.22: Chemical shift perturbation (CSPs) following the addition of 383.....	195
Figure 5.23: OSR1 CCT domain secondary structure prediction.....	197
Figure 5. 24: OSR1 CCT domain secondary structure prediction.....	198
Figure 5.25: OSR1 CCT domain predicted Structure.....	201
Figure 5.26: Graphical conclusion.....	208

LIST OF PUBLICATIONS

- KADRI, H., ALAMRI, M. A., NAVRATILOVA, I. H., ALDERWICK, L. J., SIMPKINS, N. S. & MEHELLOU, Y. 2017. Towards the Development of Small-Molecule MO25 Binders as Potential Indirect SPAK/OSR1 Kinase Inhibitors. *ChemBioChem*, 18, 460-465.
- ALAMRI, M. A., KADRI, H., ALDERWICK, L. J., SIMPKINS, N. S. & MEHELLOU, Y. 2017. Rafoxanide and Closantel Inhibit SPAK and OSR1 Kinases by Binding to a Highly Conserved Allosteric Site on Their C-terminal Domains. *ChemMedChem*, 12, 639-645.
- ALAMRI, M. A., KADRI, H., DHIANI, B. A., MAHMOOD, S., ELZWAWI, A. & MEHELLOU, Y. 2017. WNK Signaling Inhibitors as Potential Antihypertensive Drugs. *ChemMedChem*, 12, 1677-1686.
- ALAMRI, M. A., KADRI, H., JEEVES M., ALDERWICK, L. J., A. & MEHELLOU, Y. 2018. The Photosensitizing Clinical Agent Verteporfin is an Inhibitor of SPAK and OSR1 Kinases. *ChemBioChem*, DOI: 10.1002/cbic.201800272.
- MEHELLOU, Y., ALAMRI, M. A., DHIANI, B. A., KADRI, H. 2018. C-terminal Phosphorylation of SPAK and OSR1 Kinases Promotes Their Binding and Activation by the Scaffolding Protein MO25. *Biochemical and Biophysical Research Communications*. 503(3), 1868-1873.

CHAPTER 1: INTRODUCTION

1.1 Human protein kinases: An overview

1.1.1 Protein kinases

Protein phosphorylation is a fundamental aspect of cellular function and physiological processes such as metabolism, division, movement, survival and apoptosis. Hence, disruption to protein phosphorylation processes may give rise to diseases (Cohen, 2002b). A series of phosphorylation events occurs inside cells and these are catalysed by enzymes known as protein kinases, one of the largest families of enzymes in eukaryotes (collectively referred to as the kinome). The human kinome comprises 518 protein kinases (Manning et al., 2002) and around 20 lipid kinases (Heath et al., 2003). The human protein kinase superfamily is broadly classified into typical or conventional protein kinases, which contain 478 kinases, and atypical kinases, which contain 40 kinases that lack sequence similarity to the typical eukaryotic protein kinases domain but still possess catalytic kinase activity. Typical protein kinases are the largest family of protein kinases and have been subdivided into seven groups based on catalytic domain sequence similarity: AGC, CAMK, CK1, CMGC, STE, TK and TKL, as shown in **Figure 1.1** (Manning et al., 2002).

Historically, phosphorylase kinase was the first protein kinase to be purified and characterized by Fischer and Krebs during their pioneering research into the regulation of glycogen metabolism by protein phosphorylation in 1955 (Fischer and Krebs, 1955). Ten years later, Krebs's group discovered the second protein kinase: protein kinase A (PKA) (a cAMP-dependent protein kinase) (Walsh et al., 1968). Since then, more protein kinases and their catalytic activities, as well as their implications for human illnesses, have been reported (Taylor and Kornev, 2017). Indeed, the link between kinase deregulation and disease progression was first observed in 1970, when the (Src)

oncogene, a gene linked to the pathogenesis of cancer, was confirmed as a tyrosine protein kinase (Collett and Erikson, 1978). By the mid-1980s, protein kinases had been recognized as a major biomolecules in signal transduction inside cells in response to both intra- and extracellular stimuli (Krebsk, 1985). Subsequently, they emerged as reliable therapeutic targets particularly after the first X-ray crystal structure of the catalytic domain of protein kinase A was described in 1991 (Knighton et al., 1991). Such interest in protein kinases as targets in the discovery of new drugs resulted in the first approved protein kinase inhibitor, Imatinib (Gleevec), by the US Food and Drug Administration (FDA) in 2001 (Capdeville et al., 2002).

It is now established that protein kinase genes make up almost 2% of all human genes and up to 30% of the proteins in humans are subject to phosphorylation (Ubersax and Ferrell Jr, 2007, Manning et al., 2002). In addition, more than 400 human diseases, including cancer, diabetes, autoimmune, cardiovascular, inflammatory and nervous disorders are associated with protein kinase dysregulation. To date, 38 small molecule protein kinase inhibitors have been clinically used or utilized during clinical investigations, rendering protein kinases as highly important cellular regulatory machines and therapeutic targets (Fischer, 2017, Patterson et al., 2014).

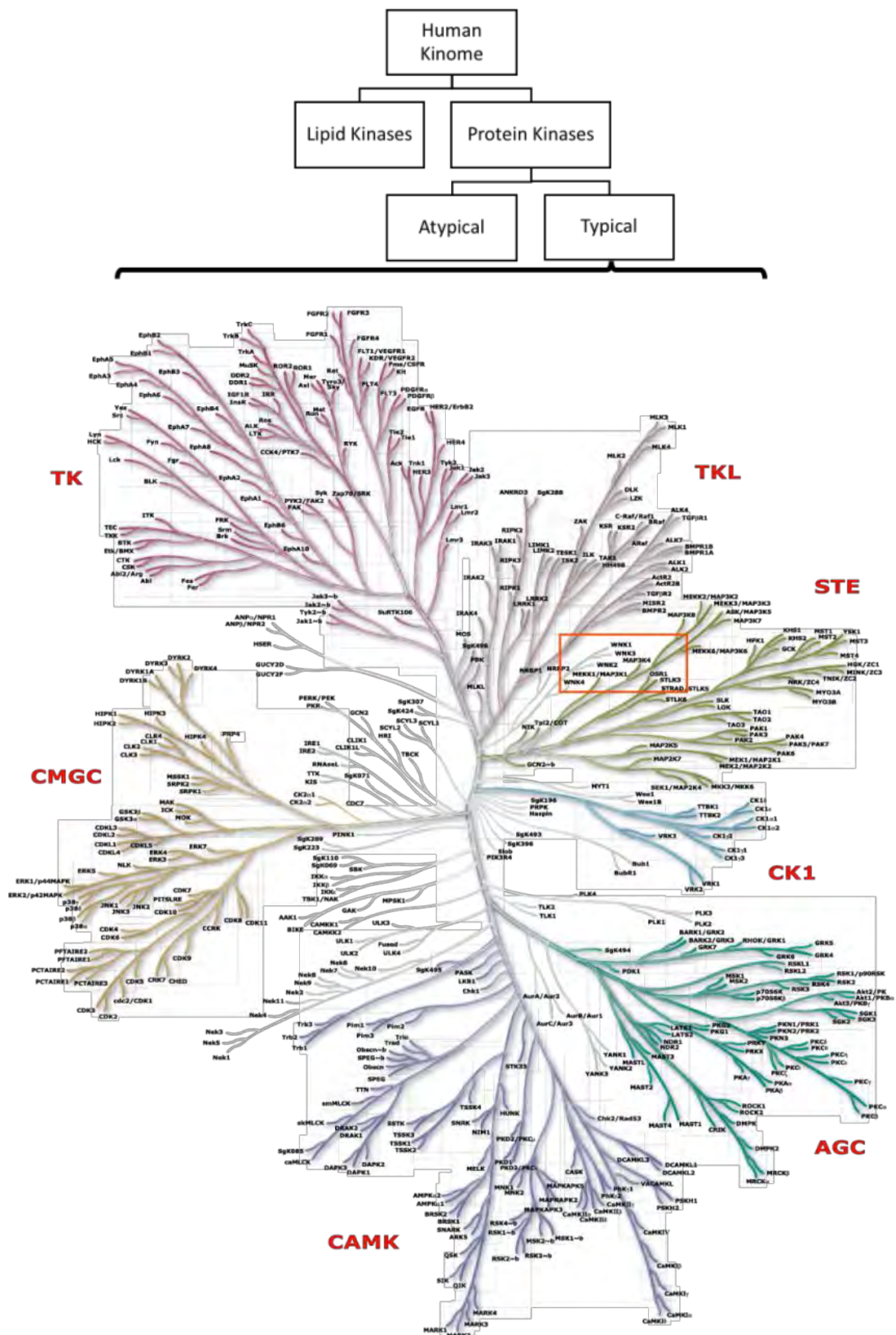


Figure 1.1: Human kinome. A dendrogram summarizing the classification of human kinases, which includes 478 evolutionarily related protein kinases. **AGC**, containing protein kinase A (PKA), protein kinase G (PKG), and protein kinase C (PKC) families; **CAMK**, Ca²⁺/calmodulin-dependent protein kinases; **CK1**, Casein kinase 1; **CMGC**, containing cyclin-dependent kinase (CDK), mitogen-activated protein kinase (MAPK or MAP kinase), glycogen synthase kinase 3 (GSK3) and Cdc2-like kinase (CLK) families; **STE**, homologues of yeast Sterile 7, Sterile 11 and Sterile 20 kinases; **TK**, tyrosine kinases; **TKL**, tyrosine kinase-like. Pseudokinases, protein kinases that lack critical residues for phosphate transfer, such as RCG (Receptor guanylate cyclases) pseudokinases, are not shown. The distance along the branch between kinases is proportional to the divergence between their sequences. The atypical kinase group, including 40 divergent protein kinases lacking sequence homology to the conserved eukaryotic kinase domain, is not shown. Kinases that were studied in this thesis, WNK, SPAK and OSR1, are shown in the red rectangle. The protein kinome tree adapted from Cell Signaling Technology, Inc. (www.cellsignal.com).

1.1.2 Catalytic reaction of eukaryotic protein kinases

Protein kinases are known by their catalytic activity, the phosphorylation of a protein substrate in which the chemical structure of the substrate is modified by transferring the γ -phosphate group of the adenosine-5'-triphosphate (ATP) molecule onto the hydroxy group of specific tyrosine (Tyr), serine (Ser) and/or threonine (Thr) amino acid residues, referred to as phosphorylation sites, within the protein substrate. Although Tyr, Ser, Thr are the three amino acids that have been extensively studied in the field of protein phosphorylation, histidine (His) phosphorylation has also been looked into (Srivastava et al., 2016). Notably, a recent report from the Eyers lab in Liverpool reported the discovery of extensive phosphorylation of arginine (Arg), lysine (Lys), aspartate (Asp) and glutamate (Glu) in human cell extracts (Hardman et al., 2017). The phosphorylation process is a reversible phenomenon. The enzymes that remove phosphates from phospho-amino acids are called phosphatases (**Figure 1.2**) (Cohen, 2002a). In most cases, reversible phosphorylation alters the biological functions of target proteins through conformational rearrangements leading to the alteration of kinase enzymatic activity, stability, localization and association with other proteins or small molecules such as lipids and sugars (Hunter, 2000). Based on the catalytic specificity of kinases and the type of amino acids they phosphorylate, these eukaryotic protein kinases are subdivided into three main classes: serine/ threonine kinases (STK), tyrosine kinases (TK) and dual specificity kinases (DSK), which are able to phosphorylate both Ser/Thr and Tyr (Roskoski, 2012).

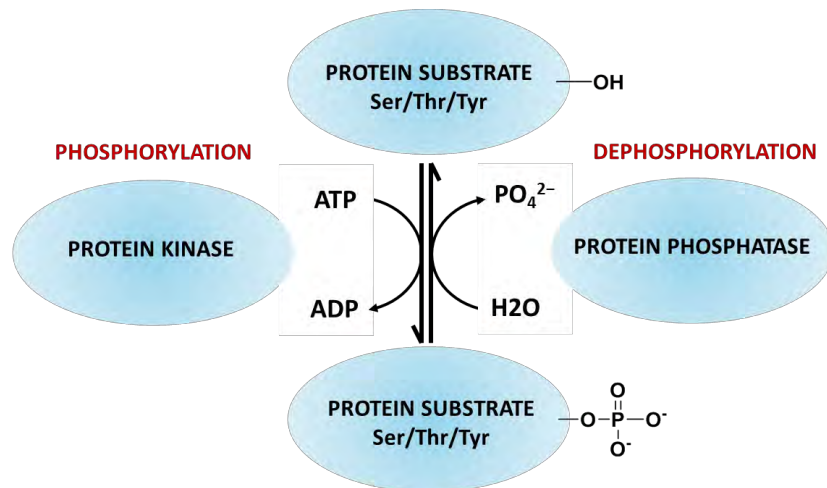


Figure 1.2: Reversible protein phosphorylation reactions. The mechanism of the phosphorylation and dephosphorylation of protein substrates consists of a protein substrate, protein kinase, protein phosphatase and ATP as the source of a transferable phosphate group. Protein kinases catalyse the phosphorylation reaction by transferring the γ -phosphate group from an ATP molecule to specific residues of the protein substrate producing a phosphorylated protein substrate and ADP. Protein phosphatases catalyse the dephosphorylation reaction by cleaving the phosphoric acid monoester of the phosphorylated protein to produce a hydroxyl group of the protein substrate and a free phosphate ion.

1.1.3 Protein kinases structure and function

The overall structure of protein kinases is organized into a kinase domain (also called the catalytic domain) that mediates the function of the protein kinase and other structural elements outside the kinase domain that serve as regulatory or targeting modules (Jin and Pawson, 2012, Fabbro et al., 2015). The kinase domains of most protein kinases are conserved in both sequence and structure (Hanks and Quinn, 1991, Hanks and Hunter, 1995). In contrast, the regulatory domains of different protein kinases differ in the overall folds and local structural motifs thus providing the diversity required for maintaining pathway specificity (Li and Palmer, 2009). The kinase domain is a bilobal structure, formed by approximately 250-300 amino acid residues and consisting of an amino-terminal (*N*-terminal) and a carboxyl-terminal (*C*-terminal) lobes that can also be subdivided into a total of 12 functional subdomains (**Figure 1.3**) (Sim et al., 2012). The *N*- and *C*-lobes are linked by a hinge region in subdomain V which contains conserved residues that form essential parts of the catalytic machinery and the magnesium (Mg^{2+})-ATP binding pocket (Torkamani et al., 2008).

The *N*-terminal lobe comprises approximately 100 amino acid residues and contains subdomains I-IV. It is formed primarily by five antiparallel β -sheets, including a glycine-rich loop (or P-loop) within subdomain I, subdomain II, and one α -helix (an α_C helix within subdomain III). The glycine-rich loop is a flexible chain with a conserved sequence: GxGxxG. This loop extends over the top of the ATP molecule, positioning the γ -phosphate for catalysis. Furthermore, subdomain II contains the key catalytic lysine residue (K72 in PKA) that coordinates and stabilizes the α and β phosphates of the ATP molecule. The α_C helix accommodates the conserved glutamic acid residue (Glu91 in PKA), which makes a salt bridge with the catalytic lysine in subdomain II to stabilize the

overall shape of the kinase domain. Indeed, rotating the *N*-terminal of the α C helix in a suboptimal position for catalysis (' α C helix-out') results in an inactive state of the kinase. Moreover, the 'gatekeeper' methionine residue (M120 in PKA) is an important residue located deep in the ATP pocket within the hinge region and controls access to the 'back pocket' of the kinase. This residue is often mutated in protein kinases making them resistant to small molecule kinase inhibitors (Fabbro et al., 2012).

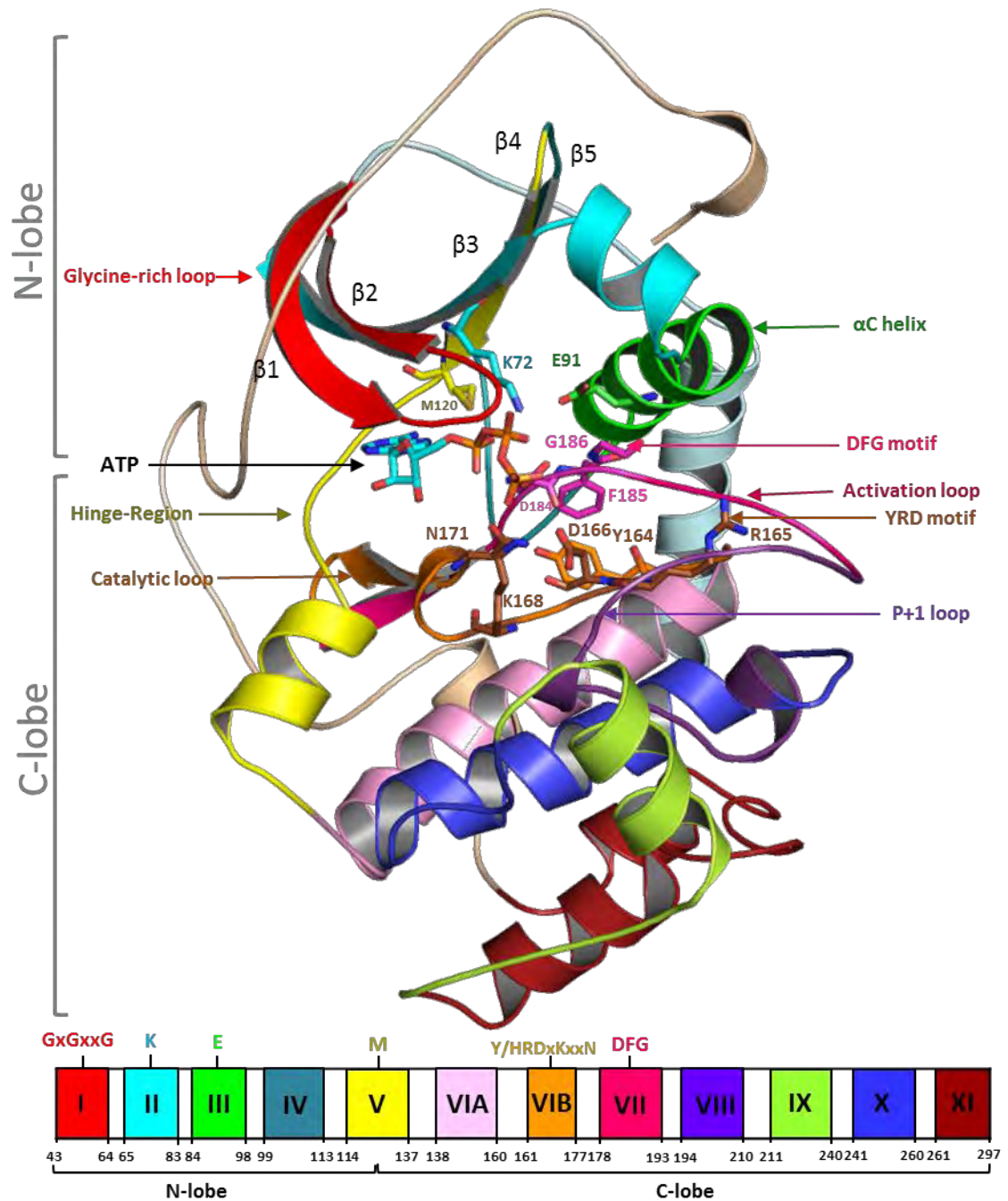


Figure 1.3: Anatomy of the eukaryotic catalytic kinase domain. A ribbon diagram of protein kinase A (PKA) bound to an ATP molecule (PDB ID: 1ATP). The PKA kinase domain is illustrated in a standard orientation, with the typical bilobal structure of protein kinases: *N*-lobe and *C*-lobe. Kinase subdomains are illustrated in different colours and the key functional elements of the kinase domain are labelled.

On the other hand, the C-terminal lobe (a large lobe) contains subdomains VIA-XI. It is formed mainly by a series of α -helices and is involved in peptide-substrate recognition and catalysis. Importantly, this lobe contains the catalytic loop and activation segment region. The catalytic loop comprises the HRD (His-Arg-Asp) motif (H is a Y in PKA) that serves as a catalytic triad that is responsible for catalysing the phosphoryl transfer reaction. The activation segment region is made up of several significant regions, including the P+1 loop, as well as the activation loop (A-loop) that contains the conserved DFG (Asp-Phe-Gly) motif. The DFG motif is also called the magnesium-coordinating loop because the aspartic acid residue (Asp 184 in PKA) coordinates the Mg^{2+} at the ATP binding pocket (Verkhivker, 2016). In addition, the phenylalanine residue of the DFG motif participates with the residues from the catalytic loop (H/YRD motif), activation loop and α C helix in forming the hydrophobic regulatory spine (R-spine) and catalytic spine (C-spine) that allows the DFG motif to adapt the DFG-in or -out conformations, which ultimately regulate kinase activation. The DFG-out conformation occurs when the phenylalanine of the DFG motif moves out of the hydrophobic pocket, disrupting the orientation of the aspartic acid residue and sterically blocking the ATP pocket (**Figure 1.4**) (Kornev et al., 2008).

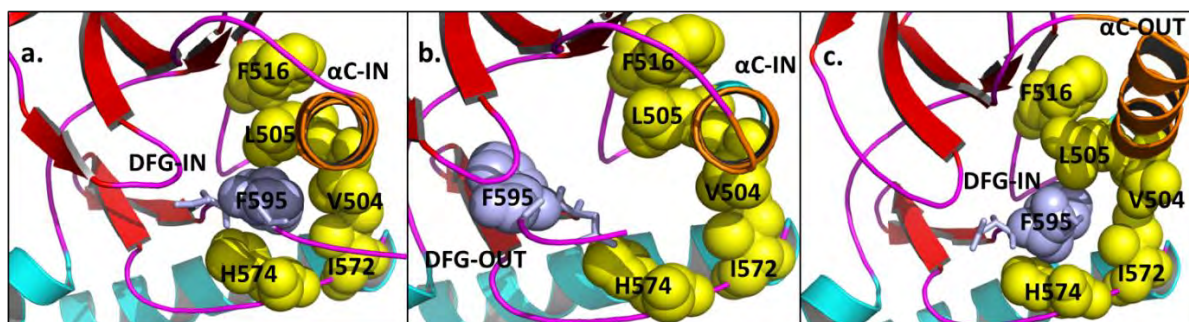


Figure 1.4: Active and inactive conformations of protein kinases. A close-up of the binding site of the B-Raf kinase adapting three different conformational states: (a) DFG-in/ α C helix-in (PDB: 2FB8); (b) DFG-out/ α C helix-in (PDB: 1UWH); and (c) DFG-in/ α C helix-out (PDB: 3C4C). R-spine residues appear as yellow spheres. The phenylalanine (F595) of the DFG motif is shown in purple, the α C helix in orange. The dynamic equilibrium between active and inactive kinase states is controlled via switching the conformational states of DFG in the A-loop, H/YRD motif and α C helix, in which DFG-in/ α C helix-in is active, DFG-in/ α C helix-out is inactive, and DFG-out/ α C helix-in is an inactive kinase state (Verkhivker, 2016). Figures were prepared using PyMOL 1.3.

1.1.4 Protein kinases in human diseases

Since 30% of human proteins are subjected to modification by protein kinases, it is not surprising that dysregulations of this process could be manifested in human diseases (Cohen, 2001). Examples of diseases and phenotypes that result from mutations in protein kinases are listed in **Table 1.1**. Generally, mutations in protein kinases can be classified into five major types based on the subsequent physiological effect that results from these mutations (Reva et al., 2011, Radivojac et al., 2008). These are: (i) Loss of function mutations that cause a normal molecular function to turn-off; (ii) gain of function or activating mutations which cause a molecular function to be constitutively active when compared to normal function (Radivojac et al., 2008); (iii) switch of function mutations that cause a mutated protein to acquire new specific interactor(s) and, consequently, new biological function(s); (iv) drug resistance mutations that take place to overcome the inhibitory effect of a drug (Reva et al., 2011); (v) no-contributing function (passenger) mutations that do not participate in disease development and progression (Radivojac et al., 2008). Among these, loss and gain of function mutations are the most common mutations-causing diseases in humans (Reva et al., 2011).

It must also be noted that some naturally occurring pathogens and toxins exert their effect by altering the activity of specific protein kinases. For example, *Bacillus Anthracis* secretes a virulence factor that can inhibit mitogen-activated protein kinase kinases (MAPKK) signalling called *Anthrax* toxin. The latter is a potent protease that hydrolyses the MAPKK protein kinase and is known to be a causative-agent of *Anthrax* (Krachler et al., 2011).

Human Disease	Protein Kinase
Neuroblastoma	ALK
Early-onset Parkinson disease 6	PINK1
Insulin-resistant diabetes with acanthosis	INSR
Early obesity, hyperphagia and developmental delay	NTRK2
Severe-combined immunodeficiency (T cell-negative)	ZAP70
Atypical lipodystrophy	AKT2
Primary pulmonary hypertension 1	BMPR2
Epileptic encephalopathy Lennox–Gastaut type	MAPK10
Glycogen storage disease type 9A	PHKA2

Table 1.1: Diseases caused by mutations in particular protein kinases. **ALK**, Anaplastic lymphoma kinase; **PINK1**, Pantothenate kinase 1; **INSR**, Insulin receptor; **NTRK**, The neurotrophic tyrosine kinase receptor type 2; **ZAP70**, Zeta-chain-associated protein kinase 70; **AKT2**, RAC-beta serine/threonine-protein kinase; **BMPR2**, Bone morphogenetic protein receptor type II; **MAPK10**, Mitogen-activated protein kinase 10; **PHKA2**, Phosphorylase b kinase regulatory subunit alpha, liver isoform. Table adapted from (Lahiry et al., 2010).

1.1.5 Structural basis for protein kinase inhibition with small molecules

The molecular basis for kinase inhibition was established during the late 1980s when small-molecule inhibitors against the epidermal growth factor receptor (EGFR) were reported (Yaish et al., 1988). Since then, several kinase inhibitors based on various chemical scaffolds, physicochemical properties and pharmacological profiles have been published. Most of the reported kinase inhibitors, including most of the current FDA-approved drug molecules, are steady-state ATP-competitive inhibitors that act by blocking the ATP binding pocket, the most druggable site in protein kinases (Wu et al., 2016). The ATP pocket is an evolutionarily conserved site located between the two *N*- and *C*-lobes of the catalytic domain on a kinase (**Figure 1.5**). This pocket appears as a deep cleft with a large surface area and high potential for polar interactions. The presence of polar interaction allows for the rational design of ATP pocket binders with a high binding affinity (Battistutta et al., 2005). Despite successes in the application of this approach, as several ATP-competitive inhibitors have been approved for clinical use, the development of kinase inhibitors with outstanding selectivity within the kinome is still a significant challenge, not only in terms of minimizing side effects, but also to allow the treatment of chronic non-life-threatening illnesses (Fabbro, 2015). Therefore, targeting less conserved allosteric sites has been proposed as an alternative approach to overcome this challenge (Wu et al., 2015).

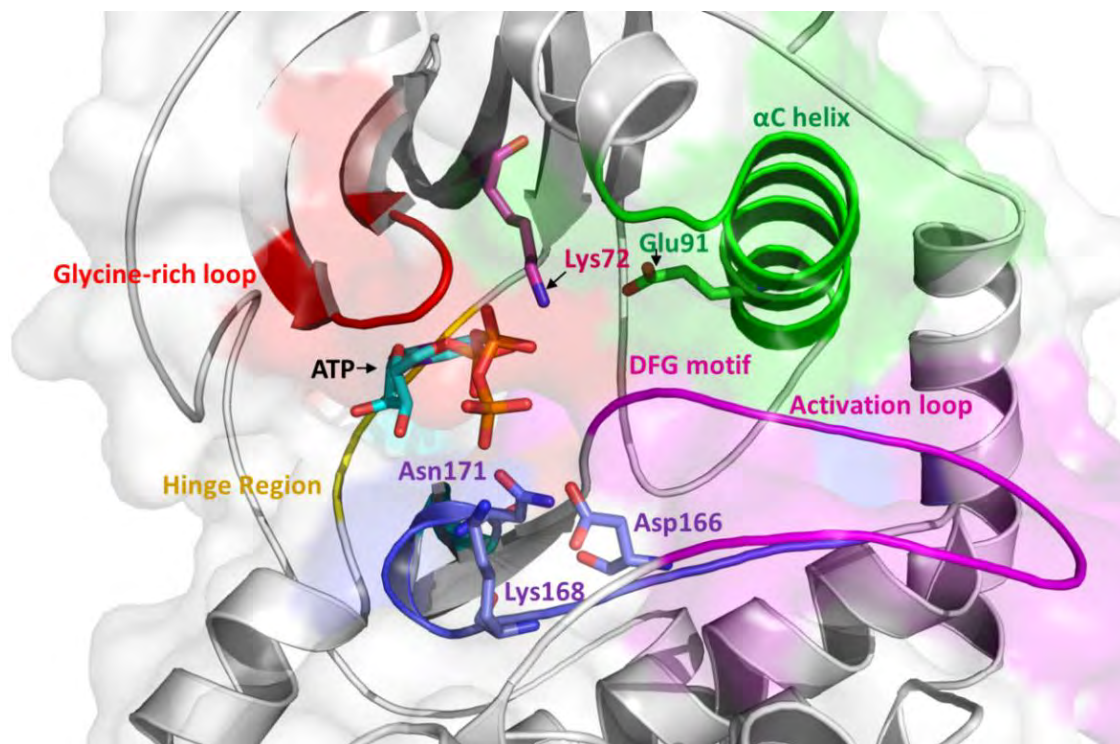


Figure 1.5: ATP binding site of PKA. The ATP molecule and the key residues in the ATP binding site are shown in sticks of different colours. The figure was prepared using PyMOL 1.3 based on PKA crystal structure (PDB ID: 1ATP) (Knighton et al., 1991).

Based on the X-ray crystal structures of several kinase inhibitors bound to their protein kinase targets, small-molecule kinase inhibitors are classically divided into ATP-competitive and non-ATP-competitive inhibitors. ATP-competitive inhibitors bind to the adenine base pocket of the ATP binding site and connect both kinase lobes by forming hydrogen bonds with the hinge region (Vulpetti and Bosotti, 2004).

ATP-competitive inhibitors are further classified in reference to the conformation of the DFG motif into type I, I $\frac{1}{2}$ and II inhibitors (**Figure 1.6**) (Roskoski Jr, 2016). Type I inhibitors, such as gefitinib, bind to the active conformation of the kinase (DFG-Asp-in, α C-helix-in) (Yun et al., 2007) (**Figure 1.6a**). Type I $\frac{1}{2}$ inhibitors, such as sunitinib, bind to the inactive conformation of the kinase (DFG-Asp-in, α C-helix-out) (Martin et al., 2012) (**Figure 1.6b**). Type II inhibitors bind to and stabilize the inactive form of the kinase (DFG-Asp-out), such as imatinib (Nagar et al., 2002) (**Figure 1.6c**).

In contrast, the non-ATP-competitive inhibitors or allosteric kinase inhibitors are defined as molecules that occupy a pocket outside the ATP binding site, with no interaction with the conserved hinge region which include type III and IV inhibitors (Roskoski Jr, 2016). Type III inhibitors, such as TAK-733, bind to an allosteric pocket adjacent to the ATP binding site (Dong et al., 2011) (**Figure 1.6d**). Type IV inhibitors bind to an allosteric pocket distant from the ATP binding site, such as GNF-2 (Zhang et al., 2010) (**Figure 1.6e**). However, some ATP-competitive inhibitors are allosteric by nature, as they bind to a pocket that stabilizes the inactive kinase conformation, hence blocking ATP binding.

Type V inhibitors are bivalent inhibitors, such as lenvatinib, which bind to two different pockets (Okamoto et al., 2014) (**Figure 1.6f**). While types I to V are reversible,

non-covalent inhibitors, type VI, such as afatinib, are irreversible, covalent, kinase inhibitors that target key cysteine residues within the catalytic domain (Solca et al., 2012) **(Figure 1.6g).**

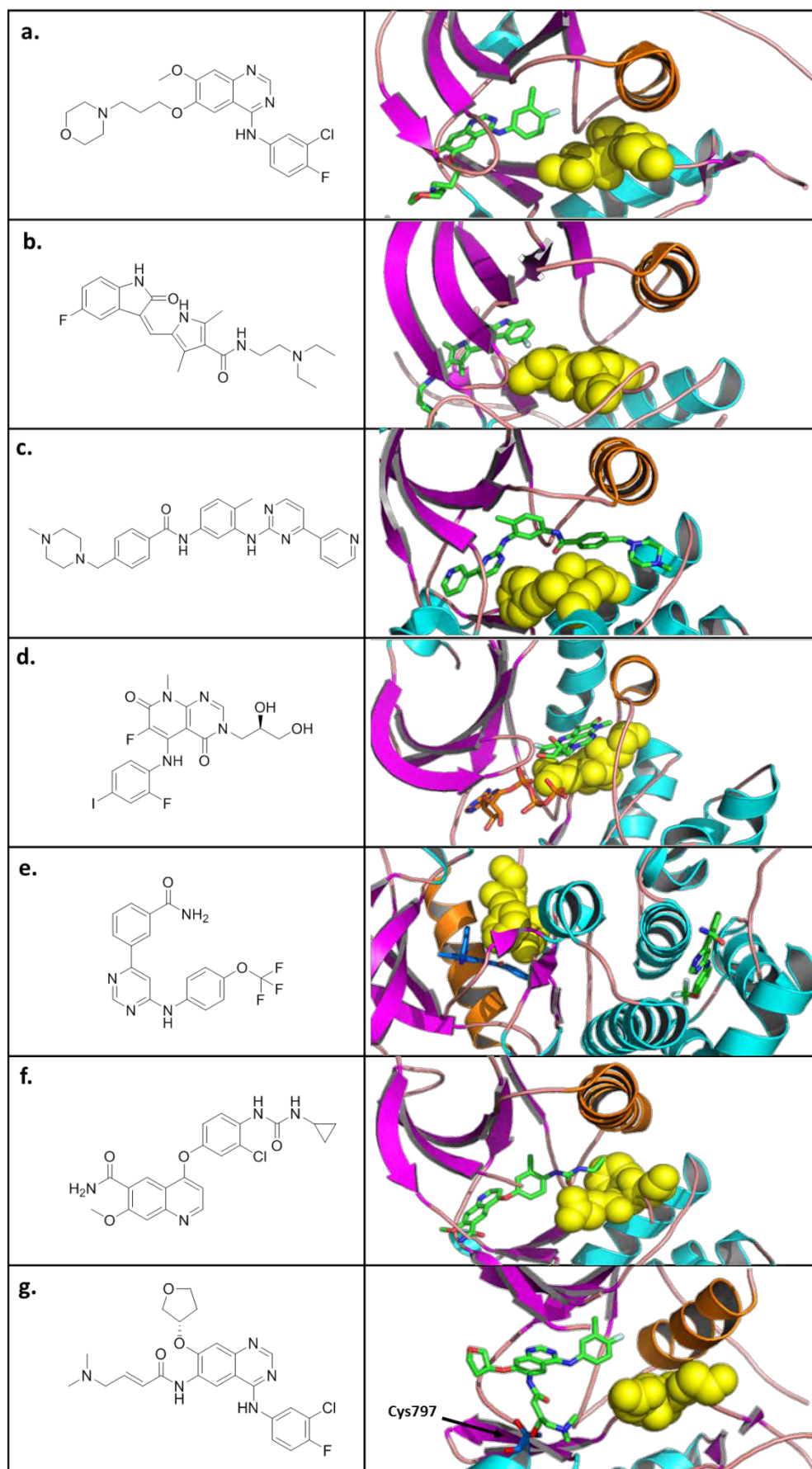


Figure 1.6: Chemical structures and binding modes of different protein kinase inhibitors.

(a) Chemical structure of gefitinib (type I inhibitor). EGFR kinase domain in complex with gefitinib (green) (on right) (PDB: 2ITY). (b) Chemical structure of sunitinib (type I_{1/2} inhibitor). CDK2 kinase domain in complex with sunitinib (green) (on right) (PDB: 3TI1). (c) Chemical structure of imatinib (type II inhibitor). c-Abl kinase domain in complex with imatinib (green) (on right) (PDB: 1IEP). (d) Chemical structure of TAK-733 (type III inhibitor). MEK 1 kinase domain in complex with TAK-733 (green) (on right) (PDB: 3PP1). (e) Chemical structure of GNF-2 (type IV inhibitor). c-Abl kinase domain in complex with GNF-2 (green) (on right) (PDB: 3K5V). (f) Chemical structure of lenvatinib (type V inhibitor). VEGFR2 kinase domain in complex with lenvatinib (green) (on right) (PDB: 3WZD). (g) Chemical structure of afatinib (type VI inhibitor). EGFR kinase domain in complex with afatinib (green) (on right) (PDB: 4G5J). Afatinib forms a covalent bond with Cysteine 797 (blue). DFG motif is shown in yellow spheres and the α C helix in orange colour. Figures were prepared using PyMOL 1.3.

1.2 Regulation of blood pressure by the WNK-SPAK/OSR1 signalling pathway

1.2.1 Hypertension

High blood pressure (hypertension) is a major health challenge and is recognized as the leading risk factor for fatal cardiovascular diseases, such as stroke, heart attack and heart failure (Bromfield and Muntner, 2013). Hypertension is defined as a systolic blood pressure > 130 millimetres of mercury (mmHg) and a diastolic blood pressure > 80 mmHg, whereas normal blood pressure should be $< 120/80$ mmHg (ACCFoundation, 2018). Accordingly, lowering blood pressure by 10 mmHg reduces the risk of cardiovascular events by 20% (Ettehad et al., 2016). Hypertension affects more than one billion people worldwide and the number increased greatly after the recent redefining of hypertension, which now includes stage 1 hypertension that was previously labelled pre-hypertension (McManus and Mant, 2018). Many aspects are involved in blood pressure regulation. These include internal factors, such as genetic susceptibility, as well as external factors, such as obesity and salt intake (Murthy et al., 2017). Indeed, the kidney plays a major role in maintaining normal blood pressure level. Several clinical, physiological and genetic studies have indicated that hypertension occurs when the kidney fails to excrete excess amounts of salts at the normal level of blood pressure (Wadei and Textor, 2012, Guyton, 1991).

Analyses of rare monogenic syndromes of hypertension provide an insight into the molecular mechanism of blood pressure regulation (Ehret and Caulfield, 2013). Familial hyperkalemic hypertension (FHHT) syndrome (also called Gordon syndrome) is among the monogenic types of hypertension and is characterized by hypertension, hyperkalemia, hypercalciuria and metabolic acidosis (Paver and Pauline, 1964). The clinical signs of

FHHt syndrome can be treated effectively with a low dose of a thiazide diuretic, which targets the thiazide-sensitive sodium (Na)-chloride (Cl) cotransporter (NCC) in the kidney (Mayan et al., 2002). On the other hand, Gitelman syndrome is an inverse phenotype of the monogenic form of hypotension, characterized by hypotension, hypokalemia, hypocalciuria and metabolic alkalosis (Simon et al., 1996b). Gitelman syndrome patients have loss-of-function mutations in NCC ion cotransporters (Simon et al., 1996b). Whereas, FHHt syndrome is caused by mutations in four connected genes: WNK1, WNK4, CUL3 (Cullin3) and KLHL3 (Kelch-like 3) (Boyden et al., 2012, Wilson et al., 2001). The genes encode enzymes that form part of the WNK-SPAK/OSR1 signalling cascade, the master regulator of ion homeostasis in the kidney and hence blood pressure regulation (Hadchouel et al., 2016, Alessi et al., 2014).

1.2.2 WNK-SPAK/OSR1 signalling pathway

The WNK-SPAK/OSR1 pathway is a novel signalling cascade composed of cytoplasmic serine-threonine kinases: with-no-lysine (K) kinases (WNKs); STE20/SPS1-related proline-alanine-rich protein kinases (SPAKs); and oxidative stress-responsive 1 (OSR1); as well as a series of sodium, potassium and chloride ion cotransporters (collectively referred to as cation- chloride cotransporters, or CCCs) (Alessi et al., 2014). This signalling pathway has been confirmed as a key regulator of human blood pressure (Murthy et al., 2017). The puzzle of the WNK-SPAK/OSR1 signalling pathway began in 2001 when Wilson and colleagues identified mutations in the genes encoding WNK1 and WNK4 as being responsible for a rare autosomal dominant hereditary form of hypertension, termed familial hyperkalemic hypertension (FHHt) syndrome, also known as Gordon syndrome or pseudohypoaldosteronism type 2 (PHAII) (Wilson et al., 2001). The sensitivity of Gordon syndrome to thiazide therapy, which underlines the

pathogenesis of the disease, highlights the importance of downstream targets. Therefore, research efforts have been dedicated to uncovering the complex relationship between the CCCs of the SLC12A family and WNK kinases (Richardson and Alessi, 2008). This section reviews the major components of WNK-SPAK/OSR1-CCCs signalling.

1.2.2.1 WNK kinases

WNK kinases (WNKs) are a unique subfamily of serine-threonine kinases that have atypical positioning of the conserved catalytic lysine residue when compared with all other protein kinases (Xu et al., 2000). As mentioned under Section 1.1.3 above, the catalytic lysine in protein kinases is usually located in subdomain II of the protein kinase domain (Knighton et al., 1991) (**Figure 1.7a**). However, in WNKs the catalytic lysine residue (Lys233) is located in subdomain I within the glycine-rich loop of the kinase domain. The normal position of the catalytic lysine residue in subdomain I corresponds to cysteine 250 (Cys250) in WNKs. This residue (Cys250) is unlikely to be involved in WNK catalytic activity (McCormick and Ellison, 2011). The unique position of the catalytic lysine in subdomain 1 may allow for phosphorylation of inaccessible substrates (He et al., 2007). The structure of the WNK kinase domain follows a classical bilobal structure and folding pattern. Despite the unusual position of the catalytic lysine, this residue is oriented towards the active site in the cleft, similar to what is observed in other protein kinases (**Figure 1.7b**) (Min et al., 2004).

In mammals, there are four WNK isoforms (1-4) encoded by different genes (Verissimo and Jordan, 2001, Wilson et al., 2001, Xu et al., 2000). All WNK members comprise an *N*-terminal kinase domain that is 85-95% homologous to the WNK1 kinase (**Figure 1.7d**) and forms a distinct branch of the phylogenetic tree of the human kinome (**Figure 1.1**) (Manning et al., 2002).

WNK1 was the first to be identified as a relatively large protein with 2,382 amino acids in length and a molecular weight of 250 kDa (Xu et al., 2000). In contrast, WNKs 2, 3 and 4 are approximately 2,297, 1,800 and 1,243 amino acids long, with a molecular weight of 240, 198 and 130 kDa, respectively (Verissimo and Jordan, 2001, Wilson et al., 2001, Xu et al., 2000). In addition to the kinase domain, WNKs possess an autoinhibitory domain and an autophosphorylation domain that regulate their basal kinase activity. Additionally, WNKs have other regions that contribute to protein interactions including two to three coiled-coil domains, proline-rich regions and short acidic motifs conserved among the WNK kinases (**Figure 1.7c**) (Huang et al., 2007).

A mutation within the acidic motifs of WNK4 (residues 557-567) causes Gordon syndrome (**Figure 1.7c**) (Richardson and Alessi, 2008, Wilson et al., 2001). The proline-rich sequence (PxxP) allows WNKs to interact with the Src homology 3 (SH3) domain containing proteins such as intersectin and ArhGAP12 (Okada et al., 2011, He et al., 2007).

WNKs in general have an ubiquitous expression profile in tissue and cell lines (McCormick and Ellison, 2011). However, the kidney-specific WNK1 (KS-WNK1) is a variant truncated form of WNK1 with predominant expression in the distal convoluted tubule in the kidney (Xu et al., 2002). Several studies have revealed that WNKs act as upstream regulators of the WNK signalling pathway and play critical roles in the regulation of cell signalling, survival, migration, and proliferation, organ development and, most importantly, the regulation of ion homeostasis and blood pressure (Huang et al., 2007, Shekarabi et al., 2017). To date, SPAK and OSR1 protein kinases are the only two validated physiological substrates of WNKs.

1.2.2.2 SPAK and OSR1 Kinases

SPAK (Sterile 20 [STE20]/SPS1-related proline/alanine-rich kinase) and OSR1 (oxidative stress responsive kinase 1) are two related mammalian members of the Ste20-related kinases of mitogen-activated protein kinase-like kinases (MAPK) (Ushiro et al., 1998, Tamari et al., 1999). In particular, they belong to the germinal centre kinase (GCK) VI subfamily of Ste20-related kinases, which is composed of four members: SPAK, OSR1, STRAD α , and STRAD β (**Figure 1.8**). Of the catalytic domain residues of SPAK/OSR1 and STRAD pseudokinases, 90.3% are conserved. However, STRAD pseudokinases lack key catalytic residues (Gagnon and Delpire, 2012).

SPAK and OSR1, referred to as STK39 and OXSR1 in GenBank, are highly related homologues and their primary amino acid sequences are 73% identical (**Figure 1.9**) (Marshall et al., 2005). They both possess a T-loop kinase domain in their *N*-terminal region that is 96% identical, similar to the other members of the Ste20 kinase subfamily. In addition to the kinase domain, SPAK and OSR1 kinases also share two highly conserved regulatory domains, known as the serine motif (S-motif) and the *C*-terminal regulatory domain (CCT). Unlike OSR1, SPAK has a unique extra *N*-terminal region that consists of 42 amino acid residues containing 24 alanine and 12 proline residues (Vitari et al., 2006). The S-motif, also called PF1 (PASK and Fray 1 (Drosophila homolog)), comprises 52 amino acids, and includes the highly conserved WEW (tryptophan-glutamic acid-tryptophan) motif, which mediates the association of the SPAK/OSR1 kinases to a scaffolding protein termed mouse only protein-25 (MO25) [also referred to as calcium binding protein 39 (CAB39)] (Filippi et al., 2011). The CCT domain, also called PF2, is 92 amino acids long and is 79% identical in sequence in both SPAK (residues 456-547) and OSR1 (residues 436-527). The CCT domain is required for the binding of SPAK and OSR1 to the specific RFX/[V/I] (Arg-Phe-Xaa-Val/Ile) motifs within both upstream activators (WNKs) and downstream substrates (CCC cotransporters). Downstream substrates include the Na⁺-Cl⁻ cotransporter (NCC), Na⁺-K⁺-2Cl⁻ cotransporters 1 and 2 (NKCC1 and NKCC2), and K⁺-Cl⁻ cotransporters (KCCs) (Vitari et al., 2006).


```

SP|Q9UEW8|STK39_HUMAN MAEPSPGSPVHVQLPQQAAPVTAAAAAPAAATAAPAPAPAPAPAPAPAAQAVGWPICR 60
SP|O95747|OXSRI_HUMAN -----MSEDSSALPWSINR 14
                                     :  :.*: * * *

SP|Q9UEW8|STK39_HUMAN DAYELQEVIGSGATAVVQAALCKPRQERVAIKRINLEKCQTSMDLLKEIQAMSQCCHPN 120
SP|O95747|OXSRI_HUMAN DDYELQEVIGSGATAVVQAAYCAPKKEKVAIKRINLEKCQTSMDLLKEIQAMSQCCHPN 74
                      * * * * * * * * * * * * * * * * * * * * * * * * * * * * * * * * * * * * * * * * * * *

SP|Q9UEW8|STK39_HUMAN VVTYYTSFVVKDELWLVMKLLSGGSMLDIIKYIVNRGEHKNGVLEEAIATILKEVLEGL 180
SP|O95747|OXSRI_HUMAN IVSYTTSFVVKDELWLVMKLLSGGSLVDIIKHIVAKGEHKSGVLDESTIATILREVLEGL 134
                      :*:*:*:*:*:*:*:*:*:*:*:*:*:*:*:*:*:*:*:*:*:*:*:*:*:*:*:*:*:*:*:*:*:*:*:*:*:*:*:*:*

SP|Q9UEW8|STK39_HUMAN DYLRHNGQIHRDLKAGNILLGEDGSSVQIADFGVSAFLATGGDVTRNKVRKTFVGTFCWMA 240
SP|O95747|OXSRI_HUMAN EYLHKNQIHRDVKAGNILLGEDGSSVQIADFGVSAFLATGGDITRNKVRKTFVGTFCWMA 194
                      :*:*:*:*:*:*:*:*:*:*:*:*:*:*:*:*:*:*:*:*:*:*:*:*:*:*:*:*:*:*:*:*:*:*:*:*:*:*:*:*

SP|Q9UEW8|STK39_HUMAN PEVMEQVRGYDFKADMWSFGITAEIATGAAPYHKYPPMKVLMMLTLQNDPPTLETGVEDK 300
SP|O95747|OXSRI_HUMAN PEVMEQVRGYDFKADIWSFGITAEIATGAAPYHKYPPMKVLMMLTLQNDPPSLETGVQDK 254
                      *****:*:*:*:*:*:*:*:*:*:*:*:*:*:*:*:*:*:*:*:*:*:*:*:*:*:*:*:*:*:*:*:*:*:*

SP|Q9UEW8|STK39_HUMAN EMMKKYGKSFRLKLLSLCLQKDPSKRPTAAELLKCKFFQAKKNREYLIEKLLTRTPDIAQR 360
SP|O95747|OXSRI_HUMAN EMLKKYGKSFRLKLLSLCLQKDPEKRPTAAELLRHKFFQAKKNKEFLQEKTLQAPTISR 314
                      **:*:*:*:*:*:*:*:*:*:*:*:*:*:*:*:*:*:*:*:*:*:*:*:*:*:*:*:*:*:*:*:*:*:*:*:*:*:*

SP|Q9UEW8|STK39_HUMAN AKKVRVPVPGSSGHLHKTEDGDWEWSDDDEMDEKSEEGKAAFSQEKSRVRKEENPEIAVSAS 420
SP|O95747|OXSRI_HUMAN AKKVRVPVPGSSGRLHKTEDGGWEWSDDDEFDEESEGKAAISQLRSPRVKESISNSSELFPT 374
                      *****:*:*:*:*:*:*:*:*:*:*:*:*:*:*:*:*:*:*:*:*:*:*:*:*:*:*:*:*:*:*:*:*:*:*

SP|Q9UEW8|STK39_HUMAN -----TIPEQIQS-----LSVHDSQGPPNAN-----EDYREASSCAV 452
SP|O95747|OXSRI_HUMAN TDPVGTLLQVPEQISAHLPQAPAGQIATQPTQVSLPPTAEPAKTAQALSSGSGSQETKIPI 434
                      :*:*:*:*:*:*:*:*:*:*:*:*:*:*:*:*:*:*:*:*:*:*:*:*:*:*:*:*:*:*:*:*:*:*:*:*:*

SP|Q9UEW8|STK39_HUMAN NLVLRRLRNSRKELNDIRFEFTPGRDADGVSQELFSAGLVDGHDVVIVAANLQKIVDDPK 512
SP|O95747|OXSRI_HUMAN SLVLRRLRNSKKELNDIRFEFTPGRDTAEGVSQELISAGLVDGRDLVIVAANLQKIVEEPQ 494
                      .*****:*:*:*:*:*:*:*:*:*:*:*:*:*:*:*:*:*:*:*:*:*:*:*:*:*:*:*:*:*:*:*:*:*:*

SP|Q9UEW8|STK39_HUMAN ALKTLTFKLASGCDGSEIPDEVKLIGFAQLSVS 545
SP|O95747|OXSRI_HUMAN SNRSVTFLKASGVEGSDIPDDGKLIGFAQLSIS 527
                      : : : : * * * * * * * * * * * * * * * * * * * * * * * * * * * * * * * * * *

```

Figure 1.9: Sequence alignment of human OSR1 and SPAK kinases. Key structural regions are highlighted: the proline/alanine-rich region of SPAK and the kinase domain, MO25 binding motif, regulatory C-terminal domain of both human SPAK and OSR1 are in red, yellow, light-green and grey, respectively. Amino acid sequences and alignments were retrieved from the UniProt database.

The structures of the conserved SPAK and the OSR1 kinase domains show that they adapt a canonical kinase fold similar to that of other protein kinases (Taylor IV et al., 2015, Lee et al., 2009, Torkamani et al., 2008). There is an overlap between both structures, with an overall root-mean-square deviation (RMSD) value of 0.99 Å (**Figure 1.10a**) (Taylor IV et al., 2015). This may suggest an overlap in their functions with respect to that of WNK1 (Dbouk et al., 2014). Moreover, both SPAK and OSR1 form a domain-swapped dimer in which the P+1 loop that is located in the C-terminus of the activation segment and the following α EF helix are swapped between dimer-related monomers (**Figure 1.10b and 1.10c**) (Taylor IV et al., 2015, Lee et al., 2009). The domain-swapped dimer occurs when one structural part of a protein molecule is exchanged with the identical part of the partner protein molecule (Li and Palmer, 2009). This structural feature is also observed in other Ste20-related kinases such as human SLK (Ste20-like kinase) and is suggested to be a possible mechanism for *trans*-autophosphorylation between two identical protein kinases (Pike et al., 2008).

Generally, SPAK and OSR1 display an overlap in their organ/tissue protein expression profiles (Delpire and Gagnon, 2008). However, they are distinct mRNA transcriptional levels. The expression of SPAK is found to be abundant in the brain, pancreas, salivary glands, adrenal glands and testes, and less in the heart, lung, kidney, stomach, intestine, ovaries, thymus, spleen, and skeletal muscle. In contrast, the expression of OSR1 is highest in heart and skeletal muscle, followed by the liver, small intestine and colon (Delpire and Gagnon, 2008).

Unlike OSR1, SPAK has three distinct isoforms (Murthy et al., 2017). The first isoform is full-length SPAK (FL-SPAK) and has ubiquitous tissue expression with higher expression in the heart, brain and testes (Rafiqi et al., 2010). The second isoform is

SPAK2, which lacks the *N*-terminal proline-rich region and part of the catalytic domain and is also expressed ubiquitously in tissues. The third isoform is kidney-specific SPAK (KS-SPAK) and is expressed only in the kidney (McCormick et al., 2011).

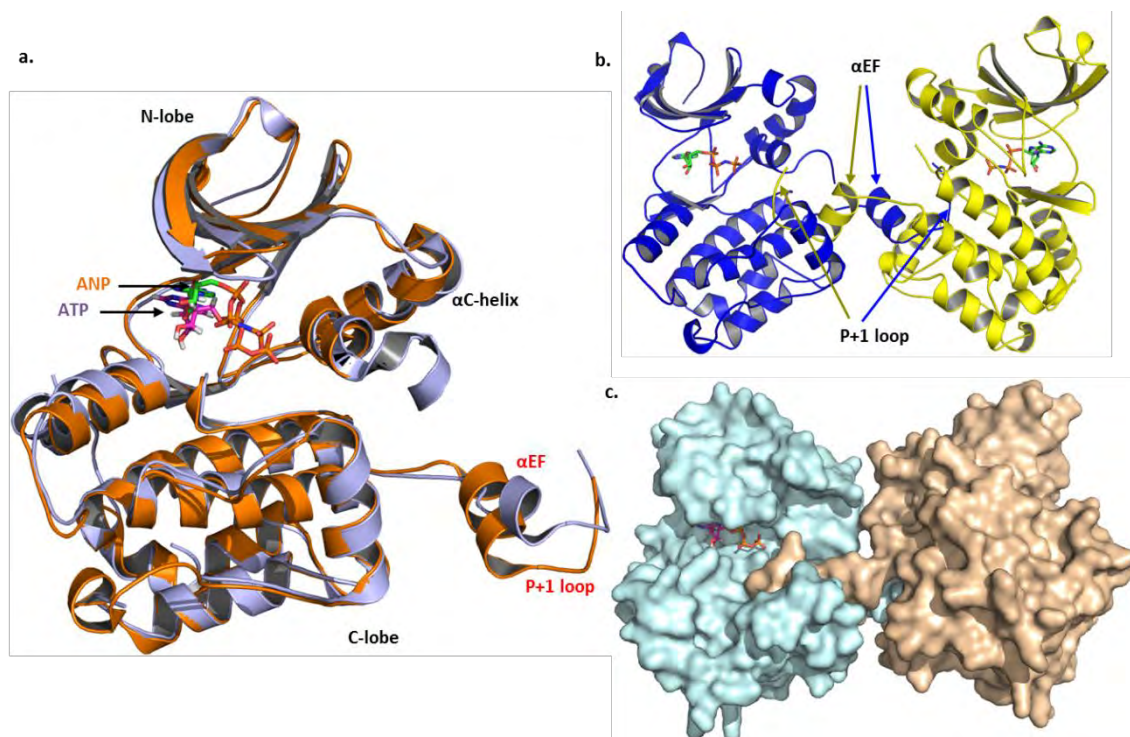


Figure 1.10: 3D structures of SPAK and OSR1 kinase domains. (a) A ribbon representation of the structural alignments of the OSR1 (orange) and SPAK (mauve) kinase domains. Structural elements involved in domain-swapped dimer are labelled in red. (b) A ribbon representation of the OSR1 kinase domain forming a domain-swapped dimer. Each monomer of OSR1 interacts with another identical monomer via the P+1 loop and α EF helix. (c) Molecular surface representation of the SPAK kinase domain forming a domain-swapped dimer. Structures were prepared using PyMOL 1.3 based on SPAK (PDB: 3DAK) and OSR1 (PDB: 5D9H) crystal structures.

1.2.2.3 Cation-Chloride Cotransporters (CCCs)

In epithelial cells, ion entry into and out of cells is mediated by specific plasma membrane proteins. The Na^+/K^+ -ATPase (Na^+ and K^+ -dependent adenosine triphosphatase) solute pump utilises ATP to control sodium exit and potassium entry into cells against their concentration gradients (primary active transporters). This process generates electrochemical gradients that constitute a driving force for Na^+ influx and K^+ efflux, which allows these ions to transport alone or coupled with a partner anion (Cl^-) following their gradients via secondary ion transporters. Secondary ion transporters are very active in terms of transcellular ion transport, in which one cation (Na^+ or K^+) is coupled with one chloride ion (Cl^-). This process occurs with a stoichiometry of 1:1 to maintain the transmembrane potential without change, which is why these types of transports are referred to as electroneutral CCCs (Gamba, 2005).

The CCCs of the solute carrier family 12A (SLC12A) are divided into two main types: Cl^- -importing and Na^+ -driven cotransporters (NCC, NKCC1 and NKCC2, collectively known as N[K]CCs), and Cl^- -exporting, K^+ -driven cotransporters (KCC1–4, collectively known as KCCs) (Arroyo et al., 2013). The Na^+ -2 Cl^- cotransporter (NCC) is the major cotransporter encoded by the SLC12A3 gene and is also called a thiazide-sensitive cotransporter because it is the specific target for known thiazide diuretics. NCCs are widely expressed in the kidney, where their main function is to control salt reabsorption in the distal convoluted tubule (DCT) (Moes et al., 2014). In contrast, the Na^+ - K^+ - Cl^- cotransporter (NKCC1) and Na^+ - K^+ -2 Cl^- cotransporter (NKCC2) are encoded by SLC12A2 and SLC12A3 genes, respectively, and are both inhibited by furosemide (loop diuretics). NKCC1 is expressed in various tissues, including the heart, vascular smooth muscle, and endothelial cells (Arroyo et al., 2013). In addition to the role

of NKCC1 as a clinical target for known loop diuretics, bumetanide, several *in vivo* studies have demonstrated its effect on the regulation of smooth vascular muscle tone (Meyer et al., 2002). NKCC2 is a kidney-specific carrier and is the master regulator of salt reabsorption in the thick ascending limb (TAL) of the loop of Henle (Arroyo et al., 2013). A mutation in NKCC2 causes a Mendelian hereditary disorder resembling Gitelman syndrome, which is termed Bartter syndrome type II (Simon et al., 1996a). On the other hand, K^+ - Cl^- cotransporters (KCC1-4) are encoded by SLC12A4, SLC12A5, SLC12A6, and SLC12A7, respectively (Gamba, 2005). A mutation in KCC3 is detected in Andermann syndrome, which is characterized by seizures and motor and sensory neuropathies (Howard et al., 2002).

The balance between N[K]CCs and KCCs in maintaining the intercellular chloride ion has significant implications for different physiological processes, including transcellular ion transports, cell volume regulation and neuronal excitability (Alessi et al., 2014). Accordingly, a decrease in intracellular Cl^- ions induces the activation of N[K]CCs and the deactivation of KCCs by phosphorylation. In contrast, an increase in intracellular Cl^- ions induces the deactivation of N[K]CCs and the activation of KCCs by dephosphorylation. This tightly controlled process suggests the involvement of the Cl^- -sensitive protein kinase that is found in the WNKs family (Hadchouel et al., 2016).

1.2.2.4 Regulation of WNK Signalling

WNKs are positively regulated by several factors including salt intake, cell volume and thickness and extracellular osmotic pressure as well as by some hormones such as aldosterone, angiotensin II, vasopressin and insulin (Uchida et al., 2014). In cell culture, WNKs can be activated by either hypoosmotic (hypotonic low-chloride conditions, which induce cell swelling and Cl^- efflux) or hyperosmotic stress (which

induces cell shrinking and Cl^- influx) (Richardson and Alessi, 2008). WNK1 activation induces phosphorylation at serine residue 382 (Ser382) located within its *N*-terminal T-loop (kinase domain). Consistent with this, a mutation of Ser382 into Ala abolishes WNK1 activity whereas its mutation into glutamate produces a constitutively active kinase (Zagórska et al., 2007). In addition, the stimulation of WNK1 and WNK4 kinases triggers their translocation to ‘vesicular structures’ (trans-Golgi-network derived vesicles or recycling endosomes), a process mediated by the WNK non-catalytic *C*-terminal domain (Shaharabany et al., 2008, Zagórska et al., 2007). However, the implications of WNK relocation for WNK function are still unknown (Richardson and Alessi, 2008).

The mechanism by which WNKs sense intracellular chloride is not fully understood (Dbouk et al., 2016). Recent studies have suggested the presence of catalytic lysine in subdomain I that might be involved in sensing intracellular Cl^- concentration by WNK1 (Piala et al., 2014). The Cl^- ion blocks autophosphorylation and stabilizes the inactive conformation of WNK1 by binding to a small pocket formed by two leucine residues, Leu369 and Leu371, within the activation loop in the kinase domain (Piala et al., 2014). Notably, the decrease in intracellular Cl^- concentration in a hypoosmotic condition activates all WNK isoforms to different extents depending on the level of reduction in Cl^- concentration (Terker et al., 2016, Bazúa-Valenti et al., 2015, Piala et al., 2014). The latter places WNKs as common intracellular-chloride sensors (Huang and Cheng, 2015). On the other hand, the activation of WNK1 kinase by hyperosmotic stress could result from an indirect mechanism in which WNK4 signalling, the negative regulator of WNK1, is inhibited by increasing the intracellular Cl^- ion concentration more than the WNK1 signalling inhibition thereby stimulating WNK1 activity (Dbouk et al., 2016).

The second mechanism of WNK regulation is through controlling its abundance by the ubiquitin-proteasome system (Ohta et al., 2013). This system involves a scaffolding protein known as cullin3 (CUL3), which binds to another key protein called Kelch-like 3 (KLHL3), which acts as a substrate recognition protein to form the CUL3-KLHL3 E3 ubiquitin-ligase complex. This complex acts as an upstream regulator of WNKs by recruiting WNKs for ubiquitination through binding to the conserved acidic motifs to induce their proteasome-dependent degradation (Wakabayashi et al., 2013, Shibata et al., 2013, Ohta et al., 2013).

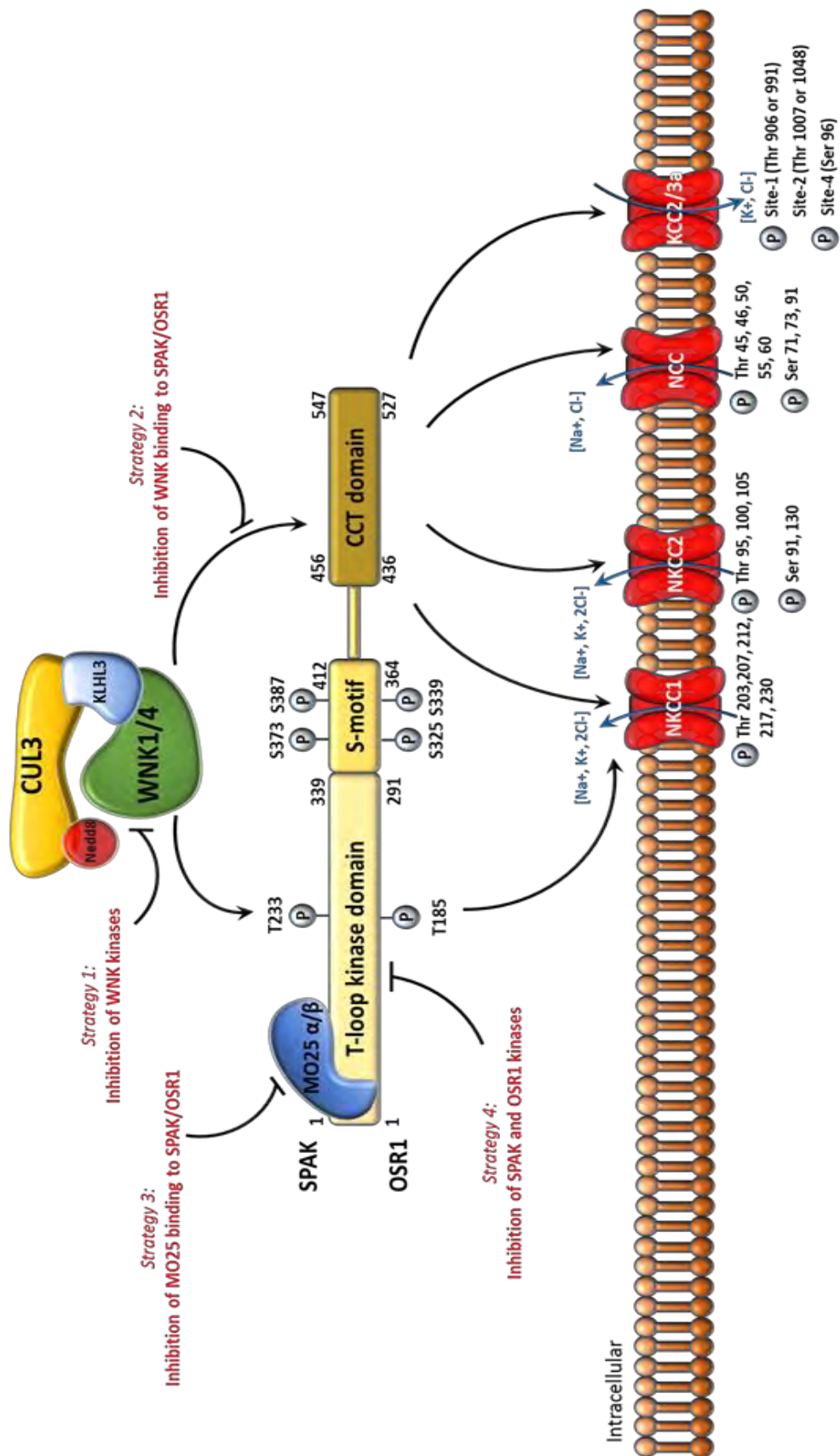


Figure 1.11: Regulation of the WNK-SPAK/OSR1 signalling pathway. CUL3 assembles with KLHL3 to form a cullin-RING E3 ubiquitin-ligase complex that mediates the ubiquitination of WNKs. WNK 1-4 phosphorylate SPAK and OSR1 kinases on their T-loops, Thr233 and Thr185, respectively. Subsequently, SPAK and OSR1 bind MO25, a scaffolding protein (there are two isoforms of human MO25: α and β). Active SPAK and OSR1 in a complex with MO25 phosphorylate a selection of CCCs at different phosphorylation sites. The current strategies (1-4) discovered among WNK-signalling inhibitors are highlighted. Ub: ubiquitin. S-motif: Serine-motif. CCT: conserved C-terminal. Figure adapted from (AlAmri et al., 2017b).

WNK activation triggers SPAK and OSR1 C-terminal domains (CCT) to interact with specific motifs within upstream WNKs, termed RFX[V/I]. All WNK isoforms contain at least two RFX[V/I] motifs (**Figure 1.7**) (Gagnon et al., 2007, Vitari et al., 2006, Gagnon et al., 2006). In addition to its role as a multi-purpose docking site for different substrates, the CCT domain is involved, crucially, in regulating the basal SPAK and OSR1 kinase activity via the stabilization of inactive conformation in the absence of WNKs stimulation (Li et al., 2014). Subsequently, WNKs activate SPAK and OSR1 through phosphorylation of two conserved threonine and serine residues: threonine 233 (Thr233) in SPAK and threonine 185 (Thr185) in OSR1, which exist within the catalytic T-loop domains, as well as serine 373 (Ser373) in SPAK and serine 325 (Ser325) in OSR1, which are located within the S-motif (**Figure 1.11**) (Vitari et al., 2005). In addition, the activation of SPAK and OSR1 facilitates recruitment of MO25, an adapter protein, that binds to WEW (tryptophan-glutamic acid-tryptophan) residues in the S-motif region and enhances the basal kinase activity of SPAK and OSR1 (**Figure 1.9**) (Filippi et al., 2011). A mutation of Thr233 in SPAK or Thr185 in OSR1 into Ala prevents their activation by WNKs, whereas their mutation into glutamate (mimicking endogenous phosphorylation) increases their basal activity and prevents further activation by WNKs (Zagórska et al., 2007, Vitari et al., 2006). In contrast, the mutation of Ser373 in SPAK and Ser325 in OSR1 into Ala did not affect their activation by WNKs (Zagórska et al., 2007, Vitari et al., 2006). Although the role of phosphorylation sites located in the S-motif is still not clear, Thr233 in SPAK and Thr185 in OSR1 are recognized as the on and off switches for the WNK signalling pathway (Richardson and Alessi, 2008). Moreover, the phosphorylation and activation of SPAK and OSR1 by WNKs stimulates the phosphorylation of serine and threonine residues located in the C-terminal close to

the RFX[V/I] motifs in WNKs, such as serine 1261 (Ser1261) and threonine 1020 (Thr1020) in WNK1 and WNK4, respectively. Such an event leads to the dissociation of the WNK-SPAK/OSR1 complex by releasing the SPAK and OSR1 CCT from upstream activators (WNKs) (Zagórska et al., 2007, Villa et al., 2007).

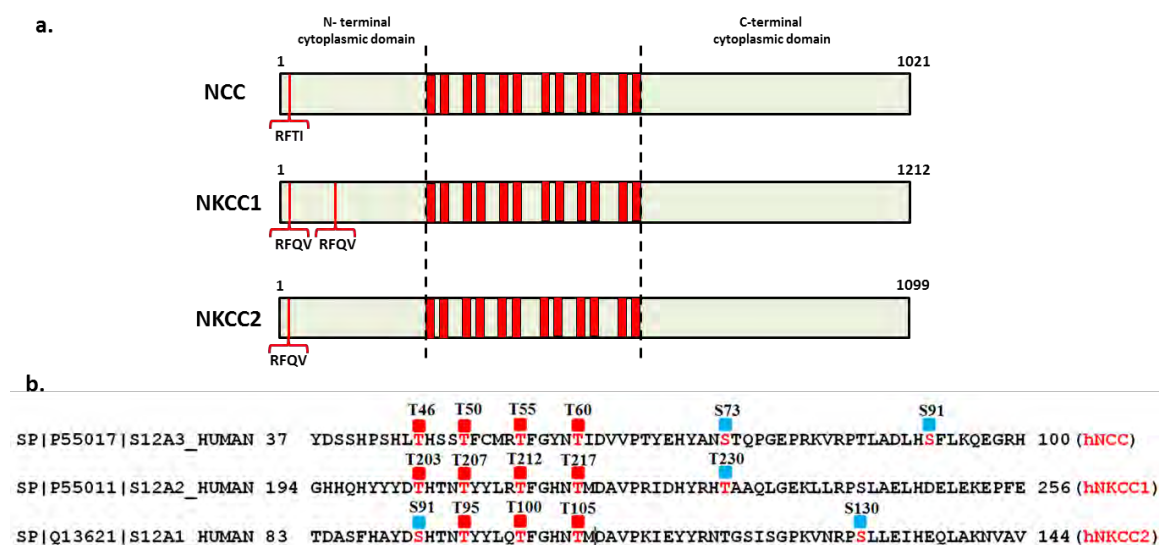


Figure 1.12: Structural analysis of SLC12A cotransporters. (a) Domain structure of NCC, NKCC1 and NKCC2. Red regions represent transmembrane domains between *N*- and *C*-terminal cytoplasmic domains. **(b)** Sequence alignment of residues from the *N*-terminal of human NCC, NKCC1 and NKCC2. Phosphorylation sites are illustrated in red and marked with red symbols for identical residues or blue symbols for non-identical residues. The numbers above the symbols indicate the residue number in the protein sequences. Amino acid sequences and alignments were retrieved from the UniProt database.

As a consequence, active SPAK and OSR1 act as upstream activators for the downstream SLC12A family of ion cotransporters (NCC, NKCC1 and NKCC2) (Moriguchi et al., 2005). SPAK and OSR1 interact with WNKs and ion cotransporters through their C-terminal domains in the same manner (Vitari et al., 2006). While distribution of RFX[V/I] motifs in WNKs varies, the RFX[V/I] motifs in NCC, NKCC1 and NKCC2 cotransporters are located in their N-terminal domains (**Figures 1.7 and 1.12**) (Vitari et al., 2006). Unlike NCC and NKCC2, NKCC1 possesses two RFX[V/I] motifs and has a low expression profile in the kidney (Gagnon et al., 2007). Interestingly, most SPAK and OSR1 phosphorylation sites on NCC, NKCC1 and NKCC2 are highly conserved suggesting that SPAK and OSR1 regulate the phosphorylation and activation of cotransporters through the same mechanism (**Figure 1.12**) (Richardson and Alessi, 2008). Human NKCC1 is activated by SPAK and OSR1 through the introduction of phosphate groups at several conserved threonine residues within its N-terminal domain (Thr203, Thr207, Thr212, Thr217 and Thr230) (Vitari et al., 2006, Darman and Forbush, 2002). Indeed, phosphorylation of NKCC1 at Thr203/Thr207/Thr212 is essential for maximal transporter activity (de los Heros et al., 2014).

Similarly, NCC directly interacts with and is phosphorylated by active SPAK and OSR1 at multiple conserved residues (Thr46, Thr50, Thr55, Thr60, Ser73 and Ser91) within its N-terminal domain (Yang et al., 2010, Richardson et al., 2008). A mutation of Thr60 in NCC, which is equivalent to Thr217 in human NKCC1, prevents activation of NCC in cells (Richardson et al., 2008). In humans, the mutation of Thr60 into Met causes Gitelman syndrome (Maki et al., 2004). In contrast, activation of NKCC2 by SPAK and OSR1 results from its phosphorylation at various residues (Thr95, Thr100, Thr105, Ser91 and Ser130) (Ponce-Coria et al., 2008, Giménez and Forbush, 2005). Notably, Thr100

and Thr105 in human NKCC2 are equivalent to Thr212 and Thr217 in human NKCC1 and Thr55 and Thr60 in human NCC (Rinehart et al., 2005, Giménez and Forbush, 2005). These serial phosphorylation events induce the translocation of ion cotransporters from intercellular vesicles to the plasma membrane surface (Cai et al., 2006). This is suggested to be the proposed mechanism by which WNK-SPAK/OSR1 signalling controls and regulates ion cotransporters (Richardson and Alessi, 2008).

1.3 Validation of the WNK-SPAK/OSR1 signalling pathway as a novel target for the treatment of hypertension

Human genetic data and animal disease models are essential tools for target identification and validation (Sweis, 2015). Accordingly, genetic studies of various components of WNK-SPAK/OSR1 signalling transduction have demonstrated the crucial role of this pathway in the regulation of blood pressure. Starting with the upstream regulators of WNK kinases in humans, a defective CUL3-KLHL3 E3 ligase complex exhibiting a Gordon syndrome phenotype with severe signs and symptoms was compared with that caused by mutations in WNK1 and WNK4 (Hadchouel et al., 2016). The mutation in KLHL3 caused a dominant or recessive form of the disease state while the mutation in CUL3 caused the most severe form of Gordon syndrome (Boyden et al., 2012). Consistent with this, KLHL3^{R528H/} knock-in mice expressing KLHL3 with a mutation in Arg528 into His (mimicking human FHt disease) exhibited salt-sensitive hypertension, hyperkalaemia and metabolic acidosis with a significant increase in the expression of WNK1 and WNK4. This mutation is found to prevent the binding of KLHL3 to the acidic motif of WNKs thereby inhibiting WNK degradation (Susa et al., 2014). In addition, a mouse model with a deletion mutation in Cullin3 (residues 403-459) (mimicking human FHt disease) was suggested to induce the degradation of KLHL3

leading to increased WNK expression levels and severe Gordon syndrome (Schumacher et al., 2015).

On the other hand, mutations in WNKs caused an increase in salt reabsorption and hypertension as a result of a significant increase in the expression of corresponding proteins. In humans, the gain-of-function mutation in WNK1 is caused by a large deletion of the first intron of the gene which leads to an increase in WNK1 protein abundance. Consistent with human genetic studies, WNK1^{+/^{FHHt}} mouse models (mimicking human FHHt disease) exhibited an FHHt phenotype due to the altered effects of WNK1 in the function of the distal nephron ion cotransports along with an increase in WNK1 expression specifically in the distal convoluted tubule (DCT) and connecting tubule (CNT) (Vidal-Petiot et al., 2013). In contrast, heterozygous deletion of WNK1 (WNK1^{+/-}) in mice exhibited a significant reduction in blood pressure (Zambrowicz et al., 2003). Whereas a mouse model homozygous for the WNK1 mutation (WNK1^{-/-}) died due to embryonic development defects, homozygous (KS-WNK^{-/-}) knock-out mice displayed salt-sensitive hypertension along with an increase in the activity of NCC (Liu et al., 2010, Zambrowicz et al., 2003).

In the case of WNK4, several missense mutations in the acidic motif of WNK4 have been identified in humans. These mutations impair the binding of WNK4 to KLHL3 thereby inhibiting WNK4 degradation (Ohta et al., 2013). Consistent with this observation in humans, WNK4^{D561A/+} knock-in mice (mimicking human FHHt disease) manifested FHHt syndrome. This mutation impaired WNK4 binding to KLHL3, thereby increasing free WNK4 protein abundance (Yang et al., 2007). In contrast, mice overexpressing WNK4 displayed a Gitelman syndrome-like phenotype (Lalioti et al., 2006). The findings from this last study may support the hypothesis that WNK4 is a

negative regulator of WNK1.

SPAK has been identified as a novel hypertension susceptibility gene due to a strong association between common variants of SPAK and blood pressure (Wang et al., 2009). Furthermore, SPAK homozygous ($\text{SPAK}^{-/-}$) and heterozygous ($\text{SPAK}^{+/-}$) knock-out variants are viable and exhibited a significant decrease in total and phosphorylated NCC in the kidney as well as p-NKCC1 in aortic tissue and blood vessels. This led to an increased salt and water excretion and a vasodilation effect, respectively, which led to a remarkable reduction in blood pressure in mice (Yang et al., 2010). Notably, a deletion mutation of $\text{SPAK}^{-/-}$ in mice resulted in a significant increase in p-OSR1, total NKCC2, and p-NKCC2 (Yang et al., 2010). In addition, $\text{SPAK}^{\text{T243A/T243A}}$ knock-in mice displayed low blood pressure along with a significant decrease in total and phosphorylated NCC and NKCC2 (Rafiqi et al., 2010).

Unlike SPAK, homozygous ($\text{OSR1}^{-/-}$) knock out was lethal at the embryonic stage and caused defective angiogenesis and cardiovascular development (Xie et al., 2013). However, mice with a heterozygous deletion of OSR1 ($\text{OSR1}^{+/-}$) were viable with significant reduction in p-NKCC1 in aortic tissue and kidney and exhibited low blood pressure. In addition, the homozygous deletion of kidney tubule-specific (KSP) OSR1 ($\text{KSP-OSR1}^{-/-}$) presented a Bartter-like syndrome due to the decrease in the phosphorylation and activity of NKCC2 in the TAL and increased abundance and activity of NCC (Lin et al., 2011).

Collectively, the above biochemical and genetic studies support the notion that targeting the WNK-SPAK/OSR1-SLC12A signalling cascade with small-molecule inhibitors provides an attractive opportunity for discovering a novel class of antihypertensive agents (Alessi et al., 2014).

1.4 Strategies for inhibiting WNK-SPAK/OSR1 signalling

Effective control of hypertension is a significant clinical challenge (Jaffe et al., 2013). Indeed, 30% of hypertensive people develop resistant hypertension, which is an advanced and complicated form of the disease that is defined as uncontrollable hypertension despite adherence to a combination of three or more antihypertensive drugs (Calhoun et al., 2008). Despite evidence that optimal hypertension care and therapy can lead to adequate control of high blood pressure and prevent potential cardiovascular complications, such results are not achieved in many cases. The difficulty in controlling hypertension using currently available medications stems from allergies to some of the current approved antihypertensive agents as well as intolerable side effects and high drug-drug interaction profiles, which affect patients' compliance with these often life-long management plan (WHO, 2013).

Consequently, the limitations of the available antihypertensive drugs, as well as current advances in the understanding of the genetic basis of the disease state, have prompted considerable interest in discovering and developing new antihypertensive medications with novel mechanisms of action, better efficacy and tolerability as well as favourable toxicity profiles (Patterson et al., 2014). For the past 15 years, WNK signalling has been intensively studied as a novel approach in the development of a new class of antihypertensive agents. The inhibition of WNK signalling may reduce high blood pressure by the dual mechanisms that combine diuretic and vasodilation effects. This is because WNK signalling inhibitors would inhibit all three ion cotransporters: NCC, NKCC1 and NKCC2. Notably, simultaneous inhibition of NCC and NKCC2 would synergistically increase the potency of such inhibitors because NCC and NKCC2 mediate around 25% of total salt reabsorption in the kidney as well as overcome the major side

effect associated with solo thiazide therapy use (i.e. potassium wasting) (Alessi et al., 2014). In addition, WNK-SPAK/OSR1-SLC12A inhibitors would exert a greater impact particularly in the treatment of hypertensive patients with hyperaldosteronism or hyperinsulinaemia (Nishida et al., 2012). Currently, four molecular targets are exploited to inhibit WNK signalling (**Figure 1.11**) (AlAmri et al., 2017b). This section discusses the current approaches used to inhibit WNK signalling and the different reported WNK signalling small-molecule inhibitors.

1.4.1 Targeting WNK kinases

Based on their mode of action, current WNK inhibitors can be divided into ATP-competitive and non-ATP-competitive (allosteric) (AlAmri et al., 2017b).

1.4.1.1 ATP-competitive inhibitors of WNK kinases

As mentioned under section 1.2.2.1, WNK kinases possess a unique ATP binding site. The crystal structure of inactive WNK1 (Ser382), in which autophosphorylation is prevented by the mutation of Ser382 into Ala, illustrates that the presence of the catalytic lysine (Lys233) within the glycine-rich loop places it 13 Å away from the key glutamic acid (Glu268) in the α C helix. Therefore, a large pocket at the back of the ATP binding site near the cysteine residue (Cys250) in subdomain I exists (**Figure 1.7b**) (Min et al., 2004). This structural feature has been exploited in the design of selective small molecule inhibitors that target the ATP binding site of WNK kinases (AlAmri et al., 2017b).

The first selective pan-inhibitor of WNK kinases was recently reported (Yamada et al., 2016a). A high-throughput screening approach was utilised to screen the Novartis chemical library, which consists of ~1.2 million compounds. This exercise led to the identification of hit compound (hit 1), IC_{50} = 856 nM, as a promising WNK1 inhibitor *in*

vitro (**Figure 1.13a**). Further optimisation steps led to the discovery of a more potent and orally bioavailable inhibitor, WNK463, which inhibited all WNK isoforms in the low-nanomolar concentration range (WNK1 IC_{50} = 5 nM, WNK2 IC_{50} = 1 nM, WNK3 IC_{50} = 6 nM, WNK4 IC_{50} = 9 nM) (**Figure 1.13a**). In cells, WNK463 inhibited the endogenous WNK kinases at 106 nM. WNK463 was selective for WNK kinases when screened against a large panel of kinases at a high concentration of 10 μ M, as only two out of 442 human kinases screened exhibited > 50% inhibition. Structural studies suggested that WNK463 binds to WNK kinases with high affinity regardless of their phosphorylation state. Remarkably, the co-crystal structure of WNK463 with the kinase domain of WNK1 S382A indicated that WNK463 binds to the hinge region of the ATP binding site and extends towards the WNK-specific back pocket through a narrow tunnel, which takes place as a result of the unusual placement of the catalytic lysine residue within subdomain I in the glycine-rich loop (**Figure 1.13b**). Subsequent *in vivo* studies on spontaneously hypertensive rats (SHRs) have demonstrated that WNK463 causes a dose-dependent decrease in blood pressure and an increase in rat heart rate. In addition, there was a dose-dependent increase in urine output along with Na^+ and K^+ excretion rates. In mouse models overexpressing human WNK1, WNK463 caused a significant reduction in blood pressure. In mice kidney lysate samples, a dose-dependent decrease in the phosphorylation of the WNK substrates, SPAK and OSR1 kinases, was observed. The latter provided a compelling evidence that the observed effects caused by WNK463 were due to the inhibition of WNK kinases *in vivo* (Yamada et al., 2016a).

Despite promising *in vitro* and *in vivo* results, the development of WNK463 into a potential clinical antihypertensive drug candidate was discontinued due to preclinical safety profile issues (Yamada et al., 2016a). These were most likely due to the ubiquitous

expression of WNK kinases, WNK1 in particular, as well as the lack of WNK463 selectivity across the four isoforms of WNK kinases, which might have key roles in other biological and physiological processes beyond blood pressure regulation (AlAmri et al., 2017b).

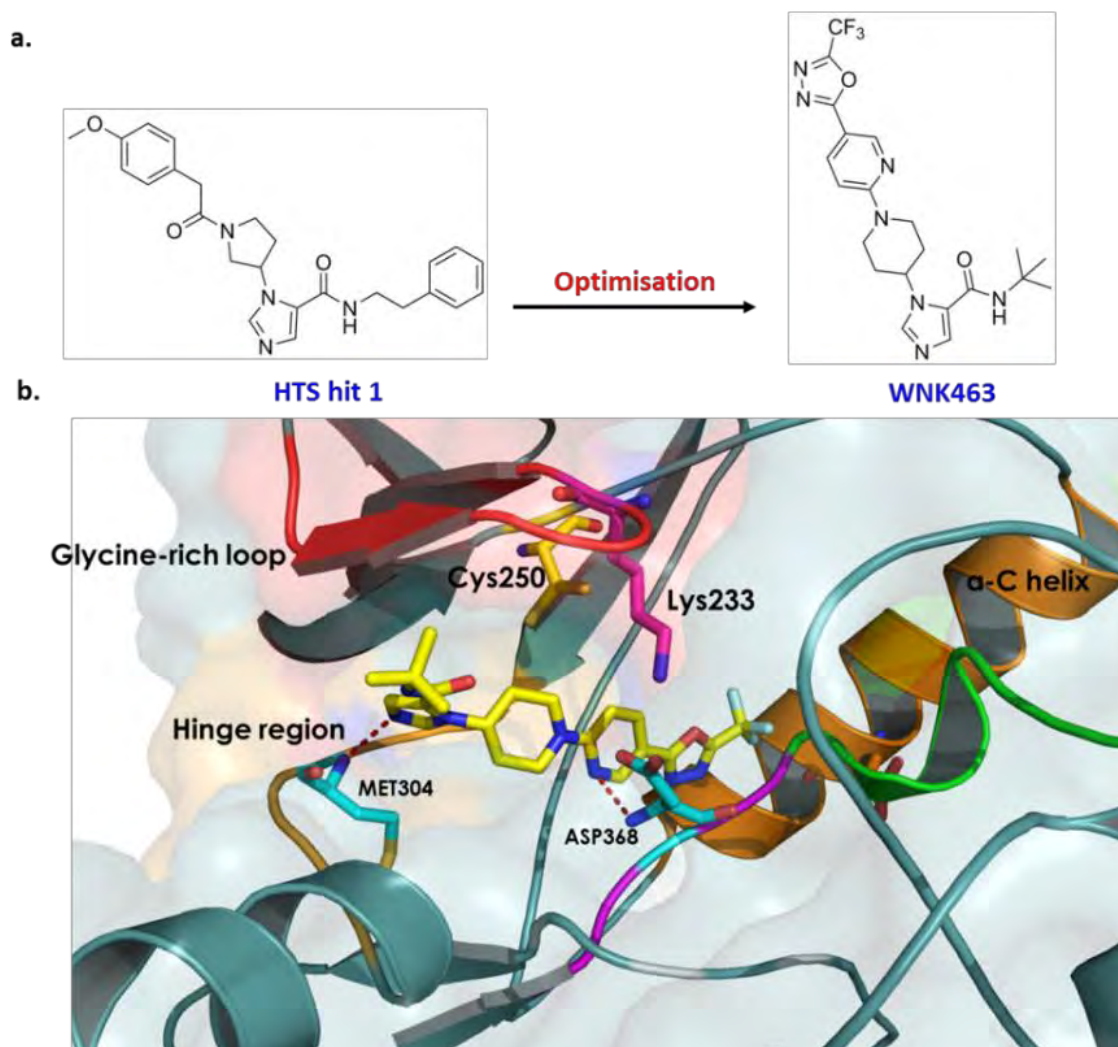


Figure 1.13: Discovery of a WNK kinase ATP-competitive inhibitor. (a) ChemDraw Professional 15.1 was used to draw the chemical structures of hit 1 and WNK463. (b) Crystal structure of the WNK1 kinase domain in a complex with WNK463 (yellow) (PDB code: 5DRB). Figure adapted from (AlAmri et al., 2017b).

1.4.1.2 Non-ATP Competitive (Allosteric) Inhibitors of WNK Kinases

The same Novartis group also discovered the first allosteric inhibitor of WNK kinases (Yamada et al., 2016b). Unlike the inhibition of protein kinases by targeting the ATP binding site, allosteric inhibition is a valuable approach to improving the selectivity profile of an inhibitor by targeting less conserved regions within the protein kinase. As a result of the lack of structural information about allosteric sites on WNK kinases, the rational design of such an inhibitor is limited (AlAmri et al., 2017b). Accordingly, a high-throughput screening of the Novartis chemical library was conducted at a high ATP concentration, which led to the identification of compound 1 (**Figure 1.14a**). This compound exhibits a good selectivity profile for the WNK1 kinase across a panel of 31 protein kinases. Further medicinal chemistry optimisation led to the design of compound 2 (WNK476), which is a selective inhibitor for all WNKs (1-4) with an average IC_{50} of 0.570 μ M at different ATP concentrations suggesting that it binds to an allosteric site (**Figure 1.14a**). The crystal structure of WNK1 in a complex with WNK476 (PDB ID: 5TF9) revealed that it binds to an allosteric pocket adjacent to the ATP binding site displaying a type III-like allosteric binding mode (DLG-in/ α C-out) conformation (**Figure 1.14b**). In cells, WNK476 exhibited potent inhibition of ion-cellular uptake by NKCC1 in a dose-dependent manner (Yamada et al., 2016b).

Despite these encouraging *in vitro* results, WNK476 had poor pharmacokinetic profiles and so was not taken into further *in vivo* studies. Nevertheless, further structure-activity relationship studies led to the discovery of a potent allosteric WNK inhibitor, compound 11, with a good selectivity profile when tested against a panel of 442 protein kinases (**Figure 1.14c**). Interestingly, compound 11 was a 1000-fold more selective for

WNK1 than WNK4 and 57-fold over WNK2. In rats, this compound exhibited low bioavailability and moderate clearance. Moreover, the deuterated analogue of compound 11, namely, compound 12, has been synthesized to improve pharmacokinetic profiling studies (**Figure 1.14c**). Accordingly, in transgenic mice overexpressing human WNK1, oral dosage of compound 12 produced a significant reduction in systolic blood pressure in a dose-dependent manner. Furthermore, in SHRs treated with compound 12, dose-dependent diuresis, natriuresis and kaliuresis were observed (Yamada et al., 2017). These results provided further evidence that allosteric inhibition of WNK protein kinase activities results in a robust reduction in blood pressure.

The discovery of the above compounds indicates that WNK protein kinases can be targeted efficiently with potent and selective small-molecule inhibitors. However, achieving selectivity within the four WNK isoforms still poses a challenge. Therefore, the lack of selectivity across WNK isoforms may have contributed to the unexpected *in vivo* side effects observed, especially with WNK kinase ATP-competitive inhibitors such as WNK463 (AlAmri et al., 2017b).

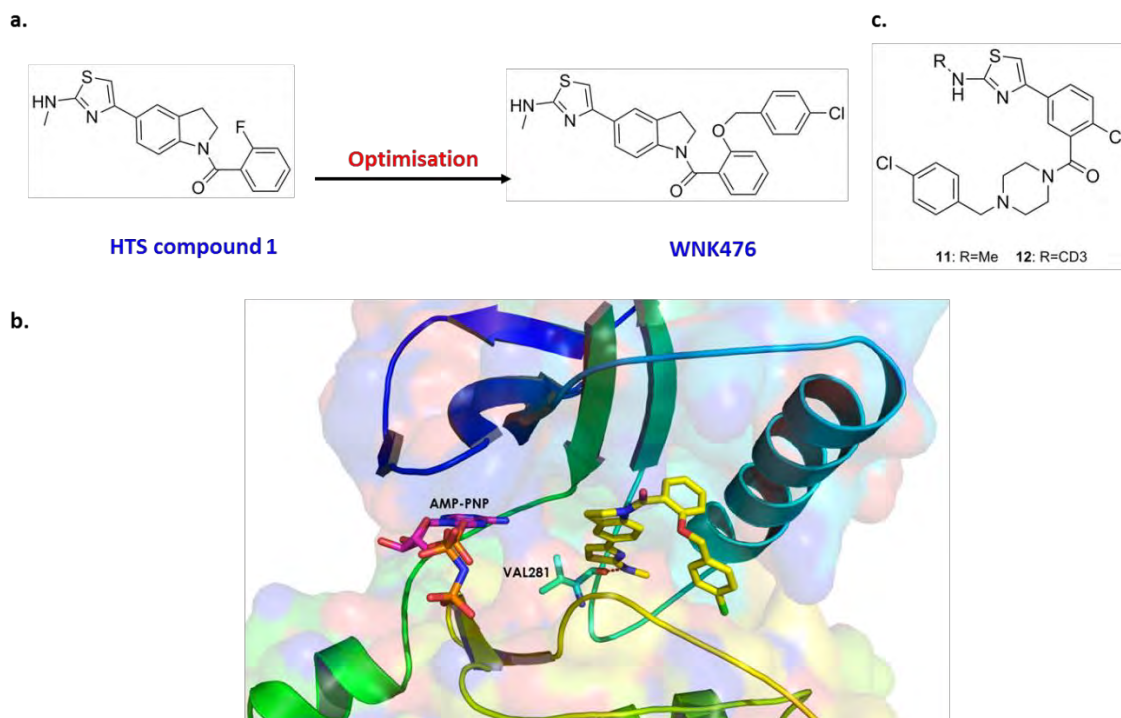


Figure 1.14: Discovery of a WNK kinase allosteric inhibitor. (a) Chemical structure of compound 1 and WNK476 (b) Crystal structure of the WNK1 kinase domain in a complex with WNK476 (yellow) (PDB code: 5TF9). (c) Chemical structure of compounds 11 and 12. Figure adapted from (AlAmri et al., 2017b).

1.4.2 Targeting WNK binding to SPAK/OSR1 kinases

Despite the targeting of protein-protein interactions (PPIs) being identified as a serious challenge, there has been exponential growth in this approach as a modern tool in target-based drug discovery and many PPI inhibitors are currently undergoing clinical trials as treatments for several diseases (AlAmri et al., 2017b). Accordingly, the known binding motifs, RFX[V/I] on WNK, and CCCs that mediate the binding to the C-terminal domains (CCT) of SPAK (456–547) and OSR1 (436-527) could be exploited to identify WNK and SPAK/OSR1 interaction inhibitors. The crystal structure of the OSR1 C-terminal domain (CCT) in complex with RFQV peptide derived from upstream WNK4 (PDB ID: 2V3S) demonstrated that CCT adapts a unique folding pattern and has two adjacent hydrophobic pockets referred to as primary and secondary pockets (**Figure 1.15a**). The RFQV peptide binds to the OSR1 CCT through the primary pocket, which appears as a surface-exposed groove, while the function of the other, secondary, pocket remains unknown (**Figure 1.15a**). Further mutation analysis has identified that two key residues located in the primary pocket of the OSR1 CCT domain are crucial for RFQV peptide binding: leucine 473 (Leu473) and aspartic acid 459 (Asp459) (**Figure 1.15b**). Consistent with this observation, a point mutation in one of these residues was shown to abolish the binding of RFQV to OSR1 CCT *in vitro* as well as preventing the endogenous co-immunoprecipitation of WNK1 and NKCC1 by OSR1 (Villa et al., 2007). SPAK^{L502A/L502A} knock-in mice with a point mutation of Leu502 to Ala in the SPAK CCT (equivalent to Leu473 in human OSR1) exhibited a remarkable decrease in the phosphorylation and expression of NCC and NKCC2 along with a significant reduction in blood pressure (Zhang et al., 2015).

Mori and colleagues exploited this potential approach and identified STOCK1S-50699 ($IC_{50} = 37 \mu M$, $K_d = 32 \mu M$) and STOCK2S-26016 ($IC_{50} = 16 \mu M$, $K_d = 20 \mu M$) as the first WNK-SPAK binding inhibitors after screening > 17,000 compounds using a fluorescent correlation spectroscopy screening method (**Figure 1.15c**) (Mori et al., 2013). These molecules have distinct chemical scaffolds and both bind to SPAK CCT and inhibit its binding to WNK4-RFQV peptide *in vitro*. In the cell-based assay, both compounds reduced the endogenous phosphorylation and activation of SPAK, NCC and NKCC1 in the low-micromolar concentration range in a dose-dependent manner. In addition, STOCK1S-50699 exhibited a good selectivity profile for SPAK when tested against a panel of 150 protein kinases (de los Heros et al., 2014). STOCK1S-50699 has been widely used as a WNK signalling inhibitor since 2013 compared with STOCK2S-26016, which is rarely used. Unfortunately, these two molecules lack potency and general drug-like properties, e.g. high logP values (cLogP = 6.112 for STOCK1S-50699 and 4.776 for STOCK2S-26016), which limited their *in vivo* studies (AlAmri et al., 2017b).

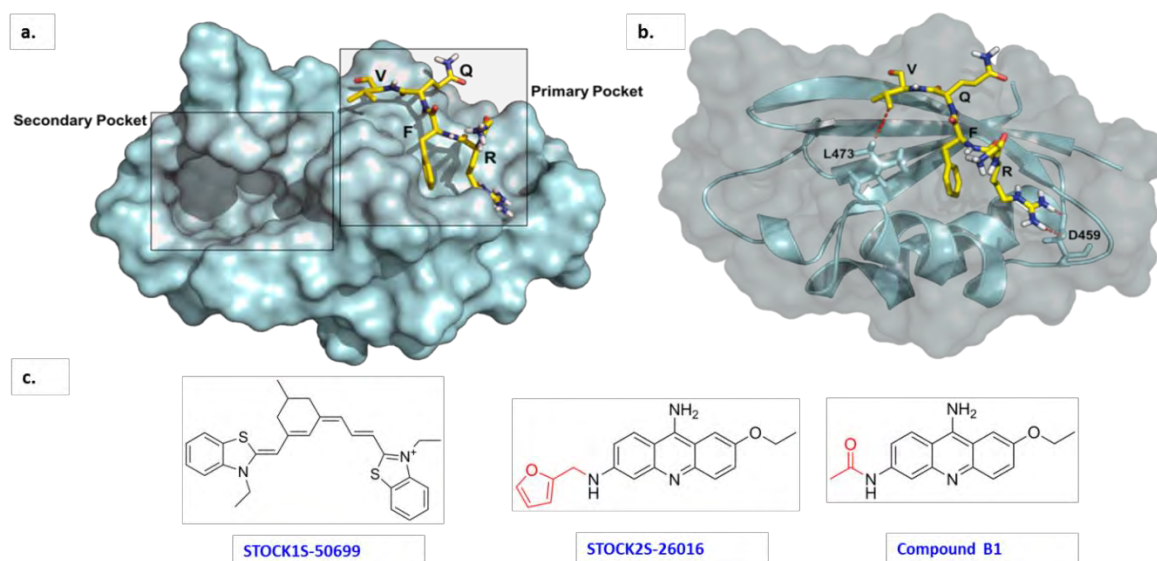


Figure 1.15: Discovery of WNK-SPAK/OSR1 binding inhibitors. (a) Molecular surface representation of OSR1 CCT in a complex with RFQV derived from WNK4 (yellow) (PDB ID: 2V3S). The primary and secondary pockets of OSR1 CCT are highlighted. (b) A ribbon representation of OSR1 CCT in a complex with RFQV derived from WNK4 (yellow). Key residues on the OSR1 CCT involved in the interaction with RFQV are labelled. (c) ChemDraw Professional 15.1 was used to draw the chemical structures of different WNK-SPAK/OSR1 interaction inhibitors. Figure adapted from (AlAmri et al., 2017b).

The detailed structure-activity relationship of STOCK2S-26016 was recently reported (Ishigami-Yuasa et al., 2017). Previously, it was shown that replacement of the flexible methylfuran moiety with a rigid smaller non-hydrophobic moiety, for example, compound B1, resulted in loss of activity (**Figure 1.15c**) (Mori et al., 2013). Since there is no crystal structure for SPAK or OSR1 CCT in a complex with these inhibitors, the loss of activity due to this chemical modification is difficult to rationalize (AlAmri et al., 2017b).

In a recent study, several derivatives of STOCK2S-26016 were synthesized with a modification around three positions, including the 2-furanylmethylamino, ethoxy, and amino groups. These efforts yielded several active compounds with better potency than STOCK2S-26016 (**Figure 1.16**). First, the replacement of 2-furanylmethyl with a *para*-benzamide moiety substituted with a *meta*-electron withdrawing group, for example, the nitro or cyano group, increased the activity significantly, such as in compounds 1 and 2. Similarly, introducing (4-cyanophenyl) urea substitution produced potent inhibitors, such as compounds 5 and 6. Notably, the substitution of the ethoxy group with a methoxy or hydroxyl group did not alter the activity, indicating that this part of the molecule may not be involved in the interaction with the protein, such as compounds 5 and 6. Interestingly, elimination of the amino group or its replacement with bulky substitutions, for example, a phenyl group, resulted in a loss of activity, such as seen with compounds 3 and 4. This indicated that the polar amino group forms hydrogen bonds that are crucial for the binding of these compounds (Ishigami-Yuasa et al., 2017).

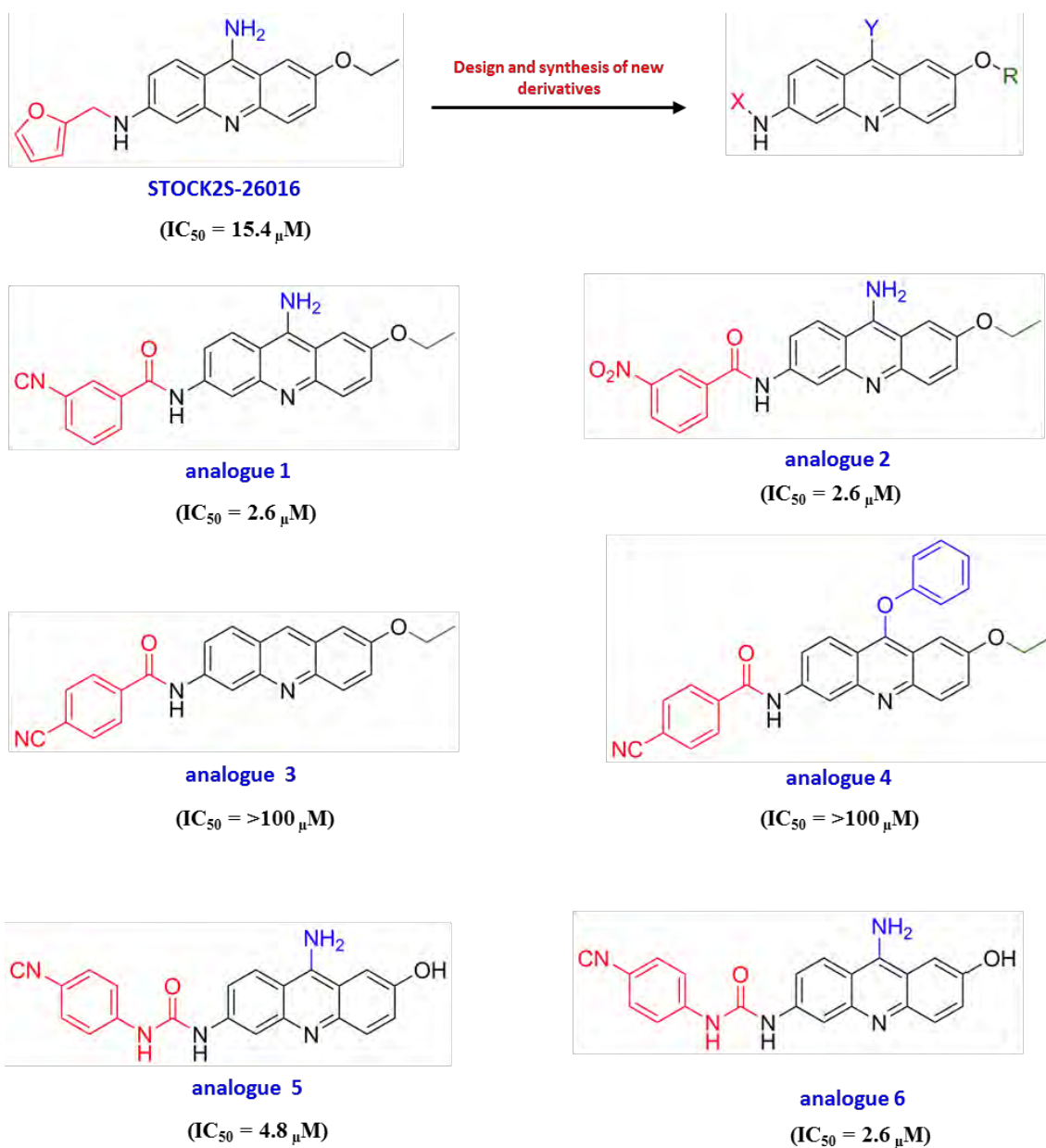


Figure 1.16: Chemical structures of STOCK2S-26016 and its different analogues. ChemDraw Professional 15.1 was used to draw the compound structures. Figure adapted from (AlAmri et al., 2017b).

1.4.3 Targeting SPAK and OSR1 kinases

Targeting SPAK and OSR1 kinases has been an attractive approach to inhibiting WNK signalling and discovering novel antihypertensive agents (AlAmri et al., 2017b). Since SPAK and OSR1 are closely related in their amino acid sequences and tissue expression profiles, the discovery of small-molecule inhibitors that could differentiate between SPAK and OSR1 by targeting one of them selectively poses a challenge. Indeed, dual SPAK and OSR1 kinase inhibition is predicted to be more efficacious in high blood pressure treatment than solo SPAK or OSR1 inhibition, as such inhibitors would lead to the inhibition of both NKCC1 and NKCC2 ion cotransporters, which are regulated by SPAK and OSR1 phosphorylation, respectively (Alessi et al., 2014).

In 2014, the first two SPAK kinase inhibitors were discovered: STOCK1S-14279 ($IC_{50} = 0.26 \mu M$, $K_d = 0.77 \mu M$) and Closantel (antiparasitic agent, $IC_{50} = 0.7 \mu M$) (**Figure 1.17a**) (Kikuchi et al., 2014). STOCK1S-14279 was discovered by screening > 20,000 small-molecule compounds using a novel enzyme-linked immunosorbent assay (ELISA)-based screening system, while Closantel was identified by utilising a drug repositioning strategy through screening a library of 840 existing drugs using the same screening system.

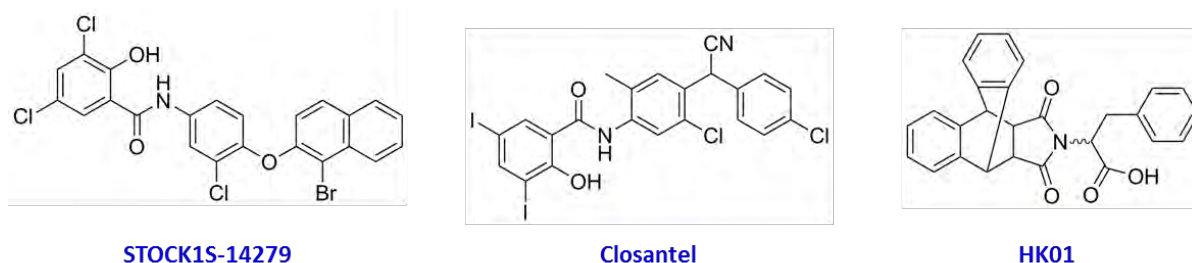


Figure 1.17: Chemical structures of STOCK1S-14279, Closantel and HK01. ChemDraw Professional 15.1 was used to draw the compound chemical structures.

A profiling study using the RapidKinase48 panel revealed that both compounds have a good specificity profile. Interestingly, these two compounds are structurally related and inhibit SPAK kinase activity in an ATP-independent manner suggesting that they may act as allosteric inhibitors rather than ATP-competitive inhibitors. In mpkDCT and MOVAS cells, both molecules inhibited SPAK catalytic activity and prevented the phosphorylation and activation of NCC and NKCC1 in the sub-micromolar concentration range. In mice, these compounds produced a significant reduction in blood pressure within 30 minutes along with a significant decrease in the phosphorylation of NCC in the kidney and NKCC1 in the aorta. Notably, a rapid recovery of blood pressure within 120 minutes post-acute-administration was observed indicating that the observed outcomes were possibly due to the vasodilation effects of SPAK inhibition rather than diuretic effects. In addition, while the prolonged administration of STOCK1S-14279 was lethal, mice treated with Closantel exhibited a reduction in NKCC2 indicating that it can also inhibit OSR1. Moreover, after seven days of administration, Closantel had no effect on mouse blood pressure and serum electrolyte levels suggesting that Closantel may only be effective on hypertensive mice (Kikuchi et al., 2014).

1.4.4 Targeting SPAK/OSR1 binding to MO25

Scaffolding proteins play a crucial role in regulating many fundamental biological processes. This is mainly due to their ability to regulate the catalytic activities of a number of enzymes, such as kinases, phosphatases and ubiquitin ligases. An example of these is MO25, a scaffolding protein that binds to a series of STE20 protein kinases, primarily SPAK and OSR1. Indeed, the binding of MO25 to these two kinases results in a ca. 80-100-fold increase in their kinase activities *in vitro* (Filippi et al., 2011). Therefore, inhibiting the interaction between SPAK/OSR1 and MO25 using small-molecule would

inhibit the MO25-dependent activation of SPAK and OSR1 kinase while their basal SPAK and OSR1 kinase activity would be retained. This approach might be favourable for this clinical indication, hypertension, as the target is to reduce high blood pressure and a robust inhibition of SPAK or OSR1 may lead to hypotension (AlAmri et al., 2017b).

The above novel indirect approach was exploited, whereby a diverse library of 4,000 compounds was screened using a novel fluorescence polarisation assay. The screening led to the discovery of HK01 as a binder of MO25 ($K_d = 127 \mu\text{M}$) (**Figure 1.17**). This compound inhibited the binding of a 16-mer WEW peptide derived from SPAK to MO25 *in vitro* ($IC_{50} = 78 \mu\text{M}$). In addition, it inhibited the MO25-dependent activation of OSR1 in *in vitro* cell-free and cell-based assays. Despite the low potency of HK01, it provided evidence that targeting MO25, a scaffolding protein, is a valuable approach to the indirect inhibition of SPAK and OSR1 (Kadri et al., 2017).

In summary, WNK-SPAK/OSR1 signalling pathway is composed of serine/threonine protein kinases that play a central role in blood pressure regulation. Compelling genetic, animal and biochemical studies have indicated the inhibition of this signalling pathway as an attractive approach to discover new antihypertensive agents. In this thesis, different drug discovery approaches were utilised to discover novel inhibitors of WNKs signalling pathway by targeting SPAK and OSR1 intermediate kinases with small-molecule inhibitors. In chapter III, structure-based virtual screening was conducted against an in-house library of FDA approved-drugs. In chapter IV, high-throughput screening strategy was utilised to screen a chemical library composed of FDA approved-drugs and a diverse set of compounds. In chapter V, NMR-based fragment screening against in-house fragments library was conducted.

1.5 Hypothesis

SPAK and OSR1 kinases could be specifically targeted and inhibited by small molecules and these would lead to a reduction in blood pressure.

CHAPTERII: MATERIALS AND METHODS

2.1 Molecular biology

2.1.1 Bacterial strains

MAX Efficiency™ DH5α™ Competent Cells (Invitrogen, cat# 18258012) were used in plasmid carriage and propagation. Single-Use BL21(DE3) pLysS Competent Cells (Promega, cat# L119B) were used in fusion protein induction and expression.

2.1.2 Generation of bacterial competent cells

10 µL of DH5α or BL21 competent cells were added to 10 mL Luria-Bertani (LB) broth medium in 50 mL sterile falcon tube to make an overnight culture in incubator shaker at 37 °C at 200 rpm. On the following day, 625µL of cells were transferred into 50 mL (LB) medium in 200 mL conical glass flask and left to grow at the same condition until the optical density (OD) at 600 nm reach ~ 0.5-0.7. The OD was monitored using the Jenway Genova spectrophotometer. Cell suspension was then transferred into a sterile 50 mL falcon tube and centrifuged at 3000 g at 4 °C for 10 minutes. Pellet was then resuspended gently in 1 mL ice cold 0.1M CaCl₂ and placed on ice for 1 hour. Then, cells were pelleted at 2500 g at 4 °C for 10 minutes. Cells were resuspended again in 1 mL ice cold 0.1M CaCl₂ and placed on ice for 15 minutes. Then, 0.5 mL of 80% filter-sterilised glycerol was added. Cells were mixed and aliquoted into 1.5 mL Eppendorf tubes in 100 µL each and store at -80 °C. All bacterial cultures and procedures were carried out in sterile environment under a Bunsen burner.

2.1.3 Transformation of bacterial cells

DH5α or BL21 competent cells were thawed on ice for few minutes. 5 µL of plasmid DNA was added to 50 µL competent cells in a sterile 1.5 mL Eppendorf tube and placed on ice for 15-20 minutes. Cells were heat-shocked at 42 °C for 90 seconds and then quickly incubated in ice for 10 minutes. Bacterial transformation culture was then spread

onto LB Broth agar plates supplemented with 100 µg/mL ampicillin (Sigma Aldrich, cat# A0166) using sterile L-shaped cell spreaders and let to incubate overnight at 37°C. On the following day, a single colony was picked up using a sterile pipette tip and transferred to 200 mL LB Broth medium supplemented with 100 µg/mL ampicillin in 500 mL conical glass flask. The culture was incubated overnight in an incubator shaker at 37 °C at 180 rpm. Bacterial glycerol stocks were prepared by mixing 0.5 mL of bacteria culture with 0.5 mL of 80% filter-sterilised glycerol into 1.5 mL Eppendorf tubes. These stocks were stored at -80°C.

2.1.4 DNA Extraction and Purification.

Plasmid DNA was extracted and purified from bacterial cells using Qiagen Plasmid Maxi kit (Qiagen cat#12163) according to manufacture protocol. Briefly, A 500 mL bacterial culture in LB broth supplemented with 100 µg/mL ampicillin was first grown overnight in an incubator shaker at 37°C at 180 rpm. In the following day, bacterial culture was harvested by centrifuging in beckman coulter avanti J-26 Xp centrifuge at 8000 rpm for 15 minutes at 4°C. The bacterial pellet was then resuspended in 10 ml buffer P1 with gentle mixing. Then, 10 mL buffer P2 was added to lyse cells by mixing up and down few times until cell suspension becomes blue in colour. Then, solution was left to settle down at room temperature for 5 minutes. Afterward, 10 mL ice cold buffer P3 was added and mixed well to give a white colour solution. Then, solution was incubated on ice path for 20 minutes. Cells solution was then transferred into 50 mL polypropylene copolymer centrifuge tubes (Thermo Scientific, cat# 3119-0050) and centrifuged at 14000 rpm for 30 minutes at 4°C. Clear supernatant was collected and applied to a QIAGEN-tip (pre-washed with 10 mL Buffer QBT) and washed twice with 30 mL buffer QC under gravity flow. Then, the bound DNA was eluted into a 50 mL falcon tube by

adding 15 mL pre-warmed buffer QF. DNA was then precipitated by adding 10.5 mL room temperature isopropanol (Fisher Scientific, cat# P/7507/17). After mixing, solution was centrifuged at 18000xg for 30 minutes at 4°C. The DNA pellet was then washed with 5 mL of 70% sterile-filtered ethanol and centrifuged at 18000xg for 10 minutes at 4°C. DNA pellet was left to dry for 5 minutes and then re-dissolved in 1 mL of nuclease-free water (Promega, Cat# P119C). The purified plasmid DNA was quantified using NanoDrop 2000 and then aliquoted in 1.5 mL Eppendorf tubes 50 µl each and stored at -20 °C.

Gene Name	Plasmid	Species	Tag	Expression System	DU number
OSR1	pGEX-GST-OSR1(433–end) WT	Human	GST	Bacterial	10096
OSR1	pGEX-OSR1 (433 – end) L440A	Human	GST	Bacterial	10332
OSR1	pGEX-OSR1 (433 – end) L473A	Human	GST	Bacterial	10321
OSR1	pGEX-OSR1 (433 – end) V07A	Human	GST	Bacterial	10331
OSR1	pGEX-OSR1 T185E full-length	Human	GST	Bacterial	6231
OSR1	pGEX-OSR1 T185E 1-342	Human	GST	Bacterial	6363
SPAK	pGEX-SPAK (452-end)	Human	GST	Bacterial	41572
SPAK	pGEX-SPAK T233E full-length	Human	GST	Bacterial	6246
NKCC2	pGEX-NKCC2 1-174	Human	GST	Bacterial	13763
MO25	pGEX-6-MO25 alpha	Human	GST	Bacterial	2945
OSR1	pEBG-OSR1 T185E full-length	Human	GST	Mammalian	6130
OSR1	pEBG-OSR1 T185E+V507A	Human	GST	Mammalian	10687
OSR1	pEBG-OSR1 T185E+S443A	Human	GST	Mammalian	10693
OSR1	pEBG-OSR1 T185E+D459A	Human	GST	Mammalian	6696
OSR1	pEBG-OSR1 T185E+L440A	Human	GST	Mammalian	10688
OSR1	pEBG-OSR1 T185E+L473A	Human	GST	Mammalian	6699

Table 2.2: List of cDNA Clones. All cDNA clones were purchased from the Division of Signal Transduction Therapy (University of Dundee) in a volume of 10 μ L at a concentration between 10-100 ng/ μ L.

Buffer (1X)	Content
Buffer P1 (Resuspension buffer)	<ul style="list-style-type: none"> 50 mM Tris-HCl pH 8.0 10 mM EDTA 100 µg/mL RNase A
Buffer P2 (Lysis buffer)	<ul style="list-style-type: none"> 200 mM NaOH 1 % SDS 0.1 % LyseBlue
Buffer P3 (Neutralisation buffer)	<ul style="list-style-type: none"> 3 M Potassium acetate pH 5.5
Buffer QC (Washing buffer)	<ul style="list-style-type: none"> 1 M NaCl 50 mM MOPS pH 7.0 15 % (v/v) isopropanol
Buffer QF (Elution buffer)	<ul style="list-style-type: none"> 1.25 M NaCl 50 mM Tris HCl pH 8.5 15 % (v/v) isopropanol

Table 2.3: Qiagen Plasmid Maxi kit buffers.

2.1.5 DNA quantification and purity determination

The concentration of purified DNA was determined using NanoDrop 2000 (Thermo Fisher Scientific) by measuring the absorbance of one drop (~ 2µl) of purified DNA at 260 nm using nuclease-free water as a blank control. Each absorbance (A_{260}) unit is equivalent to approximately 50 µg/mL of DNA. DNA purity was assessed by calculating the absorbance ratio at 260 and 280 nm ($A_{260/280}$) and 260 and 230 nm ($A_{260/230}$) in which ~ 1.8 and ~ 2-2.2 are standard values for pure DNA sample, respectively (Desjardins and Conklin, 2010).

2.1.6 DNA sequencing

DNA samples were prepared by adding 700 ng from purified plasmid DNA to 4.8 pMol primers (Sigma Aldrich, Custom DNA Oligos). The pGEX- vector primers

sequencing were: (GexF) 5'-CCAGCAAGTATATAGCATGG-3' (forward primer) and (GexR) 5'-CCGGGAGCTGCATGTGTCAGAGG-3' (reverse primer) while the primers for pEBG- vector were: (GexF) 5'-CCAGCAAGTATATAGCATGG-3' (forward primer) and (Ebgrev) 5'-GGGGTGCAAGGACCCAGATGG-3' (reverse primer). The samples were prepared in nuclease-free water at 15 µL final volume and then sent to the Functional Genomics and Proteomics Facility at the School of Biosciences, University of Birmingham to run the experiments. Sequencing results were analysed by Chromas Lite 2.1.1. software and then aligned against nucleotide collections (nr/nt) using BLAST database.

2.1.7 Protein expression and purification

2.1.7.1 Expression and purification of proteins from *Escherichia coli* (*E.coli*)

Purification of GST-fusion protein was described previously (Filippi et al., 2011). All pGEX-6P-1 constructs encoding *N*-terminal GST-tagged proteins were transformed into BL21 (DE3) *E.coli* cells as described in section 2.1.3. Overnight pre-culture was made from a single colony from a plate agar or from 2-3 µL 80% glycerol stock into 200 mL LB Broth medium in 500 mL conical glass flask supplemented with 100 µg/mL ampicillin and grown in an incubator shaker at 37 °C at 180 rpm. Next day, 25 mL of overnight pre-culture was inoculated in one liter of LB medium containing 100 µg/mL ampicillin and left to grow under the same condition until the optical density at 600 nm (OD₆₀₀) reached 0.6-0.7. 250 µM isopropyl-D-galactosidase (IPTG) (Sigma Aldrich, cat# I6758) was then added to induce protein expression. Then, cells were cultured for additional 16 hours in an incubator shaker at 26 °C at 180 rpm. The cells were then collected by centrifugation in beckman coulter avanti J-26 Xp centrifuge at 3500xg at 4°C for 30 minutes. The pellet was resuspended either in 10 mL ice cold phosphate

buffered saline (PBS) (Sigma Aldrich, cat# D8662) and stored at - 80°C or in 50 mL ice cold bacterial lysis buffer and incubated in ice path at 4°C for 30 minutes. Bacteria were lysed further by sonication, for 30 seconds on/off round 6 times. Lysates were centrifuged at 25,000 g at 4°C for 30 minutes. The supernatant was collected and incubated overnight with 2 mL/L of glutathione-Sepharose beads (GE Healthcare, cat# 17527901) (pre-washed three times with bacterial lysis buffer) to affinity purified GST-tagged proteins. The beads were then washed with normal buffer, high salt buffer and buffer A, respectively, two time each. The GST-proteins were eluted with elution buffer containing 20mM reduced L-glutathione (Alfa Aesar, cat# J62166). For NKCC2 1-174, the GST tag was cleaved using PreScission protease enzyme (GE Healthcare, cat# 27084301). Proteins were then concentrated to 100-500 µl using amicon ultra-15 centrifugal filter units (3 kDa and 10k Da cut-off) (Fisher Scientific, cat# UFC900324 and UFC901008) and aliquoted into 1.5 mL Eppendorf tubes in 10 µL each and store at -80 °C.

2.1.7.2 Expression and purification of ^{15}N and ^{13}C isotopically labelled proteins from *Escherichia coli* (*E.coli*) for NMR studies

^{15}N -labelled OSR1 (433-end) and SPAK (425-end) or double-labelled ^{15}N - ^{13}C -OSR1 (433-end) C-terminal domains wild types were transformed, expressed and purified according to the protocol described in 2.1.6.1. However, M9 minimal medium was used instead of LB broth medium, in which ammonium- ^{15}N chloride and D-Glucose- $^{13}\text{C}_6$ were used as sole sources of nitrogen and carbon, respectively. The proteins expressions were induced for 16 hours in an incubator shaker at 18°C at 180 rpm. Proteins were then purified by cleaving the GST by PreScission protease enzyme as mentioned above.

Buffer (1X)	Compositions	
Bacterial Lysis Buffer	▪ 50 mM Tris-HCl, pH 7.5	
	▪ 150 mM NaCl	
	▪ 1 mM EGTA	
	▪ 1 mM EDTA	
	▪ 270 mM Sucrose	
	▪ 0.5 mg/mL Lysozyme (Sigma Aldrich, cat#62970)	
	▪ 0.3 mg/mL DNase (Roche, cat#10104159001)	
	Protease Inhibitor	▪ 1 mM PMSF (Phenylmethanesulfonyl fluoride)
		▪ 1 mM Benzamidine
		▪ 0.01% (v/v) 2-Mercaptoethanol (Sigma Aldrich, cat#M6250)
Normal Buffer	▪ Bacterial lysis buffer without lysozyme and DNase	
High Salt Buffer	▪ Normal buffer	
	▪ 500 mM NaCl	
Buffer A	▪ 50 mM Tris-HCl, pH 7.5	
	▪ 1 mM EGTA	
	▪ 0.1% (v/v) 2-Mercaptoethanol (fresh)	
Elution Buffer	▪ Buffer A, pH 8	
	▪ 20 mM Reduced L-Glutathione	
	▪ 150 mM NaCl	
PreScission Protease Buffer	▪ Buffer , pH 8	
	▪ 150mM NaCl	
	▪ 40 µL (80 units) of PreScission protease per Liter	

Table 2.4: List of buffers used for proteins purification.

2.1.8 Protein quantification and purity determination

Protein concentration was determined by Bradford assay by measuring the absorbance of coomassie brilliant blue G-250 dye at 595 nm (Bradford, 1976). Standard solutions were prepared by dissolving bovine serum albumin (BSA) (Sigma Aldrich, cat#A2153) in phosphate buffered saline (PBS) (Sigma Aldrich, cat# D8662) at different concentrations ranged from 0.125 to 5 mg/mL. The measurement of protein concentration was done by mixing either 5 μ L of standard solutions or 2 μ L of protein with 280 μ L of Bradford reagent (Sigma Aldrich, cat# B6916) in a sterile 96-well polystyrene round bottom plates (Corning, cat#3596) in triplicate. Then the absorbance was measured at 595 nm using a BMG FLUOstar Omega plate reader.

The protein purity and yield were confirmed by dodecyl sulfate polyacrylamide gel electrophoresis (SDS-PAGE) with coomassie instantblue staining using bovine serum albumin (BSA) (Sigma Aldrich, cat#A2153, purity \geq 96% (agarose gel electrophoresis)) at different concentrations as standards. In-house gel was casted using mini-protean short plates (Bio-Rad, cat#1653308) with mini-protean spacer plates with 1.0 mm integrated spacers (Bio-Rad, cat#1653311) with 10-15 wells combs at 10, 12 or 15% resolving gel (depend on the molecular weight of the target protein). Samples were loaded in the gel at 0.5, 1 and 3 mg/mL concentrations. Protein ladder (Geneflow, cat# S6-0024) was loaded in each gel to analyse the molecular weight of proteins. Electrophoresis was run in a tank (Bio-RAD, cat#1658000EDU) filled in with running buffer at 185 V for 1 hour. Then gel was placed in 5 mL coomassie instantblue staining (Expedeon, cat# ISB1L) for 30 minutes before washing with deionised water. A clear photo of the gel was imported into ImageJ software (National Institute of Health) to assess protein purity and correct protein concentration in comparison with BSA.

Resolving Gel (15mL)	10% (mL)	12% (mL)	15% (mL)
1.5 M Tris pH 8.8	5	5	5
30% Acrylamide	4	6	7.5
H₂O	5.9	3.9	2.4
20% SDS	0.075	0.075	0.075
10% APS	0.075	0.075	0.075
TEMED	0.025	0.025	0.025

Table 2.5: Components of SDS-PAGE resolving gel. APS: Ammonium Persulphate Solution.
TEMED: N,N,N',N'-Tetramethylethylenediamine

Stacking Gel (5mL)	mL
0.5 M Tris pH 6.8	0.62
30% Acrylamide	0.883
H₂O	3.82
20% SDS	0.025
10% APS	0.05
TEMED	0.005

Table 2.6: Components of SDS-PAGE stacking gel.

2.1.9 Growth media

2.1.9.1 LB broth and LB broth agar media

LB Broth medium was prepared by dissolving each 1.1g tablet of LB Broth (Lennox) (Sigma Aldrich, cat#L7275) in 48.3 mL deionised water in either 2L or 5L conical glass flask. The prepared medium was then autoclaved under 121°C. The LB agar plate was prepared by dissolving each 1.68 g tablet of LB Broth with agar (Lennox) (Sigma Aldrich, cat#L7025) in 48.3 mL deionised water in a glass bottle. The prepared medium was then autoclaved for 20 minutes under 121°C. The glass bottle was allowed to cool slightly then 100 µg/mL ampicillin was added and mixed. Then 15-20 mL aliquots each dispensed into a 10 cm diameter Petri dish. The plates were left to dry, solidified at room temperature, and stored at 4 °C for maximum one week.

Chemical	g/L
Tryptone	10
Yeast Extract	5
NaCl	5
Inert binding agents	2.2
Agar (in LB agar)	13.72

Table 2.7: Components of LB broth and LB broth agar media.

2.1.9.2 M9 minimal medium

Medium was made by dissolving M9 salts (**Table 2.8**) in 900 mL deionised water. Then, the pH was adjusted to 7.4 before making the volume up to 950 mL. The prepared mixture was transferred into conical flask and autoclaved under 121°C. 50 mL of fresh-filtered nutrient mix was then added to make up 1L of M9 minimal medium.

Chemical	Vendor	g
Na ₂ HPO ₄ (anhydrous)	Sigma Aldrich, cat#71636	6
KH ₂ PO ₄ (anhydrous)	VWR Chemicals, cat# 26936.260	3
NaCl	Merck Millipore, cat# 567440	0.5

Table 2.8: Component of M9 salts

Chemical	Vendor	amount
1 M CaCl ₂	▪ Sigma Aldrich, cat# 449709	10μl
1 M MgSO ₄	▪ Sigma Aldrich, cat# M8179	2mL
1M FeCl ₃	▪ Scientific Laboratory Supplies, cat# CHE1994	400μL
20 mg/mL Thiamine	▪ Sigma Aldrich, cat# T4625	1mL
¹⁵ NH ₄ Cl	▪ Cambridge Isotope, cat# NLM-467-5	1 g
Glucose	▪ Sigma Aldrich, cat# G8270 (Unlabeled)	2g
(¹³ C-labelled if required)	▪ Cambridge Isotope, cat# CLM-1396-5 (¹³ C-labelled)	
Metal Mix*	7 mM ZnSO ₄ ▪ Sigma Aldrich, cat #Z0251	0.5 mL
	1mM MnSO ₄ ▪ Sigma Aldrich, cat #M8179	
	5 mM H ₃ BO ₃ ▪ Sigma Aldrich, cat #B6768	
	1 mM CuSO ₄ ▪ Sigma Aldrich, cat #451657	

Table 2.9: Composition of nutrient mix.* Metal mix was prepared separately in deionised water at 100 mL

2.2 Cell culture

2.2.1 Cell line culture

A HEK293 (Human Embryonic Kidney) cell line was maintained in T-75 culture flask in Dulbecco's modified Eagle's medium (DMEM) (Sigma Aldrich, cat#D6429) supplemented with 10% (v/v) fetal bovine serum (Gibco, cat#10270), 2 mM L-glutamine, 100 units/mL penicillin-streptomycin solution (Hyclone, cat#SV30010) at 37 °C in a humidified 5% CO₂ incubator. Once cells reach 75-85% confluency, cells were passed on to a new T-75 flask. Cells medium was removed by aspiration and then cells were washed by 2 mL pre-warmed PBS. After washing with PBS, 2 mL of trypsin (Gibco, cat#12605-010) solution was added to the cells and the flask incubated for 2 minutes in the incubator. 10 mL of pre-warmed full medium was then added to the cells to form homogenous cell suspension by pipetting up and down gently. 2 mL of cell suspension was then transferred to a new T-75 culture flask with 8 mL of a new growth medium.

2.2.2 Transient transfection of mammalian HEK-293 cells

Polyethylenimine (Poly-sciences, car#23966-1) was used to transfect HEK293 cells with plasmid DNA. HEK293 cells were plated in 10-cm petri dishes by adding 2 mL of cell suspension to 3 mL of new growth media. When cultures at 40% confluency, cells were transfected with 1 mL of transfection mixture. Transfection mixture was prepared by mixing 3 µg of plasmid DNA with 20 µL of 1 mg/mL Polyethylenimine in 1 mL of free DMEM medium (Durocher et al., 2002). The mixture was vortexed for 2 minutes and then incubated for 20 minutes at room temperature. Transfection mixture was then added evenly to cells and placed in the incubator after gentle mixing. Cells were lysed 36 hours post-transfection with 0.3 mL ice-cold cell lysis buffer and centrifuged at 12,000 g 4 °C

for 10 minutes to collect the protein. Protein expression was detected using standard polyacrylamide gel electrophoresis (SDS-PAGE)/western blot.

2.2.3 Cell treatments and inhibition assay

For the inhibition assay, HEK-293 cells were cultured on 6-well plates by adding 1 mL of cell suspension to 2 mL of new growth media. Once cells at 75-80% confluency, cells were incubated with 0.1% (v/v) DMSO (as a vehicle control) or compounds that were dissolved in 100% (w/v) DMSO at indicated concentrations for 40 minutes. Then, media cells were removed by aspiration and 3 mL of pre-wormed low chloride hypotonic buffer were added subsequently to activate WNK signalling for 30 minutes. Cells were washed with 1 mL pre-wormed PBS and then lysed with 150 μ L ice cold cells lysis buffer per well. Cells were further lysed using cell scrapers (Sarstedt, cat# 83.1830) and transferred to 1.5 mL Eppendorf tubes and centrifuged at 12,000 g for 10 minutes at 4 °C to collect the protein. The proteins concentrations were measured using Bradford assay as described in 2.1.7. 1 μ g/ μ L protein samples were finally prepared in 1x SDS buffer. Final DMSO concentration was 0.1%.

2.2.4 Western blot and immunoblot

SDS Samples were boiled for maximum 5 minutes in water path at 90 °C and then subjected to 10% SDS/PAGE. Gels were prepared as described in 2.1.7. 30 μ L of 1 μ g/ μ L proteins were loaded in the gel. Electrophoresis was run as described in 2.1.7. However, for western blot, the proteins were transferred from the gel on to nitrocellulose membranes (GE Healthcare, cat# 10600007). The membranes were blocked with blocking buffer for 45 minutes on platform shaker (Grant-bio). The membranes were then incubated with primary antibody (anti-phospho-SPAK antibody, anti-phospho-NKCC1 antibody and anti-total NKCC1 antibody were prepared in 5% (w/v) dried

skimmed milk in TBS-T while anti-total SPAK antibody, anti-GAPDH antibody and anti-GST antibody were prepared in 5% (w/v) bovine serum albumin (BSA) /TBS-T) for 1 hour at room temperature or overnight at 4°C. Then the membranes were washed with TBS-T four times for 10 minutes each and incubated with secondary antibody (anti-sheep antibody in 5% (w/v) dried skimmed milk in TBS-T and anti-rabbit antibody in 5% (w/v) BSA/TBS-T). The membranes then washed with TBS-T four times for 10 minutes each. The detection was done by adding chemiluminescent detection reagent (ECL) (GE Healthcare, cat# RPN2106) to the membranes and developing an auto-radiographic film (GE Healthcare, cat# 28906846). Immunoblots were developed using a film automatic processor (Konica Minolta Medical, SRX-101) and films were scanned with at 300 dpi resolution on a scanner (PowerLook 1000; UMAX). ImageJ software (National Institutes of Health) was used for western blot quantification. Data analysis was completed with GraphPadPrism 6.0.

Primary Antibody	Dilution	Secondary Antibody	Dilution
Sheep SPAK phospho-Ser373 (University of Dundee, cat# S670B)	2 µg/mL	Anti-sheep- HRP (Abcam, cat# ab97130)	1:10000
Sheep SPAK total (University of Dundee, cat# S365D)	2 µg/mL	Anti-sheep- HRP (Abcam, cat# ab97130)	1:10000
Rabbit SPAK total (Cell signaling, cat# 2281S)	1:1000	Anti-rabbit- HRP (Abcam, cat# ab97130)	1:2500
Sheep NKCC1 phospho-Thr 203+Thr 207+Thr 212 (University of Dundee, cat# S763B)	2 µg/mL	Anti-sheep- HRP (Abcam, cat# ab97130)	1:10000
Sheep NKCC1 total (University of Dundee, cat# S022D)	2 µg/mL	Anti-sheep- HRP (Abcam, cat# ab97130)	1:10000
Rabbit GAPDH (glyceraldehyde-3-phosphate dehydrogenase) (Cell signaling, cat# 2118)	1:5000	Anti-rabbit- HRP (Santa Cruz Biotechnology, cat # NPAS1)	1:2500
Rabbit GST-total (Glutathione S-transferase proteins) (Cell signaling, cat# 2625S)	1:5000	Anti-rabbit- HRP (Santa Cruz Biotechnology, cat # NPAS1)	1:2500

Table 2.10: List of antibodies used for western blot.

Buffer (1X)	Chemicals		Amount
Hypotonic low-chloride buffer	HEPES (4-(2-hydroxyethyl)-1-piperazineethanesulfonic acid)		7.5 mM
	Na ⁺ Gluconate		67.5 mM
	K ⁺ Gluconate		2.5 mM
	CaCl ₂		0.25 mM
	MgCl ₂		0.25 mM
	Na ₂ HPO ₄		0.5 mM
	Na ₂ SO ₄		0.5 mM
Cells Lysis Buffer	Tris-HCl (pH 7.5)		50 mM
	EDTA		1 mM
	EGTA		1 mM
	Sodium Fluoride		50 mM
	Sodium Pyrophosphate		5 mM
	Sodium Orthovanadate		1 mM
	Nonidet-P40		1% (w/v)
	Sucrose		0.27 M
	Protease Inhibitors	2-Mercaptoethanol	0.1% (v/v)
		PMSF	0.1 mM
		Benzamidine	0.1 mM
SDS Sample Buffer (4X)	Tris-HCl, pH 6.8		240 mM
	SDS		8%
	Glycerol		40%
	Bromophenol blue		0.04%
	2-Mercaptoethanol		5%
Running Buffer	SDS		34.6 mM
	Tris-base		25 mM
	Glycine		192 mM
Transfer Buffer	Tris-base		48 mM
	Glycine		39 mM
	Methanol (fresh)		20% (v/v)
TBS-T Buffer (Tris-buffered saline)-Tween	Tris-HCl (pH 7.5)		50 mM
	NaCl		150 mM
	0.2% (v/v) Tween-20		0.2% (v/v)
Blocking Buffer	Dried Skimmed Milk in TBS-T		10% (w/v)

Table 2.11: List of buffers used for cell culture work.

2.3 Binding assay

2.3.1 Biotin-RFQV pull-down

For screening compounds for WNK-SPAK/OSR1 binding inhibitors, 500 µg HEK-293 cells total lysates were precleared by adding 100 µl aliquot of streptavidin beads (GE Healthcare, cat#17-5113-01) equilibrated in cells lysis buffer (pre-washed 3x with phosphate-buffered saline, PBS) and incubated for 10 minutes at 4 °C on Eppendorf tubes rotator. Then, 250 µg of precleared HEK-293 cells total lysates were incubated with either DMSO as a vehicle control or inhibitors at indicated concentrations for 2 hours at 4 °C on Eppendorf tubes rotator. 3 µg of biotinylated RFQV-containing peptide derived from WNK4 (biotin-SEEGKPQLVGR**RFQ**VTSSK) (GL Biochem, cat# 331938) were added and incubated under the same condition for further 15 minutes at 4 °C. AFQV-containing peptide (GL Biochem, cat# 372447) derived from WNK4 (biotin-SEEGKPQLVGA**AFQ**VTSSK) and STOCK1S-50699 (Vitas-M Laboratory, cat# STK874217) were used as controls. Then, 20 µl aliquot of streptavidin beads equilibrated in cells lysis buffer were added and incubated for 15 minutes on Eppendorf tube rotator. After the incubation, beads were washed with 1 mL cells lysis buffer and Buffer A two times each with gently mixing, respectively. Then beads were boiled with 1x SDS sample buffer in water bath at 90 °C for 5 minutes and subjected to SDS-PAGE.

For studying the effect of mutations in OSR1/SPAK secondary pocket on RFQV-OSR1 binding, HEK293 cells were transfected, as described in 2.2.2, with GST-OSR1 1-527 wild type (WT) and GST-OSR1 1-527 with different mutations in the secondary pocket including L440A, S443A and V507A as well as OSR1 1-527 with mutations in the primary pocket including L473A and D459A as controls. 250 µg of precleared cell lysates were incubated with 3 µg of biotinylated RFQV for 15 minutes at 4 °C. Then, 20

μl aliquot of streptavidin beads were added and incubated for 15 minutes on Eppendorf tubes rotator. After the incubation, beads were washed and boiled with 1x SDS sample buffer as described above and subjected to SDS-PAGE.

2.3.2 Fluorescence polarisation assay

The RFQV-peptide (CCPGCCGGSEEGKPQLVGRFQVTSSK) (GL Biochem, cat# 507103) powder was initially resuspended in 50 mM ammonium bicarbonate solution, pH 8. Subsequently, it was labeled with FIAsh-EDT₂ fluorophore (Carbosynth, cat# FF23296) which binds covalently to the CCPGCC *N*-terminal motif on the RFQV peptide. The labeling step was achieved by incubating 10 μM of peptide with 30 μM of FIAsh-EDT₂ in 500μl dialysis buffer in the dark at 4 °C for 2 hours. The peptides were then dialysed for 4 hours into dialysis buffer using a Mini Dialysis kit with 1 kDa cut-off (GE Healthcare, cat# 80-6483-94) and then for another 12 hours with changed dialysis buffer. The optimum FIAsh-EDT₂ concentration that exhibited about ten times more fluorescence intensity signal compared to background controls was 10 nM. For fluorescence polarisation, 10 nM of FIAsh-EDT₂-labelled peptide was mixed with proteins at various concentrations (0.01-10 μM) in dialysis buffer at a final volume of 30 μl. A BMG PheraStar plate reader was used to measure the fluorescence polarisation, with an excitation and emission wavelengths of 485 nm and 538 nm, respectively (Zhang et al., 2015). Assay was performed in a black flat-bottomed 384-well plate (Greiner) in triplicate with at least 12 data points per curve.

Dialysis Buffer	
Tris-HCl (pH 7.5)	50 mM
NaCl	150 mM
Dithiothreitol (DTT)	2 mM

Table 2.12: Compositions of dialysis buffer.

2.4 Functional assay

2.4.1 ADP-Glo kinase assay

In vitro cell-free based biochemical ADP-Glo™ assay (V7002) was developed and optimised for 96- and 384-well plates at 25 µL and 5 µL total reaction volumes, respectively, according to Promega's instructions. For evaluating the effect of mutations on the kinase activity of OSR1 protein kinase, 350 µg of HEK293 cell lysates overexpressing GST- tagged OSR1 T185E full length, WT or with mutations in the secondary pocket of OSR1 C-terminal domain including L440A, S443A and V507A was incubated with 10 µl GST-sepharose beads (GE Healthcare, cat# 17527901) in 1.5 mL Eppendorf tube at 4 °C for 1 hour. Then, the suspension was centrifuged at 3,000 g at 4 °C for 2 minutes. The beads were then washed twice with ice-cold lysis buffer containing 0.5 M NaCl and twice with buffer A. An aliquot of 10 µl of the kinase-loaded sepharose beads was used in a kinase assay using 0.25 mM CATCHtide (RRHYYYDTHNTYY LRTFGHN TRR) (GL Biochem, cat# 204155) as a substrate (Vitari et al., 2006). Kinase reactions were performed in 1.5 Eppendorf tubes for 40 min at 30 °C on Eppendorf thermoblock (Labnet) with gentle agitation in 25 µl reaction buffer consisting of 50 mM

Tris-HCl, 10 mM MgCl₂, 0.1% (v/v) 2-mercaptoethanol and 0.1 mM ATP (Vitari et al., 2006). Empty beads wells were used as background control. The mixture was then transferred to a white flat-bottomed 96-well plate (Greiner) and developed according to Promega's ADP-Glo kit instructions by adding reagent 1 at 25 µl to each well and after incubation of the plate for 40 minutes at room temperature, reagent 2 was added to each well at 40 µl (Zegzouti et al., 2009). The plate was subsequently read after 1 hour incubation at room temperature on a BMG FLUOstar Omega plate reader.

For determining the IC₅₀ values of the inhibitors, the kinase assay was performed in a white flat-bottomed 384-well plate (Greiner) by incubating 1 µL of either DMSO only at zero inhibitor concentration or increasing concentrations of inhibitors with 0.2 µM of constitutively active GST-proteins at 5 µL total reaction volume containing 50 mM Tris-HCl, 10 mM MgCl₂, 0.1% (v/v) 2-mercaptoethanol, 0.05% tween-20 and 0.1 mM ATP in buffer A employing GST cleaved NKCC2 1-174 or CATCHtide (RRHYYYDTHNTYYLR-TFGHNTRR) as substrates at 5 µM and 250 µM final concentrations, respectively. The plate was covered with parafilm-wrap and centrifuged for 10 seconds in microplate centrifuge (VWR). The kinase reaction was performed at 30 °C for 30 minutes on microplate shaker incubator (Labnet). The kinase activity was assayed as described above.

In Chapter III, recombinant GST-OSR1 T185E 1-342 (cat# DU6363) and recombinant GST-SPAK T233E (1 - 547) (cat# DU6245) were purchased from the Division of Signal Transduction Therapy (University of Dundee). SPAK kinase has a low kinase activity profile *in vitro* comparing to OSR1. Therefore, mouse only protein-25 (MO25) a scaffolding protein was added to the kinase reaction at 5 µM final concentration (Filippi et al., 2011).

For studying the effect of Verteporfin (Sigma Aldrich cat# SML0534) on MST3 kinase, kinase assay was conducted using ADP-Glo™ Assay kit using same protocol described above by incubating 0.1 μ M of recombinant MST3 (1-431) (Division of Signal Transduction Therapy, University of Dundee) with 0.3 mg/mL myelin basic protein (MBP) (Sigma Aldrich cat# M1891) as a substrate (Filippi et al., 2011). For inhibition studies, increasing concentrations of each compound were tested in four replicates with at least 10-18 data points per curve. Curve fitting and data analysis was completed with GraphPadPrism 6.0. Final DMSO concentration is 4%.

2.4.2 Screening in-house FDA chemical library using ADP-Glo kinase assay

2.4.2.1 Preparation of in-house FDA Chemical Library

An in-house library of ~1,200 FDA approved drugs (The Birmingham Drug Discovery Facility, School of Biosciences, University of Birmingham) was obtained in stock solutions of 100 μ M by dissolving drugs in Buffer A in presence of 20% DMSO and 0.05% Tween-20 at 200 μ L total volume. 144 diverse library were also added to the library to make total of 1,344 compounds in four sealed polyethylene 384-well plates (Greiner). Library was stored at -20 °C.

2.4.2.2 Library Screening Protocol

The screening of the chemical library was conducted using optimised ADP-Glo kinase assay against GST-OSR1 T185E employing NKCC2 1-174 as a substrate as described in section 2.4.1. Screening was run in duplicate (two independent plates) using 50 μ M Rafoxanide (Sigma Aldrich, cat# 34042) and Closantel (Sigma Aldrich, cat#

34093) as positive controls. Screening data and screening plan were illustrated in **Table 2.13** and **Table 2.14**, respectively.

Assay	<ul style="list-style-type: none"> ▪ Type of assay: <i>In vitro</i> cell-free based biochemical ADP-Glo™ Max Assay (V7002).
	<ul style="list-style-type: none"> ▪ Target: Recombinant human OSR1.
	<ul style="list-style-type: none"> ▪ Primary measurement: Detection of ADP production.
	<ul style="list-style-type: none"> ▪ Key reagents: <ul style="list-style-type: none"> ○ 0.2 μM Human OSR1 T185E (in-house), 5 μM NKCC2 1-174 (in house) ○ 0.1mM ATP, Buffer A (PH 7.5), 50mM Tris (PH 7.5), 10mM MgCl₂.
Library	<ul style="list-style-type: none"> ▪ Library size: 1344 in four 384-well plates.
	<ul style="list-style-type: none"> ▪ Library composition: 1200 FDA-approved drug molecules + 144 diverse set of small molecules at 100μM in 20% DMSO solution, 0.05% Tween 20.
	<ul style="list-style-type: none"> ▪ Source: University of Birmingham.
Screen	<ul style="list-style-type: none"> ▪ Format: White, flat-bottomed Greiner 384-well plates.
	<ul style="list-style-type: none"> ▪ Total reaction volume: 5μl.
	<ul style="list-style-type: none"> ▪ Controls: 50 μM Closantel and Rafoxanide.
	<ul style="list-style-type: none"> ▪ Concentration(s) tested: 20 μM., 0.05% Tween 20, 4% DMSO.
Post-Hits analysis	<ul style="list-style-type: none"> • Hit criteria: > 40%.

Table 2.13: Chemical library screening data.

	1	2	3	4	5	6	7	8	9	10	11	12	13	14	15	16	17	18	19	20	21	22	23	24
A	B	DMSO	Clo	A02	A02	A03	A03	A04	A04	A05	A05	A06	A06	A07	A07	A08	A08	A09	A09	A10	A10	A11	A11	A2
B	B	DMSO	Clo	B02	B02	B03	B03	B04	B04	B05	B05	B06	B06	B07	B07	B08	B08	B09	B09	B10	B10	B11	B11	B2
C	B	DMSO	Clo	C02	C02	C03	C03	C04	C04	C05	C05	C06	C06	C07	C07	C08	C08	C09	C09	C10	C10	C11	C11	A3
D	B	DMSO	Clo	D02	D02	D03	D03	D04	D04	D05	D05	D06	D06	D07	D07	D08	D08	D09	D09	D10	D10	D11	D11	B3
E	B	DMSO	Clo	E02	E02	E03	E03	E04	E04	E05	E05	E06	E06	E07	E07	E08	E08	E09	E09	E10	E10	E11	E11	A4
F	B	DMSO	Clo	F02	F02	F03	F03	F04	F04	F05	F05	F06	F06	F07	F07	F08	F08	F09	F09	F10	F10	F11	F11	B4
G	B	DMSO	Clo	G02	G02	G03	G03	G04	G04	G05	G05	G06	G06	G07	G07	G08	G08	G09	G09	G10	G10	G11	G11	A5
H	B	DMSO	Clo	H02	H02	H03	H03	H04	H04	H05	H05	H06	H06	H07	H07	H08	H08	H09	H09	H10	H10	H11	H11	B5
I	B	DMSO	Raf	A02	A02	A03	A03	A04	A04	A05	A05	A06	A06	A07	A07	A08	A08	A09	A09	A10	A10	A11	A11	A6
J	B	DMSO	Raf	B02	B02	B03	B03	B04	B04	B05	B05	B06	B06	B07	B07	B08	B08	B09	B09	B10	B10	B11	B11	B6
K	B	DMSO	Raf	C02	C02	C03	C03	C04	C04	C05	C05	C06	C06	C07	C07	C08	C08	C09	C09	C10	C10	C11	C11	A7
L	B	DMSO	Raf	D02	D02	D03	D03	D04	D04	D05	D05	D06	D06	D07	D07	D08	D08	D09	D09	D10	D10	D11	D11	B7
M	B	DMSO	Raf	E02	E02	E03	E03	E04	E04	E05	E05	E06	E06	E07	E07	E08	E08	E09	E09	E10	E10	E11	E11	A8
N	B	DMSO	Raf	F02	F02	F03	F03	F04	F04	F05	F05	F06	F06	F07	F07	F08	F08	F09	F09	F10	F10	F11	F11	B8
O	B	DMSO	Raf	G02	G02	G03	G03	G04	G04	G05	G05	G06	G06	G07	G07	G08	G08	G09	G09	G10	G10	G11	G11	A9
P	B	DMSO	Raf	H02	H02	H03	H03	H04	H04	H05	H05	H06	H06	H07	H07	H08	H08	H09	H09	H10	H10	H11	H11	B9

Table 2.14: Screening protocol in 384 well-plate. Compounds were screened at 20μM. Screening was performed in 5μL total reaction volume by adding 1μL of either 4% DMSO (highlited with orange) or compounds (highlited with white) into 4μL reaction buffer containing 0.2 μM OSR1 T185E and 5 μM NKCC2 1-174 on microplate shaker incubator at 30°C for 30 minutes. Closantel (Clo, highlited with blue) and Raxofanide (Raf, highlited with yellow) were tested at 50 μM as positive controls. Assay was performed in duplicate in two separated plates. B: background.

2.4.2.3 Assay performance.

The assay parameters were calculated according to the following equations

(Iversen et al., 2006, Zhang et al., 1999):

$$Z' = 1 - \frac{3 \sigma \text{ positive} + 3 \sigma \text{ negative}}{|\mu \text{ positive} - \mu \text{ negative}|}$$

$$S/N = \frac{\mu \text{ negative} - \mu \text{ positive}}{\sigma \text{ positive}}$$

$$S/B = \frac{\mu \text{ negative}}{\mu \text{ positive}}$$

Where σ and μ are the standard deviations and means of the positive (total reaction mixture with NKCC2 1-174 substrate in absence of OSR1 T185E kinase) and negative (total reaction mixture with NKCC2 1-174 substrate in presence of OSR1 T185E kinase) controls, respectively. The reported values were the average of three independent experiments of 16 replicates performed on different days.

Post screening, in addition to the Z' factor, the signal window (SW) and coefficient of variation (CV%) were determined for each plate based on the following equations:

$$SW = \frac{|\mu \text{ negative} - \mu \text{ positive}| - 3X|\sigma \text{ negative} + \sigma \text{ positive}|}{\sigma \text{ negative}}$$

$$CV\% = \left(\frac{\sigma \text{ negative}}{\mu \text{ negative}} \right)$$

The reported values for each plate were the average for two plates with 16 replicates per each

2.4.3 Selectivity profiling

The kinase profiling study was performed by International Centre for Kinase Profiling (ICKP) MRC, UK using the premier screen service <http://www.kinase-screen.mrc.ac.uk/> (in collaboration with Professor Dario Alessi, University of Dundee). Verteporfin was tested against a series of 140 protein kinase enzymes in duplicates \pm SD at a final concentration of 1 μ M following the protocol described previously (Bain et al., 2007). In our study, proteins that were inhibited by $\geq 70\%$ are considered targets for Verteporfin. Data were analysed by Excel 2016.

2.5 Molecular modelling

2.5.1 Binding mode assessment

Autodock Vina 1.1.2 (Trott and Olson, 2010) was used for docking study. OSR1 C-terminal domain 433-527 (PDB ID: 2V3S) and OSR1 1-303 kinase domain (PDB ID: 2VWI) PDB files were retrieved from RCSB protein data bank database (www.rcsb.org) while the compounds' PDB files were either downloaded from PubChem

(<https://pubchem.ncbi.nlm.nih.gov/>) or generated using ChemDraw. Discovery Studio 4.5 (Accelrys, San Diego, CA, USA) was used to prepare protein files by removing ligands, water molecules and protein dimers to produce a single protein monomer as the crystal structure of OSR1 C-terminal domain (PDB ID: 2V3S) appears as dimers while OSR1 1-303 kinase domain (PDB ID: 2VWI) appears as tetramers. AutoDock Tool 1.5.6 software was then used to convert PDB files of proteins and ligands into PDBQT format (Sanner, 1999). Unbiased docking approach was performed using the following grid box parameters as input in the configuration file for docking and screening compounds against OSR1 C-terminal domain (PDB ID: 2V3S):

size_x = 40

size_y = 40

size_z = 40

center_x = -2.342

center_y = -1.09

center_z = 25.822

Exhaustiveness = 50

Moreover, the grid box parameters used in the input configuration file for docking and screening compounds against OSR1 1-303 kinase domain (PDB ID: 2VWI):

size_x = 42

size_y = 52

size_z = 66

center_x = 92.774

center_y = 150.204

center_z = -15.28

Exhaustiveness = 50

The docking results were visualised and analysed using Discovery Studio 4.5 and figures were generated using PyMOL Molecular Graphics System 1.3.

2.5.2 Structure-based virtual screening (SBVS)

Autodock Vina in PyRx 0.8 (virtual screening tool) was used to carry out the structure-based virtual screening (SBVS) of 1,200 FDA-approved compounds against OSR1 C-terminal domain 433-527 (PDB ID: 2V3S). Library of compounds was obtained from The Birmingham Drug Discovery Facility, School of Biosciences, University of Birmingham in a single SDF file. The 1,200 FDA compounds were divided randomly into groups of 100 compounds using Discovery Studio 4.5 (Accelrys, San Diego, CA, USA) and saved as PDB files and docked separately. The PDB files were imported individually into open babel tool of PyRx software and converted into AutoDock PDBQT format. Grid box was set to cover the whole protein structure, OSR1 C-terminal domain (PDB ID: 2V3S), for unbiased docking using the following coordinates as input in the configuration file:

size_x = 25

size_y = 25

size_z = 25

center_x = -2.31.910

center_y = 0.121

center_z = 26.332

Exhaustiveness = 8

Docking results were exported in Excel sheet and compounds were ranked based on the docking energy scores and subjected to manual inspection and structural analysis.

2.6 Nuclear magnetic resonance (NMR)

2.6.1 Fragment library

A diverse fragment library of ~ 384 commercially available compounds at 200 mM stock in 100% (v/v) D₆-DMSO was provided by Dr Mark Jeeves (Henry-Welcome NMR building, University of Birmingham). The compounds were selected and purchased from Maybridge and Sigma Aldrich based on their physicochemical properties including molecular weight (110-250 g/mole), diversity of chemical scaffolds, solubility in an aqueous buffer (2 mM in water) and suitability for primary drug discovery screening. The compounds were grouped into cocktails of four in 96-loose well matrix plates to minimising the experimental running time as well as the amount of protein required. The cocktails were prepared based on the compounds ¹HNMR spectrum which was recorded and checked for each fragment. All NMR experiments and data analysis was carried out in collaboration with Dr Mark Jeeves.

2.6.2 Ligand-based NMR screening experiment

The screening of fragment library was carried out by STD (saturation transfer difference)-NMR and water-ligand observed via gradient spectroscopy (waterLOGSY) against unlabelled GST-tagged OSR1 C-terminal domain 433-527 and unlabelled GST-tag only as a reference to eliminate possible GST-tag binders (Klages et al., 2007). Proteins were first diluted in NMR running buffer containing 50 mM Tris-d₁₁ pH 7.4, 150 mM NaCl and 1 mM dithiothreitol. NMR samples were prepared by adding each cocktail at 1 mM final concentration to a mixture of 10 µM of either unlabelled OSR1 C-terminal domain or unlabelled GST-tag, 20% deuterium oxide (D₂O) and 3% (v/v) D₆-DMSO (5% final DMSO concentration) in NMR running buffer at 50 µL total sample volume.

Samples were mixed in short thread vials and then transferred into 1.7 mm NMR sample tubes using a Gilson GX- 271 liquid handler.

STD-NMR and waterLOGSY experiments were carried out, consecutively, on the same sample, on a Bruker 600 MHz spectrometer at 25°C equipped with a Z-axis gradient CryoProbe. Each experiment was run for approximately 45 minutes in a total of 90 minutes for each cocktail sample.

For STD-NMR experiments, irradiation frequency was -0.5 ppm for the “on resonance” in which the only frequency that contains protein resonances region will be irradiated and 30 ppm for “off resonance” in which no NMR spectra were observed to be perturbed. The difference between the two spectrums was then calculated. For the WaterLOGSY experiments, the water resonance frequency was selectively perturbed by excitation of the bulk water magnetisation between 4.6 and 4.7 ppm. Both experiments results were processed by NMRPipe (Delaglio et al., 1995) and analysed using TOPSPIN (version 3.2, Bruker Biospin) by comparing STD and WaterLOGSY spectra with ^1H -NMR spectrum for individual compounds.

2.6.3 STD-NMR competition assay for ligand binding specificity

STD competition experiment was conducted using the same method described above. RFQV (CCPGCCGGSEEGKPQLVGR**RFQ**VTSSK) peptide, with $K_d = 8$ nM to the primary pocket of OSR1 C-terminal domain (Vitari et al., 2006), was dissolved in 100% (v/v) D_6 -DMSO at 5 mM stock solution. NMR samples were prepared by adding RFQV peptide at 50 μM final concentration to a mixture of the compound at 1 mM final concentration, 10 μM of unlabelled OSR1 C-terminal domain, 20% deuterium oxide (D_2O) and 3% (v/v) D_6 -DMSO (5% final DMSO concentration) in NMR running buffer at 50 μL total sample volume. Final DMSO concentration was 5%.

2.6.4 ^1H - ^{15}N HSQC for studying the suitability of C-terminal domains of SPAK and OSR1 for NMR studies

^{15}N - ^1H NMR heteronuclear single quantum coherence (HSQC) experiment was acquired on a Bruker 600 MHz spectrometer equipped with a z-axis gradient CryoProbe at 25 °C. Samples were prepared as described above. ^1H - ^{15}N NMR HSQC spectra was recorded in presence of ~ 0.2 mM ^{15}N -OSR1 CCT or ^{15}N -SPAK CCT, 20% deuterium oxide (D_2O) in NMR running buffer at 50 μL total sample volume to assess the suitability of ^{15}N -OSR1 CCT or ^{15}N -SPAK CCT for NMR studies.

2.6.5 Sequence-specific ^1H , ^{13}C and ^{15}N backbone resonance assignments of the C-terminal domain of human OSR1

Triple resonance NMR experiments for backbone assignment of OSR1 C-terminal domain were performed on a Bruker 600 MHz spectrometer equipped with z-axis gradient triple-resonance CryoProbe at 25°C. Backbone assignments were achieved by a combination of 3D backbone assignment experiments including of HNCA, HNCOC, HNCACOC, HN(CO)CA, HNCACB, HN(CO)CACB experiments as well as ^1H - ^{15}N HSQC and ^{15}N - ^1H HMBC (Heteronuclear Multiple Bond Correlation) 2D NMR experiments (Wishart and Sykes, 1994). Experiments were run on uniformly double labelled ^{15}N - ^{13}C OSR1 CCT at ~0.2 mM final concentration in NMR running buffer containing 50 mM Tris- d_{11} pH 7.4, 150 mM NaCl and 1 mM dithiothreitol. Sequence-specific assignment was processed by NMRPipe and analysed using CcpNmr Analysis (Vranken et al., 2005).

2.6.5.1 HNCO and HN(CA)CO

The HNCO experiment was conducted to determine the connectivity of backbone amide resonance of the residue (i) to the resonance of C' (carbonyl carbon) of proceeding residue (i-1) (**Figure 2.1a**). The HN(CA)CO is a complementary experiment that

determine the connectivity of backbone amide resonance of the residue (i) to both the resonance of C' (carbonyl carbon) of proceeding residue (i-1) as well as the resonance of C' (carbonyl carbon) of residue (i) (**Figure 2.1b**).

2.6.5.2 HNCA and HN(CO)CA

The HNCA experiment was conducted to determine the connectivity of backbone amide resonance of the residue (i) to the resonance of C α of residue (i) and the resonance of C α of residue (i-1) (**Figure 2.1c**). The HN(CO)CA is a complementary experiment that determine the connectivity of backbone amide resonance of the residue (i) to the resonance of C α of residue (i-1) (**Figure 2.1d**).

2.6.5.3 HNCACB and HN(CO)CACB

The HNCACB experiment was conducted to determine the connectivity of backbone amide resonance of the residue (i) to the resonances of C α and C β of both residue (i) and (i-1) (**Figure 2.1e**). The HN (CO)CACB is a complementary experiment that determine the connectivity of backbone amide resonance of the residue (i) to the resonance of C β of residue (i-1) (**Figure 2.1f**).

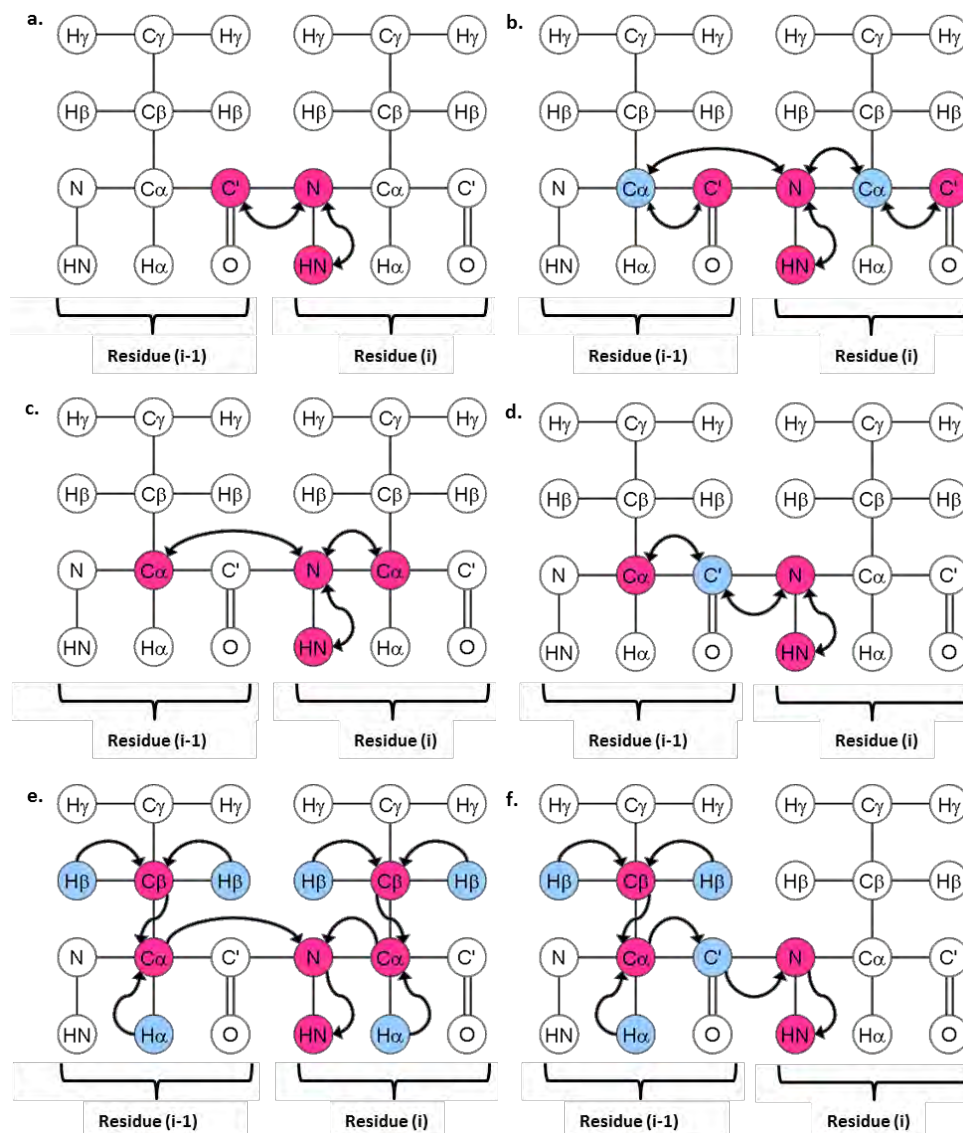


Figure 2.1: 3D TROSY-based backbone assignment experiments. Representation of magnetisation transfer pathway for backbone assignment of (a) HNCO (b) HN(CA)CO (c) HNCA (d) HN(CO)CA (e) HNCACB and (f) HN(CO)CACB. Nucleus highlighted in pink indicates that resonance for this is observable in the experiment. Nucleus highlighted in grey is not observable in the experiment but participates in the magnetization transfer. Figure adapted from Protein NMR (<http://www.protein-nmr.org.uk>).

2.6.6 Chemical shift mapping (chemical shift perturbations (CSPs))

To confirm compounds binding and their binding residues, ^1H - ^{15}N NMR HSQC was performed against ~ 0.2 mM ^{15}N -OSR1 CCT in absence (apo-protein) and presence of compounds. Then, two spectra were overlapped to observe specific residue chemical shift perturbations and map these residues to OSR1 CCT backbone assignment. RFQV peptide was tested as a positive control at 50 μM final concentration. STOCK2S-26016 (Tocris Bioscience, cat# 5570) and Rafoxanide were tested at 200 μM at 5% D_6 -DMSO. Confirmatory screening was conducted for positive fragment hits at 1mM final concentration using the same procedure. Data were processed by NMRPipe and analysed using TOPSPIN version 3.2.

2.6.7 Analysis of chemical shift perturbations (CSPs)

Chemical shift perturbations ($\Delta\delta$) or backbone amide changes were calculated for each residue in ^1H - ^{15}N NMR HSQC spectrum according to the following equations (1) and (2):

$$\Delta\delta (\text{H, N}) = \delta_{\text{bound}} - \delta_{\text{free}} \quad (1)$$

$$\Delta\delta (\text{H, N}) = \sqrt{(\Delta\delta\text{H})^2 + (0.154 \times \Delta\delta\text{N})^2} \quad (2)$$

Where $\Delta\delta\text{H}$ and $\Delta\delta\text{N}$ are the ^1H and ^{15}N amide chemical shift changes induced by ligands binding and the resulting structural changes. Chemical shift perturbations ($\Delta\delta$) were defined as the difference between the corresponding chemical shifts in the bound (δ_{bound}) and free (δ_{free}) states of the OSR1 CCT (Williamson, 2013).

2.6.8 Secondary structure prediction of OSR1 CCT based on NMR chemical shifts

Secondary structure of OSR1 CCT was predicted by TALOS+ (torsion angle likelihood obtained from shift and sequence similarity) server (<https://spin.niddk.nih.gov/bax/software/TALOS/>) (Shen et al., 2009a) and CSI (chemical shift index) server (<http://csi3.wishartlab.com>) (Hafsa et al., 2015) using backbone NMR chemical shifts. CcpNmr Analysis was used to convert chemical shift into TALOS or BMRB (BioMagResBank) formats to be used as inputs for TALOS+ and CSI servers, respectively.

2.6.9 Predication of OSR1 C-terminal domain 3D structures

3D structure of OSR1 CCT was predicted using Chemical-Shift-ROSETTA (CS-Rosetta) server (<https://csrosetta.bmr.b.wisc.edu/csrosetta/submit>) based on OSR1 CCT NMR Chemical Shifts (Shen et al., 2008). OSR1 CCT NMR Chemical Shifts was obtained by TALOS+ (torsion angle likelihood obtained from shift and sequence similarity) server. Best model with best RMDS score was considered.

**CHAPTER III: DETERMINE THE EFFECT OF
THE SECONDARY POCKET OF SPAK AND
OSR1 ON THEIR KINASES ACTIVITY**

3.1 Introduction

Human SPAK and OSR1 protein kinases have a 92 amino acids conserved carboxy-terminal (CCT) domain, which are 79% identical in their primary amino acids sequence. The CCT domain consists of four antiparallel β -strands packed against two large and one small α -helix in a unique folding pattern (Villa et al., 2007) (**Figure 3.1a**). The CCT domain of human SPAK (456-547) and human OSR1 (436-527) bind to RFxV (Arg-Phe-Xaa-Val) motifs of the upstream WNK and downstream ion co-transporters (Villa et al., 2007). It has been shown that an 18-mer peptide derived from human WNK4 and contains the RFQV motif binds to OSR1 CCT with high affinity ($K_d = 8$ nM) and a single point mutation within RFQV peptide, particularly the arginine, phenylalanine or valine residue, abolishes the binding to SPAK and OSR1 (Vitari et al., 2006). The co-crystal structure of 18-mer RFQV peptide derived from WNK4 kinase with human OSR1 CCT domain revealed that a negatively charged pocket formed by the interface between $\alpha 1$ and $\beta 2$ in the CCT domain termed; primary pocket is responsible for mediating the binding to the upstream and downstream protein partners (**Figure 3.1a**). Interestingly, the crystal structure illustrated that the CCT domain possess another highly conserved pocket termed; secondary pocket formed by a large loop connecting $\alpha 3$ to $\beta 4$ (**Figure 3.1a**) (Villa et al., 2007). Notably, the role of the secondary pocket remained elusive for many years.

The work described in this chapter was built upon our finding that STOCK1S-50699, which was discovered as SPAK-WNK binding inhibitor, was able to disrupt the binding of biotinylated-RFQV peptide to endogenous SPAK at only high concentration of ≥ 300 μ M (**Figure 3.1b**). However, in HEK293 cells, which endogenously express WNK signalling proteins, STOCK1S-50699 was a potent inhibitor of WNK signalling as the phosphorylation of SPAK at Ser373 that specifically phosphorylated by WNK kinases

as well as its substrate NKCC1 at Thr203, Thr207 and Thr212 were completely inhibited at a concentration nearly three-fold lower than the cell-free based assay IC_{50} value (~10 μ M) (**Figure 3.1c**). Since STOCK1S-50699 was reported as SPAK CCT domain binder with a good selectivity profile, these paradoxical observations between the inhibitory effect of STOCK1S-50699 determined by cell-based and cell-free based assays suggested that STOCK1S-50699 may bind to another site within the CCT domain of SPAK and OSR1 and that causes the observed increase in the activity in cells. Accordingly, we hypothesised that STOCK1S-50699 may bind to the secondary pocket of SPAK and OSR1 CCT domains, which may play a role as an allosteric binding site.

3.2 Aim

The overall aim of this chapter was to explore the impact of the secondary pocket on the catalytic activity of SPAK and OSR1 and whether it is amenable to targeting by small molecules.

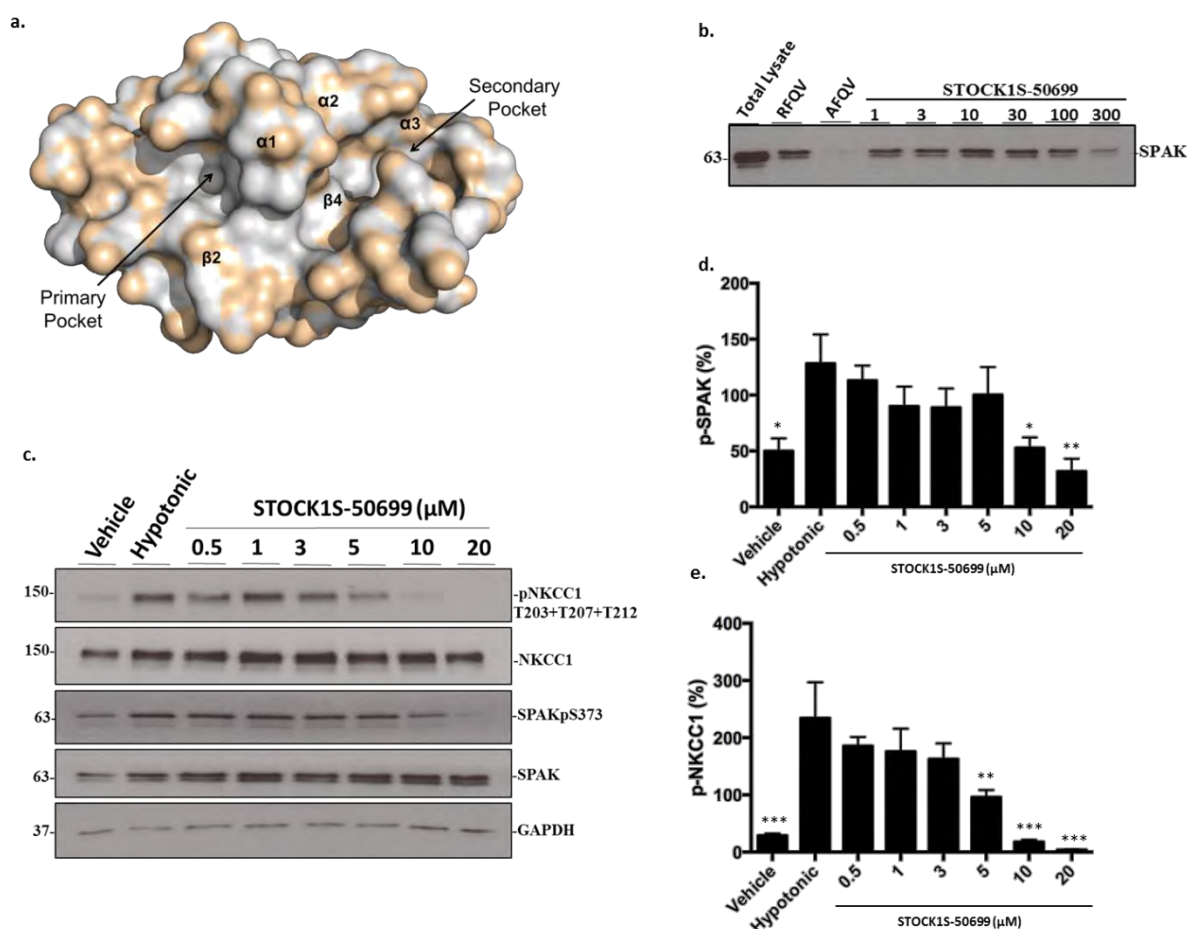


Figure 3.1: Characterisation of the inhibitory effect of STOCK1S-50699 in *in vitro* cell-free based assays and in HEK293 cells. (a) A crystal structure of the human OSR1 CCT domain (433-end) (PDB ID: 2V3S) showing the key primary and secondary pockets. (b) Biotinylated 18-mer RFQV peptide was used to pull down endogenous SPAP from HEK293 cells in the absence or presence of STOCK1S-50699 at the indicated concentrations; Total lysate, RFQV and AFQV samples were treated with DMSO. The biotinylated 18-mer AFQV peptide was used as a reference control. (c) STOCK1S-50699 inhibits endogenous SPAP kinase in HEK293 cells. HEK293 cells were first treated with STOCK1S-50699 at the indicated concentrations (or DMSO as a vehicle control) for 30 min and then either untreated or treated with low-chloride hypotonic buffer for 30 min to activate WNK-SPAP/OSR1 signalling. The cells were then harvested, and the lysates were probed for phospho-NKCC1 T203, T207 and T212, total NKCC1, phospho-SPAPs373, total SPAP and GAPDH as a loading control. (d) pSPAP and (e) pNKCC1 were quantified relative to GAPDH. The data were reported as mean ($n=4$, \pm SEM); *** $p < 0.001$, ** $p < 0.01$, * $p < 0.05$. A one-way ANOVA test followed by Tukey's test were used to compare the results. Final DMSO concentration is 0.1%. Data shown in (b) is representative of three independent repeats.

3.3 Results

3.3.1 Evaluation of the effect of secondary pocket mutations on OSR1 T185E catalytic activity

Initially, the effect of the secondary pocket on the catalytic activity of OSR1 was investigated. To do this, the secondary pocket was mutated at amino acid residues that line this pocket namely, L440, S443 and V507 into alanine (**Figure 3.2a**). These three mutations were introduced to GST-tagged OSR1 T185E, where threonine 185 (Thr185) was mutated into glutamic acid (to mimic WNK phosphorylation at this site) making the OSR1 kinase constitutively active *in vitro* (Vitari et al., 2005). GST-tagged full length (FL) OSR1 T185E with and without single point mutations in the CCT domain was overexpressed and purified from HEK293 cells (see Method and Method section 2.2.2). The catalytic activity of these kinases was determined using Promega's luminescence ADP-Glo™ kinase assay (see Method and Method section 2.4.1) (Zegzouti et al., 2009). As shown in **Figure 3.2b**, out of the three mutations studied, L440A and V507A showed statistically significant reduction in the kinase activity of OSR1 T185E as compared to the control. However, mutation of S443 into alanine did not affect the kinase activity of OSR1 T185E.

3.3.2 Evaluation of the effect of secondary pocket mutations on OSR1 CCT domain ability to bind upstream WNK kinase

3.3.2.1 Biotin–streptavidin pull down assay

To investigate whether the L440A, S443A and V507A secondary pocket mutations have any effect on the ability of OSR1 CCT domain to bind WNK kinases, a biotin–streptavidin pulldown assay was carried out. In this assay, a biotinylated 18-mer RFQV-peptide derived from human WNK4 was used to pull down OSR1 from a HEK293

cell lysate overexpressing either GST-OSR1 FL wild type (WT) or its derivatives that carry single point mutations in the secondary pocket (see Method and Method section 2.3.1). As a reference, two GST-OSR1 proteins with single point mutations, D459A and L473A, in their primary pocket were also overexpressed. These two mutations are known to prevent the binding of OSR1 to WNK kinases (**Figure 3.2a**) (Vitari et al., 2006). As shown in **Figure 3.2c**, the biotinylated 18-mer RFQV peptide was able to pull down endogenous GST-tagged OSR1 FL WT. Notably, mutations in the secondary pocket had no effect on the ability of biotinylated 18-mer RFQV peptide to bind to OSR1 CCT domain. In contrast, mutations in OSR1 FL WT primary pocket abolished the binding to the biotinylated 18-mer RFQV peptide. These results indicated that the secondary pocket has no influence on the binding of RFQV-peptide to the OSR1. An observation that aligns with what was noted previously by others (Vitari et al., 2006).

3.3.2.2 Fluorescence polarisation (FP) assay

To confirm that the mutations L440A and V507A in the secondary pocket of OSR1 CCT domain, which influenced the kinase activity *in vitro*, did not affect the ability of OSR1 CCT domain to bind WNK kinases, a fluorescence polarisation assay was developed and optimised for measuring the binding affinity of OSR1 CCT WT domain to an 18-mer RFQV-peptide derived from the upstream kinase WNK (see Method and Method section 2.3.2) (Zhang et al., 2015). Initially, GST-OSR1 WT protein and those with mutations in the secondary pocket (L440A and V507A) as well as in the primary pocket (L473A) were expressed and purified from *E.coli* (see Method and Method section 2.1.6.1) (**Figure 3.2d**). From the FP assay (**Figure 3.2e**) and consistent with the data presented in 3.2.2.1, the primary pocket mutation (L473A) led to a significant reduction in the binding of the OSR1 CCT domain to the WNK 18-mer RFQV-peptide (WT K_d =

2.11 μM and L473A $K_d = 13.17 \mu\text{M}$) (**Figure 3.2e**). Interestingly, the introduction of single point mutations in the secondary pocket had no effect on the binding of OSR1 to the WNK4 18-mer RFQV peptide (L440A $K_d = 1.83 \mu\text{M}$ and V507V $K_d = 1.75 \mu\text{M}$) (**Figure 3.1e**).

Together, this data represents the first evidence that the secondary pocket of OSR1 CCT domain is able to influence its kinase activity and may be exploited as an allosteric target to inhibit its kinase activity. Considering the high similarity in sequence of the CCT domain of SPAK and OSR1, 79% sequence identity, this pocket is very likely to influence the kinase activity of SPAK kinase as well.

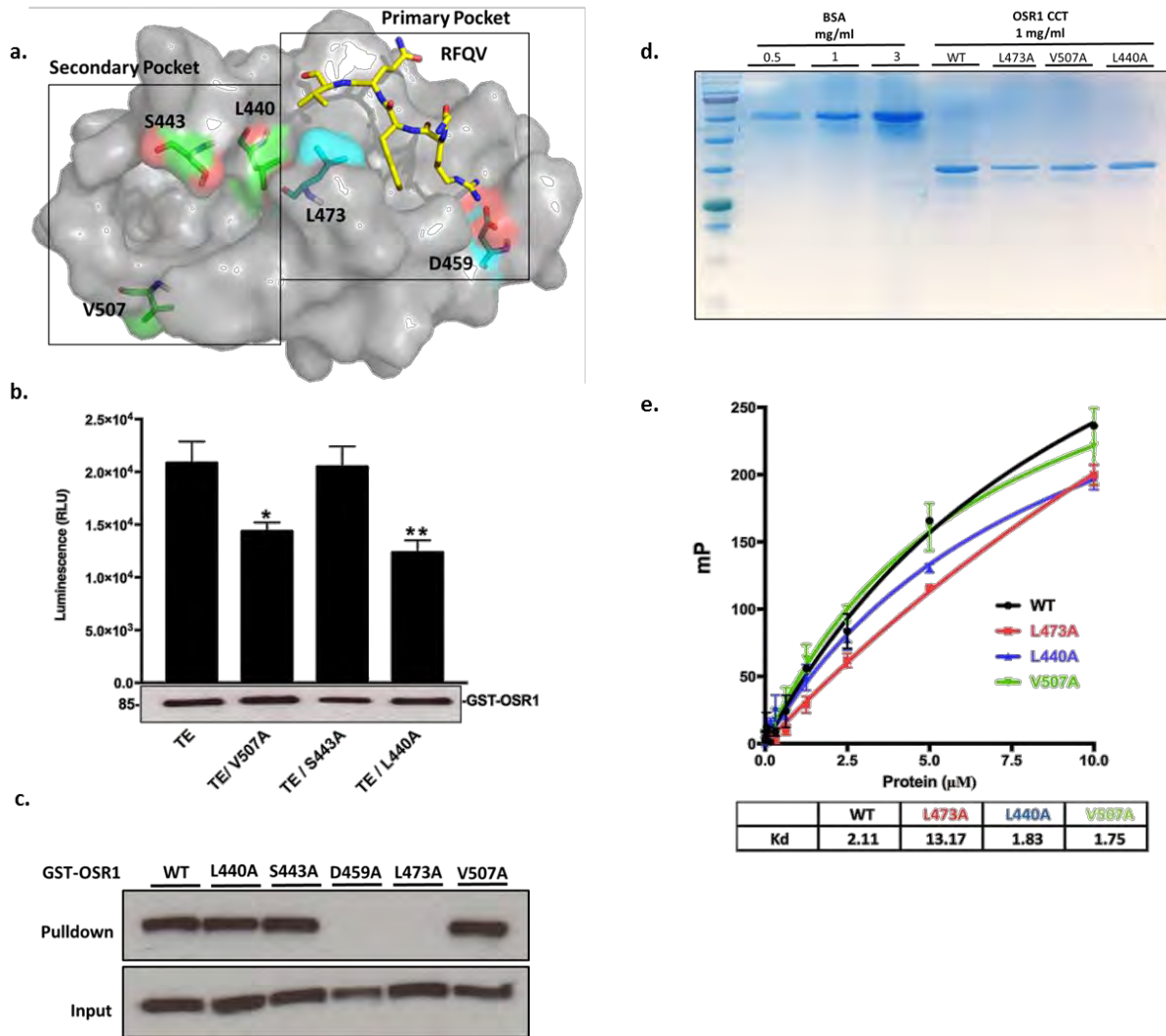


Figure 3.2: Characterisation of the effect of secondary pocket on OSR1 kinase. (a) A molecular surface representation of OSR1 CCT domain crystal structure (PDB ID: 2V3S) showing the location of the residues of interest in the secondary and primary pockets. The secondary pocket residues are shown in green colour and primary pocket key residues are in cyan colour. (b) Single mutations in OSR1 T185E secondary pocket decrease its kinase activity *in vitro*; * $p < 0.05$, ** $p < 0.01$. (c) Mutation in the OSR1 secondary pocket L440A, S443A and V507A did not affect its binding to the biotinylated-RFQV peptide. (d) Expression and purification of OSR1 CCT WT and with different mutations in the primary and secondary pockets from *E. coli*. BSA (bovine serum albumin) was used as a standard for proteins purity and concentration. (e) Fluorescence polarisation analysis of the binding of OSR1 CCT WT, primary pocket single point mutation (L473A), and secondary pocket single point mutations (L440A and V507A), to an 18-mer RFQV peptide derived from WNK4. Data shown in (b) and (e) are the average signals ($n=3$, \pm SD), Data shown in (e) is a representative of three independent repeats. Figures adapted from (AlAmri et al., 2017a).

3.3.3 Molecular docking of known WNK signalling inhibitors into OSR1 CCT domain

Molecular docking is a competent and efficient computational tool for studying how ligands fit both energetically and geometrically the binding site of a protein (Kitchen et al., 2004). By using computational methods and the 3D structure of the target protein, the investigation of the underlying molecule- protein interactions involved in ligand-protein binding at the atomic level is achievable (Lionta et al., 2014). Encouraged by the above results that the secondary pocket plays a role in regulation of OSR1 kinase activity, an *in silico* molecular docking of reported WNK signalling inhibitors (AlAmri et al., 2017b) that bind to SPAK and OSR1 into the crystal structure of human OSR1 CCT domain was conducted (PDB ID: 2V3S). For the docking, AutoDock Vina 1.1.2 software (Trott and Olson, 2010) was used to dock STOCK1S-50699, STOCK2S-26016, STOCK1S-14279 and Closantel (**Figure 3.3**), which are all reported as SPAK binders and are able to inhibit WNK signalling, into the reported crystal structure of OSR1 CCT domain (Kikuchi et al., 2014, Mori et al., 2013). An unbiased docking approach was conducted in which the grid box that represents the search space was centered to cover the whole protein (see Method and Method section 2.5.1). The docking approach was initially optimised in terms of docking exhaustiveness and subsequently validated by redocking the RFQV peptide into OSR1 CCT domain (PDB ID: 2V3S) and the PP1 Src inhibitor into the ATP pocket of hematopoietic cell kinase (HCK) (PDB ID: 1QCF). Interestingly, all possible poses for the docked WNK-signalling inhibitors were placed in the secondary pocket (**Figure 3.3a**). The only exception was the RFQV peptide and the PP1 Src inhibitor, which using the same docking procedure, resulted in the docking of these ligands only in the primary pocket of OSR1 CCT domain and the ATP binding site

of HCK, respectively, as expected (**Appendix 3.1**). Additionally, the binding energy was determined for the best binding pose of each compound (**Figure 3.3b**).

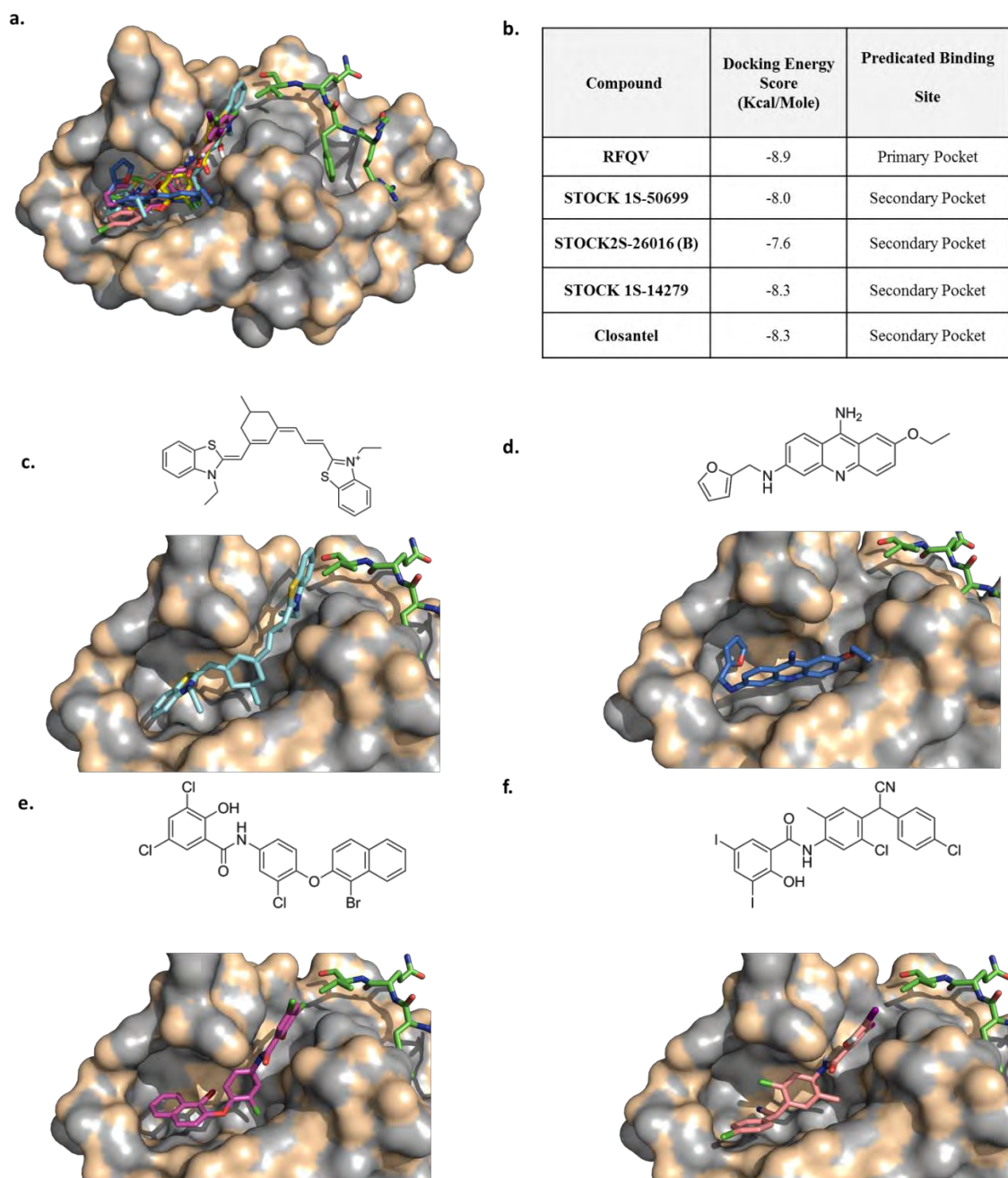


Figure 3.3: Chemical structures and docking results of four WNK-SPAK/OSR1 signalling inhibitors. (a) Autodock Vina results illustrated exclusive binding of (a) all four inhibitors, (c) STOCK1S-50699, (d) STOCK2S-26016, (e) STOCK1S-14279 and (f) Closantel to the secondary pocket of the OSR1 CCT domain (PDB ID: 2V3S). The tetrapeptide-RFQV (green sticks) binds to the primary pocket of OSR1 CCT domain. (b) A table illustrating the binding energy score of all four WNK signalling inhibitors to OSR1 CCT domain. Figure was produced using PyMOL Molecular Graphics System 1.3. Figures adapted from (AlAmri et al., 2017a).

3.3.4 Effect of STOCK1S-50699 and Closantel on OSR1 kinase activity *in vitro*

Inspired by the finding that reported WNK-signalling inhibitors docked into the secondary pocket of OSR1 CCT domain, we focused on studying STOCK1S-50699 and Closantel. For the *in vitro* characterisation of their inhibitory effects, OSR1 T185E was utilised as it exhibits a better kinase activity profile *in vitro* as compared to SPAK T233E (Filippi et al., 2011). Initially, an *in vitro* bioluminescence (non-radioactive) assay was developed and optimised using purified OSR1 T185E FL from *E.coli* (see Method and Method section 2.4.1) (**Appendix 3.2a**). In this assay, a peptide termed CATCHtide (RRHYYYDTHNTYYLRTEFGHNTRR) was employed as a kinase substrate (Vitari et al., 2006). The obtained results confirmed the ability of these two compounds (STOCK1S-50699, $IC_{50} = 40.26 \mu M$ and Closantel, $IC_{50} = 8.65 \mu M$) to inhibit OSR1 *in vitro* (**Figure 3.4a and 3.4b**). Notably, the determined *in vitro* OSR1 T185E inhibitory potency of STOCK1S-50699 ($IC_{50} = 40.26 \mu M$) is similar to that reported by other groups ($IC_{50} = 30-37 \mu M$) though different assays were used (Mori et al., 2013).

For further investigation, the inhibitory effect of STOCK1S-50699 and Closantel were tested on constitutively active truncated form of OSR1 T185E 1-342 which lacks the CCT domain. Strikingly, STOCK1S-50699 and Closantel were unable to inhibit this protein indicating that these inhibitors exert their action through binding to the CCT domain. (**Figure 3.4c and 3.4d**).

3.3.5 Effect of STOCK1S-50699 and Closantel on OSR1 kinase at different ATP-concentrations

To test whether STOCK1S-50699 and Closantel exerted their inhibitory effect due to competition with ATP in the catalytic domain, a common approach for protein kinases inhibition. The strategy was to screen the inhibitory effect of STOCK1S-50699 and Closantel at three different ATP concentrations below and above K_m value of OSR1 (see Method and Method section 2.4.1). Under current assay condition, the apparent dissociation constant (K_m) of OSR1 was 391 μ M (**Appendix 3.3**). In the case of Closantel, a purified fragment of *N*-terminal NKCC2 1-174 was used as an OSR1 substrate (Vitari et al., 2006) (**Appendix 3.2b**). As shown in (**Figure 3.4e and 3.4f**), no significant change in the IC_{50} values (45-, 50- and 37 μ M for STOCK1S-50699 and 14.09-, 12.74- and 10.97 μ M for Closantel) were observed at 0.01, 0.1 and 1mM ATP concentrations, respectively. This indicated that STOCK1S-50699 and Closantel inhibit OSR1 in an ATP-independent manner. Collectively, these results could explain the mechanism by which Closantel inhibit the activity of OSR1 T185E, which was reported as non-ATP competitive inhibitor of SPAK and OSR1 though its binding site was unknown. These results provided evidence that STOCK1S-50699 inhibits the OSR1 T185E kinase *in vitro* under assay conditions that lack the upstream activator (WNK kinases). These data was unexpected as STOCK1S-50699 was initially reported as a binding inhibitor of SPAK and OSR1 to WNK kinases (Mori et al., 2013). This made us hypothesise that STOCK1S-50699 may inhibit OSR1 by a dual mechanism of action that includes binding to the secondary pocket of OSR1 CCT domain and disrupting its binding to WNK kinases. Therefore, this dual mechanism of action of STOCK1S-50699 might rationalise the high potency of this compound in cell-based assay as compared to the cell-free based assay.

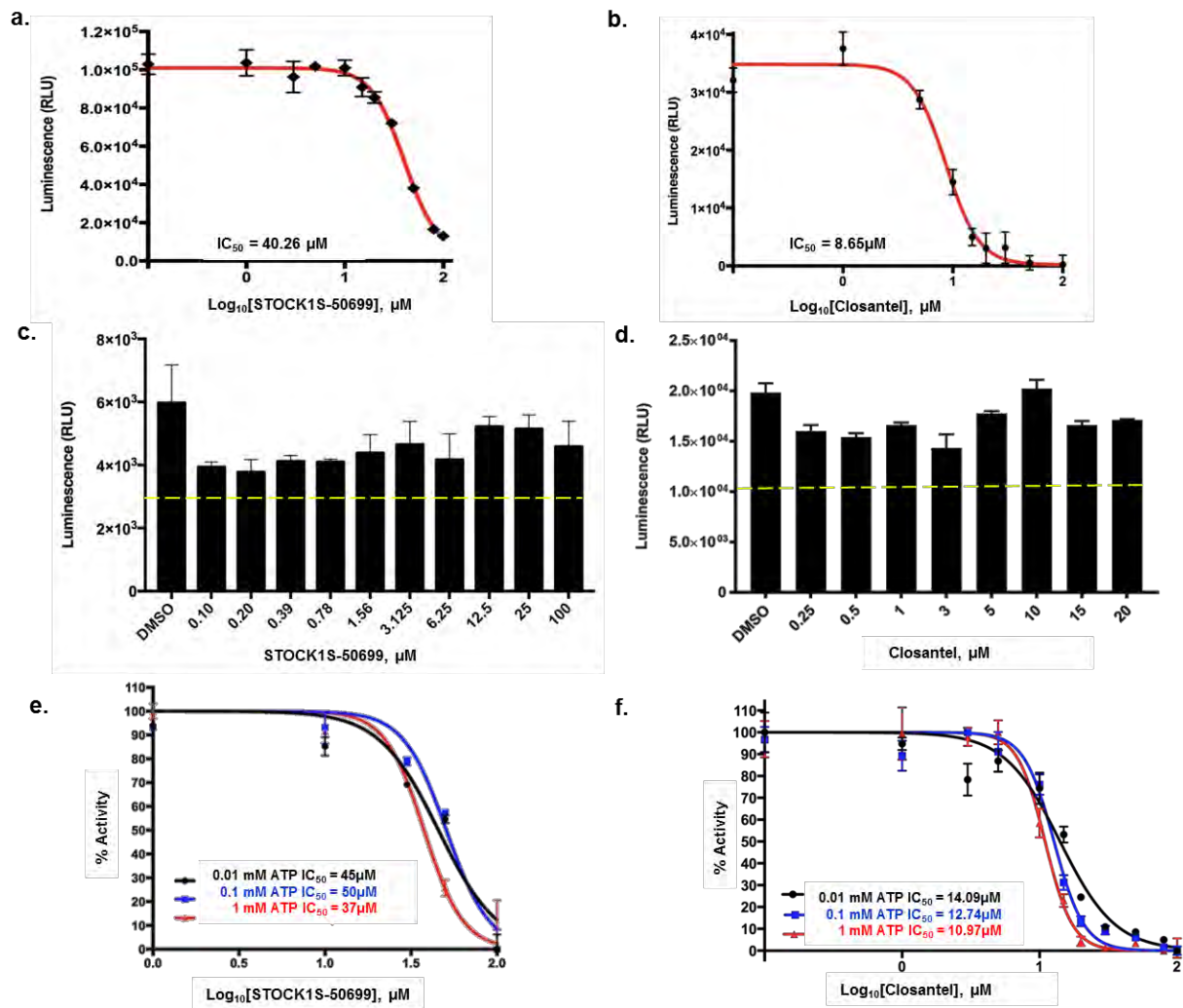


Figure 3.4: Characterisation of STOCK1S-50699 and Closantel Activity *in vitro*. ADP-Glo *in vitro* kinase assay of (a) STOCK1S-50699 and (b) Closantel is illustrating the inhibition of constitutively active OSR1 T185E FL. ADP-Glo *in vitro* kinase assay of (c) STOCK1S-50699 and (d) Closantel are illustrating that they do not inhibit truncated OSR1 T185E 1–342, which lacks CCT domain. CATCHtide was used as a kinase substrate. (e) STOCK1S-50699 and (f) Closantel inhibit OSR1 T185E in an ATP-independent manner. In this assay, CATCHtide and NKCC2 1-174 were used as kinase substrates for testing the activity of STOCK1S50699 and Closantel at different ATP concentrations, respectively. Data shown are the average signals ($n=3$, \pm SD). The dotted yellow lines in (c) and (d) indicate 50% of the maximum kinase activity. Figures adapted from (AlAmri et al., 2017a).

3.3.6 Structure-based virtual screening of 1,200 FDA-approved compounds

Structure-based virtual screening is a useful tool in the identification of potential inhibitors in a time- and cost-effective manner (Lionta et al., 2014). To further characterise the regulatory function of the secondary pocket of OSR1, an *in silico* structure-based virtual screening of in-house 1,200 FDA-approved compounds was conducted aiming to identify small-molecular inhibitors that bind to the secondary pocket of SPAK and OSR1 and inhibit their kinase activities. The screening was carried out using the molecular docking program Autodock Vina in PyRx 0.8 (see Method and Method section 2.5.2) (Trott and Olson, 2010). The library of 1,200 FDA-approved compounds was divided randomly into groups of 100 compounds and docked separately using the same unbiased docking approach described in 3.2.5. Among the top hits obtained was Rafoxanide, a potent antiparasitic agent used for treatment of infestations in animals (Swan, 1999). Rafoxanide stood out because it is structurally similar to the reported WNK signalling inhibitor, Closantel. They both have the core salicylanilide and both are anthelmintic drugs (**Figure 3.5b**). Therefore, Rafoxanide was considered for further investigations. Docking of Rafoxanide using Autodock vina into OSR1 CCT indicated that it binds to the secondary pocket (docking score = -7.8 Kcal/mol) (**Figure 3.5c**) and formed hydrogen bonds with Arg441, and Glu505 which are both located in the secondary pocket and Leu473 which is located in the primary pocket (**Figure 3.5d**).

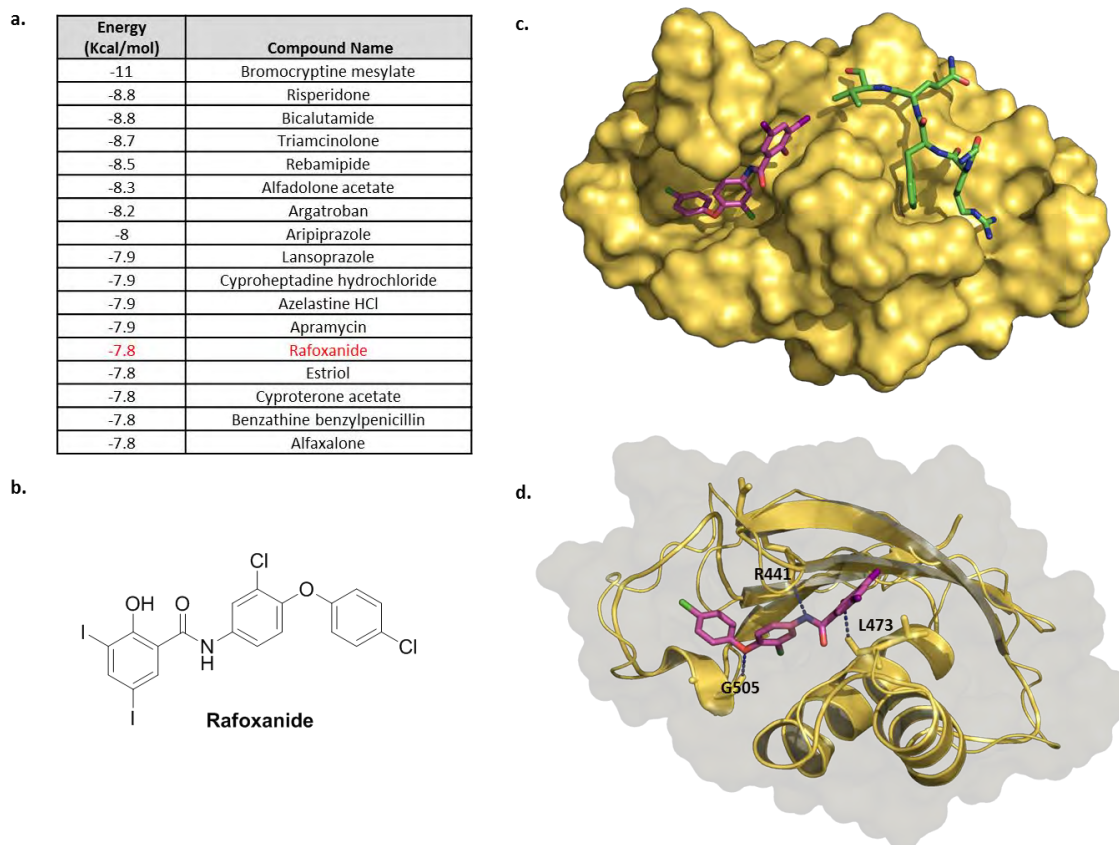


Figure 3.5: Identification of Rafoxanide using structure-based virtual screening. (a) Part of virtual screening results showing the energy score of Rafoxanide (red). (b) Chemical structure of Rafoxanide. (c) Molecular surface representation of the predicated binding mode of Rafoxanide (pink sticks) to the secondary pocket of OSR1 CCT (PDB ID: 2V3S) using Autodock vina software. RFQV peptide (green sticks) binding to the primary pocket of OSR1 CCT. (d) A ribbon representation of molecular interaction of Rafoxanide with amino acid residues in the secondary pocket of OSR1 CCT. Molecular interactions were determined using Discovery Studio 3.5 Client. Molecule modeling figures were produced using PyMOL Molecular Graphics System 1.3.

3.3.7 Characterisation of the inhibitory effect of Rafoxanide as a novel SPAK and OSR1 allosteric inhibitor

Using the same *in vitro* kinase assay described in 3.2.4, Rafoxanide inhibited the activity of constitutively active OSR1 T185E FL in a low-micromolar concentration range ($IC_{50} = 8.18 \mu M$) (**Figure 3.6a**). Rafoxanide acted like Closantel and STOCK1S-50699 and did not inhibit the kinase activity of truncated OSR1 T185E 1-342 that lacks the CCT domain indicating that it also binds the CCT domain of SPAK and OSR1 kinases (**Figure 3.6b**). Furthermore, in the ATP competition assay, Rafoxanide inhibited OSR1 T185E in an ATP-independent manner (**Figure 3.6c and 3.6d**).

Encouraging by the ability of Rafoxanide to inhibit OSR1 T185E *in vitro*, I sought to determine its activity on SPAK T233E in which threonine 233 (Thr233) was mutated into glutamic acid to mimic WNK phosphorylation at this site and produce constitutively active SPAK. To enhance the *in vitro* activity of SPAK T233E, the kinase assay for SPAK T233E was run in presence five molar excess of the scaffolding protein MO25 α which is known to significantly increase the kinase activity of SPAK (Filippi et al., 2011). The results revealed that Rafoxanide was also an inhibitor of SPAK T233E in a low-micromolar concentration range ($IC_{50} = 13.03 \mu M$) (**Figure 3.6e**). Additionally, Rafoxanide inhibited the kinase activity of OSR1 T185E in the presence of MO25 with similar activity ($IC_{50}=13.91 \mu M$) (**Figure 3.6f**).

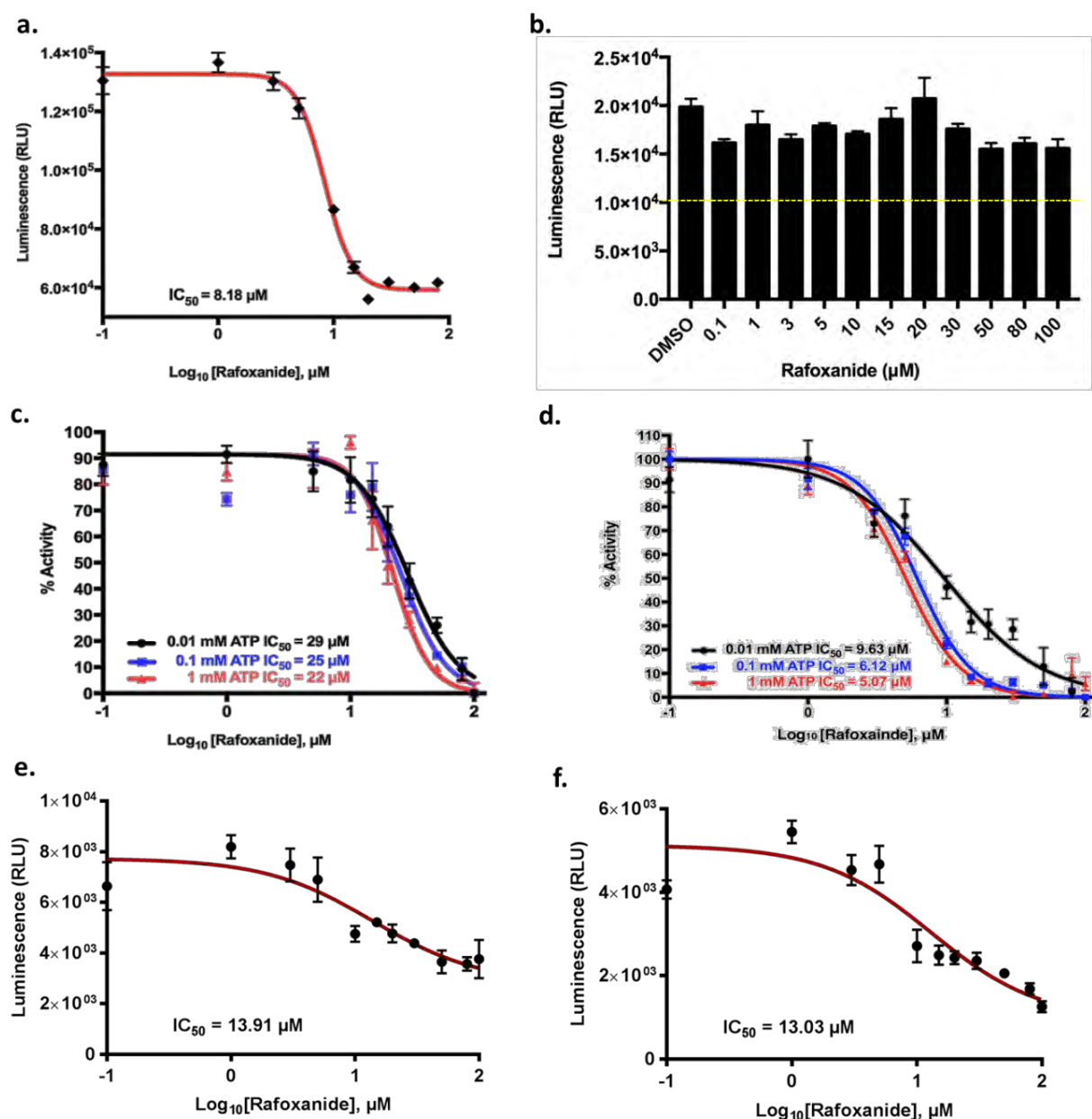


Figure 3.6: Characterisation of the activity of Rafoxanide as a novel SPAK and OSR1 allosteric inhibitor. (a) Rafoxanide inhibits OSR1 T185E FL *in vitro*. The peptide CATCHtide was used as a substrate in the *in vitro* kinase assay. (b) Rafoxanide does not inhibit the active truncated OSR1 T185E 1–342 *in vitro*. Rafoxanide inhibits OSR1 T185E in an ATP-independent manner using (c) NKCC1 (1–174) or (d) CTACHtide as a substrate in the *in vitro* kinase assay. Rafoxanide inhibits both (e) OSR1 T185E and (f) SPAK T233E *in vitro* in the presence of MO25. Data shown are the average signals ($n=3$, \pm SD). The dotted yellow lines in (c) and (d) indicate 50% of the maximum kinase activity. Figures adapted from (AlAmri et al., 2017a).

3.3.8 Effect of Rafoxanide on hypotonicity-induced WNK-SPAK/OSR1-NKCC1 signalling in HEK293 cells

Treatment of HEK293 with low chloride hypotonic buffer led to stimulation of WNK signalling and significant increase in NKCC1 phosphorylation at Thr203, Thr207 and Thr212, which are the phosphorylation sites of SPAK and OSR1 (**Figure 3.7a**). In addition, the increase in phosphorylation of SPAK at Ser373 indicated the stimulation of WNK kinase due to hypotonic buffer treatment. 10 μ M of STOCK1S-50699 was able to inhibit the WNK-SPAK/OSR1-NKCC1 signalling as judged by the absence of SPAK and NKCC1 phosphorylation at these sites in agreement with previous reports (de los Heros et al., 2014). Interestingly, Rafoxanide produced a concentration-dependent inhibition of NKCC1 phosphorylation at Thr203, Thr207 and Thr212 indicating the inhibition of SPAK and OSR1 kinase activity similar to the effect observed with Closantel (**Figure 3.7b**). Complete inhibition of the phosphorylation of these phosphorylation sites was observed at ≥ 20 μ M with both Rafoxanide and Closantel. Notably, unlike STOCK1S-50699, the phosphorylation of SPAK at Ser373 was not inhibited by Rafoxanide and Closantel providing further evidence that Rafoxanide and Closantel act by inhibiting SPAK and OSR1 kinase activity without influencing their ability to interact with upstream WNK which is responsible for phosphorylating SPAK at Ser373 in the *N*-terminal T-loop.

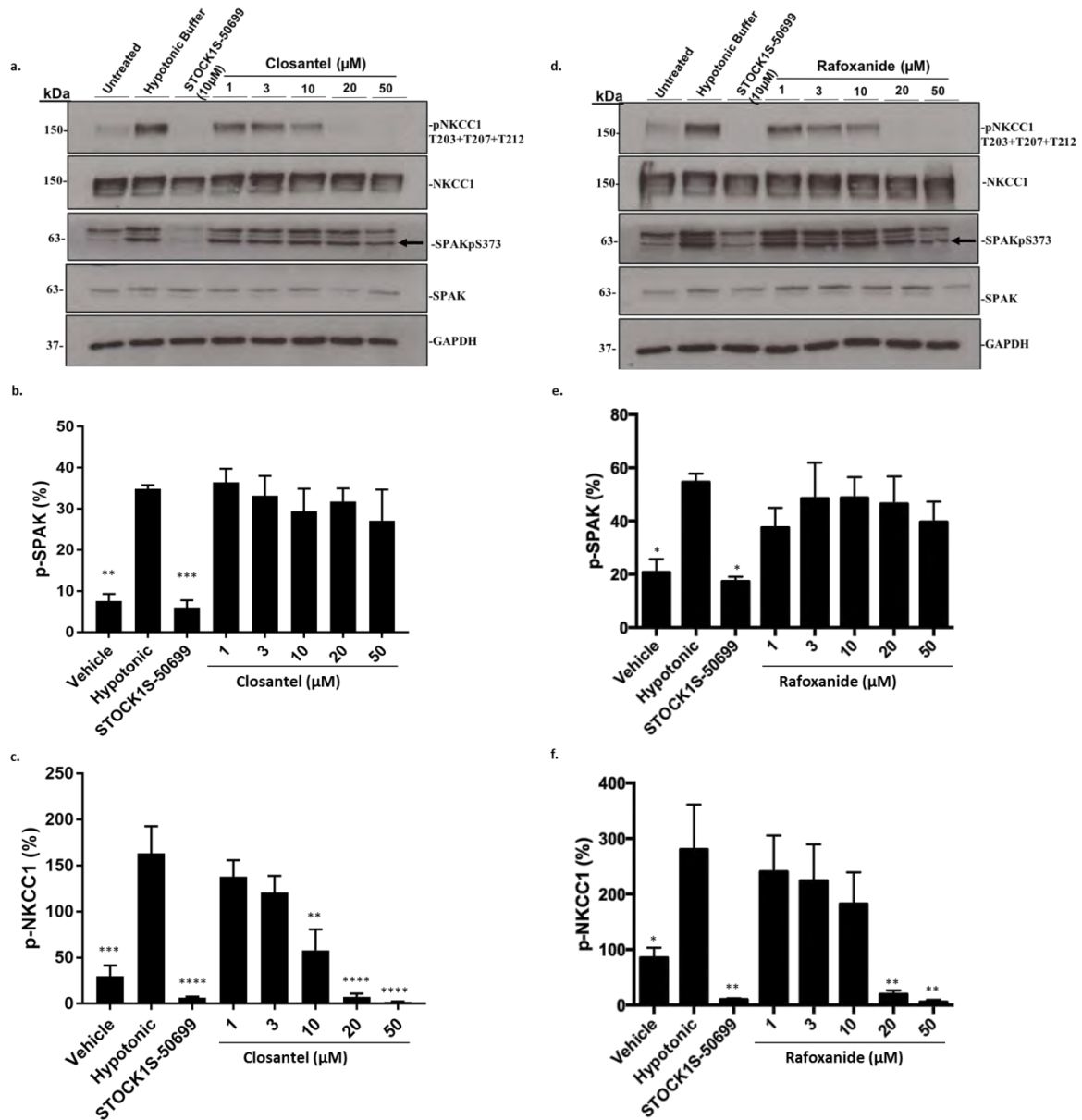


Figure 3.7: Inhibitory effect of Closantel and Rafoxanide on WNK-SPAK/OSR1 signalling in HEK293 cells. (a) Closantel and (d) Rafoxanide inhibit endogenous SPAK and OSR1 kinases in HEK293 cells in concentration dependent manner. HEK293 cells were first treated with compounds at the indicated concentrations or STOCK1S5 0699 (10 μM) for 30 min and then either left untreated or treated with hypotonic buffer for 30 min to activate WNK-SPAK/OSR1 signalling. The cells were then harvested, and the lysates were probed for phospho-NKCC1 T203, T207 and T212, total NKCC1, phospho-SPAKS373, total SPAK and GAPDH as a loading control. Bars represent quantification of blots relative to GAPDH for pSPAK and pNKCC1 for Closantel (b and c) or Rafoxanide (e and f). The data were reported as mean ($n=3$, \pm SEM); **** $p < 0.0001$, *** $p < 0.001$, ** $p < 0.01$, * $p < 0.05$. A one-way ANOVA test followed by Tukey's test were used to compare the results. Final DMSO concentration is 0.1%. Figures adapted from (AlAmri et al., 2017a).

3.3.9 Effect of Rafoxanide on OSR1 CCT domain ability to bind to WNK kinase

To further investigate that the binding of Rafoxanide to the CCT domain of SPAK and OSR1 was not through the primary pocket, a biotin-streptavidin pull down assay was performed. In this assay, a biotinylated 18-mer RFQV-peptide derived from human WNK4 was used to pull down endogenous SPAK from a HEK293 cell lysate (Villa et al., 2007). As a reference, an 18-mer AFQV-peptide was employed as a negative control as it has been shown not to bind endogenous SPAK and OSR1 (Villa et al., 2007). Prior performing the pull down, the cell lysates were incubated with either DMSO as a vehicle control or with SPAK and OSR1 inhibitors including STOCK1S-50699, Closantel, and Rafoxanide at the indicated concentrations (**Figure 3.8a**). As expected, the results illustrated that the 18-mer RFQV-peptide was efficiently able to pull down the endogenous SPAK while the 18-mer AFQV-peptide did not (Villa et al., 2007). Unlike STOCK1S-50699, Closantel, and Rafoxanide were not able to compete with 18-mer RFQV-peptide on the primary pocket even at high concentrations (up to 300 μ M) (**Figure 3.8a**). This indicated that Closantel and Rafoxanide do not compete with the RFQV for binding to the primary pocket, but instead bind the secondary pocket as observed in the experiments described above. Furthermore, an FP assay was conducted to measure the binding affinity of the 18-mer RFQV-peptide to OSR1 CCT WT in presence of Rafoxanide at three different concentrations (1, 10, and 100 μ M). Consistent with pull down assay results, Rafoxanide was unable to compete with RFQV-peptide for the binding to OSR1 CCT even at the high concentration of 100 μ M (**Figure 3.8b**). Collectively, these results suggested that Rafoxanide and Closantel have not effect on the binding of 18-mer RFQV-peptide to the primary pocket of OSR1 CCT.

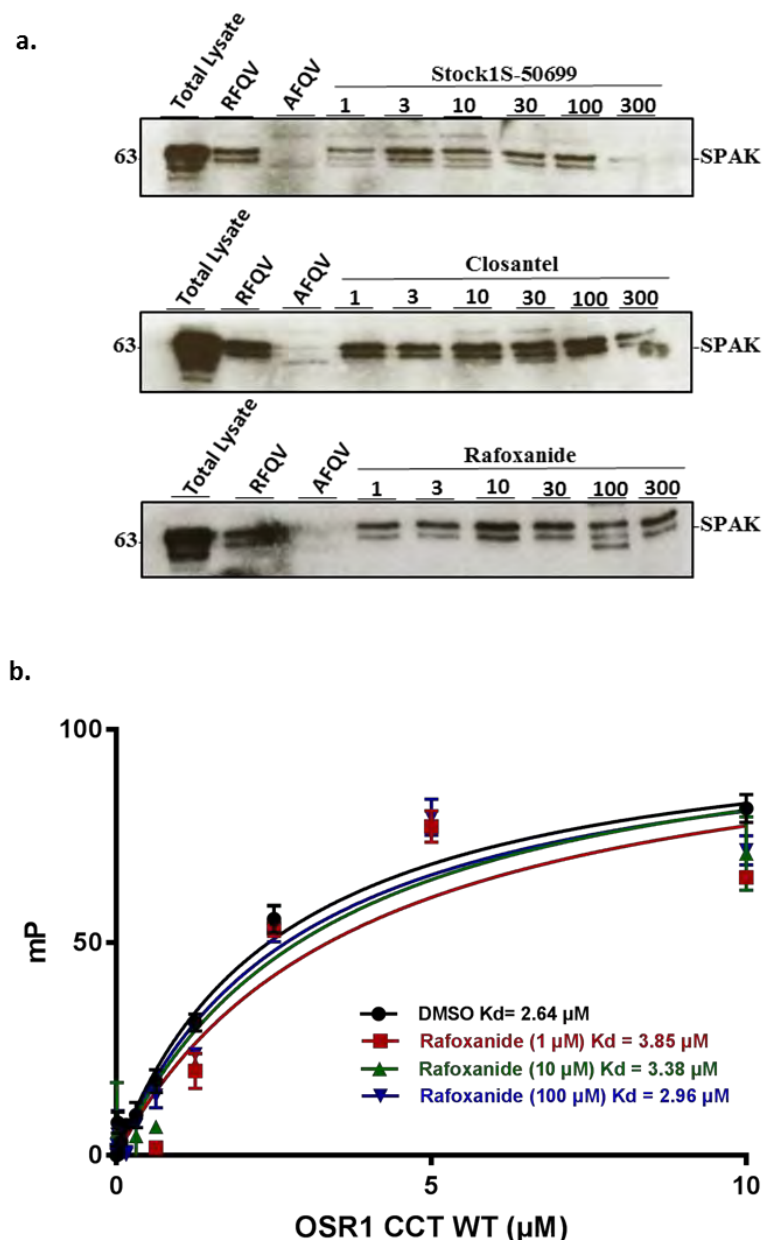


Figure 3.8: Rafoxanide and Closantel do not compete with the 18-mer RFQV peptide for binding to the primary pocket. (a) Biotinylated 18-mer RFQV peptide was used to pull down endogenous SPAK from HEK293 cells in the absence or presence of the inhibitors at the indicated concentrations. The biotinylated 18-mer AFQV peptide was used as a negative control. Data shown are representative of three independent repeats. (b) Fluorescence polarisation analysis of the binding of OSR1 CCT WT to the 18-mer RFQV peptide derived from WNK4 in the absence (DMSO) or presence of Rafoxanide at the indicated concentrations. Data shown are the average signals ($n=3$, \pm SD). **mP**: millipolarisation units. Figure adapted from (AlAmri et al., 2017a).

3.3.10 Discussion

The highly conserved CCT domain of SPAK and OSR1 plays critical roles in WNK signalling and the regulation of blood pressure *in vivo* (Zhang et al., 2015). The X-ray structure of OSR1 CCT revealed that it possesses two adjacent highly conserved pockets namely, the primary and the secondary pockets (Villa et al., 2007). The role of the primary pocket has been established as a docking site that accommodates the RFXV motif of upstream WNK kinases and downstream ion-cotransporters (Zhang et al., 2015). On the other hand, the function of the secondary pocket, which is relatively deeper and smaller than the primary pocket, remained unknown. Initial thoughts were that it binds residues beyond the RFXV motif in WNK kinases and/or ion cotransporters (Villa et al., 2007). Despite its close proximity to the primary pocket, the secondary pocket has no direct or allosteric effects on the conformation of the primary pocket and thus no effect on the binding of the RFQV motif to the CCT of SPAK and OSR1 (Villa et al., 2007, Vitari et al., 2006). However, the impact of this pocket on the basal kinase activity of SPAK and OSR1 as well as amenability to targeting by small molecules was never explored prior to the work presented in this thesis.

A series of robust *in vitro* cell-free and cell-based assays, biochemical binding and functional assays as well as molecular docking were developed and optimised to investigate the function of the highly conserved CCT secondary pocket of SPAK and OSR1 kinases

Intriguingly, a focused mutagenesis study on specific residues that line the secondary pocket revealed that a single point mutation of L440 or V507 hydrophobic residues into alanine reduced significantly the *in vitro* kinase activity of constitutively active OSR1 T185E FL (residues 1–527) (**Figure 3.2a**). Although, the alteration of a

protein by a site-specific mutagenesis could change the protein structure leading to false observations (Coleman et al., 1993), the results from subsequent biotin–streptavidin pulldown assay as well as the fluorescence polarisation assay indicated that these mutations are stable and did not alter the protein folding as the RFQV-binding groove retains function (**Figure 3.2b and d**). Consistent with previous reports, I also show that these mutations have no effect on the ability of 18-mer RFQV-peptide, derived from human WNK4, to bind to endogenously expressed OSR1 FL and bacterially expressed OSR1 CCT (**Figure 3.2b and d**) (Villa et al., 2007, Vitari et al., 2006). The obtained results suggested that the observed reduction in the kinase activity of OSR1 may result from inducing a structural conformational change, which attenuates OSR1 kinase activity through an allosteric mechanism. However, further robust site-specific mutagenesis might be beneficial for determining the effect of other residues involved in forming this pocket on the catalytic activity of SPAK and OSR1.

Using molecular docking, I showed that known WNK signalling inhibitors, namely STOCK1S-50699, STOCK2S-26016, STOCK1S-14279 and Closantel, bind to the secondary pocket of OSR1 CCT (**Figure 3.3**). These compounds have been reported to bind to either SPAK FL such as STOCK1S-14279 and Closantel or to SPAK CCT such as STOCK1S-50699, STOCK2S-26016 (Kikuchi et al., 2014, Mori et al., 2013). Since their binding site is still unknown, the obtained results provided a computational insight into the binding sites of these compounds. Additionally, these finding indicated that this pocket is amenable to being targeted by small molecules. Consistent with this, *in vitro* characterisation of the inhibitory effect of Closantel and STOCK1S-50699 suggested that they both inhibit OSR1 FL in non-ATP competitive mechanism. However, such effect was not observed when the truncated OSR1 1-342, which lacks the CCT domain,

confirming that these compounds do not bind to the OSR1 catalytic domain (**Figure 3.4**). Previous selectivity studies of Closantel and STOCK1S-50699 on a panel of kinases provided strong evidence that they are not promiscuous inhibitors (Kikuchi et al., 2014, de los Heros et al., 2014). Therefore, based on the obtained results they may both exert their inhibitory effects by binding to an allosteric site on the CCT domain of SPAK and OSR1. Intriguingly, we showed that STOCK1S-50699 may have a dual mechanism of actions in inhibiting SPAK and OSR1 kinases. The latter may explain the observations that STOCK1S-50699 was more active as WNK signalling inhibitor in cell than in cell-free based assay (**Figure 3.1 and 3.4**).

The structural-based virtual screening resulted in the identification of Rafoxanide as a novel SPAK and OSR1 kinase inhibitor (**Figure 3.5**). Rafoxanide belongs to the same chemical and therapeutic classes as Closantel (Swan, 1999). Both compounds are halogenated salicylanilide drugs and share 2-hydroxy-N-phenylbenzamide core. Notably, another derivative of this group, oxyclozanide, was inactive when tested against SPAK (Kikuchi et al., 2014). Like Closantel, the docking studies revealed that Rafoxanide binds to the secondary pocket of OSR1 (**Figure 3.5c and d**). Interestingly, the inhibitory effect of Rafoxanide on OSR1 kinase was similar to that observed with Closantel and STOCK1S-50699. In addition, Rafoxanide inhibited SPAK T233E kinase activity to the same extent of OSR1 T185E ($IC_{50} = 13.03$ and 13.91 against human SPAK T233E and OSR1 T185E FL, respectively) (**Figure 3.6f and e**).

Unlike STOCK1S-50699, which was able to inhibit the phosphorylation of SPAK at Ser373 that is specifically phosphorylated by WNK kinases, Closantel and Rafoxanide inhibited the phosphorylation of NKCC1 in HEK293 cells without affecting SPAK Ser373 phosphorylation. This indicated that Closantel and Rafoxanide are targeting SPAK

kinase directly without affecting its binding to WNK kinases, which is mediated by the CCT domain (**Figure 3.7**). Consistent with this, the results from the pull down and fluorescence polarisation analyses provided more clear evidence that Closantel and Rafoxanide have no influence on the ability of SPAK and OSR1 to bind to WNK kinases (**Figure 3.8**). It must be noted that we attempted using surface plasmon resonance (SPR) to obtain a measure of Closantel and Rafoxanide binding affinity to OSR1 CCT, but these were not successful. This was due to the highly hydrophobic nature of these compounds, $\text{clogP} = 7.63$ and 8.88 , respectively, which limited their solubility in the assay buffer.

In conclusion, the critical role of the highly conserved secondary pocket of SPAK and OSR1 in the regulation of their kinase activity was determined. The secondary pocket was validated as a possible target for the design of SPAK and OSR1 kinases inhibitors. The antiparasitic agent, Rafoxanide, was identified as a new allosteric inhibitor of SPAK and OSR1 kinases, which binds their secondary pockets. These findings will facilitate the rational design of allosteric SPAK and OSR1 kinase inhibitors that could serve as powerful tools in decoding the allosteric mechanism of WNK-SPAK/OSR1 signalling. Critically, allosteric inhibitors of SPAK and OSR1 may eventually be developed into useful agents for treating hypertension.

Rafoxanide

inhibitor of SPAK/OSR1 kinase
activity in vitro and in cells

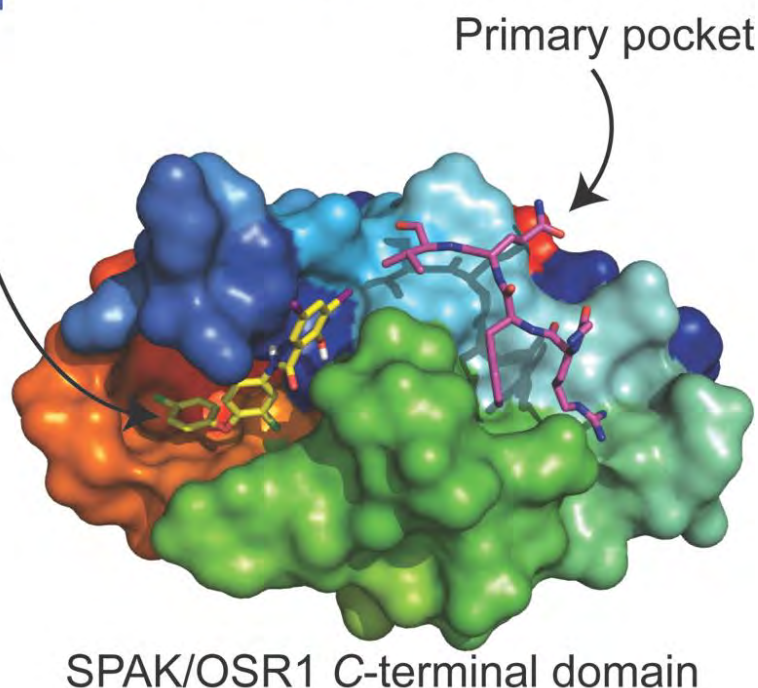
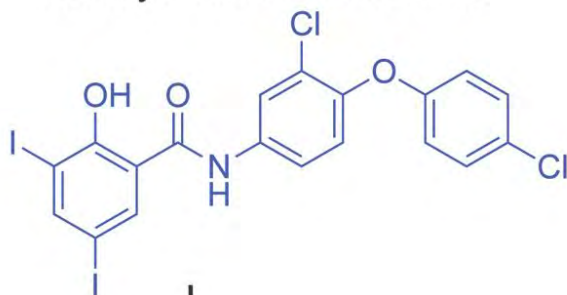


Figure 3.9: Graphical conclusion. SPAK and OSR1 kinases regulate hemostasis and electrolyte balance *in vivo*. In the present study, a small pocket on the CCT domain of SPAK and OSR1 which plays an essential role in regulating their kinase activity was identified. Using *in silico* structure-based virtual screening, Rafoxanide was discovered as a novel allosteric inhibitor of these two protein kinases. Together, these findings will facilitate the discovery of allosteric SPAK and OSR1 inhibitors with potential antihypertensive effects. Figure adapted from (AlAmri et al., 2017a).

**CHAPTER IV: IDENTIFY NEW SPAK AND
OSR1 KINASE INHIBITORS USING HIGH-
THROUGHPUT SCREENING**

4.1 Introduction

High throughput screening (HTS) is a widely used drug discovery approach in which a large library of compounds is screened against a biological target under the same condition in an automated manner (Broach and Thorner, 1996). It involves several steps such as compounds management, assay development and optimisation and library screening (Szymański et al., 2011). The degree of success in HTS outcomes depends on the quality of the assay and chemical library (Roy et al., 2010). In HTS, the library of small molecules used could be of already approved FDA-approved drug molecules or known compounds with established pharmacological activity. The purpose of using these libraries is often to repurpose a drug molecule or a clinical candidate for the possible use to treat a disease different from what it was initially discovered for. This approach has become of a great interest in both industry and academia as it significantly reduces the time and cost of the drug discovery process as the existing drugs have already undergone some clinical trials or late pre-clinical drug development (Ashburn and Thor, 2004).

4.2 Aim

The aim of this Chapter is to use HTS approach to screen an in-house library of small molecules, which consists of FDA-approved drugs and a diverse set of small-molecules, to identify potential SPAK and OSR1 kinase inhibitors.

4.3 Results

4.3.1 Optimisation of OSR1 high-throughput screening (HTS) assay

Most of the current *in vitro* kinase assays used for studying the activity of SPAK and OSR1 employ radioactive ATP (de los Heros et al., 2014, Filippi et al., 2011, Vitari et al., 2006). Therefore, we sought to develop and optimise a non-radioactive *in vitro* kinase assay compatible with HTS technologies. Accordingly, we used the Promega's ADP-Glo™ kinase assay, which is based on a luminescent ADP detection system (Zegzouti et al., 2009). For this assay, a mutant OSR1 T185E FL (1-527) was expressed and purified from *E.coli* (**Appendix 4.1a**). The mutation of threonine 185 into glutamic acid makes OSR1 constitutively active *in vitro* as it mimics WNK phosphorylation at this site (Vitari et al., 2005). In addition, a fragment of the human NKCC2 (1–174) encompassing the *N*-terminal cytoplasmic domain, which is known to be phosphorylated by SPAK and OSR1 at Thr95, Thr100, Thr105, Ser91 and Ser130, was also expressed and purified from *E.coli* and employed as a substrate (**Appendix 4.1b**) (Vitari et al., 2005). This assay was developed and used in (Chapter III) for determining the activity of SPAK and OSR1 *in vitro*. However, the assay quality and suitability for HTS has not been determined. The optimal conditions for the 384-well plate HTS-compatible *in vitro* kinase assay were found to be 0.2 μ M OSR1 T185E, 5 μ M NKCC2 (1–174) as a substrate, 0.1 mM ATP and 10 mM MgCl₂ (**Appendix 4.2a**). To evaluate the suitability of this assay for HTS, the *z'* factor was calculated and it was 0.78 (minimum ≥ 0.5) (see Material and Method section 2.4.2.3). Moreover, signal-to-noise ratio (S/N) and signal-to-background ratio (S/B), which are widely used as indicators for the quality of an assay, were determined and found to be 94.6 (minimum > 10) and 16.9 (minimum > 3), respectively, indicating the robustness of this assay. These are in line with the minimum requirements

needed for robust HTS assays (Zhang et al., 1999). Post-screening, the z' factor, signal window (SW), and coefficient of variation (CV) of each plate were calculated and compared with the minimum pass criteria to evaluate the quality of screening data. All parameters exceeded the minimum pass limits as shown in (**Appendix 4.3**) (Iversen et al., 2006, Zhang et al., 1999).

4.3.2 Screening of in-house chemical library

Initially, the assay was utilised to screen an in-house chemical library that composed of ~1,200 FDA-approved drugs and 144 diverse set of small-molecules (see **Appendix 4.4** for library composition). The screening was carried out at a single concentration of 20 μM (see Material and Method section 2.4.2.2). Considering the IC_{50} values of positive controls (Closantel= 8.65 μM and rafoxanide= 8.18 μM) which were tested by the same screening assay, (see Chapter III), the activity cut-off for hit molecule was defined as $\geq 40\%$ inhibition at 20 μM (Keserü and Makara, 2006). The primary screen led to the identification of 18 hits that inhibited OSR1 T185E kinase activity by more than 40% (**Figure 4.1**). To verify these primary hits, they were subsequently screened at two different concentrations of 10 and 50 μM using different batches of the hit compounds (**Figure 4.2**) (Keserü and Makara, 2006). Only seven compounds, Verteporfin, Toremifene, Alexidine Dihydrochloride, β -Escin, Chicago Sky Blue 6B, Chlorhexidine Dihydrochloride and Methyl Benzethonium Chloride, were found to inhibit OSR1 T185E *in vitro* in a concentration-dependent manner giving an overall hit-rate from this HTS exercise of ~0.52%.

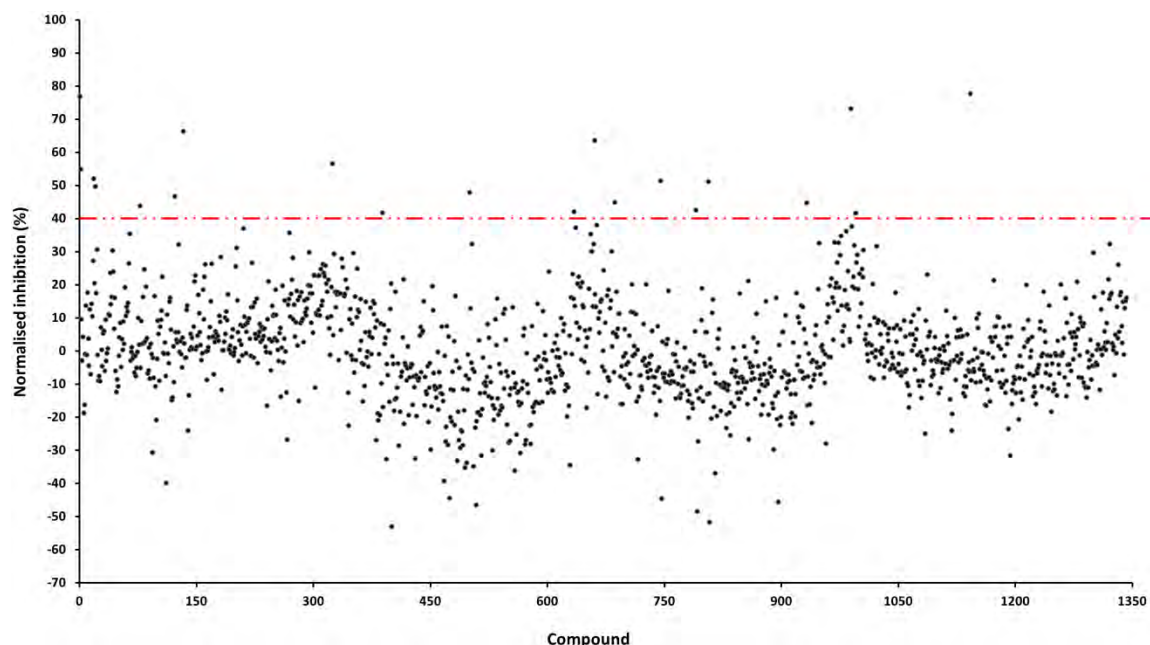


Figure 4.1: Scatterplots of the primary screening using the developed assay. The red dashed line illustrates the ‘hit’ selection criteria (> 40% Inhibition of OSR1 T185E kinase activity). The first two dots in the Y-axis are for the two positive controls, Closantel (~78%) and Rafoxanide (~55%). Each compound was screening in duplicate in two separated plate.

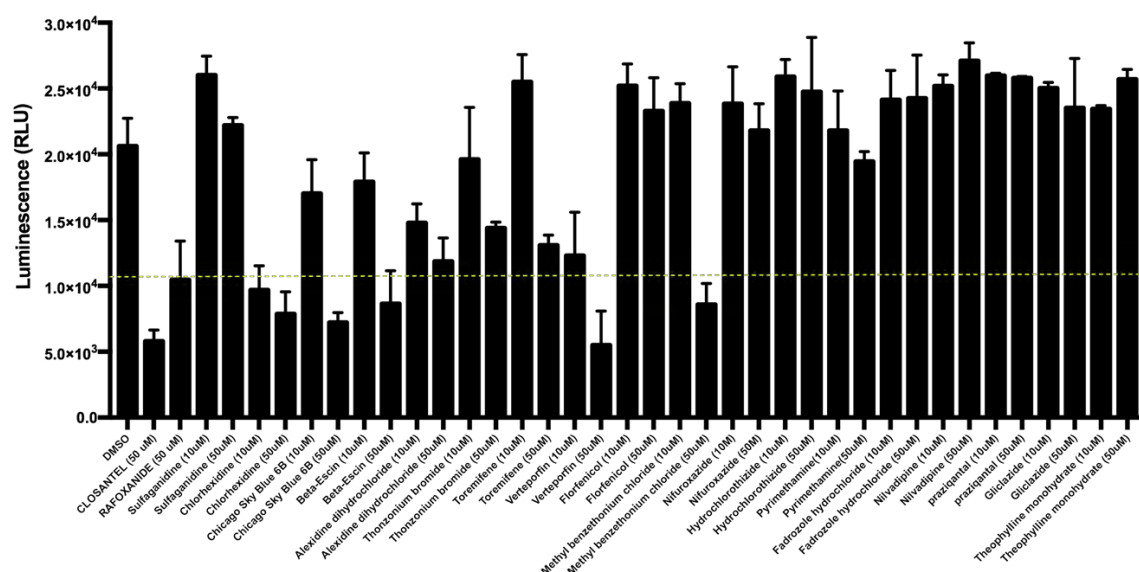


Figure 4.2: The secondary screening using the developed assay. Compounds were screened at two concentrations 10- and 50 μM in triplicate. Data presented as a mean ± SD.

4.3.3 Identification of Verteporfin (Visudyne®) as a novel and potent inhibitor of SPAK/OSR1 kinases

Subsequently, the IC_{50} values of the seven confirmed hit compounds were determined using two different OSR1 T185E substrates, the bacterially expressed human-NKCC2 (1-174) and CATCHtide peptide, a well-established SPAK/OSR1 *in vitro* substrate (Vitari et al., 2006). In addition, the effect of these compounds on the activity of truncated OSR1 T185E 1-342 that lacks the CCT domain was evaluated (see **Appendix 4.2b** for assay development using truncated OSR1 T185E 1-34 kinase). As shown in **Figures 4.3-4.9**, all of the compounds inhibited both forms of OSR1 T185E at the low micromolar concentration range. Remarkably, Verteporfin, FDA approved drug for photodynamic therapy as a photosensitizer (Fenton and Perry, 2006, Awan and Tarin, 2006), emerged as the most active inhibitor of OSR1 T185E *in vitro*, $IC_{50} = 0.207 \mu M$ (**Figure 4.3**). Chemically, Verteporfin is a benzoporphyrin derivative monoacid ring A (BPD-MA). It consists of an equimolar mixture (1:1) of the regioisomers that are distinguished by the location of the monoacid at either position 3 on ring C (BPD-MA_C) or 4 on ring D (BPD-MA_D) of the porphyrin ring (**Figure 4.3a**) (Levy, 1995). Next, the effect of Verteporfin on the activity of constitutively active SPAK T233E was tested using the same *in vitro* kinase assay (see **Appendix 4.1d** for SPAK T233E purification). The data shows that Verteporfin exhibited a similar inhibitory effect when tested against the bacterially expressed human FL SPAK T233E (1-547), $IC_{50} = 0.330 \mu M$ (**Figure 4.10a**). Such activity warranted further characterization of Verteporfin as a novel inhibitor of OSR1 and SPAK kinases.

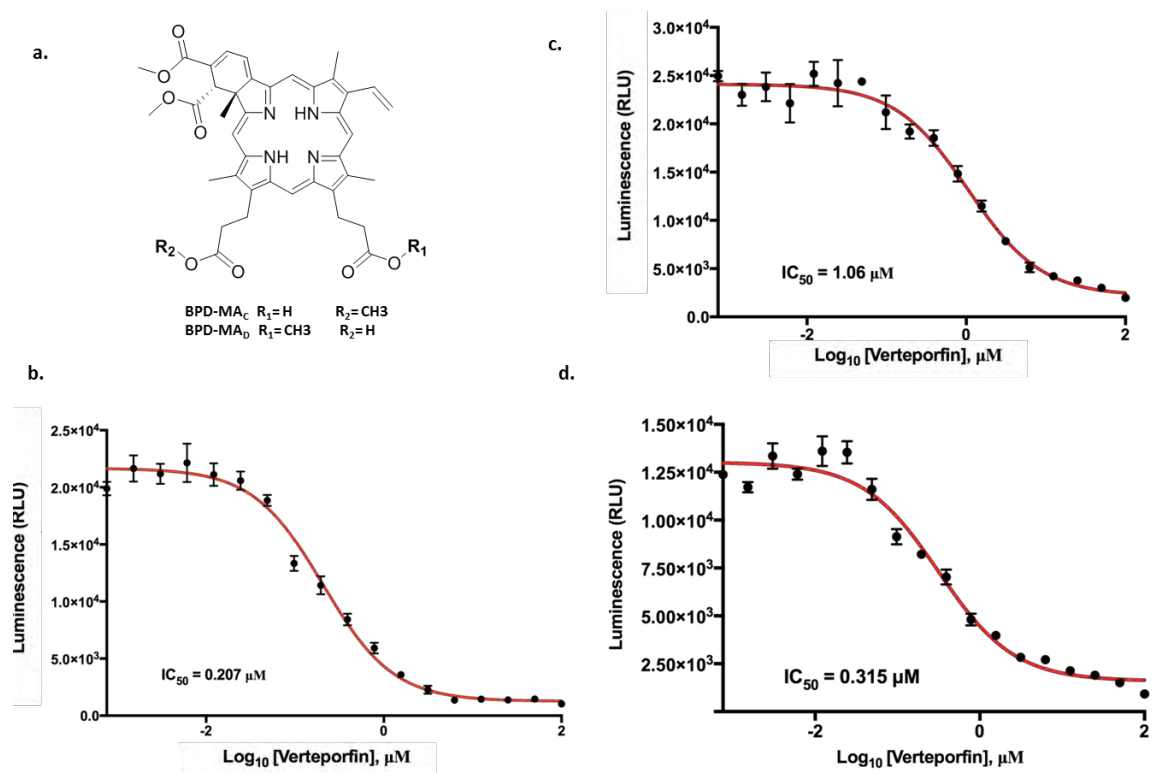


Figure 4.3: Determination of the IC₅₀ of Verteporfin. (a) The chemical structure of Verteporfin, photosensitizer drug. The kinase assay was performed using (b) CATCHtide or (c) NKCC21-174 as a substrate. (d) Effect of Verteporfin on the OSR1 T185E 1-342 using CATCHtide as a kinase substrate. Data presented as average signal ($n=4$, \pm SEM).

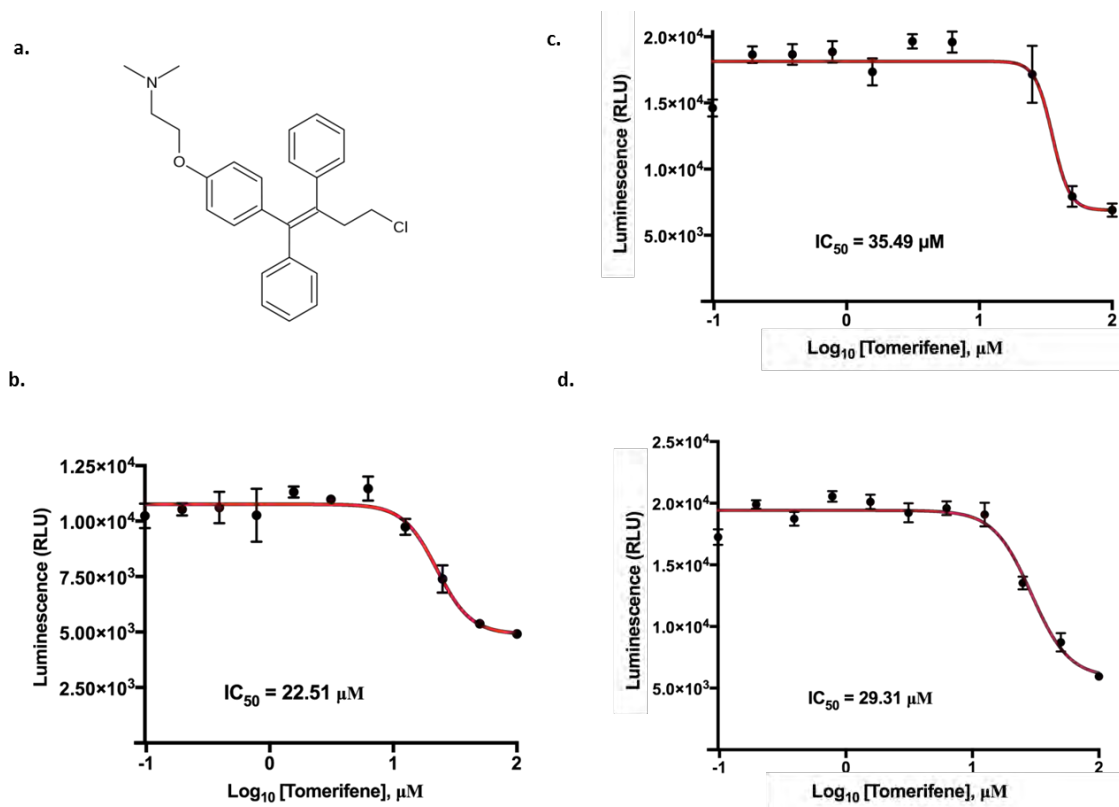


Figure 4.4: Determination of the IC_{50} of Toremifene. (a) The chemical structure of Toremifene, anticancer drug. The kinase assay was performed using (b) CATCHtide or (c) NKCC21-174 as a substrate. (d) Effect of Toremifene on the OSR1 T185E 1-342 using CATCHtide as a kinase substrate. Data presented as average signal ($n=4$, \pm SEM).

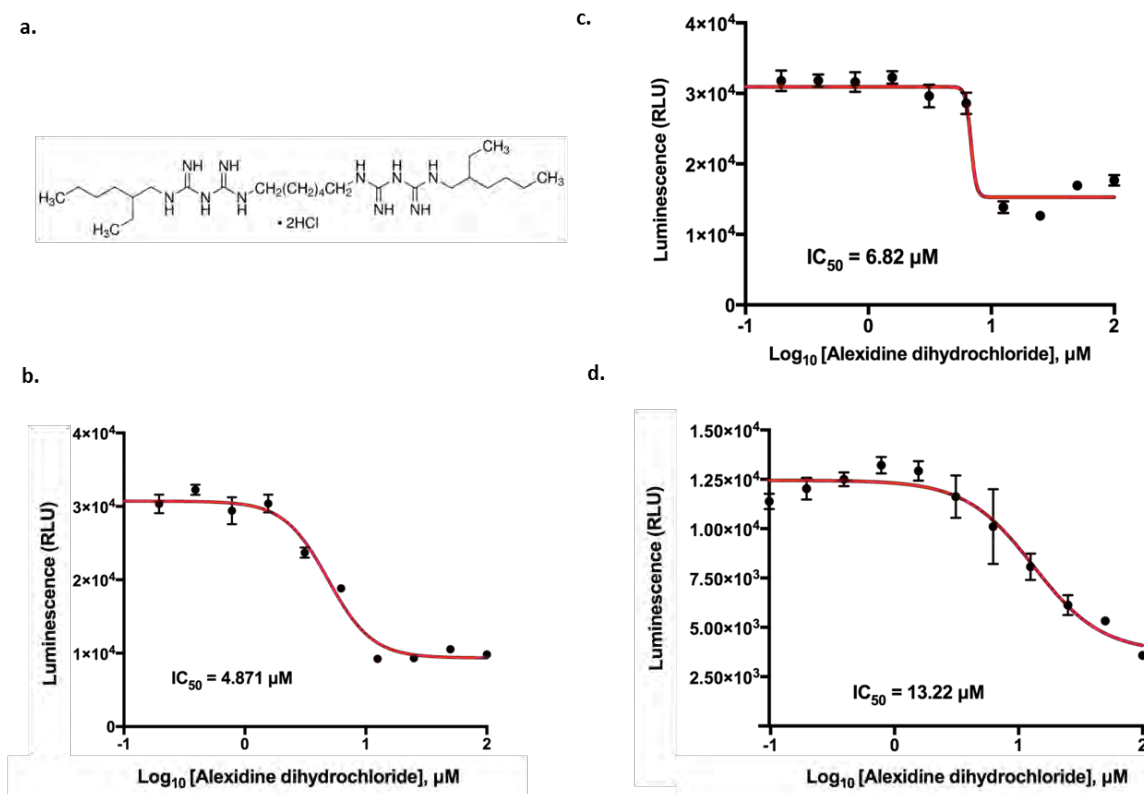


Figure 4.5: Determination of the IC_{50} of Alexidine Dihydrochloride. (a) The chemical structure of Alexidine Dihydrochloride, antibacterial agent. The kinase assay was performed using (b) CATCHtide or (c) NKCC21-174 as a substrate. (d) Effect of Alexidine Dihydrochloride on the OSR1 T185E 1-342 using CATCHtide as a kinase substrate. Data presented as average signal ($n=4$, \pm SEM).

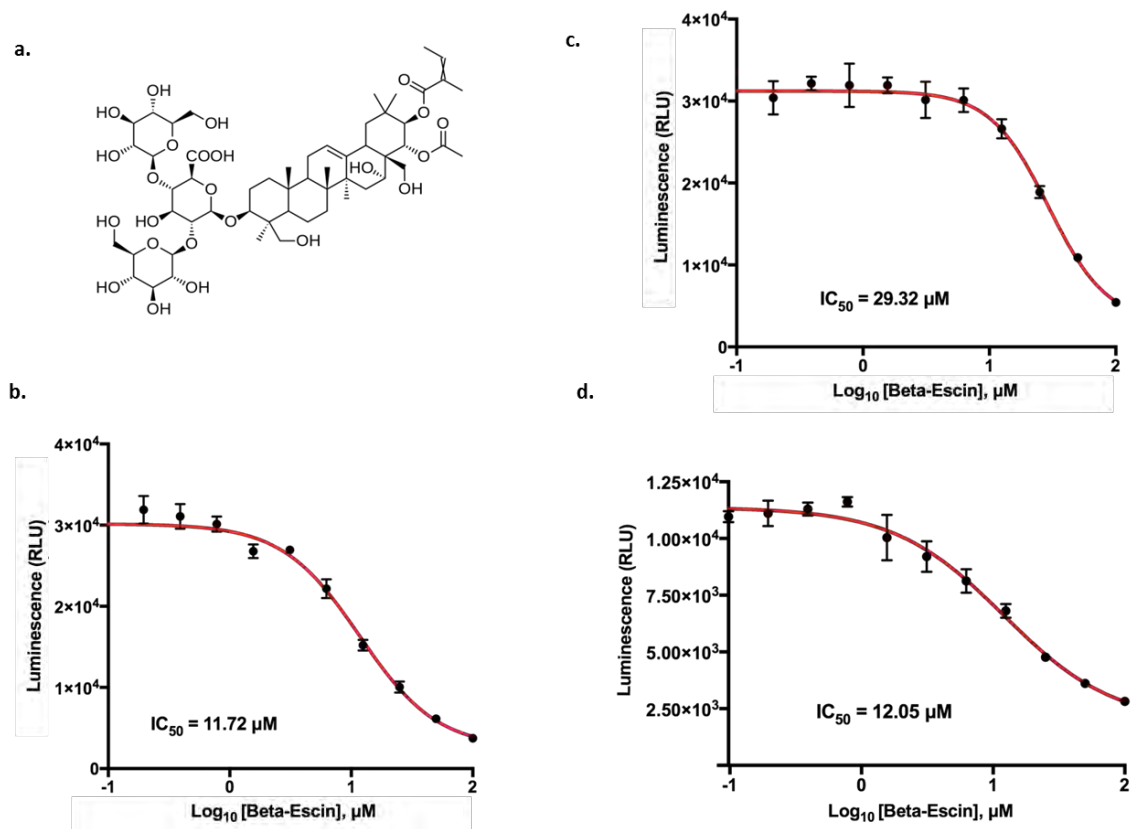


Figure 4.6: Determination of the IC_{50} of β -Escin. (a) The chemical structure of β -Escin, vasoprotective, anti-inflammatory, anti-edematous and anti-nociceptive agent. The kinase assay was performed using (b) CATCHtide or (c) NKCC21-174 as a substrate. (d) Effect of β -Escin on the OSR1 T185E 1-342 using CATCHtide as a kinase substrate. Data presented as average signal ($n=4$, \pm SEM).

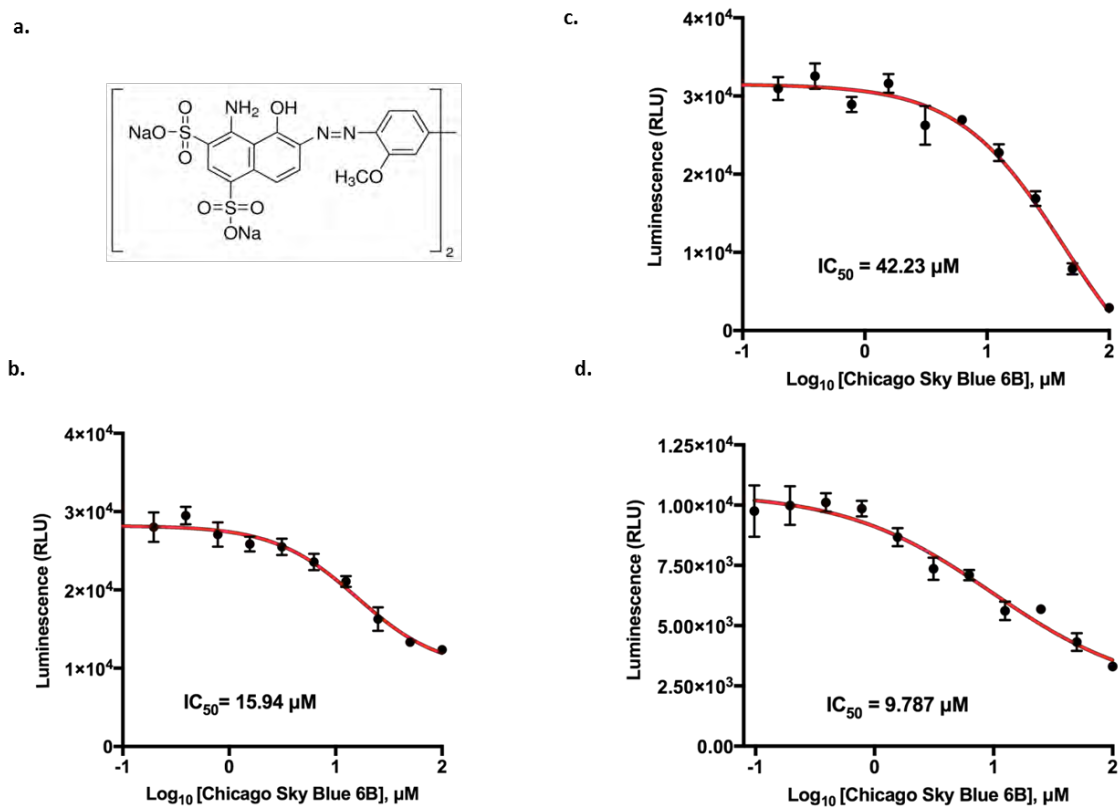


Figure 4.7: Determination of the IC_{50} of Chicago Sky Blue 6B. (a) The chemical structure of Chicago Sky Blue 6B, allosteric MIF inhibitor and VGLUT inhibitor. The kinase assay was performed using (b) CATCHtide or (c) NKCC21-174 as a substrate. (d) Effect of Chicago Sky Blue 6B on the OSR1 T185E 1-342 using CATCHtide as a kinase substrate. Data presented as average signal ($n=4$, \pm SEM).

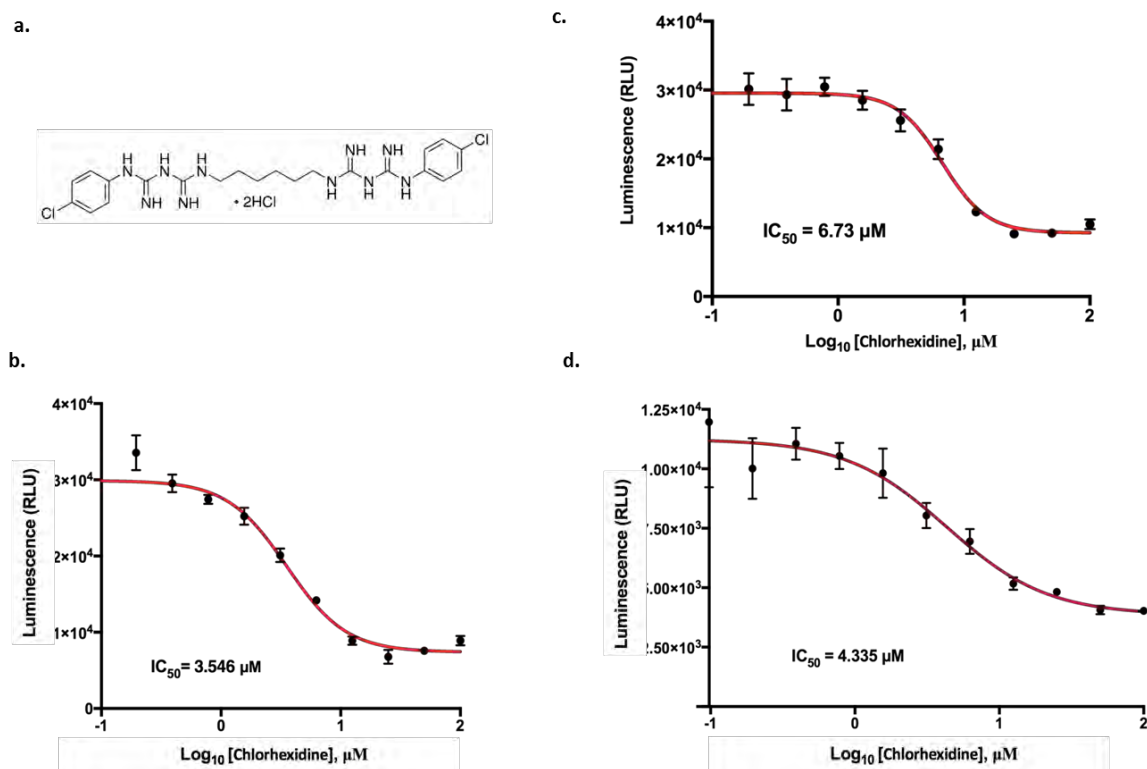


Figure 4.8: Determination of the IC_{50} of Chlorhexidine Dihydrochloride. (a) The chemical structure of Chlorhexidine Dihydrochloride, anti-microbial agent. The kinase assay was performed using (b) CATCHtide or (c) NKCC21-174 as a substrate. (d) Effect of Chlorhexidine Dihydrochloride on the OSR1 T185E 1-342 using CATCHtide as a kinase substrate. Data presented as average signal ($n=4$, \pm SEM).

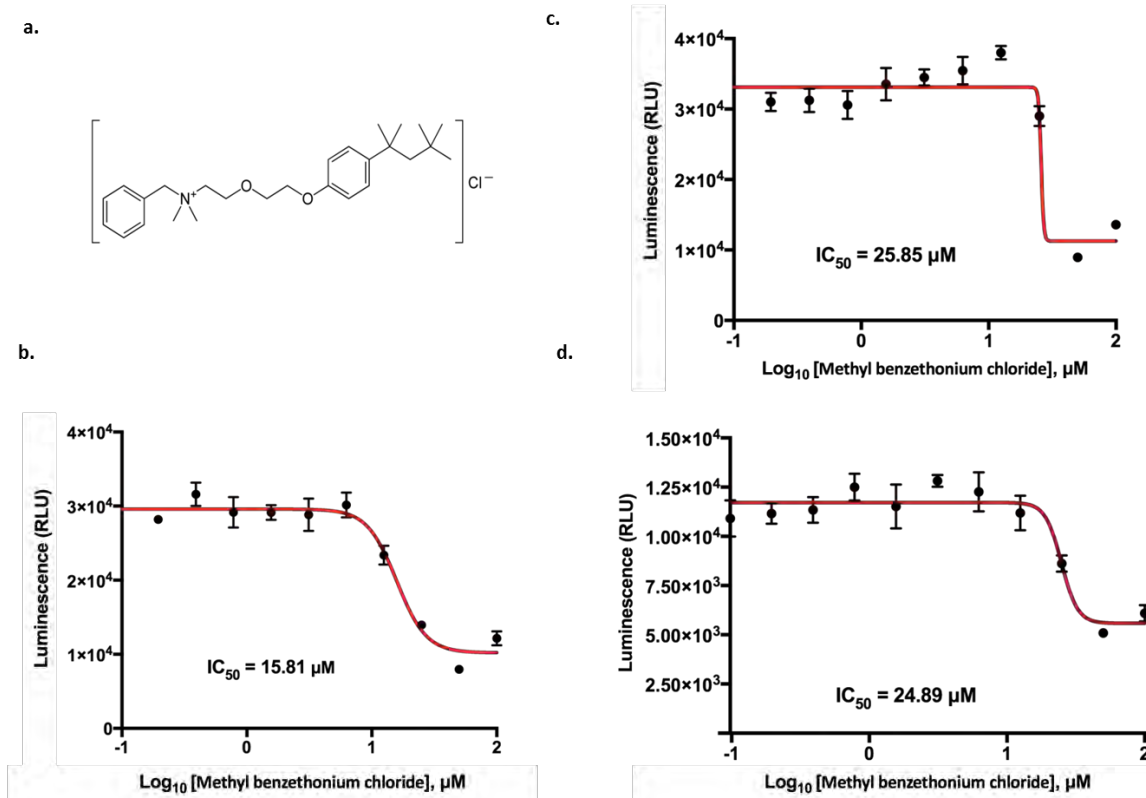


Figure 4.9: Determination of the IC_{50} of Methyl Benzethonium Chloride. (a) The chemical structure of Methyl Benzethonium Chloride, antibacterial agent. The kinase assay was performed using (b) CATCHtide or (c) NKCC21-174 as a substrate. (d) Effect of Methyl Benzethonium Chloride on the OSR1 T185E 1-342 using CATCHtide as a kinase substrate. Data presented as average signal ($n=4$, \pm SEM).

4.3.4 Characterisation of the inhibitory effect of Verteporfin on SPAK and OSR1 kinases *in vitro*

To understand the mechanism by which Verteporfin inhibits SPAK and OSR1 kinases, the *in vitro* kinase assay was conducted at three different concentrations of ATP (0.01 mM, 0.1 mM and 1 mM). The results showed that there was no significant shift in the IC₅₀ values (1.23, 1.14, and 1.72 μ M) at 0.01, 0.1 and 1mM ATP concentrations, respectively. Thus, Verteporfin was suggested to act as a non-ATP competitive inhibitor of OSR1 T185E (**Figure 4.10b**). Furthermore, to evaluate the effect of Verteporfin on the MO25-dependent activation of OSR1 T185E *in vitro*, the kinase assay was performed in presence of five molar excess of bacterially expressed human FL MO25 (**Appendix 4.1b** for MO25 purification) (Filippi et al., 2011). The results indicated that Verteporfin did not have an effect on the ability of MO25 to activate OSR1 185TE kinase *in vitro* (**Figure 4.10c**).

Notably, the presence of Mg⁺² is essential for protein kinase catalysis (Hallenbeck and Walsh, 1983) and ADP-GLO™ kinase assay performance (Zegzouti et al., 2009). Since the Verteporfin is a macrocyclic ligand with a benzoporphyrin core that has four central nitrogen atoms, it may act as a Mg⁺² chelating agent. To investigate this, the inhibitory effect of Verteporfin was evaluated at two different concentrations of MgCl₂; 1 and 50 mM. The results indicated that there was not significant shift in the IC₅₀ value at 50 mM (IC₅₀ = 1.9 μ M) compared to the IC₅₀ value at 1mM (IC₅₀ = 0.73 μ M) suggesting that Verteporfin was not a chelating agent in the kinase assay (**Figure 4.10d**). For further evidence on this, the effect of Verteporfin on the mammalian sterile 20 like kinase 3 (MST3) kinase, a protein kinase that belongs to the same family (STE-20) of protein kinases as SPAK and OSR1, was determined (Pearce et al., 2010). No inhibitory effect was observed up to 100 μ M, supporting pervious findings that Verteporfin was not a Mg⁺²

ion chelating agent (**Figure 4.10e**). Finally, to ensure that Verteporfin was not acting as a protein aggregator, the IC_{50} value of Verteporfin was determined in the presence and absence of the detergent 0.05% Tween 20. As shown in (**Figure 4.10f**), there was no dramatic shift in the IC_{50} values in presence ($IC_{50} = 1.1 \mu M$) or in absence ($IC_{50} = 3.4 \mu M$) of Tween 20 indicating that the observed inhibitory effect was not due to the induction of protein aggregation by Verteporfin.

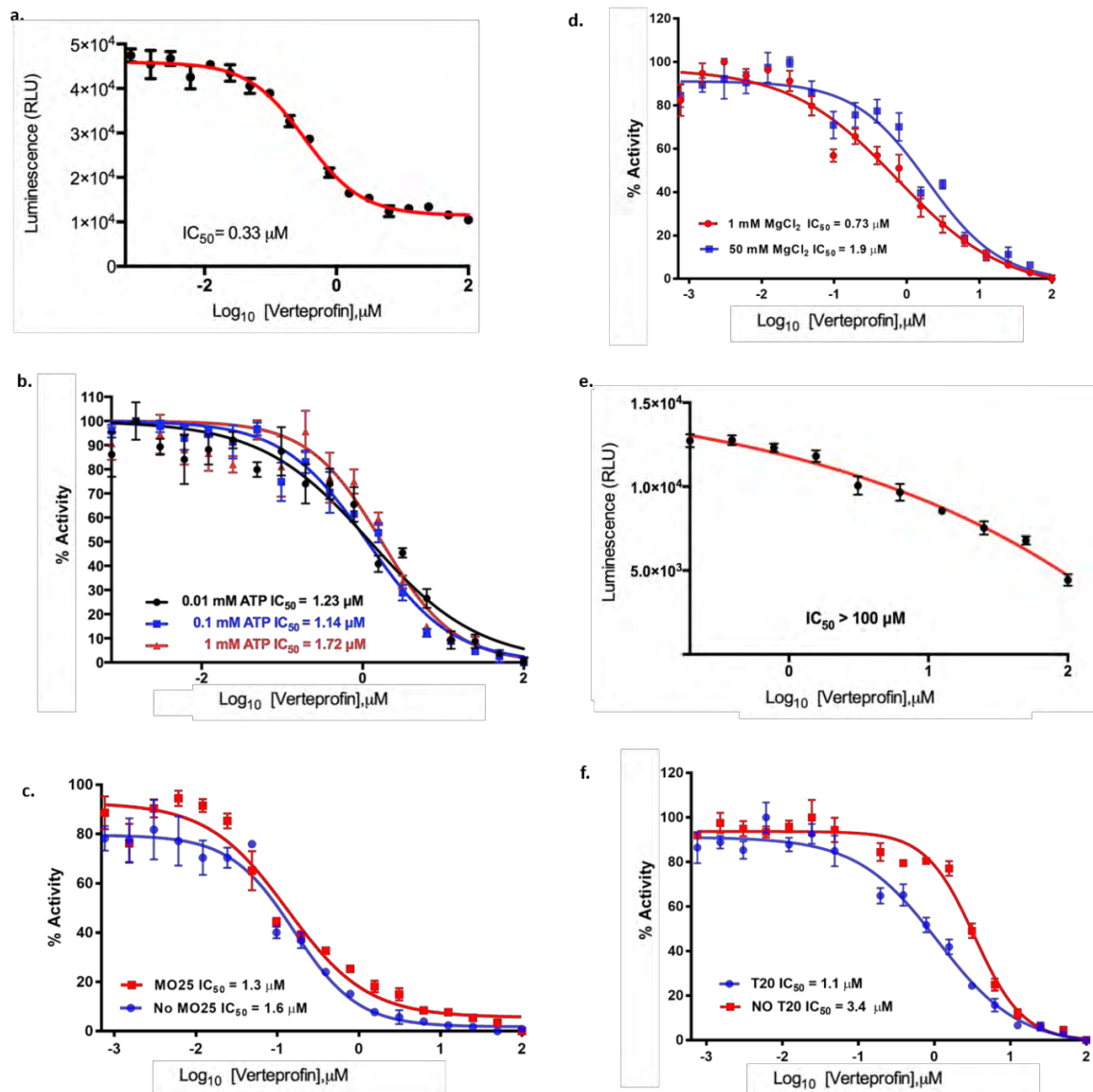


Figure 4.10: *In vitro* characterization of Verteporfin as OSR1 and OSR1 kinase inhibitor. (a) *In vitro* inhibition of SPAK T233E 1-547 by Verteporfin. CATCHtide was employed as a kinase substrate (b) Verteporfin inhibits OSR1 T185E *in vitro* in an ATP-independent manner. (c) The effect of Verteporfin on the MO25-dependant activation of OSR1 T185E 1-527. (d) The effect of MgCl_2 concentration on the ability of Verteporfin to inhibit OSR1 T185E. (e) Verteporfin does not exhibit any *in vitro* inhibition of the constitutively active serine/threonine protein kinase MST3. (f) Effect of the detergent Tween-20 on the ability of Verteporfin to inhibit OSR1 T185E. All of the kinase assays from figure (b) to (f) were carried out using NKCC2 (1-174) as OSR1 T185E substrate. The data represents average of signals ($n=4$, \pm SEM).

4.3.5 Selectivity of Verteporfin for SPAK and OSR1 across 140 protein kinases

Determining the selectivity of an inhibitor is a critical in terms of both new drug development as well as the applications of inhibitors as tools for chemical and biological research (Smyth and Collins, 2009). Accordingly, to investigate the selectivity of Verteporfin towards SPAK and OSR1, a kinase profiling study was performed against a panel of 140 protein kinases, which represent ~30% of human protein kinases, at 1 μ M final concentration (outsourced to the University of Dundee) (**Figure 4.11**). The screening was performed using a radioactive filter binding assay utilising ^{33}P labelled ATP method (Bain et al., 2007, Hastie et al., 2006). The screening revealed that Verteporfin inhibited eight more kinases by $\geq 70\%$. These kinases include the Inhibitor of Nuclear Factor Kappa-B Kinase subunit Epsilon ($\text{IKK}\epsilon$), Mammalian STE20-like Protein Kinase 2 (MST2), Germinal Center Kinase (GCK), Mitogen-Activated Protein Kinase Kinase Kinase Kinase 3 (MAP4K3), Mitogen-Activated Protein Kinase 1 (MLK1), Unc-51 Like Autophagy Activating Kinase 1 (ULK1), Unc-51-like kinase 2 (*C. elegans*) (ULK2) and the Lymphocyte-Specific Protein Tyrosine Kinase (Lck). Indeed, the two kinases, MAP4K3 and $\text{IKK}\epsilon$, were significantly inhibited by Verteporfin, so the IC_{50} values of Verteporfin against these two proteins along with OSR1 under the same assay conditions were obtained. In this case, a radioactive ^{33}P labelled ATP *in vitro* kinase assay was used (outsourced to the University of Dundee). The data revealed that Verteporfin was more potent inhibitor of Ikke and MAP4K3 than OSR1 by 40- and 25 fold with IC_{50} of 12.18, 20.12 and 506 nM, respectively (**Appendix 4.5** for IC_{50} curves).

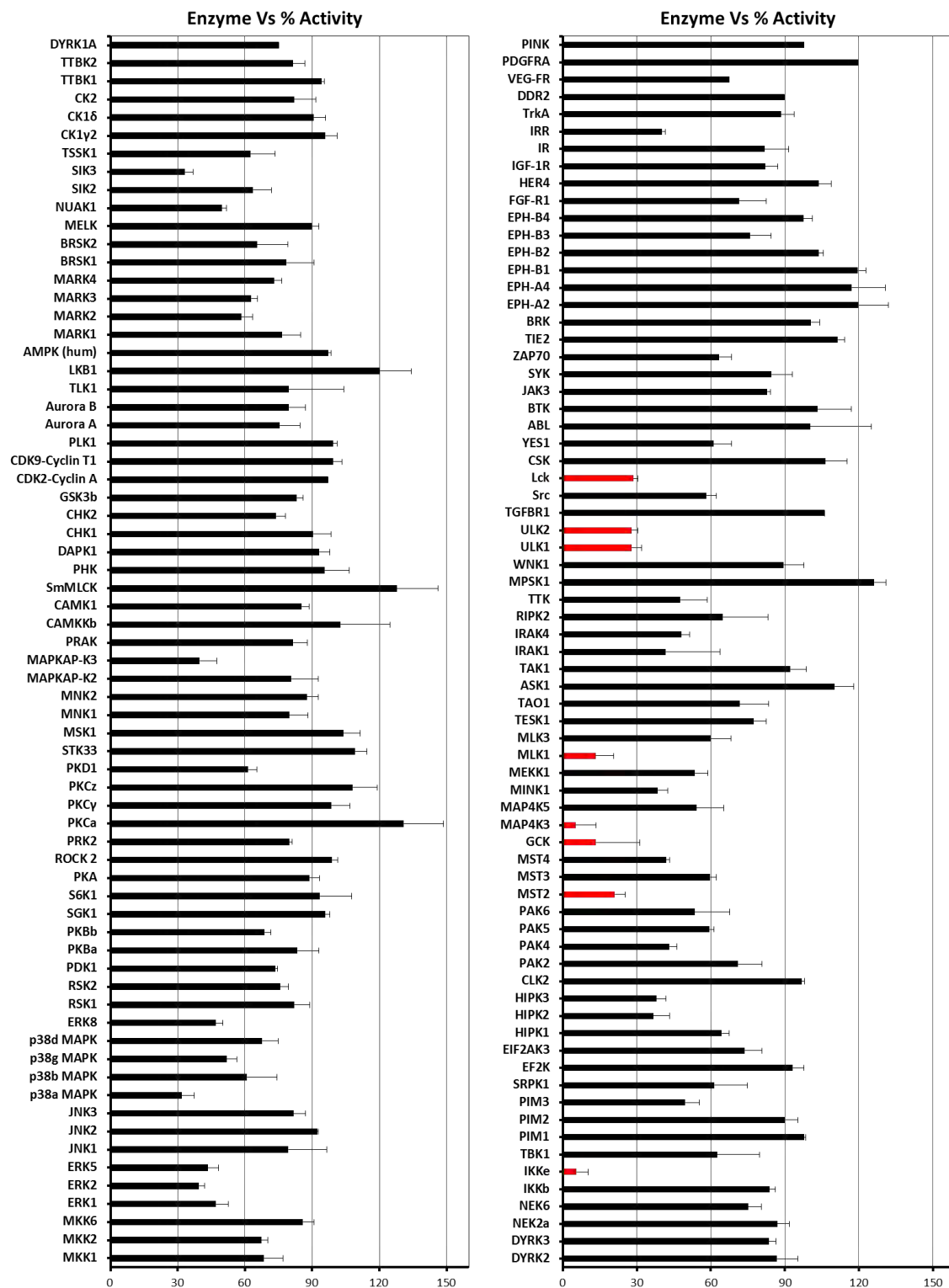


Figure 4.11: Verteporfin kinase selectivity data based on Premier Screen™ from MRC PPU International Centre for Kinase Profiling (ICKP). The kinases with ≥ 70 inhibition are showing in red bars. The data presented as a mean percentage enzyme activity remaining ($n=2$, \pm SD).

4.3.6 Verteporfin inhibited hypotonicity-stimulated WNK-signalling in dose-dependent manner

Next, the inhibitory effect of Verteporfin on SPAK and OSR1 kinases in cells was determined. HEK293 cells, which express the WNK-signalling proteins (Richardson et al., 2008) were treated with Verteporfin at different concentrations above and below IC_{50} value for 30 minutes. STOCK1S-50699, a WNK/SPAK binding inhibitor (Mori et al., 2013) and Closantel, a direct SPAK and OSR1 inhibitor (Kikuchi et al., 2014) were used as positive controls. WNK-signalling pathway was stimulated by treating cells with low-chloride hypotonic buffer for further 30 minutes. As shown in **Figure 4.12**, Verteporfin acted like Closantel and inhibited NKCC1 phosphorylation at Thr203, Thr207 and Thr212 that are specifically phosphorylated by SPAK and OSR1. Interestingly, Verteporfin did not inhibit SPAK phosphorylation at Ser373 (equivalent to OSR1 Ser325) which specifically phosphorylated by WNKs. Additionally, no significant effect on the amount of total SPAK and NKCC1 was observed. These results supported previous *in vitro* findings that Verteporfin may act as a direct inhibitor of SPAK and OSR1 kinases.

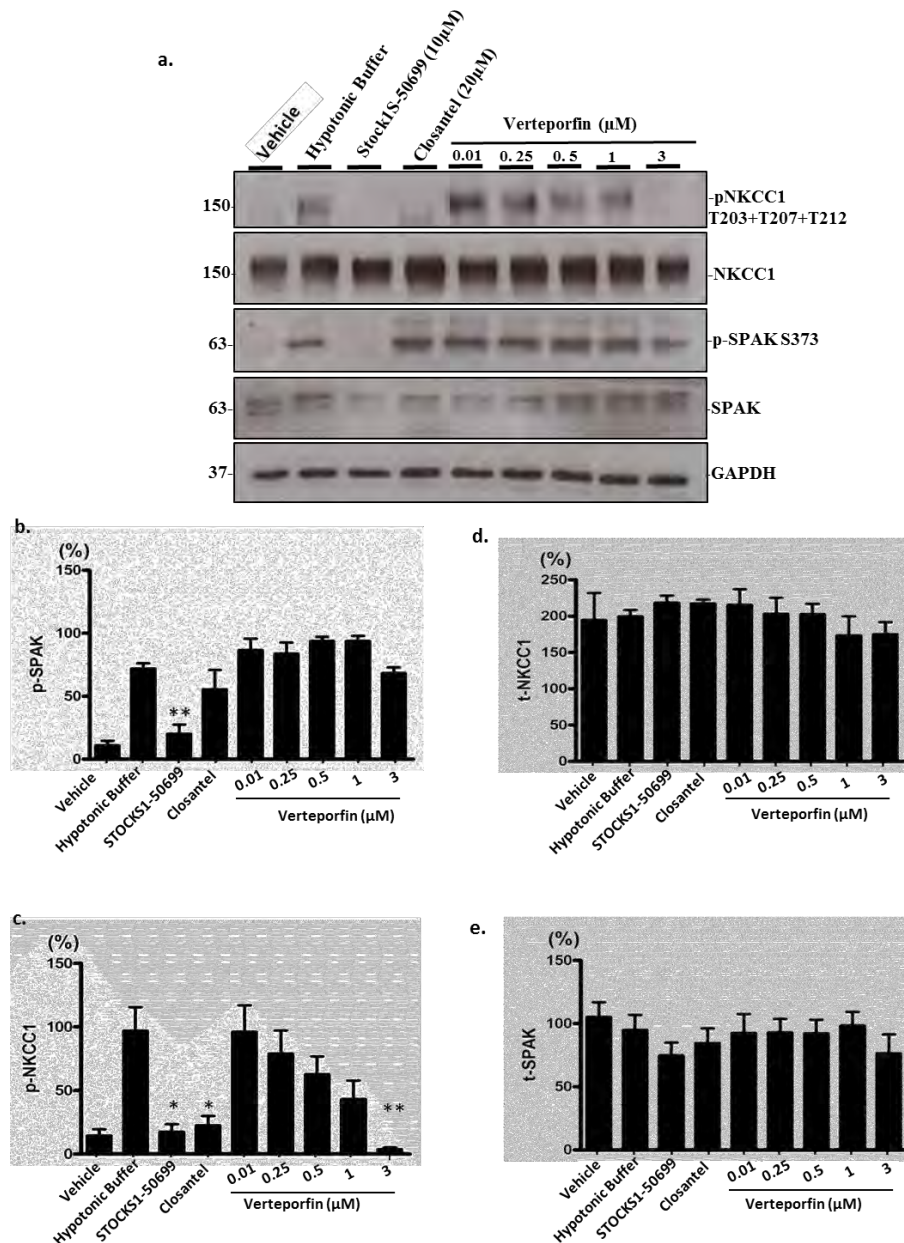


Figure 4.12: Inhibitory effect of Verteporfin on WNK-SPAK/OSR1 signalling in HEK293 cells. (a) Verteporfin inhibits the function of endogenous SPAK and OSR1 kinases in HEK293 cells in concentration dependent manner. HEK293 cells were first treated with Verteporfin at the indicated concentrations for 30 min. STOCK1S-50699 and Closantel were used as controls at 10- and 20 μ M, respectively. Then cells were either left untreated or treated with hypotonic buffer for 30 min to activate WNK-SPAK/OSR1 signalling. The cells were then lysed and probed for phospho-NKCC1 Thr203, Thr207 and Thr212, total NKCC1, phospho-SPAKSer373, total SPAK and GAPDH as a loading control. Bars represent quantification of blots relative to GAPDH for (b) pSPAK, (c) pNKCC1, (d) total-NKCC1 and (e) total-SPAK. The data were reported as a mean ($n=4$, \pm SEM), ** $p < 0.01$, * $p < 0.05$. A one-way ANOVA test followed by Tukey's test were used to compare the results. Final DMSO concentration is 0.1%.

4.3.7 Verteporfin analogues have no effect on the kinase activity of OSR1 T185E

To get some insight into the structure activity relationship of Verteporfin, the activity of two commercially available Verteporfin analogues namely, protoporphyrin IX dimethyl ester (**Figure 4.13a**) and 2,3,7,8,12,13,17,18-Octaethyl-21H,23H-porphine (**Figure 4.13b**) along with Verteporfin under the same condition against OSR1 T185E kinase using the Promega's ADP-Glo™ kinase assay were tested. In protoporphyrin IX dimethyl ester, the dimethyl phthalate moiety of Verteporfin was replaced with ethylene and methyl groups on ring A as well as the methylpropanoate moiety was added to both ring C and D. The results revealed that these replacements, particularly dimethyl phthalate moiety, decrease the activity of this compound dramatically and the IC₅₀ was estimated to be > 100 μM (**Figure 4.13c**). On the other hand, the replacement of both the dimethyl phthalate moiety on ring A as well as the methylpropanoate and/or propanoic acid on ring C and/or D with ethyl groups in 2,3,7,8,12,13,17,18-Octaethyl-21H,23H-porphine led to complete loss of the kinase activity (**Figure 4.13d**). These results suggested that the dimethyl phthalate moiety on ring A is essential for the activity of Verteporfin as SPAK and OSR1 kinase inhibitor.

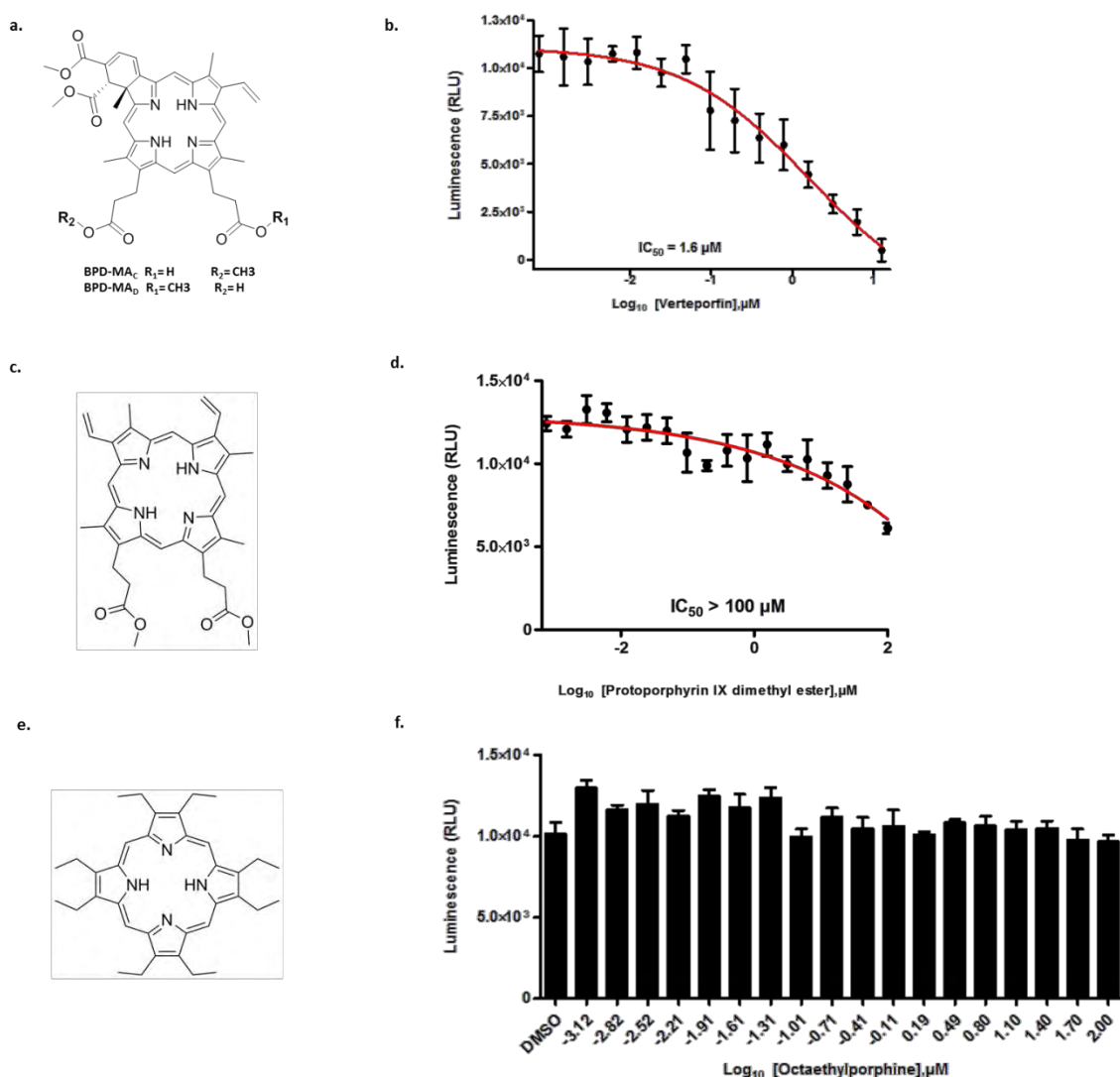


Figure 4.13: The inhibitory effect of Verteporfin's derivatives. (a) Structure of Verteporfin. (b) Effect of Verteporfin on bacterially expressed FL OSR1 T185E kinase activity (c) Chemical structure of protoporphyrin IX dimethyl ester (d) Effect of protoporphyrin IX dimethyl ester on bacterially expressed FL OSR1 T185E kinase activity (e) Chemical structure of 2,3,7,8,12,13,17,18-Octaethyl-21H,23H-porphine (f) Effect of 2,3,7,8,12,13,17,18-Octaethyl-21H,23H-porphine on bacterially expressed FL OSR1 T185E kinase activity. NKCC2 1-174 was employed as a kinase substrate. The data represents average of signals ($n=4$, \pm SEM).

4.3.8 Verteporfin binds to the activation segment of SPAK and OSR1 *in silico*

Subsequently, the potential binding mode of Verteporfin to OSR1 was explored. In order to achieve this, *in silico* molecular docking of Verteporfin into the reported crystal structure of OSR1 kinase domain 1-303 (PDB ID; 2VWI) was conducted using AutoDock Vina program (Trott and Olson, 2010). The results from this unbiased docking exercise suggested that Verteporfin may bind to a flexible region within the OSR1 kinase domain called the domain-exchanged kinase dimer or domain-swapped dimer (**Figure 4.14a**). This region is the site for hydrophobic interaction between residues from α -helix EF of the activation segment of one monomer of OSR1 protein to another monomer (Lee et al., 2009, Villa et al., 2008). At the molecular level, this interaction involved Trp192, Met193, Leu197 and Met198 from helix α EF which occupies a hydrophobic pocket made up from hydrophobic residues including: Met233, Val235, Leu236, and Leu240 (from helix α G) as well as residues Trp211 and Ile215 (from helix α F) of the neighboring molecule. Verteporfin was predicted to form hydrogen bonding with tyrosine 204 (Tyr204) and arginine 279 (Arg279) within this pocket as well as π - π stacking between tryptophan 211 (Trp211) and the isoindole-bicyclic ring of Verteporfin (**Figure 4.14b**).

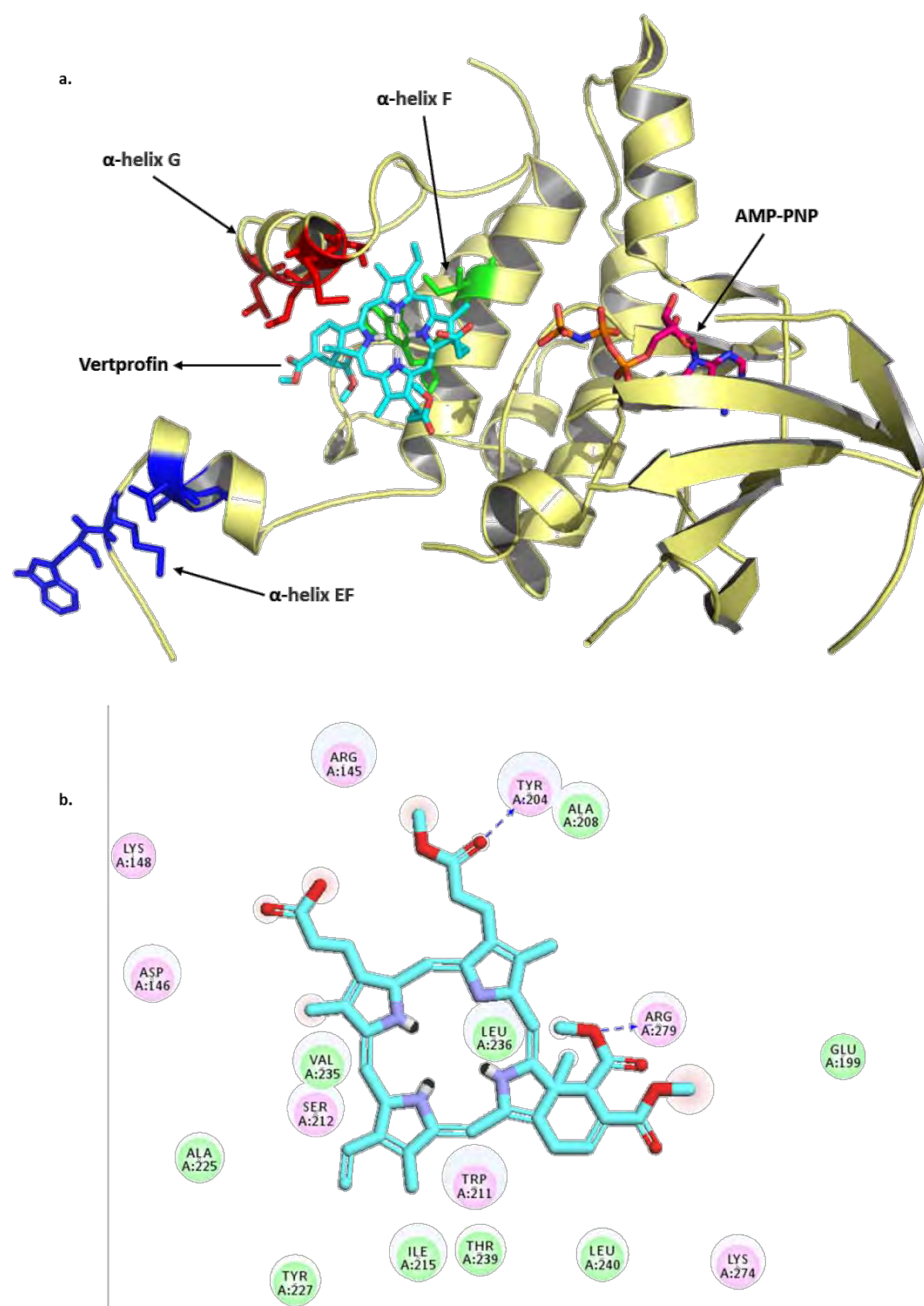


Figure 4.14: Graphical representation of the predicted binding mode of Verteporfin to OSR1 kinase domain (PDB ID: 2VWI). (a) Verteporfin (cyan) binds to a hydrophobic pocket formed by residues from α -helix G (red) and α -helix F (green). This pocket is called the domain-exchanged kinase dimer or domain-swapped dimer, the site for hydrophobic interaction between residues from α -helix EF (blue) of the activation segment of one monomer of OSR1 to another monomer. (b) AutoDock 2D representation of the interaction of Verteporfin with residues at the binding site.

4.3.9 Discussion

The current interest in drug repurposing emphasizes the value of this approach to lower the cost of drug development as well as the time for drug approval. Drug repurposing (also called drug repositioning or reprofiling) is to identify a new indication for an existing drug molecule or an abandoned pharmacotherapy (Ashburn and Thor, 2004). Indeed, the rate of success from drug repurposing process is considerably high as all subsequent steps are known such as pharmacokinetic, pharmacodynamics and safety profiles, which had already been established for approved drugs (Sardana et al., 2011). For this screening process, an efficient screening assay compatible with HTS technologies is required.

In this Chapter, a non-radioactive, easy-to-monitor, robust, reliable and cost effective HTS kinase assay based on Promiga's ADP-Glo™ kinase Assay was developed and optimised. The assay is a bioluminescent kinase assay that measures ADP produced from a kinase reaction by converting ADP into light via Ultra-Glo Luciferase (Zegzouti et al., 2009). The assay is carried out in two steps. First, termination of the kinase reaction by adding an equal volume of ADP-Glo™ reagent, which acts by depletion of the remaining ATP. In the second step, the ADP formed from the reaction is converted into ATP, which is eventually measured by using coupled luciferase-luciferin reaction (Zegzouti et al., 2009). In this assay, low amounts of compounds, proteins, substrates and kinase kit reagents are needed and this allowed us to screen in-house chemical library for novel SPAK and OSR1 kinase inhibitors.

As a result of library screening, seven hits were identified, all from FDA-approved drug chemical library (**Figure 4.2**). Despite the presence of a nonionic detergent (Tween-20) in the screening buffer, which is a recommended strategy to avoid protein aggregation

induced by compounds (Feng and Shoichet, 2006), four compounds, Alexidine dihydrochloride, Chlorhexidine dihydrochloride, Methyl Benzethonium Chloride and Chicago Sky Blue 6B, were excluded from further investigation as they have been reported as protein aggregators (Irwin et al., 2015). Nevertheless, a novel function of three drugs with different chemical scaffolds: Toremifene, β -Escin and Verteporfin was identified. These compounds were shown to inhibit the kinase activity of OSR1 kinase *in vitro* (**Figure 4.4, 4.6 and 4.3**). Toremifene (Fareston[®]) is a selective estrogen receptor modulator (SERM) used as an anticancer for treatment of advance breast cancer in a dose starting from 60 mg/kg up to 240 mg/kg per day (Mustonen et al., 2014). β -Escin (or also called Aescin) is a natural triterpene saponin with anti-oedematous, anti-inflammatory and venotonic properties (Sirtori, 2001). Noticeably, both drugs (Toremifene and β -Escin) inhibited OSR1 in a low-micromolar concentration range *in vitro* by targeting the kinase domain but not the C-terminal domain as they inhibit OSR1 T185E FL as well as the OSR1 T185E 1-342 that lacks the CCT domain to the same extent (**Figure 4.4 and 4.6**). Further *in vitro* studies are needed to validate the inhibitory effect of these two drugs on downstream ion cotransporters.

Interestingly, Verteporfin was identified as a potent inhibitor of OSR1 and SPAK in a non-ATP dependent manner. Verteporfin (Visudyne[®]) is a photodynamic therapy used for treatment of choroidal neovascularization (CNV) due to age-related macular degeneration and/or other causes (Participants, 2005). Unlike other known SPAK and OSR1 inhibitors, the results showed that Verteporfin was also able to inhibit the truncated OSR1 1-342 indicating that it may not bind to the C-terminal domain of SPAK and OSR1 (**Figure 4.3d**). Additionally, the activation of OSR1 by the scaffolding protein, MO25, was not affected by presence of Verteporfin suggesting that it may not bind to the MO25

binding grove on the S-motif (**Figure 4.10c**) (Filippi et al., 2011). The docking data suggested that Verteporfin binds to a novel allosteric binding site adjacent to the ATP binding pocket of OSR1 kinase domain (**Figure 4.12**). This pocket is the site for a key process called domain-exchange dimer or domain-swapped dimer, which mediates further activation of OSR1 by homo-dimerisation and auto-phosphorylation (Lee et al., 2009, Villa et al., 2008). Despite pervious observations that OSR1 was a monomeric in solution, it has been shown to form oligomers *in vivo* (Anselmo et al., 2006). In addition, the activation of kinases by homo-dimerisation is also observed with other kinases such as the checkpoint kinase 2 (CHK2), lymphocyte-oriented kinase (LOK) and Ste20-like kinase (SLK) (Pike et al., 2008, Oliver et al., 2006). Notably, the domain-swapped region is highly flexible region, which hampers the effort to cocrystalise SPAK or OSR1 bound to Verteporfin. However, these findings indicate that targeting the dimerization site could be exploited as a novel approach to inhibit these two highly related kinases.

The dimethyl phthalate moiety of the porphyrin core of Verteporfin was also shown to be an essential for its activity as SPAK and OSR1 kinase inhibitor. Consistent with this, two analogues of Verteporfin, protoporphyrin IX dimethyl ester and 2,3,7,8,12,13,17,18-Octaethyl-21H,23H-porphine, in which the dimethyl phthalate moiety of porphyrin core was replaced with different functional groups had no inhibitory effect on OSR1 T185E kinase *in vitro* (**Figure 4.13**). This suggested that the inhibitory effect of Verteporfin might not be nonspecific and provided further insight into the structure activity relationship of Verteporfin.

In HEK293 cells, Verteporfin inhibited the singling transduction from SPAK and OSR1 to NKCC1. While the amount of total SPAK and NKCC1 as well as phosphorylated SPAK did not change, the amount of phosphorylated NKCC1 was

inhibited completely in presence of 3 μ M of Verteporfin (**Figure 4.12**). These results validated that Verteporfin is targeting the function of SPAK and OSR1 directly with no effect on their expression profile as well as their activation by the upstream WNK kinases.

The screening of Verteporfin against a kinase panel of 140 kinases revealed that Verteporfin can inhibit a range of other kinases involved in different physiological processes. Currently, Verteporfin is widely investigated as an anticancer therapy with some studies in late preclinical stages (Zhao et al., 2017, Kang et al., 2017, Dasari et al., 2017, Gibault et al., 2016). Therefore, establishing its kinase selectivity is essential for predicting potential off-target effects. Critically, the recent discovery that Verteporfin is a potent inhibitor of WNK-signalling by targeting SPAK and OSR1 could explain the low blood pressure effect observed in animals treated with Verteporfin (Charisis et al., 2007).

In summary, in this Chapter, the discovery of Verteporfin, an FDA approved drug, as a potent inhibitor of SPAK and OSR1 *in vitro* using a novel non-radioactive HTS kinase assay was described.

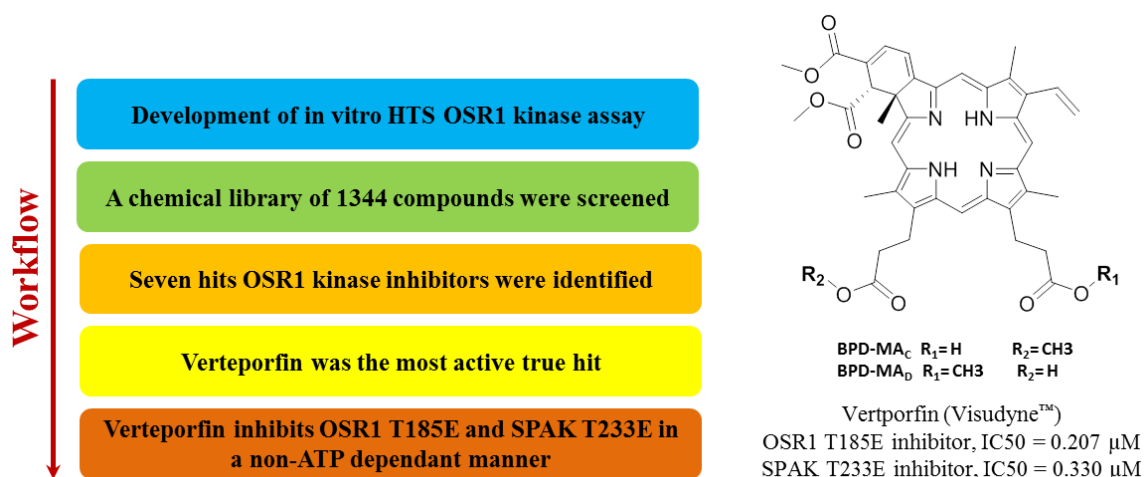


Figure 4.15: Graphical conclusion. HTS and drug repurposing are two significant approaches in early drug discovery process. A highly efficient and non-radioactive kinase assay compatible with HTS technology was developed and used to screen a chemical library, consists mainly FDA-approved drugs. Among the seven identified hits compounds, Verteporfin was the most active allosteric inhibitor of SPAK and OSR1 *in vitro*.

**CHAPTER V: USE NMR-BASED FRAGMENT
SCREENING TO IDENTIFY SPAK AND
OSR1 KINASE INHIBITORS**

5.1 Introduction

Fragment-based screening (FBS) has become a powerful method in drug discovery for identifying small ligands with affinity towards target macromolecules. As an example of such success is Vemurafenib, an FDA-approved anticancer B-Raf inhibitor that originated from FBS in 2011 (Harner et al., 2013). Typically, in FBS, a fragment refers to a small organic molecule with a molecular weight of ≤ 300 Da, number of H-bond acceptors of ≤ 3 , number of H-bond donors of ≤ 3 and clogP of ≤ 3 (Congreve et al., 2003). Due to the small size, the fragment hits from the primary screen are usually weak binders with low binding affinity as the number of molecular contacts between the fragment hits and the target protein are small. Therefore, following identification, the fragments need to be developed into larger molecules with higher affinity towards the target protein (Harner et al., 2013).

Unlike biophysical techniques (e.g. NMR spectroscopy), the detection of weak ligand binders using biochemical techniques (e.g. fluorescence-based experiments) poses extreme challenges as it is difficult to observe any change in the signal above the baseline of the assay (Harner et al., 2013). Nuclear magnetic resonance (NMR) spectroscopy is one of the most popular techniques in the application of FBS due to its sensitivity in detecting and characterising the weak binding between ligands and the target macromolecules with a dissociation constant (K_d) in the μM to mM range. (Fielding, 2003).

5.2 Aim

The aim in this Chapter is to use NMR spectroscopy and FBS to identify fragments that bind the SPAK and OSR1 kinases highly conserved *C*-terminal (CCT) domains.

5.3 Results

5.3.1 Expression and purification of GST-OSR1 CCT domain and GST-tag proteins

Initially, GST-OSR1 CCT domain (433-527) WT was expressed to be used in screening of the fragment library. In addition, the GST tag protein was also expressed to be used as a control in order to eliminate any potential GST-tag binders. Both proteins were expressed in *E.coli* and purified with a good yield (GST-OSR1 = 5.7 mg and GST = 6.85 mg per litre of culture) and purity (> 95%) as shown in **Figure 5.1** (see Materials and Methods described in section 2.1.6.1).

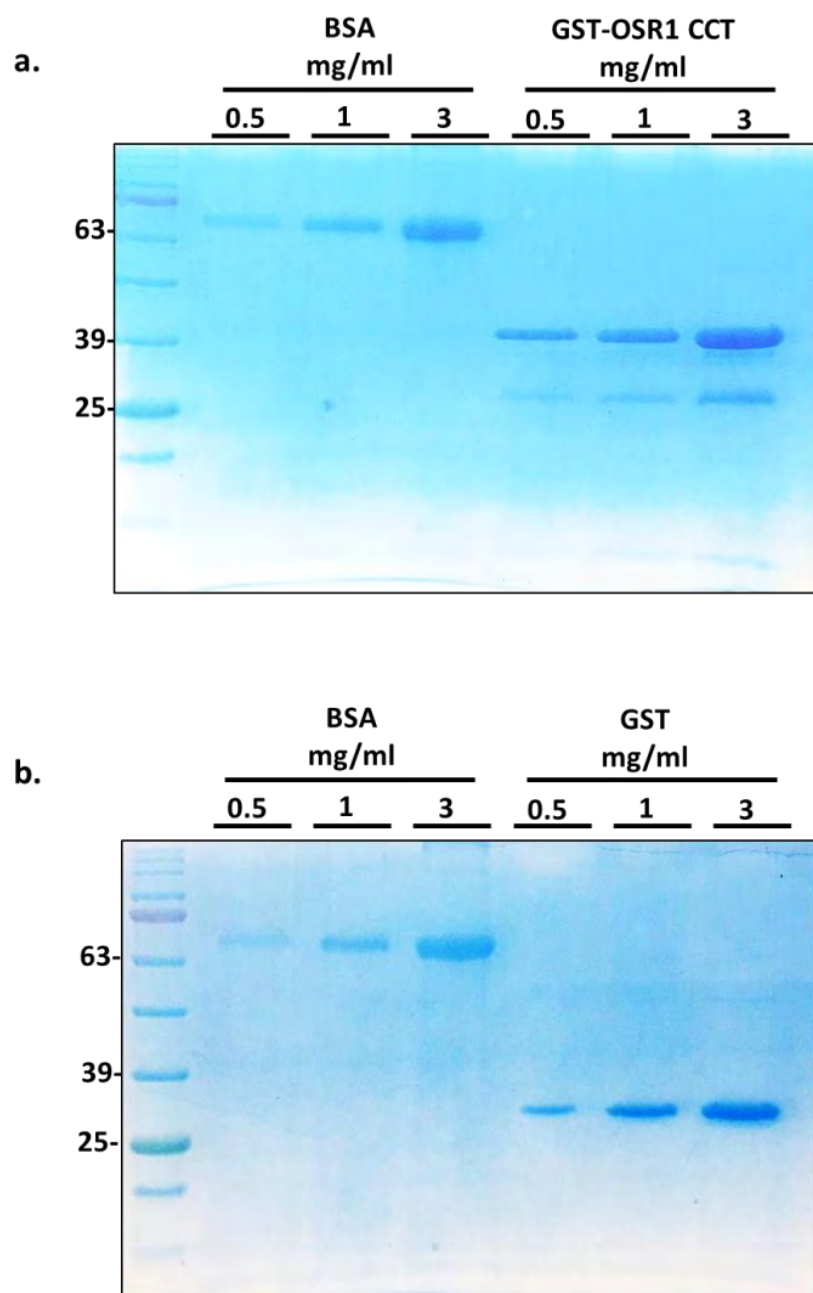


Figure 5.1: Expression and purification of proteins from *E.coli*. (a) GST-OSR1 CCT domain and (b) GST-tag constructs. (BSA) Bovine serum albumin (Sigma Aldrich, cat# A2153, purity $\geq 96\%$ determined by agarose gel electrophoresis) was used at different concentrations as standards for determinations of proteins yield and purity.

5.3.2 In-house fragment library screening by STD-NMR and waterLOGSY

The screening of the fragment library, composed of 384 compounds, was carried out using both STD (Saturation transfer difference)-NMR and waterLOGSY (Water-ligand observed via gradient spectroscopy) methods (Klages et al., 2007). These were run against both GST-OSR1 CCT domain (433-527) WT and GST-tag under the same conditions (see Materials and Methods described in section 2.6.2). These two ligand-based techniques work by monitoring the changes in the ligand resonance in solution in response to protein binding. STD-NMR and waterLOGSY experiments depend on a selective saturation of the protein and bulk water magnetisation, respectively (Viegas et al., 2011, Dalvit et al., 2001). In the STD, the saturation transfers from the protein to the bound ligand directly. The STD spectrum (I_{STD}) is a net difference between two recorded spectra including the on-resonance (I_{SAT}) where the saturation is applied to only the protein resonances as well as the off-resonance (or reference) spectrum (I_0) in which the saturation is applied away from both compound and protein resonances; ($I_{STD}=I_{SAT}-I_0$) (Lepre et al., 2004). However, in waterLOGSY, the perturbation in the bulk water magnetisation transfers from the water to the protein, bound ligand and free ligand. This NOE (Nuclear Overhauser Effect) is recorded and is either positive for a small molecule (i.e. the free ligand) or negative for a larger species (such as the protein or the ligand bound to the protein). Indeed, the signal of the protein or the ligand bound to the protein is too broad and weak to be seen. However, as the ligand dissociates from the protein rapidly its signal is sharp but retains the negative NOE from when it was bound to the protein (Dalvit et al., 2001). Notably, depending on the way the data processed, the peak of bound ligand could be positive and the unbound ligand could be negative and vice versa.

The fragment library was screened using cocktails of 4 fragments with each fragment present at a final concentration of 1 mM. In STD-NMR, a positive fragment hit within a cocktail of 4 would give a peak or peaks, in the different spectrum, correspond to that recorded for each fragment hit as a reference. In case of waterLOGSY, a compound binding to the protein would give a positive peak and vice versa non-binding compound would give a negative peak identical to that seen with a control with no protein present. In the fragment screening, a fragment that displays a positive signal in both STD-NMR and waterLOGSY against GST-OSR1 CCT domain but not GST alone was considered as a true hit. Accordingly, 27 fragment hits were identified from the primary screening as binders of OSR1 CCT domain (**Table 5.1**). Examples of STD-NMR and waterLOGSY spectra for compound 179 and 330 are shown in **Figure 5.2a** and **5.2b**, respectively (all spectra for other fragment hits are illustrated in **Appendix 5.1a-5.1i**).

	Plate number	Cocktail Reference	Compound Number
1	16	46	79
2	17	49	38-67
3	29	85	82
4	33	97	141
5	34	100	148
6	37	109	101
7	40	118	147
8	41	121	114
9	51	151	156
10	57	169	177-256
11	60	178	178-306
12	61	181	179
13	62	184	337
14	64	190	343
15	66	196	208
16	71	211	220
17	75	223	307-391
18	77	229	329-383
19	78	232	393-234
20	81	241	330
21	84	250	299

Table 5.1: List of fragment hits from primary screening of in-house 384 fragments. The fragment library was screened in a cocktail of 4 with each fragment present at a final concentration of 1 mM. NMR samples were prepared by adding each cocktail to a mixture of 10 μ M of either unlabeled GST-OSR1 CCT domain or unlabelled GST-tag, 20% deuterium oxide (D_2O) and 3% (v/v) D_6 -DMSO (5% final D_6 -DMSO concentration) in NMR running buffer (50 mM Tris- d_{11} pH 7.4, 150 mM NaCl) at 50 μ l total sample volume. Compounds that showed positive STD and waterLOGSY with GST-OSR1 CCT domain but not with GST were considered as positive hits.

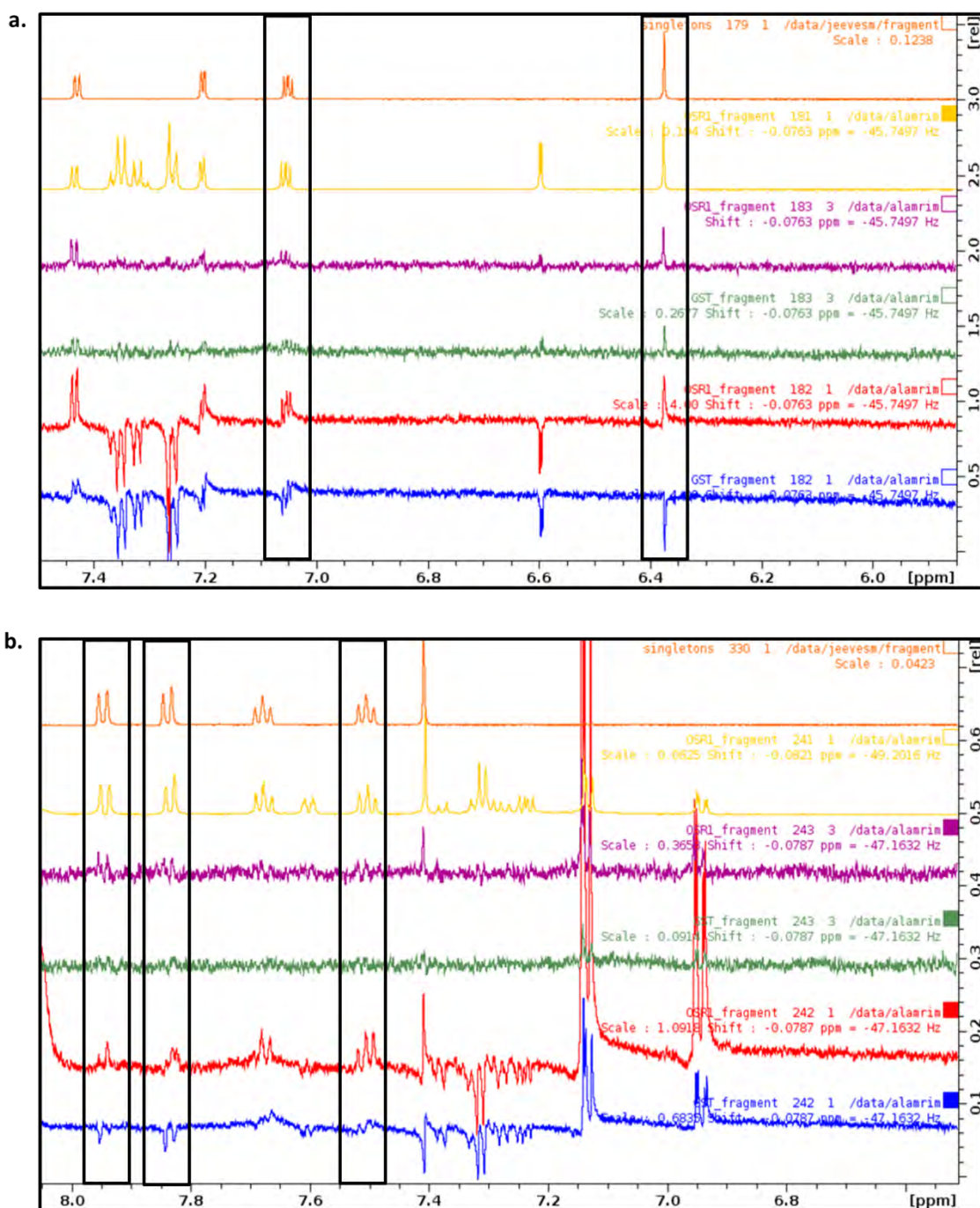


Figure 5.2: Examples for STD-NMR and waterLogsy spectra for fragment hits. Spectra of fragment hits number (a) 179 and (b) 330. The orange spectrum is for ¹H NMR reference spectrum for reference compound, yellow spectrum is for ¹H NMR reference spectrum for the cocktail sample which composed of 4 distinct fragment molecules, violet spectrum is for STD-NMR experiment with GST-OSR1 CCT domain, green spectrum is for STD-NMR experiment with GST-tag protein, red spectrum is for waterLogsy experiment with GST-OSR1 CCT domain, blue spectrum is for waterLogsy experiment with GST-tag protein. The compound peaks that tested positive in both STD-NMR and waterLogsy with GST-OSR1 CCT domain but not GST-tag protein were highlighted with black rectangle.

5.3.3 Confirmation of the fragment hits by STD-NMR

To confirm the binding of hit fragments from the primary screening, a secondary screening was performed using STD-NMR for the 27 ligands against GST-OSR1 CCT domain at a final concentration of 1 mM. In the primary screening, the on resonance and off resonance saturation in the STD-NMR experiments were set to -0.5 ppm and 30 ppm, respectively, and the intensity of the STD signals were weak. Therefore, in the secondary screening, the on resonance was set to $+0.5$ and off resonance was set to 30 ppm (not changed) to insure full saturation of protein signals as well as to improve the STD-NMR signals.

Among the identified 27 primary fragment hits, 19 fragments were confirmed to bind to OSR1 CCT domain giving a hit rate of 4.94 % (**Table 5.2**). Examples of STD-NMR spectra of compound 179 and 330 were illustrated in **Figure 5.3a** and **5.3b**, respectively (all spectra for other fragment hits are illustrated in **Appendix 5.2a-5.2m**). Notably, the secondary screening was performed against OSR1 CCT domain but not GST-tag protein as GST-tag binders were already excluded.

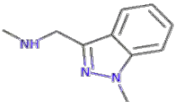
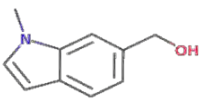
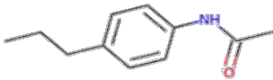
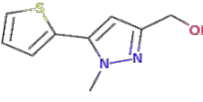
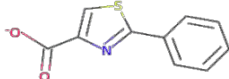
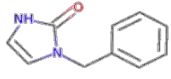
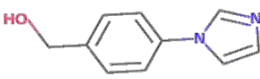
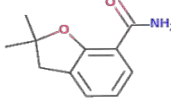
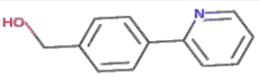
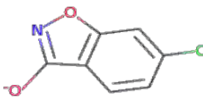
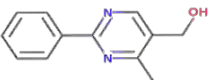
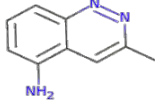
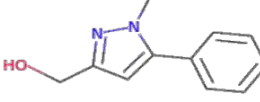
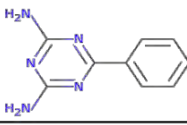
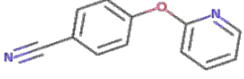
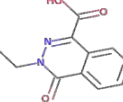
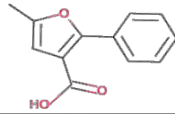
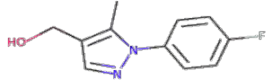
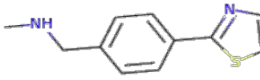
38		178	
67		179	
79		208	
101		220	
114		299	
141		307	
147		330	
148		383	
156		234	
177			

Table 5.2: Chemical structures of confirmed 19 fragment hits. With the exception of compound 67 and 220, all compounds contain at least two aromatic rings.

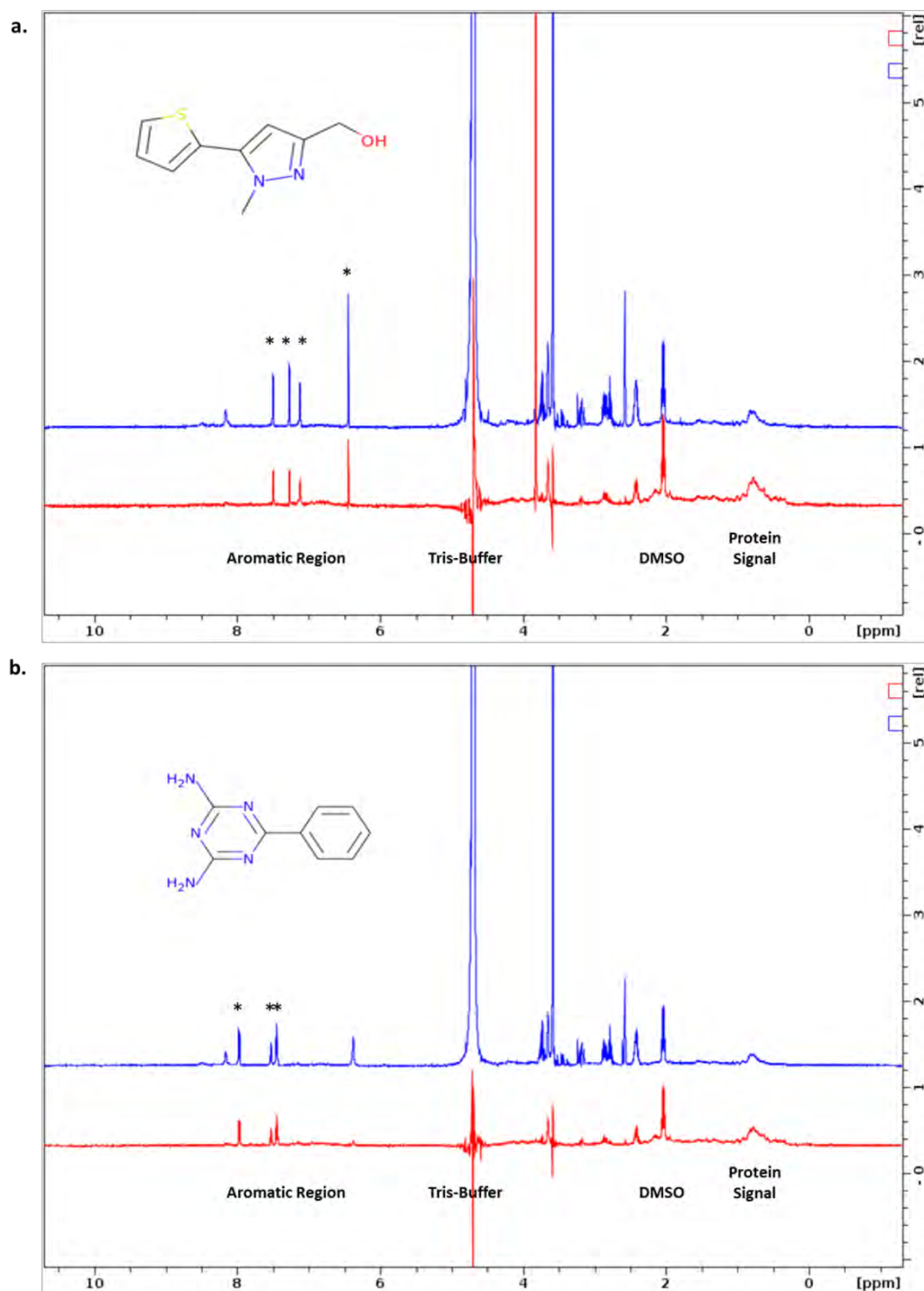


Figure 5.3: Examples for STD-NMR for confirming the binding of fragment number (a) 179 and (b) 330 to GST-OSR1 CCT domain. The blue spectrum is for ^1H NMR reference spectrum for reference compound and red spectrum is for STD-NMR experiment with GST-OSR1 CCT domain. Positive peaks in STD-NMR experiment are labelled with thick black dots in the reference. NMR spectrum regions were labelled.

5.3.4 STD-NMR competition assay for ligand binding specificity

OSR1 CCT domain possesses two adjacent pockets namely; primary and secondary pockets as discussed in Chapter III (Villa et al., 2007). The primary pocket is known to mediate the binding of SPAK and OSR1 CCT domains to the upstream WNK kinases and the downstream ion co-transporters (see Chapter III). To investigate whether the identified hit fragments bind to the primary pocket of OSR1 CCT domain, an STD-NMR competition experiment was performed at a final fragment hits concentration of 1 mM in presence of 50 μ M of the 18-mer RFQV (CCPGCCGGSEEGKPQLVGR**RFQ**VTSSK), a peptide derived from human WNK4 that binds to OSR1 CCT domain (Vitari et al., 2006). The binding affinity of RFQV to OSR1 CCT domain was determined using different biophysical techniques (SPR K_d value = 8 nM, FP assay K_d value = 2.11 μ M) (see chapter III). NMR samples were prepared as mentioned in section 5.2.3. Among the 19 hit fragments, compound 383 showed a significant decrease in the STD-NMR signal indicating that it might be displaced from the primary pocket by 18-mer RFQV peptide (**Figure 5.4a**). However, there was no change observed in the STD signals of other 18 fragment hits. This suggested that the binding of the RFQV peptide could not preclude binding of these fragments to the primary pocket or these fragments may bind to different binding sites beyond the primary pocket (see compound 179 as an example in **Figure 5.4b**). All spectra for other hit fragments are presented in **Appendix 5.3a-5.3g**.

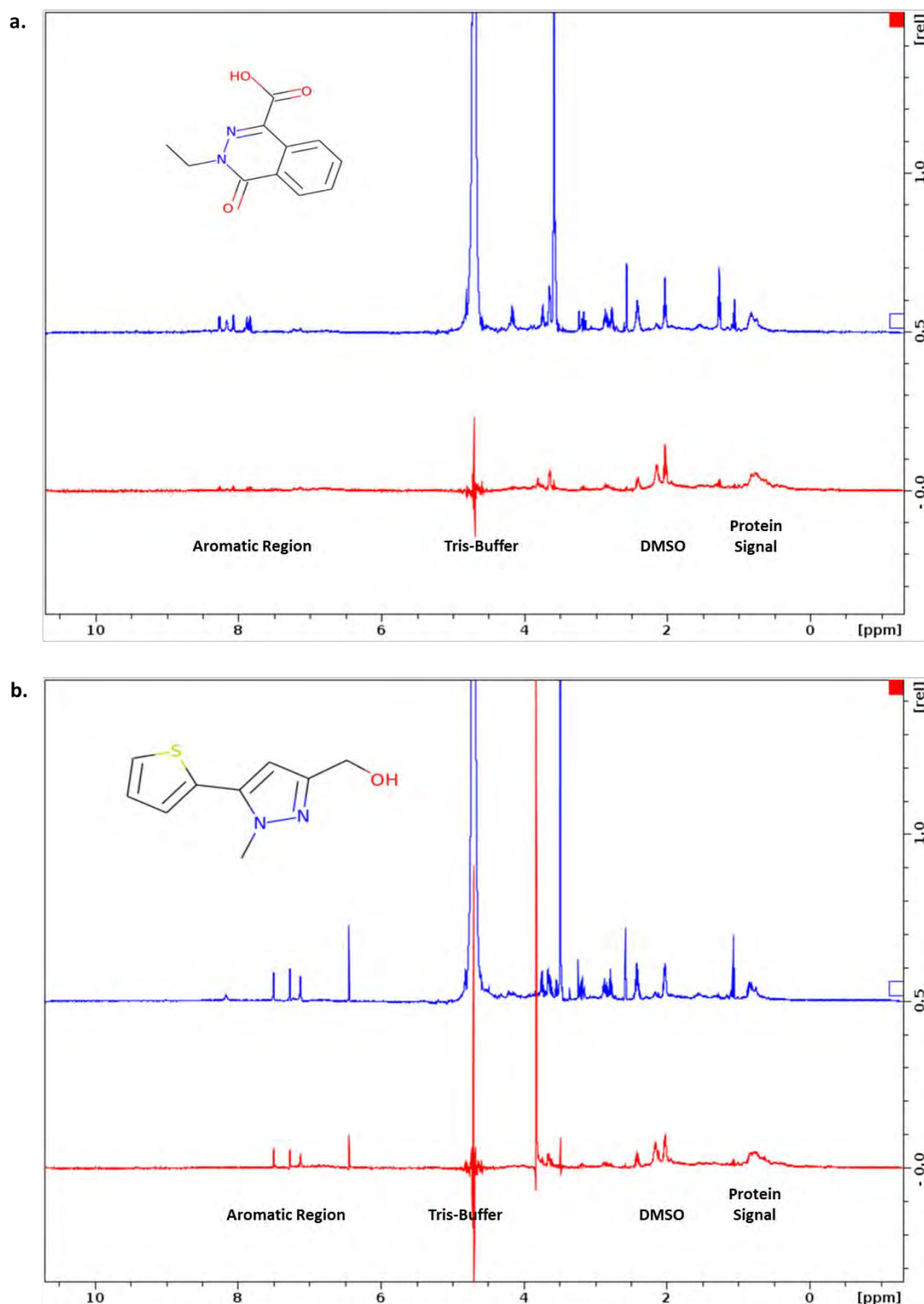


Figure 5.4: STD-NMR competition assay for ligand binding specificity. (a) Compound 383 compete with 18-mer RFQV peptide derived from WNK4 on the primary pocket as the STD-NMR peaks intensity in presence of RFQV (red) is significantly reduce as compare to STD-NMR peaks intensity in the absence of 18-mer RFQV peptide (blue). (b) Compound 179 did not compete with 18-mer RFQV peptide derived from WNK4 on the primary pocket as the STD-NMR peaks intensity did not change in in presence or absence of RFQV peptide.

5.3.5 The effect of hit fragments on the activity of OSR1 T185E and SPAK T233E *in vitro*.

The inhibitory effect of four selected hit fragments (179, 234, 330 and 383) was tested against both constitutively active GST-OSR1 T185E and GST-SPAK T233E using ADP-Glo™ kinase assay (see Materials and Methods described in 2.4.1). Both full length human GST-OSR1 T185E and GST-SPAK T233E proteins were expressed and purified from *E.coli* (**Appendix 4.1a and 4.1d**). A fragment of cytoplasmic *N*-terminal domain of NKCC2, NKCC2 1-147, was employed as the kinase substrate. The compounds were selected based on two parameters: the chemical scaffold of fragment ligand as well as the intensity of STD-NMR signal of ligand during pervious experiments. Unfortunately, none of tested compounds were able to inhibit the kinase activity of SPAK and OSR1 kinases at two concentrations of 2.5- and 5 mM (**Figure 5.5a and 5.5b**).

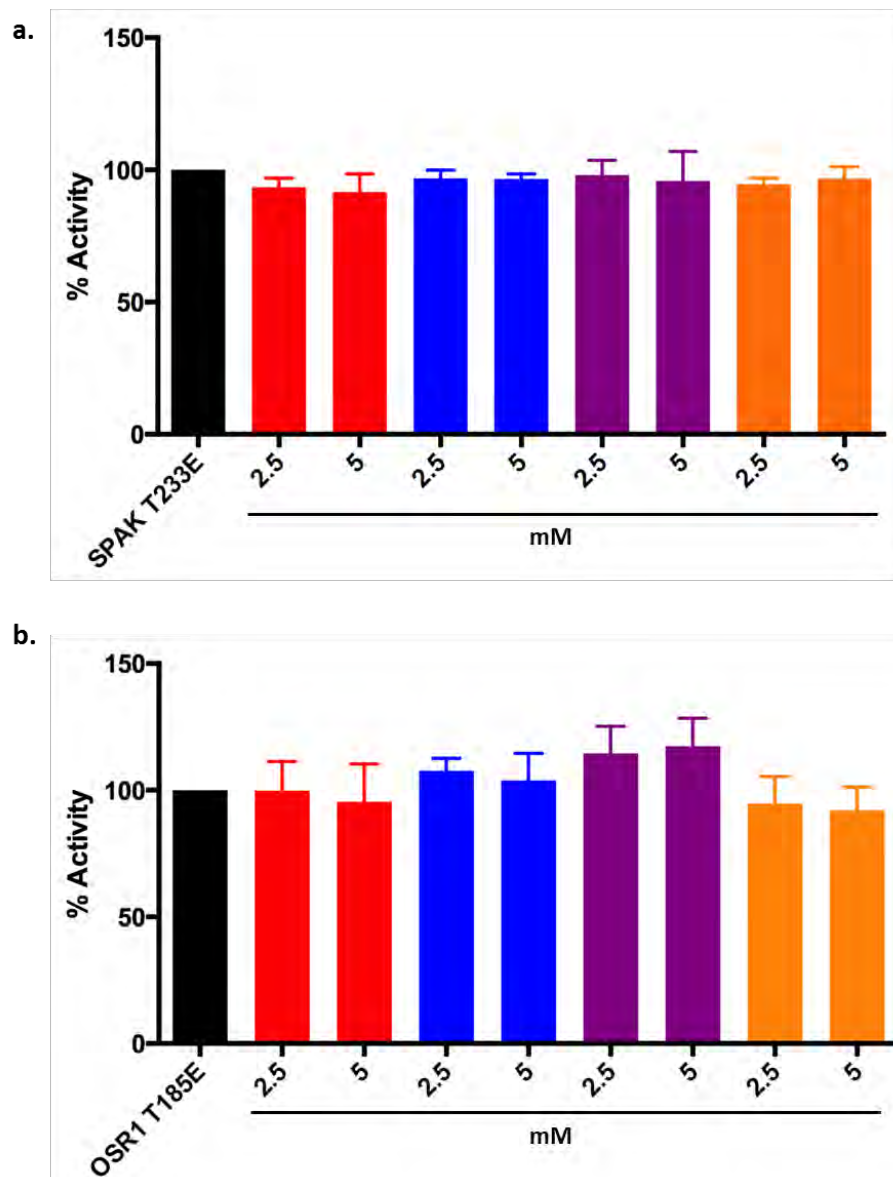


Figure 5.5: Inhibitory effect of fragment hits on the activity of SPAK and OSR1 kinases. The inhibitory effect of 179 (red), 234 (blue), 330 (violet) and 383 (orange) on the activity of constitutively active (a) GST-OSR1 T185E FL and (b) GST-SPAK T233E FL. Data presented as percentage of remaining activity relative to control ($n = 4$, \pm SEM).

5.3.6 The inhibitory effect of fragment-hybrid ligands on the activity of OSR1 T185E *in vitro*

In order to improve the *in vitro* activity of these fragment binders as inhibitors of SPAK and OSR1, fragment-hybrid molecules were designed and obtained commercially. Four hybrid-ligands were designed in which compounds Cp1, Cp2, Cp3 and Cp4 are a combination of fragments number 38-179, 383-148, 383-330 and 148-330, respectively (**Figure 5.6a**). The inhibitory effect of the designed-ligands were subsequently tested at two concentrations of 30 and 100 μ M against constitutively active GST-OSR1 T185E using the same ADP-Glo™ kinase assay and employing NKCC2 1-147 as a kinase substrate. Verteporfin, a potent SPAK and OSR1 inhibitor, was used as a control (see Chapter IV). Unfortunately, there was no significant reduction in the OSR1 kinase activity observed with any compound even at 100 μ M (**Figure 5.6b**).

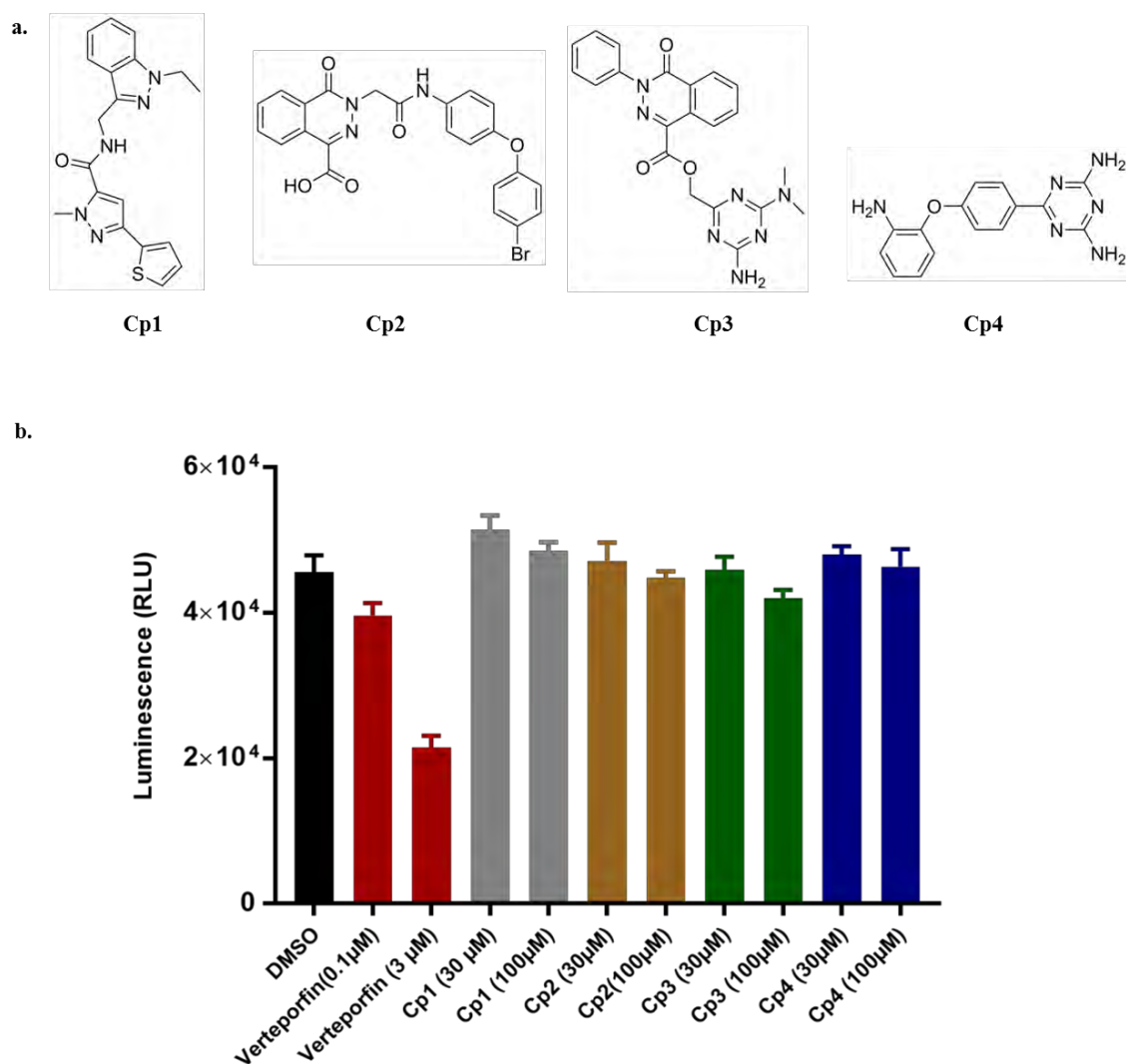


Figure 5.6: The inhibitory effect of fragment-hybrid ligands on the activity of OSR1 T185E *in vitro*. (a) Chemical structures of designed fragment hybrid-ligands. (b) The inhibitory effect of Cp1 (grey), Cp2 (gold), Cp3 (green) and Cp4 (blue) on the activity of constitutively active GST-OSR1 T185E FL. Verteporfin (dark red) was used as a positive control. Data presented as mean ($n=4$, \pm SEM).

5.3.7 Expression and purification of ^{15}N and/or ^{13}C isotopically labelled OSR1 and SPAK CCT domains

The second objective of this Chapter was to conduct a structural analysis of fragment hits to determine their binding mode in solution. Initially, ^{15}N labelled CCT domains of OSR1 (433-527) and SPAK (425-545) as well as ^{15}N - and ^{13}C - double labelled OSR1 CCT domain were obtained. Both OSR1 (433-527) and SPAK (425-545) constructs were expressed in M9 minimal media with ammonium- ^{15}N chloride ($^{15}\text{NH}_4\text{Cl}$) and/or D-Glucose- $^{13}\text{C}_6$ as sole sources of nitrogen and carbon, respectively (see Materials and Methods section 2.1.6.2). In order to cleave the GST tag from expressed CCT domain of GST-OSR1 and GST-SPAK, also PreScission protease enzyme was expressed in LB broth medium (see Materials and Methods section 2.1.6.1). All proteins were expressed in *E.coli* and purified in a good yield (PreScission protease enzyme = 11.24 mg, ^{15}N -SPAK CCT domain = 1.2 mg, ^{13}N -OSR1 CCT domain 1mg, ^{15}N - ^{13}C -OSR1 CCT domain = 1 mg per litre of culture) and purity (> 95%) as shown in **Figure 5.7**.

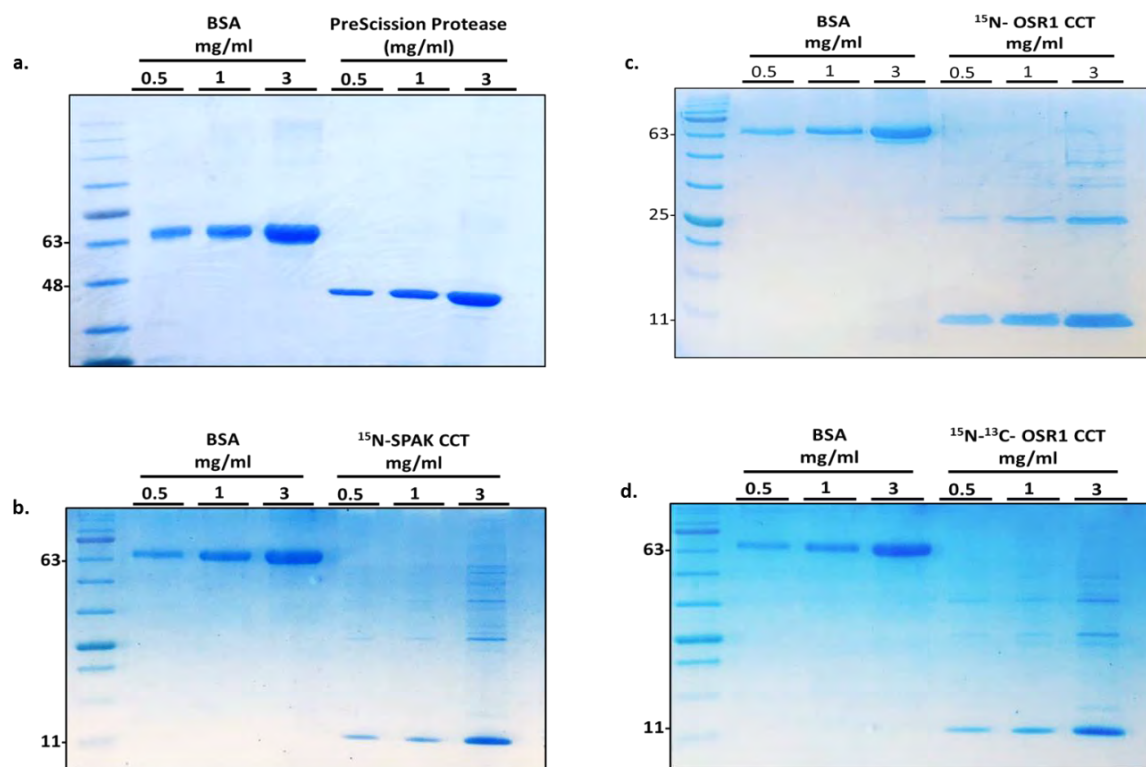


Figure 5.7: Expression and purification of proteins from *E. coli*. (a) PreScission protease enzyme, (b) ^{15}N -SPAK CCT domain (c) ^{15}N -OSR1 CCT domain and (d) ^{15}N - ^{13}C -OSR1 CCT domain were expressed and purified from *E. coli*. (BSA) Bovine serum albumin (Sigma Aldrich, cat# A2153, purity $\geq 96\%$) determined by agarose gel electrophoresis) was used at different concentrations as standards for determinations of proteins yield and purity.

5.3.8 Suitability of CCT domain of OSR1 and SPAK for NMR studies

In order to assess the suitability of CCT domain of OSR1 and SPAK for NMR structural studies, the ^1H - ^{15}N HSQC (Heteronuclear single quantum correlation)-NMR spectra of apo ^{15}N -OSR1 CCT domain as well as apo ^{15}N -SPAK CCT domain were initially obtained as they are required to assess the backbone structures and the count of amide resonance peaks of these proteins (**Figure 5.8 and 5.9**). The results indicated that both bacterially expressed CCT domains of OSR1 and SPAK are folded as shown by the dispersion of amide resonance peaks (6.5–10 ppm) ^1H -dimension (**Figure 5.8 and 5.9**). In addition, the observed uniform intensity of most of the amide resonance peaks suggested that the backbone is stable. However, there were some peaks with weak intensity indicating that these regions of the backbone have an intrinsic dynamic behaviour. The number of the backbone amide resonance peaks of CCT domains of OSR1 and SPAK were 92 cross peaks representing 100% of the total number of amino acid residues in both OSR1 CCT domain and SPAK CCT domain (**Figure 5.8 and 5.9**). The observed extra weak resonance peaks might be from the residual amino acids from the linker after GST cleavage. These results suggested that the CCT domain of OSR1 and SPAK are suitable for NMR studies.

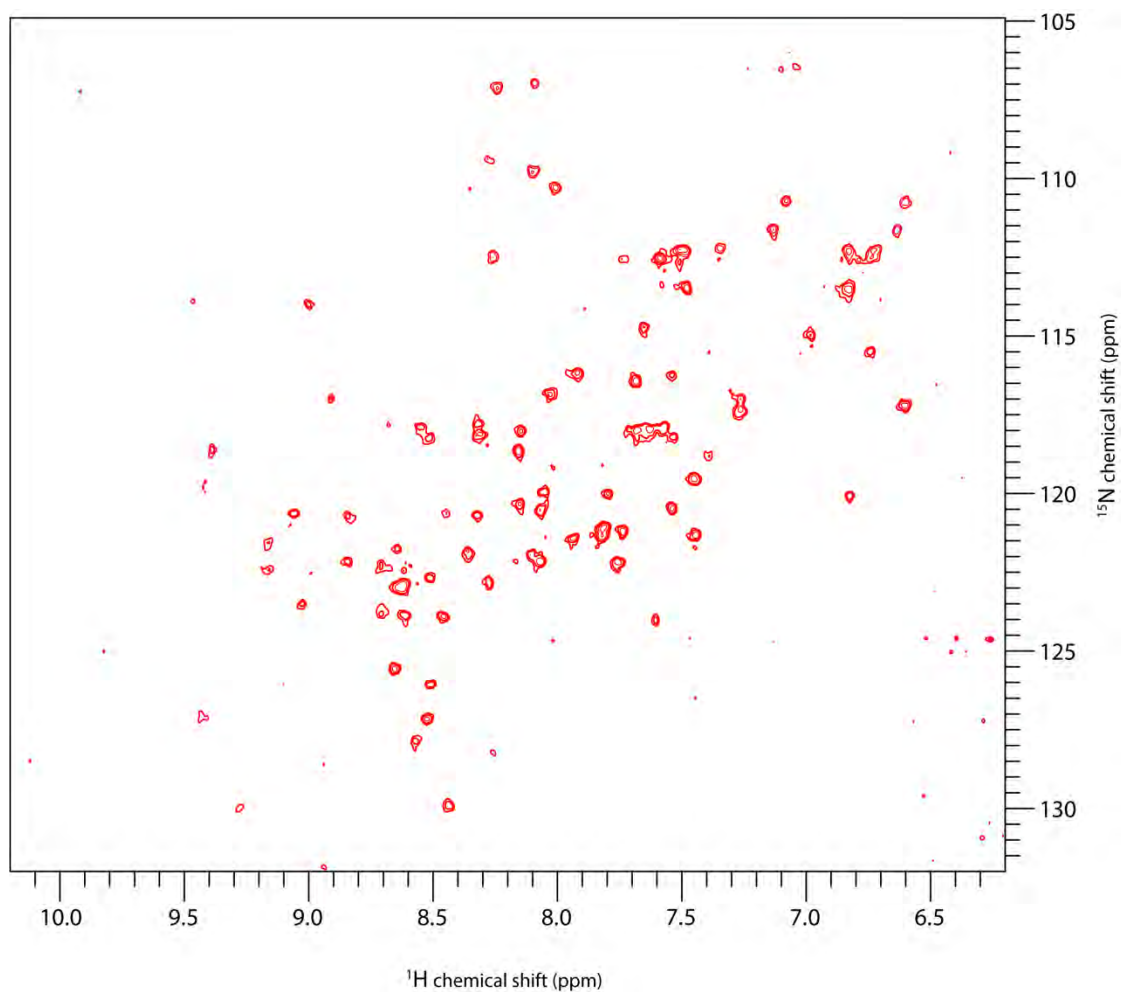


Figure 5.8: ^1H - ^{15}N HSQC spectrum of ^{15}N -OSR1 CCT domain. ^1H - ^{15}N HSQC spectrum of ^{15}N labelled OSR1 CCT domain (~ 0.2 mM) displays strong and even dispersion of amide backbone peaks. ^1H - ^{15}N HSQC spectrum was recorded in 50 mM Tris- d_{11} pH 7.4, 150 mM NaCl, 0.1% 2-mercaptoethanol at 25°C on a Bruker 600 MHz NMR spectrometer.

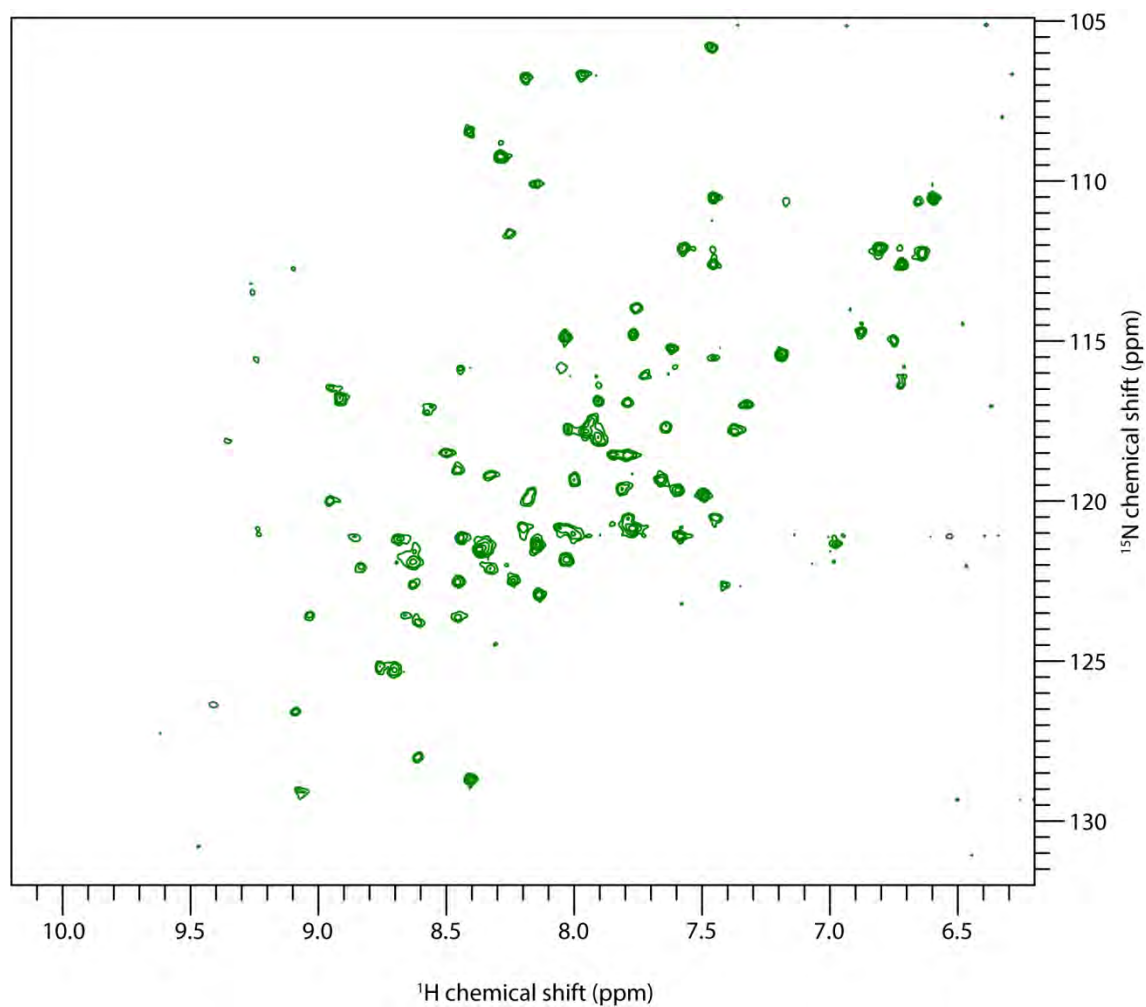


Figure 5.9: ^1H - ^{15}N HSQC spectrum of ^{15}N -SPAK CCT domain. ^1H - ^{15}N HSQC spectrum of ^{15}N labelled SPAK CCT domain (~ 0.5 mM) displays strong and even dispersion of amide backbone peaks. ^1H - ^{15}N HSQC spectrum was recorded in 50 mM Tris- d_{11} pH 7.4, 150 mM NaCl, 0.1% 2-mercaptoethanol at 25°C on a Bruker 600 MHz NMR spectrometer.

5.3.9 Sequence-specific ^1H , ^{13}C and ^{15}N backbone resonance assignments of the CCT domain of human OSR1

Subsequently, a sequential backbone assignment of the CCT domain of OSR1 was carried out in order to assign each resonance peak with its corresponding amino acid residue within OSR1 CCT domain amino acid sequence. ^{15}N and ^{13}C double labelled OSR1 CCT domain was expressed and purified from *E.coli* (**Figure 5.7d**). The assignment was obtained using TROSY versions of the triple resonance experiments in which HNCACB, HNCA, HN(CO)CACB and HN(CO)CA were used to establish the connectivity of α (CA), β (CB) carbon and HNCO and HN(CA)CO carbonyl (C') resonances for residues i and $i-1$ (see Materials and Methods section 2.6.5).

^1H - ^{15}N TROSY-HSQC of 10.250 kDa of OSR1 CCT domain was acquired on a Bruker 600 MHz NMR spectrometer at 25 °C and assigned as shown in **Figure 5.10**. The backbone amide resonances of 77 residues were assigned, representing 88% of the total 88 non-proline amino acid residues. Of the assigned amino acids, 100% include $\text{C}\alpha$, 91% include $\text{C}\beta$ and 99% C' chemical shifts (**Figure 5.11**). Due to intermediate exchange and broadening of the resonance, the backbone amide assignment of some residues was not possible including: Pro433, Ser433, Pro456, Gly457, Ala461, Pro493, Ser510, Asp511, Ile512 and Pro513 (**Figure 5.11**). Mapping the location of these unassigned residues onto the reported crystal structure of OSR1 CCT domain (PDB: 2V3S) revealed that some of these residues are located in flexible loop regions (**Figure 5.12**). In addition, the amide backbone assignment was not determined for Ile433, Val437, Ser498, Val499 and Ser525. However, the $\text{C}\alpha$, $\text{C}\beta$ and C' of some of the latter residues were assigned (**Figure 5.11**).

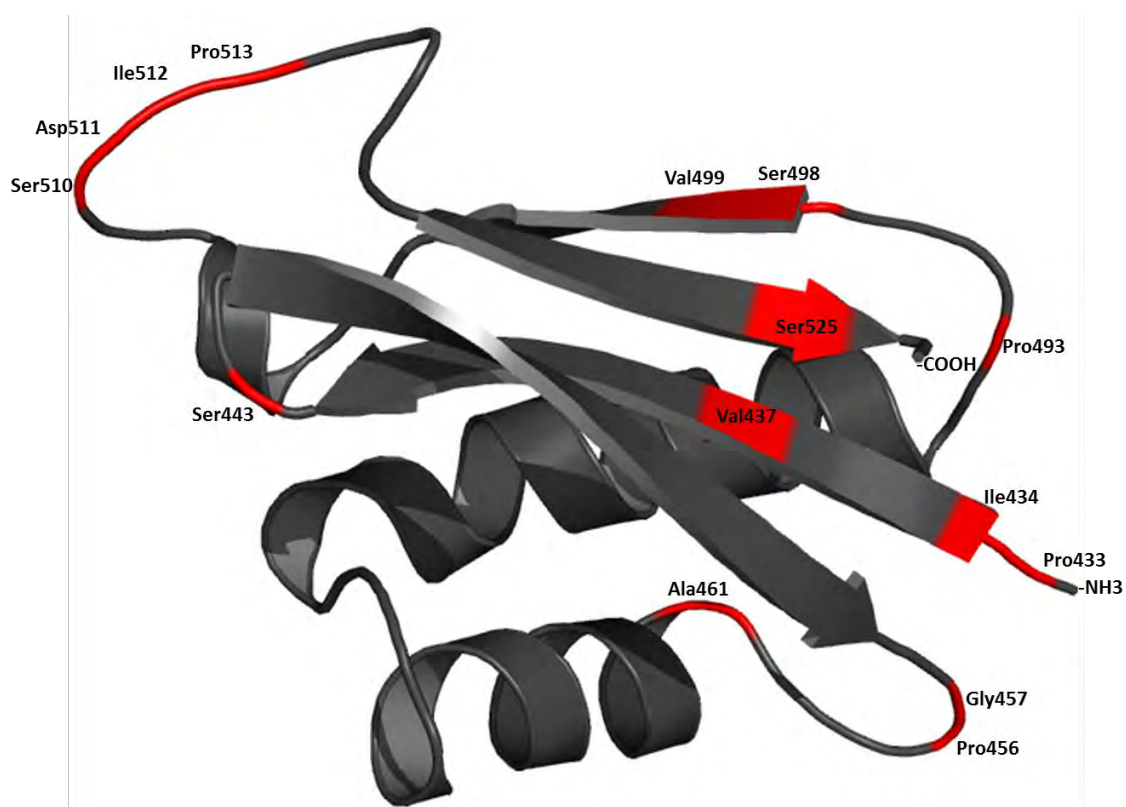


Figure 5.12: Mapping unassigned residues onto OSR1 CCT domain crystal structure (PDB: 2V3S). Regions in red correspond to unassigned amide resonances including proline residues. Pro433, Ser433, Pro456, Gly457, Ala461, Pro493, Ser510, Asp511, Ile512 and Pro513 residues are involved in unfolding flexible loops.

5.3.10 Chemical shift resonance of SPAK CCT domain is different than OSR1 CCT domain

To obtain the backbone assignment of the CCT domain of SPAK kinase, the aimed was to transfer the assignments from those acquired for the CCT domain of OSR1 CCT domain to the CCT domain of SPAK. Surprisingly, despite high sequence homology level between the CCT domain of OSR1 and SPAK, they are 79% identical in their primary amino acid sequences (**Figure 5.13a**), the backbone assignments of OSR1 CCT domain could not be transferred to SPAK. There were significant differences between both proteins chemical shifts when the ^1H - ^{15}N HSQC spectra were overlaid suggesting that although the overall secondary structure is likely to be the same they may differ somewhat in their folded conformations (**Figure 5.13b**).

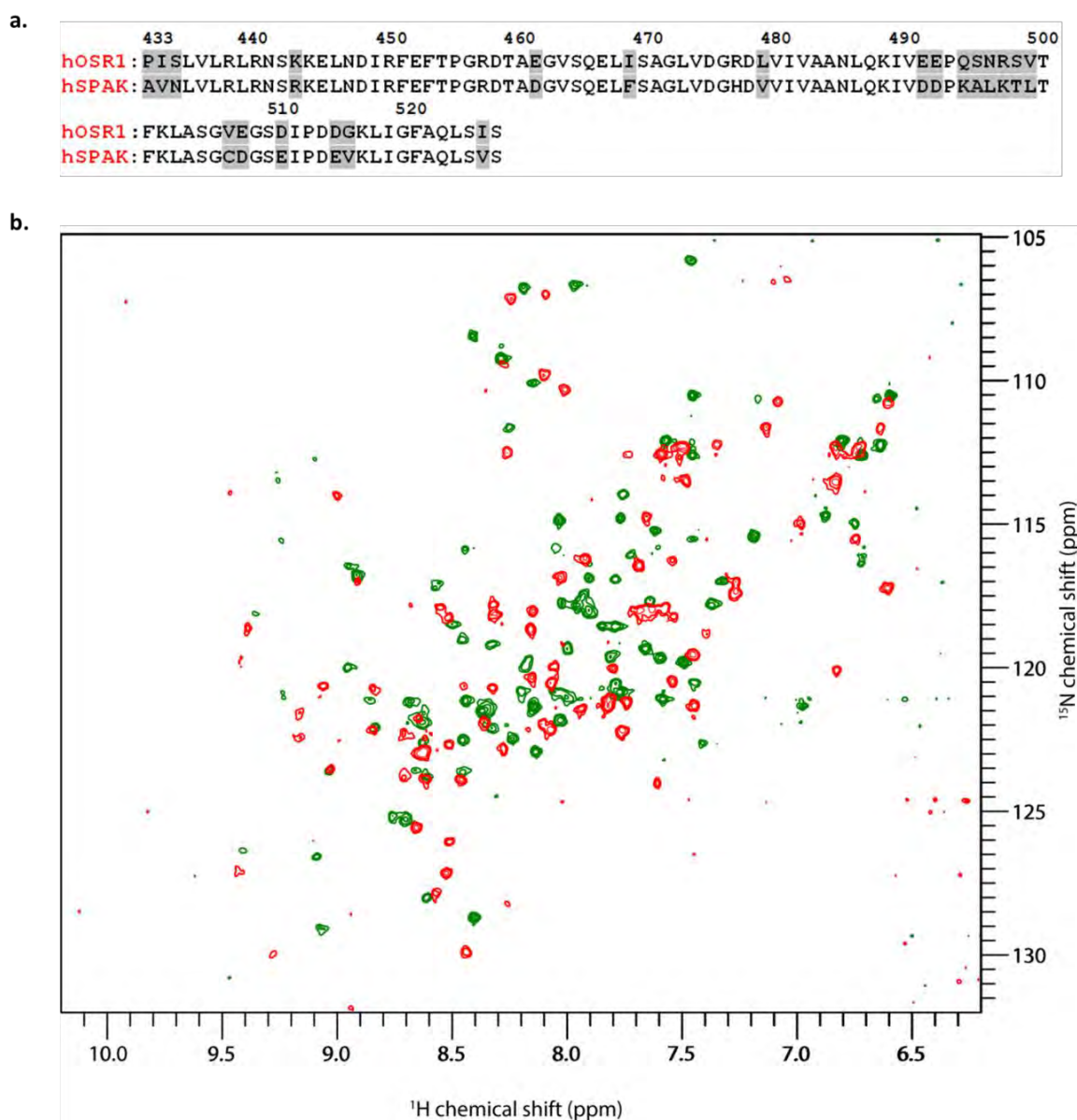


Figure 5.13: Comparison of homology sequence and ^1H - ^{15}N HSQC spectra of CCT domains of SPAK and OSR1. (a) Sequence alignment of human OSR1 and SPAK kinases. Un-conserved residues are highlighted in grey. (b) ^1H - ^{15}N HSQC spectrum of OSR1 CCT domain (red) overlapped with ^1H - ^{15}N HSQC spectrum of SPAK CCT domain (green). Both spectra were obtained under the same condition. OSR1 CCT domain assignments cannot be transferred to SPAK CCT domain as there are differences between their chemical shifts.

5.3.11 Chemical shift mapping

Chemical shift mapping (also called chemical shift perturbation (CSP)) is a commonly used protein-based NMR approach to confirm and characterise the binding of a ligand to a macromolecule in solution. This method tracks the changes in the chemical shift of a protein upon the addition of a ligand. Chemical shift mapping can be done by acquiring and comparing the two dimensional ^1H - ^{15}N HSQC (Heteronuclear single quantum correlation)-NMR spectra of a protein in the absence and presence of a ligand. ^1H - ^{15}N HSQC-NMR is highly sensitive to small changes in ligand and protein interactions (Williamson, 2013).

5.3.12 Assessment of RFQV, STOCK2S-26016 and Rafoxanide binding to OSR1 CCT domain by ^1H - ^{15}N HSQC

For further evidence on the suitability of OSR1 CCT domain for NMR structural studies, the binding of the RFQV, STOCK2S-26016 and Rafoxanide to the CCT domain of OSR1 was determined at a single concentration using ^1H - ^{15}N HSQC-NMR (see Materials and Methods section 2.6.6). The 18-mer RFQV peptide derived from WNK4 is known to bind to OSR1 CCT domain with high binding affinity (Vitari et al., 2006). STOCK2S-26016 is a SPAK CCT domain binder with a K_d value of 20 μM . It inhibits the WNK-signalling pathway by disrupting the binding of WNK to the SPAK kinase (Mori et al., 2013). Rafoxanide is a novel SPAK and OSR1 inhibitor that exerts its activity through the binding to the CCT domain of SPAK and OSR1 kinases (see Chapter III) (AlAmri et al., 2017a).

5.3.13 Chemical shift perturbation following the addition of RFQV peptide to ¹⁵N-labelled OSR1 CCT domain

The obtained results indicated that the RFQV peptide (CCPGCCGGSEEGKPQLVGR**RFQV**TSSK) induced large chemical shift perturbations when added to OSR1 CCT domain at 50 μ M final concentration (**Figure 5.14**). Additionally, some peaks, e.g. Arg451, can not be observed when the RFQV peptide was added indicating that this residue may be involved in dynamic exchange events or it shifts so far that it cannot be found (maybe under another peak) (**Figure 5.14**). The chemical shift perturbations (CSPs) was quantified and divided into three levels; small, medium and larger based on the degree of chemical shift perturbations (see Materials and Methods section 2.6.7). Accordingly, 12 residues were largely perturbed by addition of RFQV including: L440, N448, I450, F452, E453, F454, Q467, L468, A471, L473, A483, F501 (**Figure 5.15**). Interestingly, these residues, except L440, N448, are located in the primary pocket in agreement with previously reported results (Villa et al., 2007). Notably, L440, N448 are located in a close proximity to key residues involved in the topology of the primary pocket.

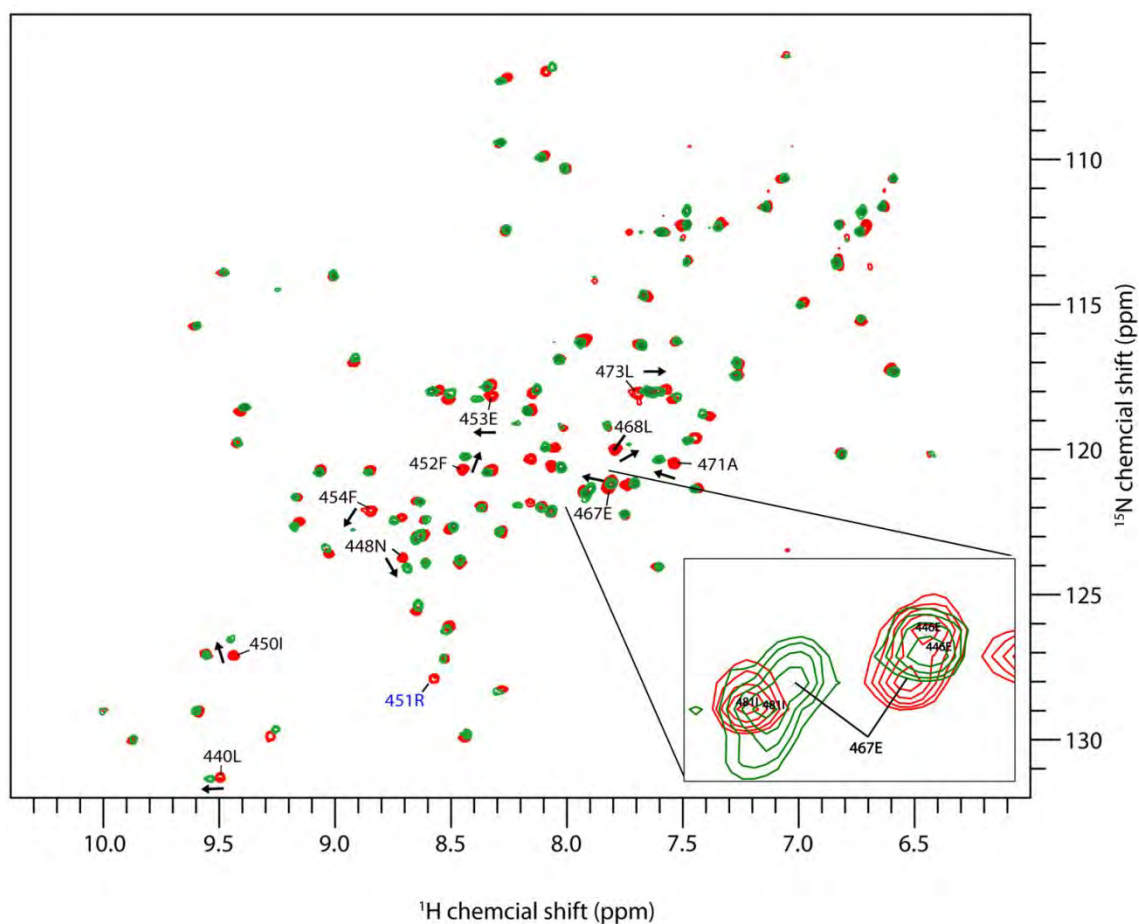


Figure 5. 14: Chemical shift perturbation following the addition of RFQV peptide to ^{15}N -labelled OSR1 CCT domain. The ^1H - ^{15}N HSQC spectrum of free OSR1 CCT domain (apo-protein) and after the addition of 50 μM RFQV peptide are shown in red and green, respectively. Residues with large chemical shift perturbations are labelled. The densely region around Glu467 residue is further expanded. Arg451 (blue) disappears when the RFQV peptide was added. The directions of chemical shift of some residues upon addition of RFQV peptide were labelled with black arrows indicating that the chemical shift changes are not due to DMSO effect.

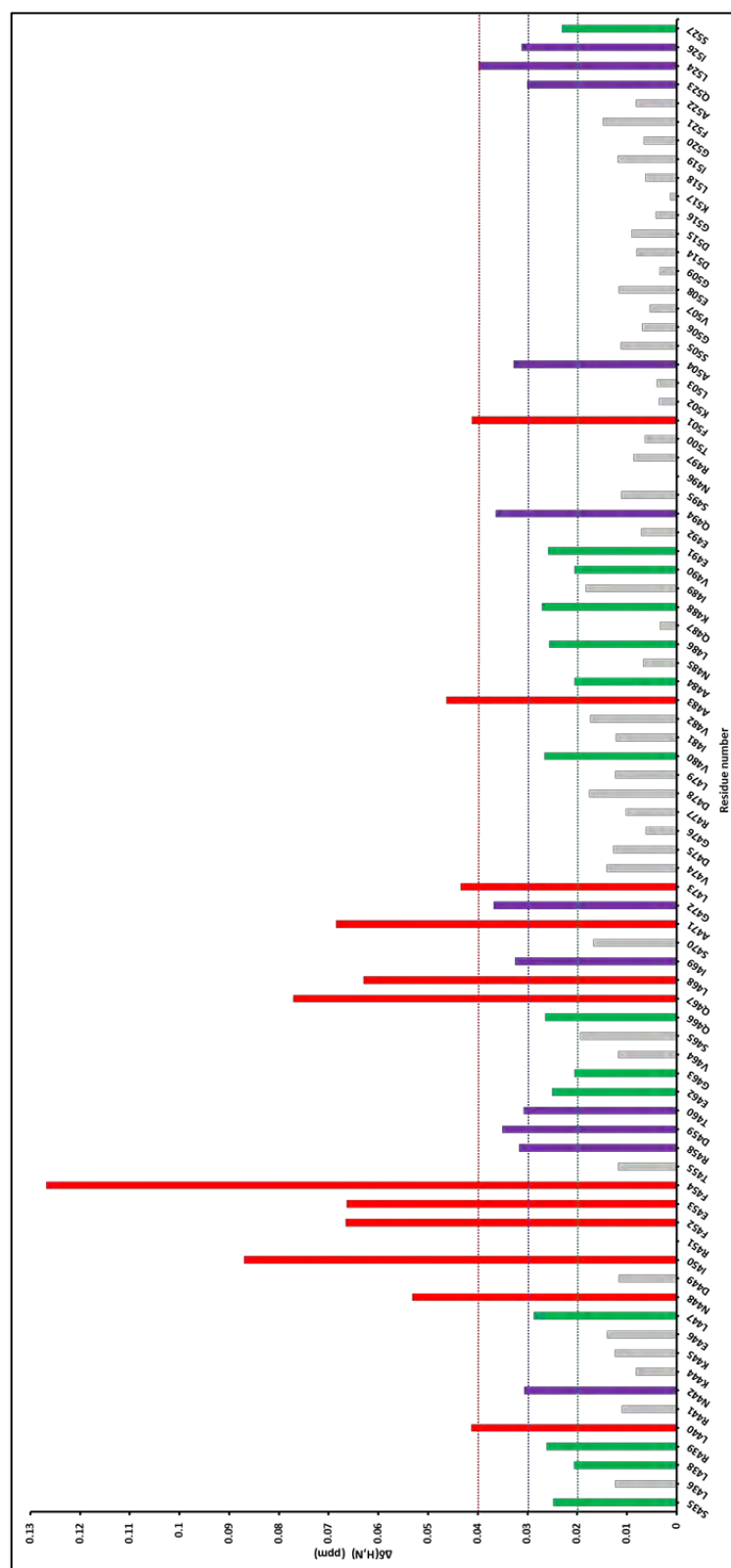


Figure 5.15: Chemical shift perturbations (CSPs) of human OSR1 CCT domain in presence of 50 μM RFQV peptide. The CSPs are plotted versus residue numbers. The dashed line in red, purple and green show cut-off $\Delta\delta > 0.04$ -, 0.03 - and 0.02 ppm indicating large, medium and small chemical shift perturbations, respectively.

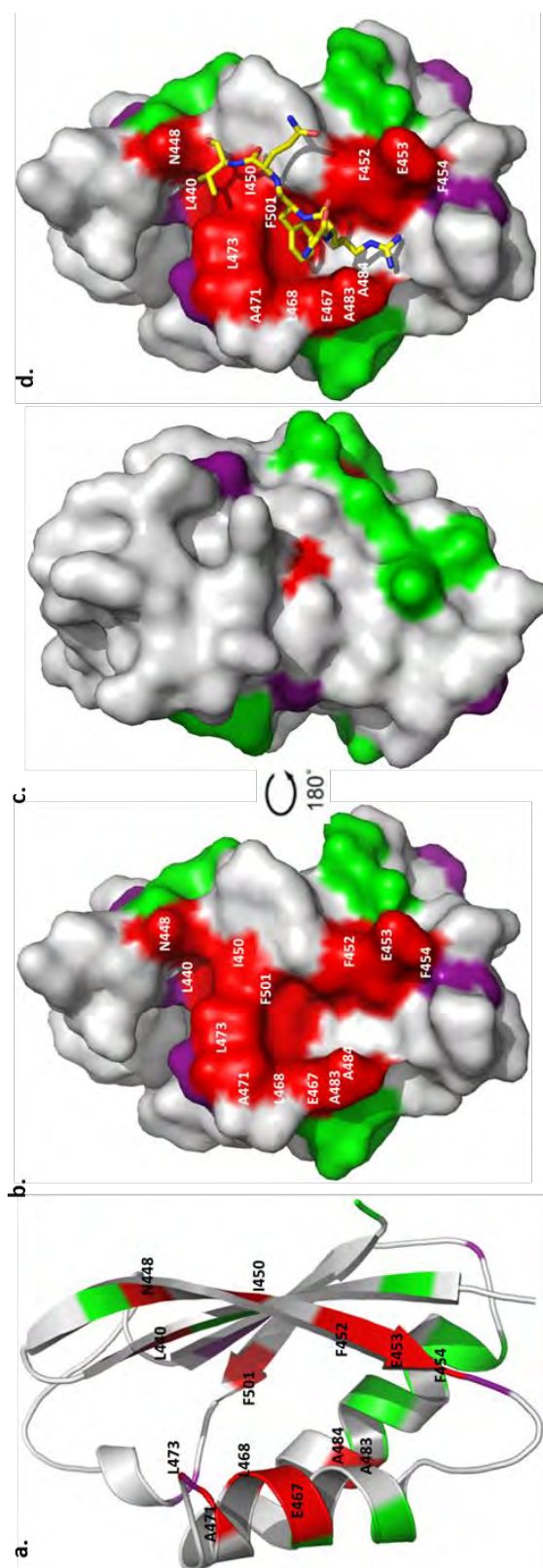


Figure 5.16: Mapping of spectral changes. Spectral changes on (a) a ribbon representation of OSR1 CCT domain (PDB:2V3S), (b) a surface representation in the same orientation, (c) a surface representation rotated by 180° around a vertical axis, (d) RFQV (yellow) binding mode to OSR1 CCT domain. Residues with larger chemical shift perturbations were labelled.

5.3.14 Chemical shift perturbation following the addition of STOCK2S-26016 and Rafoxanide to ^{15}N -labelled OSR1 CCT domain

In order to characterise the binding of STOCK2S-26016 and Rafoxanide, they were added to ^{15}N -OSR1 CCT domain at a final concentration of 200 μM in 5% (v/v) D₆-DMSO. Both compounds showed poor solubility profile in the NMR buffer (50 mM Tris- d_{11} pH 7.4, 150 mM NaCl, 5% D₆-DMSO). Nevertheless, both STOCK2S-26016 and Rafoxanide showed similar chemical shift perturbations pattern (**Figure 5.16a** and **5.16b**, respectively). The chemical shift perturbations (CSPs) of STOCK2S-26016 and Rafoxanide revealed that Lys517 was the most perturbed residue (**Figure 5.17a** and **5.17b**, respectively). Interestingly, this residue is located deep in the back of the secondary pocket (**Figure 5.18**). These results provide further evidence that these two compounds may bind to the secondary pocket as we hypothesised in Chapter III.

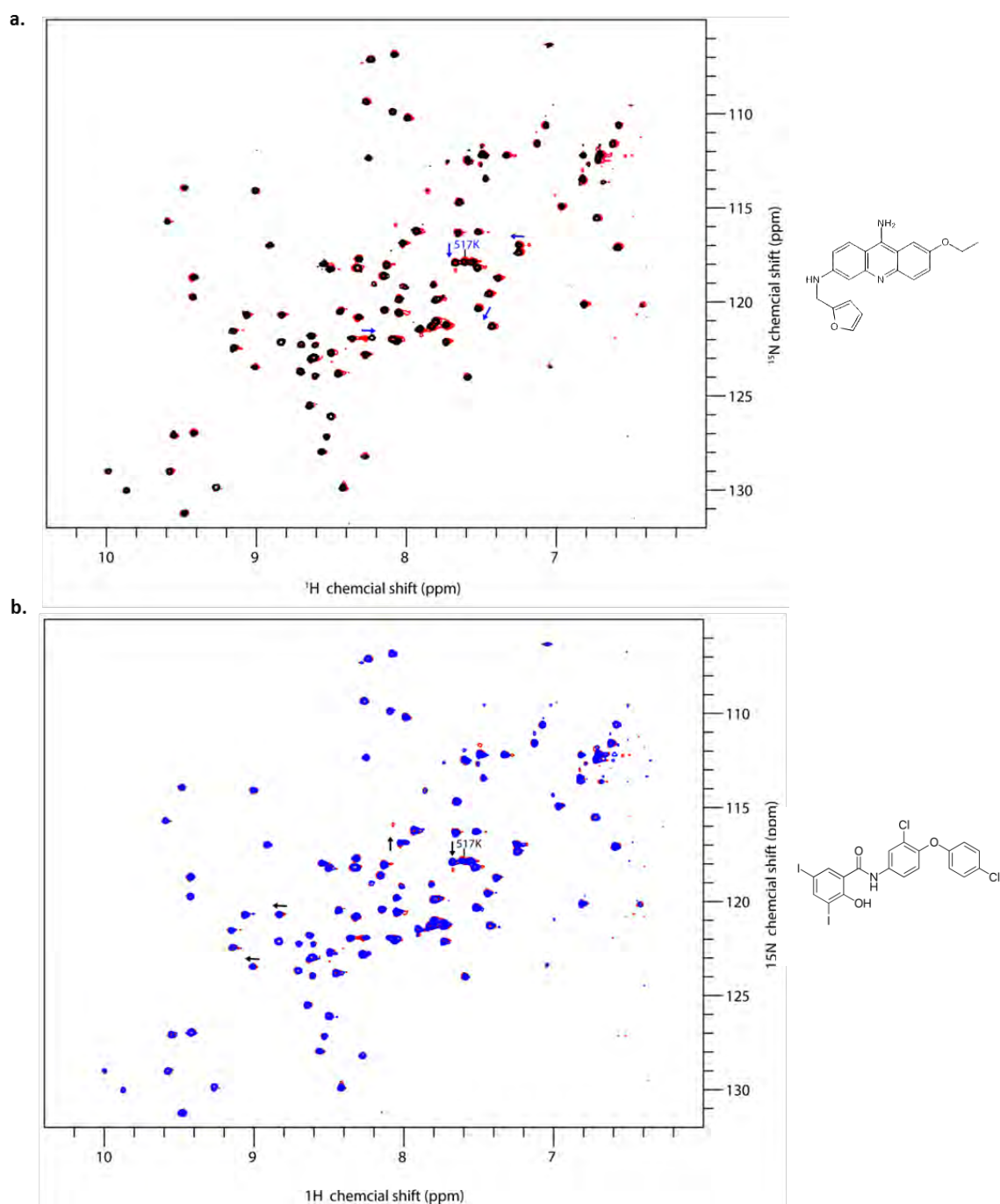


Figure 5.17: Chemical shift perturbation (CSPs) following the addition of STOCK2S-26016 and Rafoxanide. (a) The ^1H - ^{15}N HSQC of free OSR1 CCT domain (red) and after the addition of 200 μM STOCK2S-26016 (black). (b) The ^1H - ^{15}N HSQC of free OSR1 CCT domain (red) and after the addition of 200 μM Rafoxanide (blue). Lys517 was labelled. The directions of chemical shift of some residues upon addition of compounds were labelled with black arrows indicating that the chemical shift changes are not due to DMSO effect. Chemical structures of compounds are shown in the right panel.

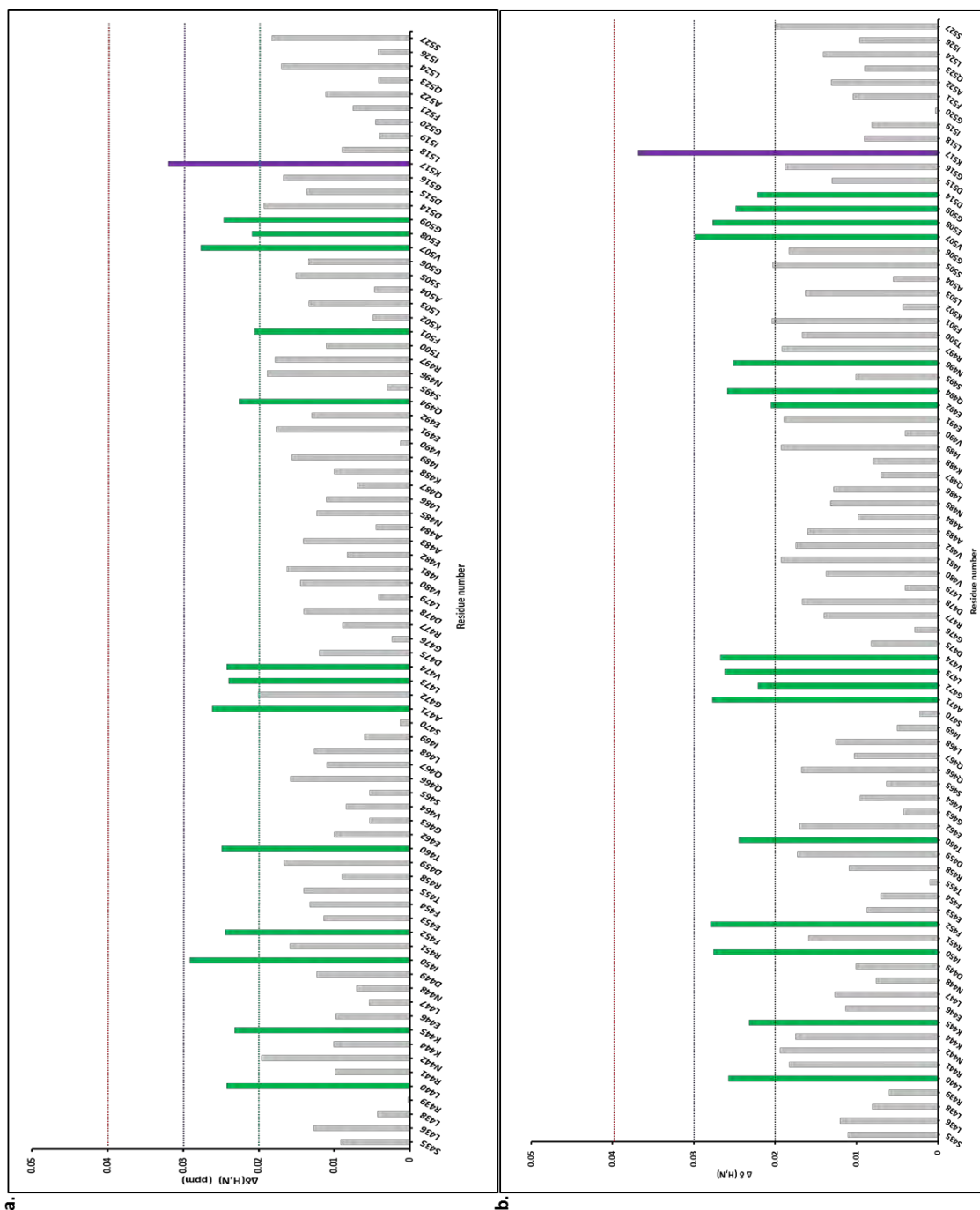


Figure 5.18: Chemical shift perturbations (CSPs) of human OSR1 CCT domain in presence of 200 μ M (a) STOCK2S-26016 and (b) Rafxanide. The CSPs are plotted versus residue numbers. The dashed line in red, purple and green show cut-off $\Delta\delta > 0.04$ -, 0.03 - and 0.02 ppm indicating large, medium and small chemical shift perturbations, respectively.

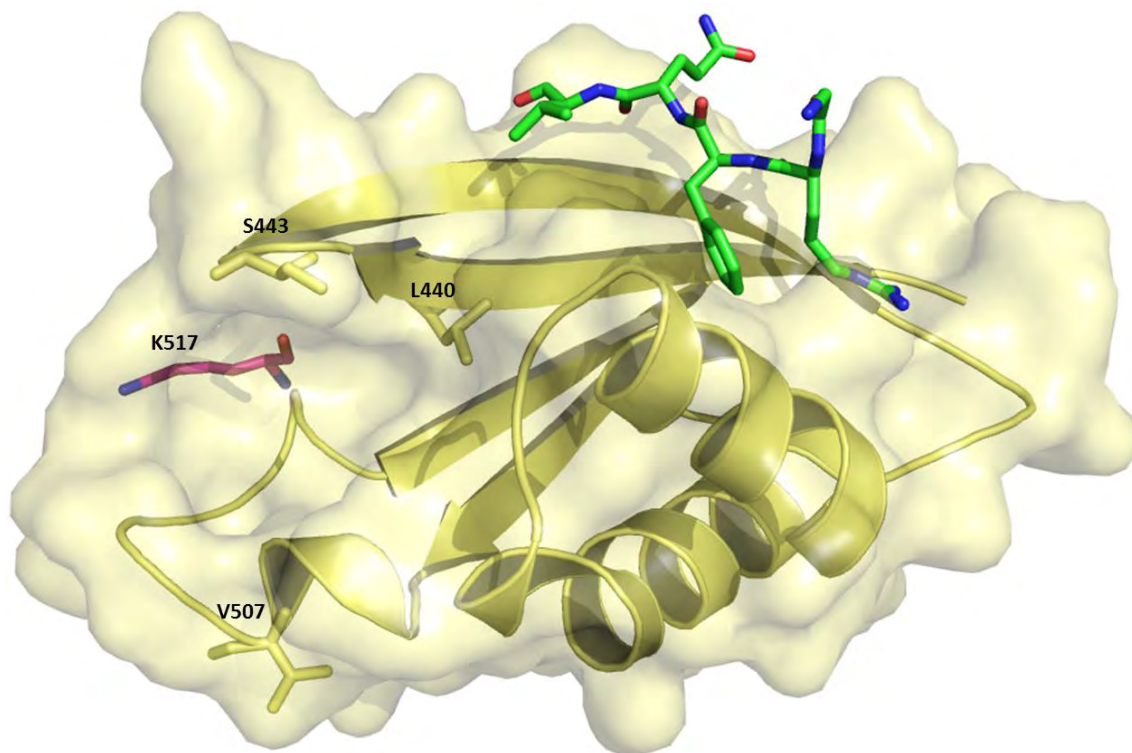


Figure 5.19: Location of Lys517 (K517) residue in the OSR1 structure. Mapping the location of K517 (purple) onto the crystal structure of OSR1 CCT domain (PDB:2V3S). K517 locates in the back of the secondary pocket of OSR1 CCT domain. Residues that line the secondary pocket (L440, S443 and V507) were shown in yellow sticks. RFQV peptide (green sticks) is binding to the primary pocket.

5.3.15 Assessment of fragment hits binding to OSR1 CCT domain by ^1H - ^{15}N HSQC

To further investigate the binding of the hit fragments obtained from the FBS to OSR1 CCT domain, ^1H - ^{15}N NMR heteronuclear single quantum coherence (HSQC) experiments were carried out in presence of hit fragments: 156, 179, 234, 330 and 383. These five compounds were selected from nineteen positive hit fragments and tested at a final concentration of 1 mM as shown in **Figure 5.20a** and **5.20b** for fragment number 156 and 179 and **Figure 5.21a** and **5.21b** for fragment number 234 and 330 and **Figure 5.22** for fragment number 383, respectively. Unfortunately, no changes in the chemical shifts were observed with all the tested fragment ligands indicating that the binding of these fragment ligands to the CCT domain of OSR1 is very weak.

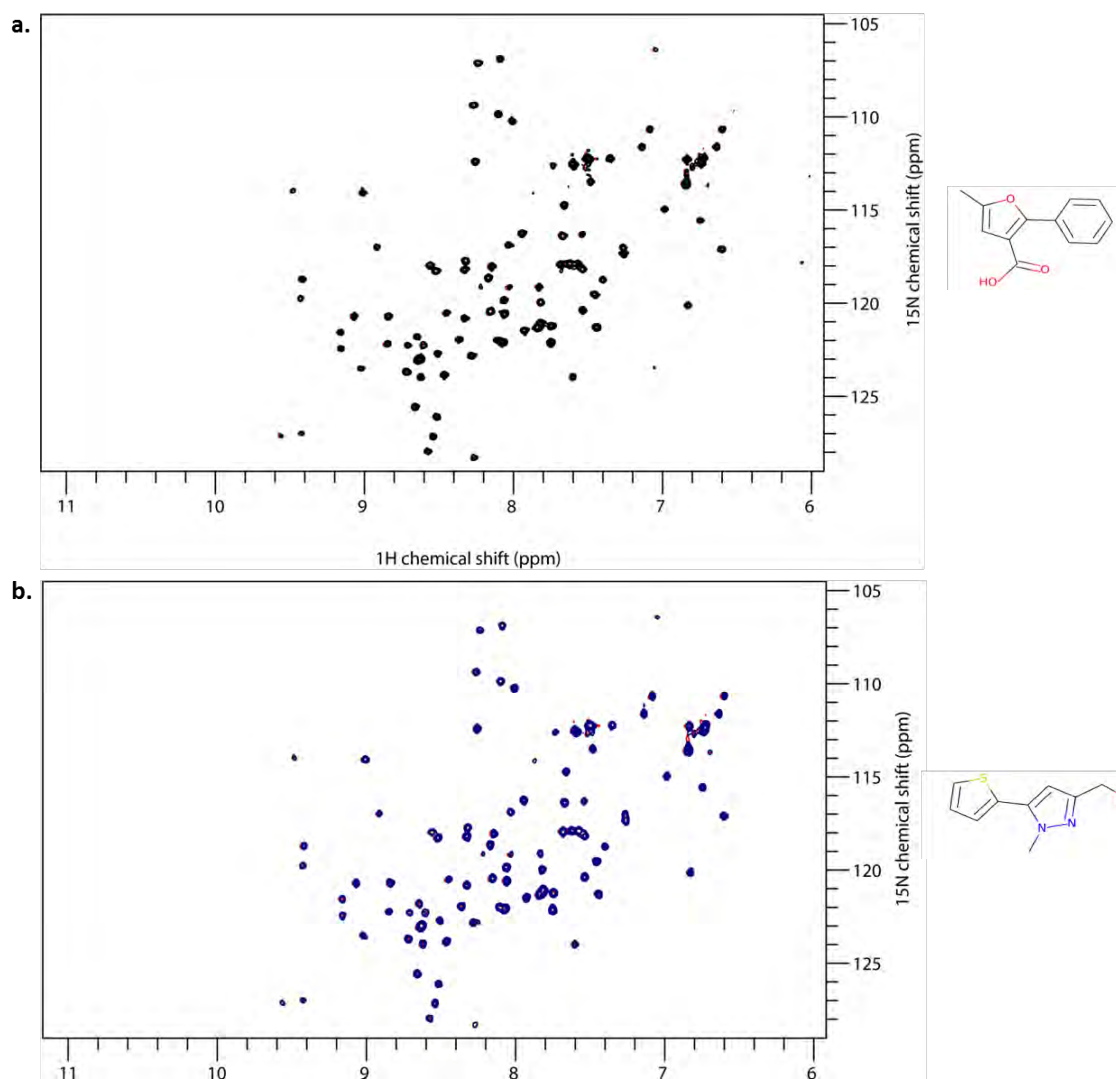


Figure 5.20: Chemical shift perturbation (CSPs) following the addition of 156 and 179. (a) The ^1H - ^{15}N HSQC of free OSR1 CCT domain (red) and after the addition of 1 mM 156 (black). **(b)** The ^1H - ^{15}N HSQC of free OSR1 CCT domain (red) and after the addition of 1 mM 179 (dark blue). Chemical structures of compounds are shown in the right panel

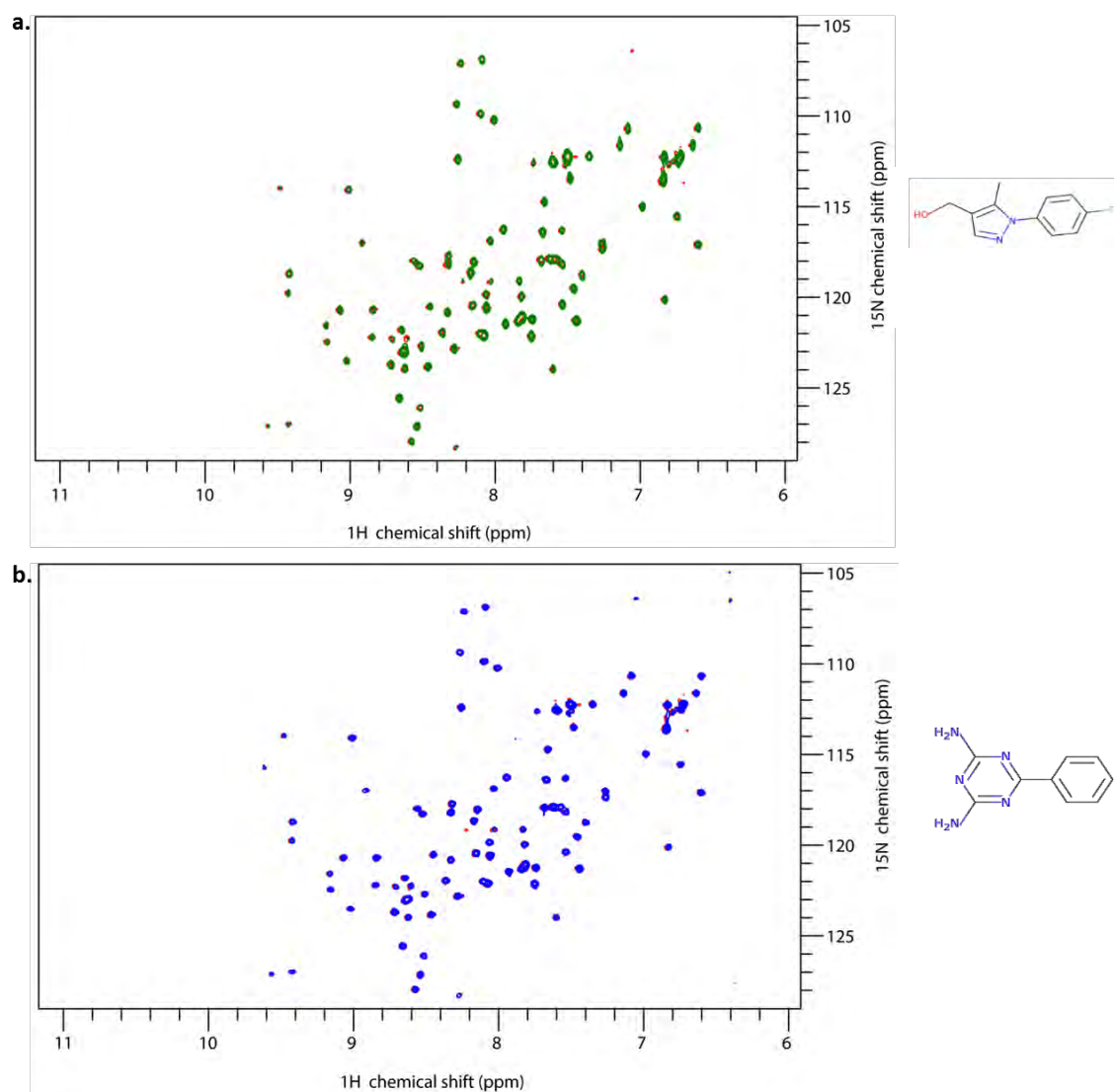


Figure 5.21: Chemical shift perturbation (CSPs) following the addition of 234 and 330. (a) The ^1H - ^{15}N HSQC of free OSR1 CCT domain (red) and after the addition of 1 mM 234 (green). (b) The ^1H - ^{15}N HSQC of free OSR1 CCT domain (red) and after the addition of 1 mM 330 (blue). Chemical structures of compounds are shown in the right panel.

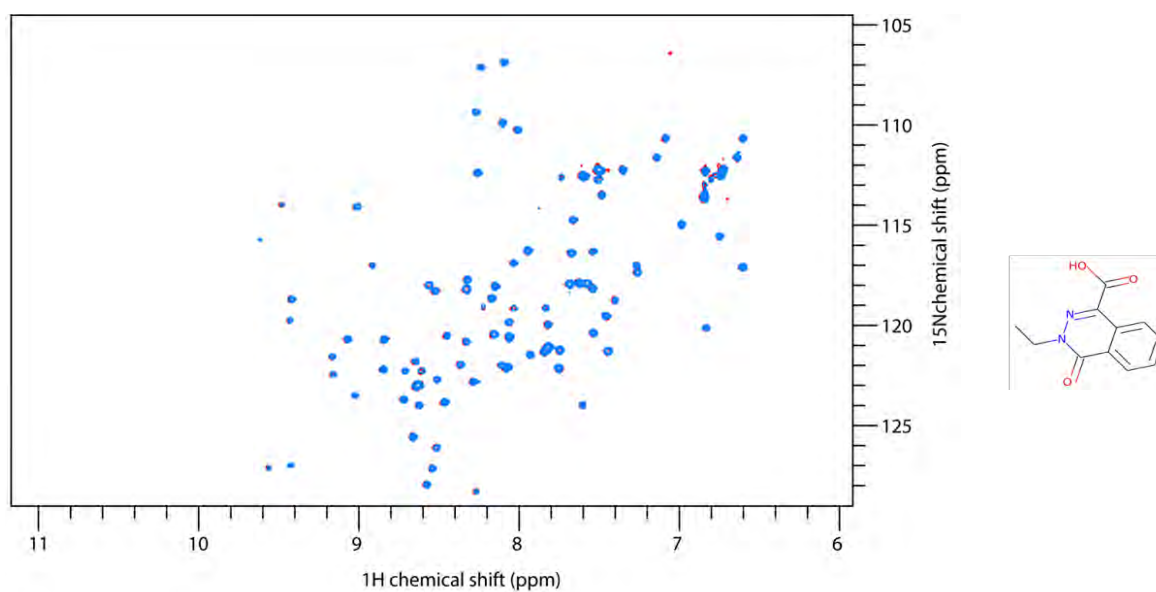


Figure 5.22: Chemical shift perturbation (CSPs) following the addition of 383. The ^1H - ^{15}N HSQC of free OSR1 CCT domain (red) and after the addition of 1 mM 383 (sky blue). Chemical structure of 383 is shown in the right panel.

5.3.16 OSR1 CCT domain secondary structure prediction based on NMR chemical shifts

Encouraged by the fact that 88% of the backbone assignments of the CCT domain of OSR1 were solved, the secondary structure of CCT domain of OSR1 was determined using TALOS+ (torsion angle likelihood obtained from shift and sequence similarity) (Shen et al., 2009a) and CSI (chemical shift index) (Hafsa et al., 2015) webserver. Both servers required the backbone assignments as input for empirical prediction of the dihedral angles phi and psi (see materials and methods 2.6.8).

A comparison of the OSR1 CCT domain secondary structure predicted by TALOS+ with the secondary structure defined by the OSR1 CCT domain crystal structure revealed that both structures have the same number and type of secondary structure elements with few differences in the C-terminal region (**Figure 5.23**). A major difference was that TALOS+ program predicted $\alpha 3$ prior to the $\beta 3$ whereas it was the opposite in the crystal structure of OSR1 CCT domain (PDB:2V3S). In the case of CSI (chemical shift index), the alpha helix ($\alpha 3$) is completely absent (**Figure 5.24**). The backbone amide group, C α , C' and C β of the amino acid residues forming the $\alpha 3$ helix (Pro493, Gln494 and Ser495) in TALOS+ secondary structure were assigned except the amide group of Pro493. Notably, the backbone amide group, C α , C' and C β of the amino acid residues corresponding to the $\alpha 3$ helix in the crystal structure (Ala505, Ser506, Gly507, Val508, Glu509) are also assigned. These results provided a new insight into the structure of OSR1 CCT domain in solution.

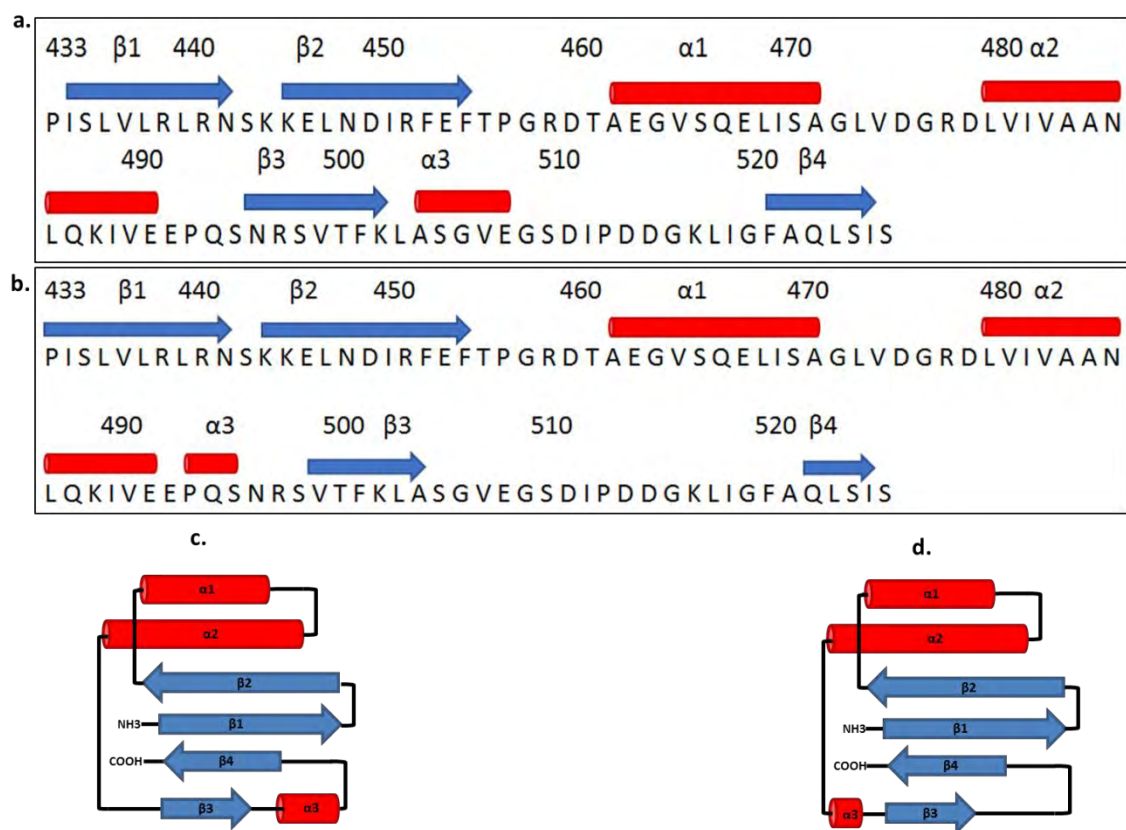


Figure 5.23: OSR1 CCT domain secondary structure prediction. The secondary structure of OSR1 CCT domain based on (a) and (c) X-ray crystal structure (PDB: 2V3S) and (b) and (d) TALOS+ webserver.

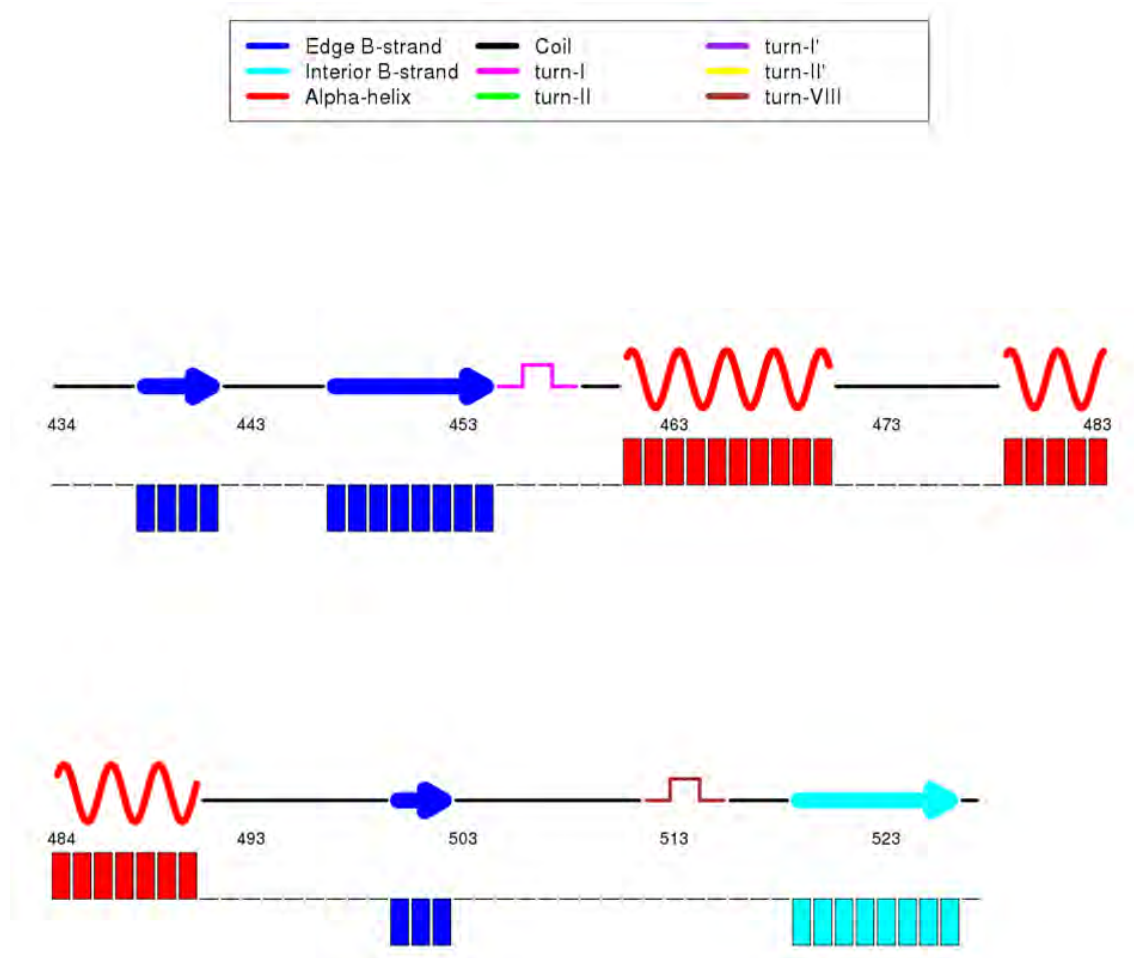


Figure 5. 24: OSR1 CCT domain secondary structure prediction. The secondary structure prediction for the OSR1 CCT domain based on the Chemical Shift Index (CSI) webserver using obtained chemical shift data.

5.3.17 Predication of OSR1 CCT domain 3D structure

Given the results in section 5.2.16, we next built a model of the CCT domain of OSR1 structure using the NMR chemical shift data that we have gathered. To achieve this, the Chemical-Shift-Rosetta (CS-Rosetta) webserver was used. CS-Rosetta is a robust fragment-based method for *de novo* protein structure generation based on $^{13}\text{C}\alpha$, $^{13}\text{C}\beta$, $^{13}\text{C}'$, ^{15}N , $^1\text{H}\alpha$ and ^1HN NMR chemical shifts (Shen et al., 2008). The main principle of CS-Rosetta is to simplify the protein fold into small peptide-fragments (typically 3 to 9 amino acid long) based on a library of known protein structures. In CS-Rosetta, this library is selected automatically based on the primary amino acid sequence for each modelled-protein (Gront et al., 2011). The same input file that was used for TALOS+ in section 5.2.16 was used to input into Rosetta. The best model structure of CCT domain of OSR1 with lowest energy score among the ten models obtained by CS-Rosetta is shown in **Figure 5.25a**. This structure was super imposed with the 1.005 Å RMS to the X-ray reference structure (PDB:2V3S) using PyMOL Molecular Graphics System 1.3 (**Figure 5.25b**). A comparison of the obtained CS-Rosetta three-dimensional model of CCT domain of OSR1 with OSR1 crystal structure indicated that both structures were very similar in their folding pattern with some differences that are notable particularly in the C-terminal region. A new structural element ($\alpha 4$) was predicted in CS-Rosetta model, and this was not observed in the TALOS+ secondary structure (**Figure 5.25a**) (see section 5.2.16). In the crystal structure, this region forms a long loop that is involved in the formation of the secondary pocket. However, the backbone assignments of the main residues that formed this $\alpha 4$ including: Ser510, Asp511, Ile512 and Pro513 residues were incomplete (**Figure 5.12**). The lack of complete assignment in this region may also be responsible for the observed change in the direction of the terminal region of OSR1 CCT

domain. Therefore, prediction within this region should be interpreted with caution. The location of $\alpha 3$ in the predicted model was between $\alpha 2$ and $\beta 3$ in agreement with the TALOS+ secondary structure (**Figure 5.25b**).

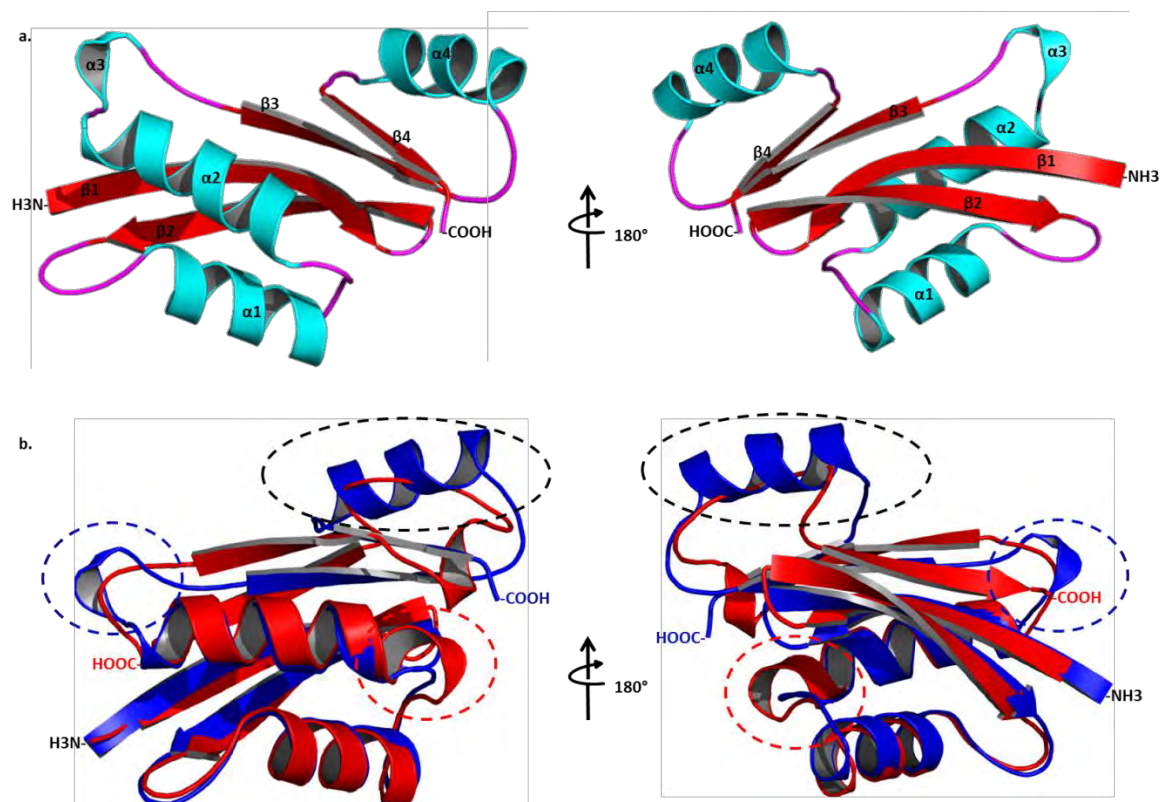


Figure 5.25: OSR1 CCT domain predicted Structure. (a) A ribbon representation of the lowest energy model generated by CS-Rosetta webserver using TALSO+ NMR chemical shift data. Structural elements were labelled. (b) A ribbon representation of superimposition of OSR1 CCT domain generated model (blue) to the OSR1 CCT domain X-ray crystal structure (PDB: 2V3S) (red). Regions in dash circles illustrated the position of $\alpha 3$ within the CS-Rosetta model (blue) and X-ray crystal structure (PDB: 2V3S) (red) of OSR1 CCT domain. Regions in black dash circles illustrated the position of new $\alpha 4$ within the CS-Rosetta model. The figure was prepared using PyMOL Molecular Graphics System 1.3.

5.3.18 Discussion

Nuclear magnetic resonance (NMR) spectroscopy is a powerful tool in drug discovery. In addition to the traditional uses of NMR as a biophysical method to elucidate the three-dimensional structures of molecules and the dynamics of bio-macromolecules as well as ligand-protein complex interactions in solution state, it is a valuable approach for the identification and characterisation of small molecule binders with weak binding affinity (Harner et al., 2013). NMR provides numerous advantages over other methods, such as the ability to study the ligand and protein interactions using both ligand-based and protein-based approaches (Sugiki et al., 2018).

In this chapter, the efforts to identify novel inhibitors of WNK signalling pathway by targeting the CCT domain of the two closely related kinases, SPAK and OSR1, using the NMR-fragment-based approach were described. Moreover, NMR structural studies were performed to characterise and validate the binding of potential fragment ligands as well as to determine the OSR1 CCT domain secondary and tertiary structures using NMR chemical shifts data.

The CCT domains of both SPAK and OSR1 emerged as valuable target to inhibit SPAK and OSR1 and reduce blood pressure (see Chapter III) (Zhang et al., 2015). The molecule weights of the CCT domain of SPAK (425-545) and OSR1 (433-527) are 13,069.63 kDa and 10,251.63 kDa, respectively, making them suitable for NMR structural studies as NMR is ideally suited to the study of proteins with molecule weights of <30 kDa (Billeter et al., 2008). However, the NMR-fragment based screening methods, particularly the STD (Saturation transfer difference)-NMR, are more reliable for large proteins (molecule weight of ≥ 20 kDa) as the spin diffusion (the process of transferring the magnetisation from the protein into small molecule) is more efficient with

larger proteins (Venkitakrishnan et al., 2012). Therefore, the screening was conducted against GST-tagged OSR1 CCT domain (36.251 kDa) as well as against GST-tag (26 kDa) to eliminate any potential GST binders.

From the screening, nineteen fragment ligands with diverse chemical scaffolds were identified as binders of OSR1 CCT domain (Table 5.2). One ligand only, 383, out of the nineteen fragment ligands did not bind in the presence of the 18-mer RFQV peptide suggesting that compound 383 may bind to the primary pocket. Therefore, compound 383 could be used as a seed for developing WNK and SPAK/OSR1 binding inhibitors that target the primary pocket. The other 18 fragment ligands were unaffected by the presence of the 18-mer RFQV peptide indicating that they might bind to different site within the CCT domain of OSR1. This could be the secondary pocket or they just bound the primary pocket in tandem with the RFQV peptide. Conclusive determination of the exact binding site of each fragment requires co-crystallisation of each fragment with OSR1 CCT domain.

In the attempt to determine the inhibitory effect of novel binders of the CCT domain of OSR1, an *in vitro* kinase assay against both SPAK and OSR1 FL kinases was conducted for selected fragment ligands at different concentrations up to 5 mM. Unfortunately, none of these fragment ligands showed any activity (**Figure 5.5**). Since the sensitivity of NMR to weak binders is approximately ≤ 10 mM (Powers, 2007), The functional assay results suggested that the binding of these fragment ligands to OSR1 CCT domain is very weak. However, a robust binding affinity of these fragment ligands using suitable binding assay e.g. SPR is essential to validate this conclusion. The efforts to obtain the binding affinity (Kd) of the confirmed fragment hits using SPR was hampered as the fragments are very small and measuring the mass increase on binding of

the fragments by SPR was challenging. To solve this issue, the amount of proteins attached to the surface must be high enough to increase the number of binding sites for the ligand (Patching, 2014). The GST antibody approach (for GST-OSR1 CCT) gave insufficient coverage on the chip to allow the binding of the fragments to be detected above the noise. Accordingly, an OSR1 CCT domain construct with biotin tag is needed in order to get sufficient coverage (Nguyen et al., 2015).

In order to improve the *in vitro* activity of these fragment ligands, hybrid molecules which consist of two chemically connected fragments were designed and obtained (Bérubé, 2016). However, this strategy did not help and all tested molecules turned to be inactive (**Figure 5.6**). Whereas the fragments linking (hybrid-molecule designed) is a common strategy in the optimisation of hit fragments, fragments growing using chemical synthesis is a more successful approach (Mondal et al., 2015). In addition, obtaining the crystal structures of the individual fragments bound to the protein would help in determination whether the linked fragments are binding to the same or close binding sites.

In the next part of the work, the focused was on the NMR protein-based studies. ^{15}N isotopically labelled CCT domain of SPAK and OSR1 kinases were successfully expressed and purified from E.coli. Additionally, their suitability for NMR structural analysis using typical ^1H - ^{15}N NMR heteronuclear single quantum coherence (HSQC) experiment at physiological pH 7.4 at 25 °C were shown. The CCT domain of OSR1 was pursued as a primary target because its bacterial expression profile is superior to SPAK CCT domain in terms of yield as well as its X-ray structure is already reported which could be useful as a reference for structural analysis studies (Villa et al., 2007). Accordingly, a double labelled ^{15}N - ^{13}C enriched OSR1 CCT domain was purified and

subsequently 88 % of the backbone amide resonances were assigned. The unassigned residues are located mostly within unstructured or unfolded regions. Indeed, long unfolded or unstructured regions within a protein are known to result in spectral overlap at the centre of the amide proton spectral region as the corresponding residues are in similar chemical environments (Frueh, 2014).

Although the CCT domain of both kinases is homologous in primary amino acid sequence and function, the backbone assignments of OSR1 CCT domain cannot be transferred to SPAK CCT domain as critical differences between their ^1H - ^{15}N HSQC spectra were observed. In fact, the backbone chemical shift data provides more structural information than amino acid sequence similarity (Shen et al., 2009b). Therefore, solving the structure of the CCT domain of SPAK is essential as it might provide more insight into the structural and functional differences between SPAK and OSR1 kinases.

Furthermore, chemical shift mapping studies of different ligands against OSR1 CCT domain were conducted. The 18-mer RFQV peptide, derived from WNK4 kinase, induced large chemical shift perturbations (CSP) to a number of amino acids mainly in the primary pocket within the OSR1 CCT domain. This indicated that the binding of the RFQV peptide may induce a large conformational changes in the CCT domain of OSR1 (and presumably SPAK) in agreement with previously reported results (Villa et al., 2008). Consistent with this, some cross peaks disappeared when the RFQV peptide was added, likely due to changes in the dynamics of the protein. The obtained results also provided further evidence on the binding of STOCK2S-26016 and Rafoxanide to the secondary pocket of OSR1 CCT domain. However, the poor solubility profiles of STOCK2S-26016 and Rafoxanide hindered the efforts in obtaining robust results from the 1D NMR-STD as well as 2D ^1H - ^{15}N -HSQC binding experiments.

On the other hand, despite the fact that they tested positive in the NMR-STD experiments, tracking the binding of identified fragment hits from the fragment-based screening using ^1H - ^{15}N -HSQC binding experiment was not possible. Whereas the protein-based experiments, e.g. HSQC, gave more reliable binding data, their sensitivity was less than ligand-based experiments, e.g. STD-NMR (Barile and Pellecchia, 2014).

Using the chemical shift data, the secondary structure of the CCT domain of OSR1 was determined. Interestingly, the calculated secondary structures using two webserver, TALOS+ and Chemical Shift Index (CSI), were similar to that of the crystal structure to certain extent with some differences in the position of alpha helix 3 ($\alpha 3$). However, the presence of unassigned long sequence (Ser510, Asp511, Ile512 and Pro513 residues) next to $\alpha 3$ helix (Ala505, Ser506, Gly507, Val508, Glu509) may cause the observed differences between both structures. Consistent with this, the predicted 3D of OSR1 CCT domain using CS-Roseatta webserver indicated that these short peptide sequences (Ser510, Asp511, Ile512 and Pro513 residues) are involved in forming a new alpha helix, which was defined as $\alpha 4$. However, prediction within this region should be interpreted with caution.

In conclusion, in this chapter established the suitability of CCT domains of SPAK and OSR1 for NMR studies was established. Several fragment ligands were identified as binders to SPAK and OSR1, which could be exploited as seeds for building molecules with high binding affinity to these two proteins. Additionally, the CCT domains of OSR1 and SPAK show differences in their overall conformation whilst likely retain the same global fold. Importantly, the backbone assignments of OSR1 CCT domain was solved which will facilitate ligands-OSR1 complex studies in the future.

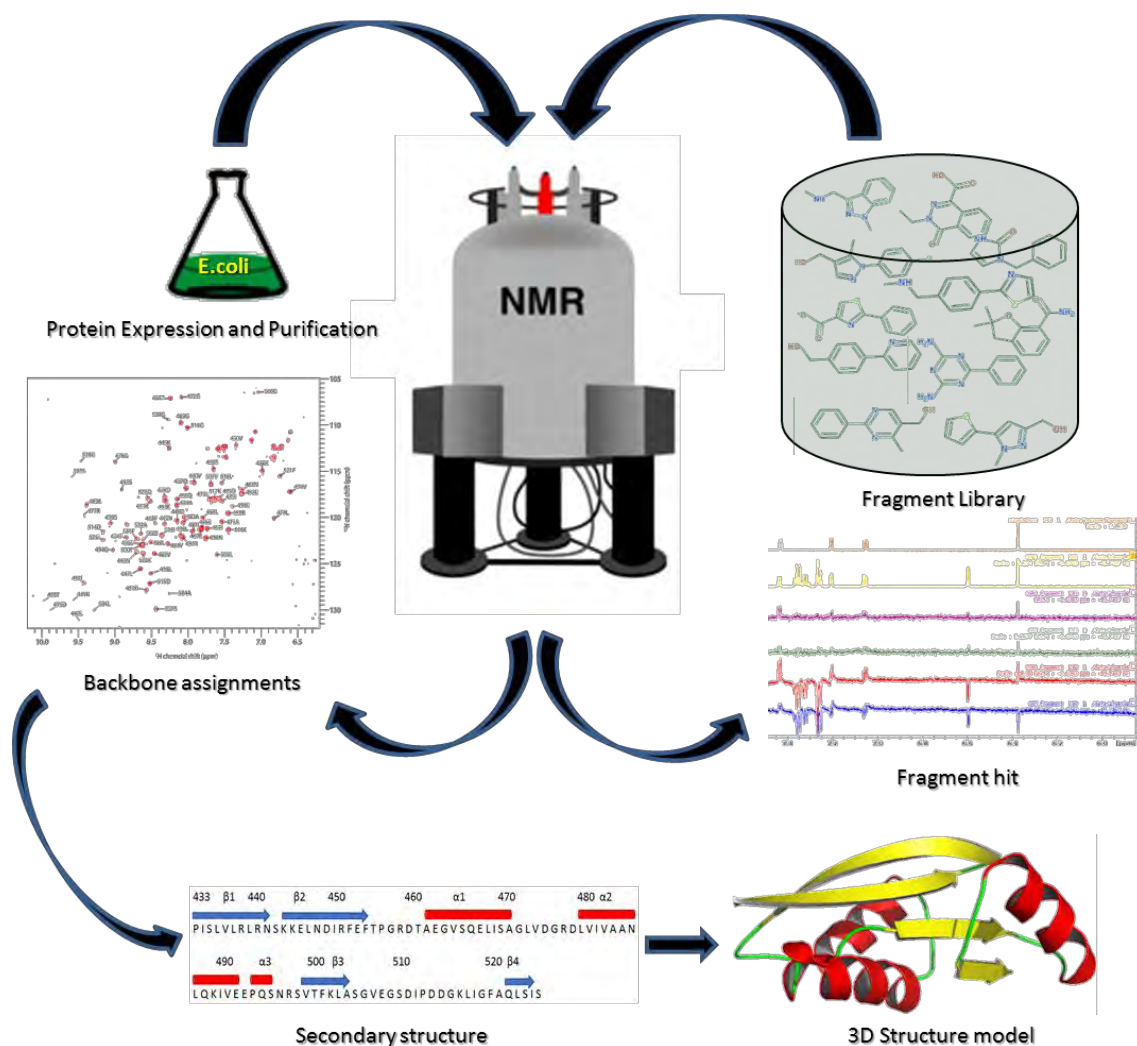


Figure 5.26: Graphical conclusion. NMR spectroscopy is a powerful tool in Drug discovery. NMR involves key steps such as preparation of fragment library and expression and purification of unlabelled and uniformly labelled proteins for fragment library screening (ligand-based NMR studies) and NMR structural studies (protein-based NMR studies), respectively. Novel fragment ligands were identified as binders to the CCT domain of OSR1 kinase using STD-NMR and waterLOGSY. The backbone assignments of OSR1 CCT domain was solved and used to determine its secondary and three-dimensional structure using TALOS+ and CS-Rosetta web servers, respectively.

CHAPTER VI: GENERAL CONCLUSIONS AND FUTURE WORK

SPAK and OSR1 are two structural and functional homologue serine/threonine-protein kinases. Both kinases play essential roles in the regulation of electrolyte homeostasis, body fluid and thus blood pressure. They act as intermediate kinases within WNK-SPAK/OSR1 signalling pathway in which their functions are regulated by the upstream WNK kinases. SPAK and OSR1 kinases ultimately regulate the functions of downstream membrane cation-chloride cotransporters (CCCs) e.g. NCC, NKCC1 and NKCC2 by phosphorylation. Genetically, gain of function mutations in WNK kinases as well as loss of function mutations in their regulators such as KLHL3 and CUL3, have been shown to cause high blood pressure in humans. Various WNK, SPAK and OSR1 animal studies have validated the essential role of this signalling cascade in the pathogenicity of this condition. Therefore, targeting SPAK and OSR1 emerged as a novel strategy in the discovery of novel antihypertensive agents.

This thesis described efforts aimed at identifying novel inhibitors of SPAK and OSR1 as potential antihypertensive agents via several drug discovery approaches. These included structure-based virtual screening (SBVS), high-throughput screening (HTS) and NMR-based fragment screening (NMR-BFS). In Chapter III, the focus was on the C-terminal domains of SPAK and OSR1 as it is the site that mediates their interaction with both upstream activators, WNK kinases, and downstream substrates, ion co-transporters. Consistently, mutations within the secondary pocket of the CCT of OSR1 reduced its kinase activity significantly. This observation provided valuable evidence on the amenability of this site to be targeted with small molecule inhibitors. Using structure-based virtual screening, Rafoxanide -an FDA approved anti-parasitic agent- was identified as inhibitor of SPAK and OSR1. The data showed that Rafoxanide bound the secondary pocket within the CCT of SPAK and OSR1. Consistently, using NMR

chemical shift perturbation studies, Rafoxanide was shown to interact, mostly, with Lys512 which is located deep in the secondary pocket with no significant effects on the residues within the primary pocket. Additionally, biochemical, computational and NMR data suggested that most of the published SPAK and OSR1 inhibitors, such as STOCK1S-50699 and STOCK2S-26016, are binding to the secondary pocket.

In Chapter IV, several FDA-approved drugs were discovered as inhibitors of SPAK and OSR1 kinases via the screening of FDA chemical library of small molecules. This led to the identification of Verteporfin as a potent non-ATP competitive inhibitor of SPAK and OSR1 kinases. To date, Verteporfin is the most potent allosteric inhibitor of SPAK and OSR1 kinases with good kinase selectivity profile. Molecular modelling studies revealed that Verteporfin bound OSR1 at a novel binding site within the domain-exchanged kinase dimer.

In Chapter V, NMR spectroscopy was used to screen an in-house library of fragments. This led to the identification of several fragments as binders to the C-terminal domain of OSR1. Although some of these fragments bound to unknown site(s) within the CCT domain of OSR1, compound 383 was shown to bind the primary pocket. This fragment could in the future be used in the design of new and potent WNK-SPAK/OSR1 inhibitors that bind the primary pocket. In addition, the suitability of the CCT domain of both kinases, SPAK and OSR1, for NMR structural studies was determined. Accordingly, the backbone assignment of isotopically labelled OSR1 CCT domain was solved. Notably, the backbone assignment of OSR1 CCT domain could not be transferred to SPAK CCT domain as there were large differences in their chemical shifts data. Using the NMR chemical shifts, the secondary structure and a data-driven 3D structure model of OSR1 CCT were obtained. Encouragingly, the secondary structure and three-

dimensional model of OSR1 CCT domain were similar to those reported for the crystal structure of OSR1 CCT with slight differences in the *C*-terminus region.

Summary of key and novel discoveries made in this work:

1. The identification of the secondary pocket in the *C*-terminal domain of SPAK and OSR1 kinases as an allosteric site that modulates their kinase functions.
2. The discovery of several potent non-ATP competitive inhibitors of SPAK and OSR1 kinases, some of which such as Rafoxanide, Verteporfin, Toremifene and β -Escin are clinically used.
3. Solving the backbone assignment of OSR1 CCT domain by NMR.
4. Shedding light into the differences in the folding patterns of both SPAK and OSR1 CCT domains, a previously unknown phenomenon.

Together, these findings contributed significantly in advancing the understanding of the SPAK and OSR1 kinases.

Future work

For future work, robust mutagenesis studies to investigate the role of residues that line up the secondary pocket as well as the domain-swapped dimer on the activity of SPAK and OSR1 might be necessary to validate the critical role of the secondary pocket on the function of SPAK and OSR1 and the binding site of Verteporfin, respectively. Furthermore, obtaining the binding affinity (K_d) of the identified small-molecule inhibitors and fragment binders to either CCT domains of OSR1 and SPAK as well as to full length proteins using appropriate biophysical binding techniques such as surface plasmon resonance (SPR) or isothermal titration calorimetry (ITC) is another aim to be

considered. Co-crystallisation of these inhibitors and fragment binders, or some of them, with SPAK and OSR1 is a necessary task to verify their binding mode and facilitate their medicinal chemistry structural optimisation. *In vivo* characterisation of the activity of the identified inhibitors particularly Rafoxanide and Verteporfin on normotensive and hypertensive animal models might be required for further validation of their effects on blood pressure.

REFERENCES

- ALAMRI, M. A., KADRI, H., ALDERWICK, L. J., SIMPKINS, N. S. & MEHELLOU, Y. 2017a. Rafoxanide and Closantel Inhibit SPAK and OSR1 Kinases by Binding to a Highly Conserved Allosteric Site on Their C-terminal Domains. *ChemMedChem*, 12, 639-645.
- ALAMRI, M. A., KADRI, H., DHIANI, B. A., MAHMOOD, S., ELZWAWI, A. & MEHELLOU, Y. 2017b. WNK Signaling Inhibitors as Potential Antihypertensive Drugs. *ChemMedChem*, 12, 1677-1686.
- ALESSI, D. R., ZHANG, J., KHANNA, A., HOCHDÖRFER, T., SHANG, Y. & KAHLE, K. T. 2014. The WNK-SPAK/OSR1 pathway: master regulator of cation-chloride cotransporters. *Science Signaling*, 7, re3-re3.
- ANSELMO, A. N., EARNEST, S., CHEN, W., JUANG, Y.-C., KIM, S. C., ZHAO, Y. & COBB, M. H. 2006. WNK1 and OSR1 regulate the Na⁺, K⁺, 2Cl⁻ cotransporter in HeLa cells. *Proceedings of the National Academy of Sciences*, 103, 10883-10888.
- ARROYO, J. P., KAHLE, K. T. & GAMBA, G. 2013. The SLC12 family of electroneutral cation-coupled chloride cotransporters. *Molecular Aspects of Medicine*, 34, 288-298.
- ASHBURN, T. T. & THOR, K. B. 2004. Drug repositioning: identifying and developing new uses for existing drugs. *Nature reviews Drug discovery*, 3, 673.
- AWAN, M. & TARIN, S. 2006. Review of photodynamic therapy. *The Surgeon*, 4, 231-236.
- BAIN, J., PLATER, L., ELLIOTT, M., SHPIRO, N., HASTIE, C. J., MCLAUCHLAN, H., KLEVERNIC, I., ARTHUR, J. S. C., ALESSI, D. R. & COHEN, P. 2007. The selectivity of protein kinase inhibitors: a further update. *Biochemical Journal*, 408, 297-315.
- BARILE, E. & PELLECCIA, M. 2014. NMR-based approaches for the identification and optimization of inhibitors of protein-protein interactions. *Chemical reviews*, 114, 4749-4763.
- BATTISTUTTA, R., MAZZORANA, M., SARNO, S., KAZIMIERCZUK, Z., ZANOTTI, G. & PINNA, L. A. 2005. Inspecting the structure-activity relationship of protein kinase CK2 inhibitors derived from tetrabromobenzimidazole. *Chemistry & biology*, 12, 1211-1219.
- BAZÚA-VALENTI, S., CHÁVEZ-CANALES, M., ROJAS-VEGA, L., GONZÁLEZ-RODRÍGUEZ, X., VÁZQUEZ, N., RODRÍGUEZ-GAMA, A., ARGAIZ, E. R., MELO, Z., PLATA, C. & ELLISON, D. H. 2015. The effect of WNK4 on the Na⁺-Cl⁻ cotransporter is modulated by intracellular chloride. *Journal of the American Society of Nephrology*, 26, 1781-1786.

- BÉRUBÉ, G. 2016. An overview of molecular hybrids in drug discovery. *Expert opinion on drug discovery*, 11, 281-305.
- BILLETER, M., WAGNER, G. & WÜTHRICH, K. 2008. Solution NMR structure determination of proteins revisited. *Journal of biomolecular NMR*, 42, 155-158.
- BOYDEN, L. M., CHOI, M., CHOATE, K. A., NELSON-WILLIAMS, C. J., FARHI, A., TOKA, H. R., TIKHONOVA, I. R., BJORNSON, R., MANE, S. M. & COLUSSI, G. 2012. Mutations in kelch-like 3 and cullin 3 cause hypertension and electrolyte abnormalities. *Nature*, 482, 98.
- BRADFORD, M. M. 1976. A rapid and sensitive method for the quantitation of microgram quantities of protein utilizing the principle of protein-dye binding. *Analytical biochemistry*, 72, 248-254.
- BROACH, J. R. & THORNER, J. 1996. High-throughput screening for drug discovery. *Nature*, 384, 14-16.
- BROMFIELD, S. & MUNTNER, P. 2013. High blood pressure: the leading global burden of disease risk factor and the need for worldwide prevention programs. *Current hypertension reports*, 15, 134-136.
- CAI, H., CEBOTARU, V., WANG, Y., ZHANG, X., CEBOTARU, L., GUGGINO, S. & GUGGINO, W. 2006. WNK4 kinase regulates surface expression of the human sodium chloride cotransporter in mammalian cells. *Kidney international*, 69, 2162-2170.
- CALHOUN, D. A., JONES, D., TEXTOR, S., GOFF, D. C., MURPHY, T. P., TOTO, R. D., WHITE, A., CUSHMAN, W. C., WHITE, W. & SICA, D. 2008. Resistant hypertension: diagnosis, evaluation, and treatment. *Circulation*, 117, e510-e526.
- CAPDEVILLE, R., BUCHDUNGER, E., ZIMMERMANN, J. & MATTER, A. 2002. Glivec (STI571, imatinib), a rationally developed, targeted anticancer drug. *Nature reviews Drug discovery*, 1, 493.
- CHARISIS, S., NAOUMIDI, I., GINIS, H. & TSILIMBARIS, M. 2007. Transcleral Ciliary Body Photodynamic Therapy With Verteporfin in pigmented Rabbits: Hypotensive Effect and Morphologic Changes After 4 Retreatments. *Investigative Ophthalmology & Visual Science*, 48, 3970-3970.
- COHEN, P. 2001. The role of protein phosphorylation in human health and disease. *European journal of biochemistry*, 268, 5001-5010.
- COHEN, P. 2002a. The origins of protein phosphorylation. *Nature cell biology*, 4, E127.
- COHEN, P. 2002b. Protein kinases—the major drug targets of the twenty-first century? *Nature reviews Drug discovery*, 1, 309.
- COLEMAN, C. S., STANLEY, B. & PEGG, A. E. 1993. Effect of mutations at active site residues on the activity of ornithine decarboxylase and its inhibition by active

- site-directed irreversible inhibitors. *Journal of Biological Chemistry*, 268, 24572-24579.
- COLLETT, M. S. & ERIKSON, R. 1978. Protein kinase activity associated with the avian sarcoma virus src gene product. *Proceedings of the National Academy of Sciences*, 75, 2021-2024.
- CONGREVE, M., CARR, R., MURRAY, C. & JHOTI, H. 2003. A 'rule of three' for fragment-based lead discovery? *Drug discovery today*, 8, 876-877.
- DALVIT, C., FOGLIATTO, G., STEWART, A., VERONESI, M. & STOCKMAN, B. 2001. WaterLOGSY as a method for primary NMR screening: practical aspects and range of applicability. *Journal of biomolecular NMR*, 21, 349-359.
- DARMAN, R. B. & FORBUSH, B. 2002. A regulatory locus of phosphorylation in the N terminus of the Na-K-Cl cotransporter, NKCC1. *Journal of Biological Chemistry*, 277, 37542-37550.
- DASARI, V. R., MAZACK, V., FENG, W., NASH, J., CAREY, D. J. & GOGOI, R. 2017. Verteporfin exhibits YAP-independent anti-proliferative and cytotoxic effects in endometrial cancer cells. *Oncotarget*, 8, 28628.
- DBOUK, H. A., HUANG, C.-L. & COBB, M. H. 2016. Hypertension: the missing WNKs. *American Journal of Physiology-Renal Physiology*, 311, F16-F27.
- DBOUK, H. A., WEIL, L. M., PERERA, G. S., DELLINGER, M. T., PEARSON, G., BREKKEN, R. A. & COBB, M. H. 2014. Actions of the protein kinase WNK1 on endothelial cells are differentially mediated by its substrate kinases OSR1 and SPAK. *Proceedings of the National Academy of Sciences*, 111, 15999-16004.
- DE LOS HEROS, P., ALESSI, D. R., GOURLAY, R., CAMPBELL, D. G., DEAK, M., MACARTNEY, T. J., KAHLE, K. T. & ZHANG, J. 2014. The WNK-regulated SPAK/OSR1 kinases directly phosphorylate and inhibit the K⁺-Cl⁻ co-transporters. *Biochemical Journal*, 458, 559-573.
- DELAGLIO, F., GRZESIEK, S., VUISTER, G. W., ZHU, G., PFEIFER, J. & BAX, A. 1995. NMRPipe: a multidimensional spectral processing system based on UNIX pipes. *Journal of biomolecular NMR*, 6, 277-293.
- DELPIRE, E. & GAGNON, K. B. 2008. SPAK and OSR1: STE20 kinases involved in the regulation of ion homeostasis and volume control in mammalian cells. *Biochemical Journal*, 409, 321-331.
- DESJARDINS, P. & CONKLIN, D. 2010. NanoDrop microvolume quantitation of nucleic acids. *Journal of visualized experiments: JoVE*.
- DONG, Q., DOUGAN, D. R., GONG, X., HALKOWYCZ, P., JIN, B., KANOUNI, T., O'CONNELL, S. M., SCORAH, N., SHI, L. & WALLACE, M. B. 2011. Discovery of TAK-733, a potent and selective MEK allosteric site inhibitor for the treatment of cancer. *Bioorganic & medicinal chemistry letters*, 21, 1315-1319.

- DUROCHER, Y., PERRET, S. & KAMEN, A. 2002. High-level and high-throughput recombinant protein production by transient transfection of suspension-growing human 293-EBNA1 cells. *Nucleic acids research*, 30, e9-e9.
- EHRET, G. B. & CAULFIELD, M. J. 2013. Genes for blood pressure: an opportunity to understand hypertension. *European heart journal*, 34, 951-961.
- ETTEHAD, D., EMDIN, C. A., KIRAN, A., ANDERSON, S. G., CALLENDER, T., EMBERSON, J., CHALMERS, J., RODGERS, A. & RAHIMI, K. 2016. Blood pressure lowering for prevention of cardiovascular disease and death: a systematic review and meta-analysis. *The Lancet*, 387, 957-967.
- FABBRO, D. 2015. 25 years of small molecular weight kinase inhibitors: potentials and limitations. *Molecular pharmacology*, 87, 766-775.
- FABBRO, D., COWAN-JACOB, S. W., MÖBITZ, H. & MARTINY-BARON, G. 2012. Targeting cancer with small-molecular-weight kinase inhibitors. *Kinase Inhibitors*. Springer.
- FABBRO, D., COWAN-JACOB, S. W. & MOEBITZ, H. 2015. Ten things you should know about protein kinases: IUPHAR Review 14. *British journal of pharmacology*, 172, 2675-2700.
- FENG, B. Y. & SHOICHET, B. K. 2006. A detergent-based assay for the detection of promiscuous inhibitors. *Nature protocols*, 1, 550.
- FENTON, C. & PERRY, C. M. 2006. Verteporfin: a review of its use in the management of subfoveal choroidal neovascularisation. *Drugs Aging*, 23, 421-45.
- FIELDING, L. 2003. NMR methods for the determination of protein-ligand dissociation constants. *Current topics in medicinal chemistry*, 3, 39-53.
- FILIPPI, B. M., DE LOS HEROS, P., MEHELLOU, Y., NAVRATILOVA, I., GOURLAY, R., DEAK, M., PLATER, L., TOTH, R., ZEQUIRAJ, E. & ALESSI, D. R. 2011. MO25 is a master regulator of SPAK/OSR1 and MST3/MST4/YSK1 protein kinases. *The European Molecular Biology Organization Journal*, 30, 1730-1741.
- FISCHER, E. H. & KREBS, E. G. 1955. Conversion of phosphorylase b to phosphorylase a in muscle extracts. *Journal of Biological Chemistry*, 216, 121-132.
- FISCHER, P. M. 2017. Approved and experimental small-molecule oncology kinase inhibitor drugs: a mid-2016 overview. *Medicinal research reviews*, 37, 314-367.
- FOUNDATION, A. C. O. C. 2018. New ACC/AHA high blood pressure guidelines lower definition of hypertension.
- FRUEH, D. P. 2014. Practical aspects of NMR signal assignment in larger and challenging proteins. *Progress in nuclear magnetic resonance spectroscopy*, 78, 47-75.

- GAGNON, K. B. & DELPIRE, E. 2012. Molecular physiology of SPAK and OSR1: two Ste20-related protein kinases regulating ion transport. *Physiological reviews*, 92, 1577-1617.
- GAGNON, K. B., ENGLAND, R. & DELPIRE, E. 2006. Volume sensitivity of cation-Cl⁻ cotransporters is modulated by the interaction of two kinases: Ste20-related proline-alanine-rich kinase and WNK4. *American Journal of Physiology-Cell Physiology*, 290, C134-C142.
- GAGNON, K. B., ENGLAND, R. & DELPIRE, E. 2007. A single binding motif is required for SPAK activation of the Na-K-2Cl cotransporter. *Cellular Physiology and Biochemistry*, 20, 131-142.
- GAMBA, G. 2005. Molecular physiology and pathophysiology of electroneutral cation-chloride cotransporters. *Physiological reviews*, 85, 423-493.
- GIBAUT, F., CORVAISIER, M., BAILLY, F., HUET, G., MELNYK, P. & COTELLE, P. 2016. Non-photoinduced biological properties of verteporfin. *Current medicinal chemistry*, 23, 1171-1184.
- GIMÉNEZ, I. & FORBUSH, B. 2005. Regulatory phosphorylation sites in the NH₂ terminus of the renal Na-K-Cl cotransporter (NKCC2). *American Journal of Physiology-Renal Physiology*, 289, F1341-F1345.
- GRONT, D., KULP, D. W., VERNON, R. M., STRAUSS, C. E. & BAKER, D. 2011. Generalized fragment picking in Rosetta: design, protocols and applications. *PloS one*, 6, e23294.
- GUYTON, A. C. 1991. Blood pressure control--special role of the kidneys and body fluids. *Science*, 252, 1813-1816.
- HADCHOUEL, J., ELLISON, D. H. & GAMBA, G. 2016. Regulation of renal electrolyte transport by WNK and SPAK-OSR1 kinases. *Annual review of physiology*, 78, 367-389.
- HAFFSA, N. E., ARNDT, D. & WISHART, D. S. 2015. CSI 3.0: a web server for identifying secondary and super-secondary structure in proteins using NMR chemical shifts. *Nucleic acids research*, 43, W370-W377.
- HALLENBECK, P. & WALSH, D. 1983. Autophosphorylation of phosphorylase kinase. Divalent metal cation and nucleotide dependency. *Journal of Biological Chemistry*, 258, 13493-13501.
- HANKS, S. K. & HUNTER, T. 1995. Protein kinases 6. The eukaryotic protein kinase superfamily: kinase (catalytic) domain structure and classification. *The Federation of American Societies for Experimental Biology Journal*, 9, 576-596.
- HANKS, S. K. & QUINN, A. M. 1991. [2] Protein kinase catalytic domain sequence database: Identification of conserved features of primary structure and classification of family members. *Methods in enzymology*. Elsevier.

- HARDMAN, G., PERKINS, S., RUAN, Z., KANNAN, N., BROWNRIDGE, P., BYRNE, D. P., EYERS, P. A., JONES, A. R. & EYERS, C. E. 2017. Extensive non-canonical phosphorylation in human cells revealed using strong-anion exchange-mediated phosphoproteomics. *bioRxiv*, 202820.
- HARNER, M. J., FRANK, A. O. & FESIK, S. W. 2013. Fragment-based drug discovery using NMR spectroscopy. *Journal of biomolecular NMR*, 56, 65-75.
- HASTIE, C. J., MCCLAUCHLAN, H. J. & COHEN, P. 2006. Assay of protein kinases using radiolabeled ATP: a protocol. *Nature protocols*, 1, 968.
- HE, G., WANG, H.-R., HUANG, S.-K. & HUANG, C.-L. 2007. Intersectin links WNK kinases to endocytosis of ROMK1. *The Journal of clinical investigation*, 117, 1078-1087.
- HEATH, C., STAHL, P. & BARBIERI, M. 2003. Lipid kinases play crucial and multiple roles in membrane trafficking and signaling. *Histology and histopathology*, 18, 989-998.
- HOWARD, H. C., MOUNT, D. B., ROCHEFORT, D., BYUN, N., DUPRÉ, N., LU, J., FAN, X., SONG, L., RIVIÈRE, J.-B. & PRÉVOST, C. 2002. The K-Cl cotransporter KCC3 is mutant in a severe peripheral neuropathy associated with agenesis of the corpus callosum. *Nature genetics*, 32, 384.
- HUANG, C.-L., CHA, S.-K., WANG, H.-R., XIE, J. & COBB, M. H. 2007. WNKs: protein kinases with a unique kinase domain. *Experimental & molecular medicine*, 39, 565.
- HUANG, C.-L. & CHENG, C.-J. 2015. A unifying mechanism for WNK kinase regulation of sodium-chloride cotransporter. *Pflügers Archiv-European Journal of Physiology*, 467, 2235-2241.
- HUNTER, T. 2000. Signaling—2000 and beyond. *Cell*, 100, 113-127.
- IRWIN, J. J., DUAN, D., TOROSYAN, H., DOAK, A. K., ZIEBART, K. T., STERLING, T., TUMANIAN, G. & SHOICHET, B. K. 2015. An aggregation advisor for ligand discovery. *Journal of medicinal chemistry*, 58, 7076-7087.
- ISHIGAMI-YUASA, M., WATANABE, Y., MORI, T., MASUNO, H., FUJII, S., KIKUCHI, E., UCHIDA, S. & KAGECHIKA, H. 2017. Development of WNK signaling inhibitors as a new class of antihypertensive drugs. *Bioorganic & medicinal chemistry*, 25, 3845-3852.
- IVERSEN, P. W., EASTWOOD, B. J., SITTAMPALAM, G. S. & COX, K. L. 2006. A comparison of assay performance measures in screening assays: signal window, Z'factor, and assay variability ratio. *Journal of biomolecular screening*, 11, 247-252.

- JAFFE, M. G., LEE, G. A., YOUNG, J. D., SIDNEY, S. & GO, A. S. 2013. Improved blood pressure control associated with a large-scale hypertension program. *Jama*, 310, 699-705.
- JIN, J. & PAWSON, T. 2012. Modular evolution of phosphorylation-based signalling systems. *Philosophical Transactions of the Royal Society B: Biological Sciences*, 367, 2540-2555.
- KADRI, H., ALAMRI, M. A., NAVRATILOVA, I. H., ALDERWICK, L. J., SIMPKINS, N. S. & MEHELLOU, Y. 2017. Towards the Development of Small-Molecule MO25 Binders as Potential Indirect SPAK/OSR1 Kinase Inhibitors. *ChemBioChem*, 18, 460-465.
- KANG, M.-H., JEONG, G. S., SMOOT, D. T., ASHKTORAB, H., HWANG, C. M., KIM, B. S., KIM, H. S. & PARK, Y.-Y. 2017. Verteporfin inhibits gastric cancer cell growth by suppressing adhesion molecule FAT1. *Oncotarget*, 8, 98887.
- KESERŰ, G. M. & MAKARA, G. M. 2006. Hit discovery and hit-to-lead approaches. *Drug discovery today*, 11, 741-748.
- KIKUCHI, E., MORI, T., ZENIYA, M., ISOBE, K., ISHIGAMI-YUASA, M., FUJII, S., KAGECHIKA, H., ISHIHARA, T., MIZUSHIMA, T. & SASAKI, S. 2014. Discovery of novel SPAK inhibitors that block WNK kinase signaling to cation chloride transporters. *Journal of the American Society of Nephrology*, ASN. 2014060560.
- KITCHEN, D. B., DECORNEZ, H., FURR, J. R. & BAJORATH, J. 2004. Docking and scoring in virtual screening for drug discovery: methods and applications. *Nature reviews Drug discovery*, 3, 935.
- KLAGES, J., COLES, M. & KESSLER, H. 2007. NMR-based screening: a powerful tool in fragment-based drug discovery. *Analyst*, 132, 692-705.
- KNIGHTON, D. R., ZHENG, J., TEN EYCK, L. F., ASHFORD, V. A., XUONG, N.-H., TAYLOR, S. S. & SOWADSKI, J. M. 1991. Crystal structure of the catalytic subunit of cyclic adenosine monophosphate-dependent protein kinase. *Science*, 253, 407-414.
- KORNEV, A. P., TAYLOR, S. S. & TEN EYCK, L. F. 2008. A helix scaffold for the assembly of active protein kinases. *Proceedings of the National Academy of Sciences*, 105, 14377-14382.
- KRACHLER, A. M., WOOLERY, A. R. & ORTH, K. 2011. Manipulation of kinase signaling by bacterial pathogens. *The Journal of Cell Biology*, jcb. 201107132.
- KREBSK, E. G. 1985. The phosphorylation of proteins: a major mechanism for biological regulation. Portland Press Limited.

- LAHIRY, P., TORKAMANI, A., SCHORK, N. J. & HEGELE, R. A. 2010. Kinase mutations in human disease: interpreting genotype–phenotype relationships. *Nature Reviews Genetics*, 11, 60.
- LALIOTI, M. D., ZHANG, J., VOLKMAN, H. M., KAHLE, K. T., HOFFMANN, K. E., TOKA, H. R., NELSON-WILLIAMS, C., ELLISON, D. H., FLAVELL, R. & BOOTH, C. J. 2006. Wnk4 controls blood pressure and potassium homeostasis via regulation of mass and activity of the distal convoluted tubule. *Nature genetics*, 38, 1124.
- LEE, S. J., COBB, M. H. & GOLDSMITH, E. J. 2009. Crystal structure of domain-swapped STE20 OSR1 kinase domain. *Protein Science*, 18, 304-313.
- LEPRE, C. A., MOORE, J. M. & PENG, J. W. 2004. Theory and applications of NMR-based screening in pharmaceutical research. *Chemical reviews*, 104, 3641-3676.
- LEVY, J. G. 1995. Photodynamic therapy. *Trends in biotechnology*, 13, 14-18.
- LI, C., FENG, M., SHI, Z., HAO, Q., SONG, X., WANG, W., ZHAO, Y., JIAO, S. & ZHOU, Z. 2014. Structural and biochemical insights into the activation mechanisms of germinal center kinase OSR1. *Journal of Biological Chemistry*, 289, 35969-35978.
- LI, Y. & PALMER, A. G. 2009. Domain swapping in the kinase superfamily: OSR1 joins the mix. *Protein Science*, 18, 678-681.
- LIN, S.-H., YU, I.-S., JIANG, S.-T., LIN, S.-W., CHU, P., CHEN, A., SYTWU, H.-K., SOHARA, E., UCHIDA, S. & SASAKI, S. 2011. Impaired phosphorylation of Na⁺-K⁺-2Cl⁻ cotransporter by oxidative stress-responsive kinase-1 deficiency manifests hypotension and Bartter-like syndrome. *Proceedings of the National Academy of Sciences*, 108, 17538-17543.
- LIONTA, E., SPYROU, G., K VASSILATIS, D. & COURNIA, Z. 2014. Structure-based virtual screening for drug discovery: principles, applications and recent advances. *Current topics in medicinal chemistry*, 14, 1923-1938.
- LIU, Z., XIE, J., WU, T., TRUONG, T., AUCHUS, R. J. & HUANG, C.-L. 2010. Downregulation of NCC and NKCC2 cotransporters by kidney-specific WNK1 revealed by gene disruption and transgenic mouse models. *Human molecular genetics*, 20, 855-866.
- MAKI, N., KOMATSUDA, A., WAKUI, H., OHTANI, H., KIGAWA, A., AIBA, N., HAMAI, K., MOTEGI, M., YAMAGUCHI, A. & IMAI, H. 2004. Four novel mutations in the thiazide-sensitive Na–Cl co-transporter gene in Japanese patients with Gitelman's syndrome. *Nephrology Dialysis Transplantation*, 19, 1761-1766.
- MANNING, G., WHYTE, D. B., MARTINEZ, R., HUNTER, T. & SUDARSANAM, S. 2002. The protein kinase complement of the human genome. *Science*, 298, 1912-1934.

- MARSHALL, W., OSSUM, C. G. & HOFFMANN, E. K. 2005. Hypotonic shock mediation by p38 MAPK, JNK, PKC, FAK, OSR1 and SPAK in osmosensing chloride secreting cells of killifish opercular epithelium. *Journal of Experimental Biology*, 208, 1063-1077.
- MARTIN, M. P., ALAM, R., BETZI, S., INGLES, D. J., ZHU, J. Y. & SCHÖNBRUNN, E. 2012. A Novel Approach to the Discovery of Small-Molecule Ligands of CDK2. *Chembiochem*, 13, 2128-2136.
- MAYAN, H., VERED, I., MOUALLEM, M., TZADOK-WITKON, M., PAUZNER, R. & FARFEL, Z. 2002. Pseudohypoaldosteronism type II: marked sensitivity to thiazides, hypercalciuria, normomagnesemia, and low bone mineral density. *The Journal of Clinical Endocrinology & Metabolism*, 87, 3248-3254.
- MCCORMICK, J. A. & ELLISON, D. H. 2011. The WNKs: atypical protein kinases with pleiotropic actions. *Physiological reviews*, 91, 177-219.
- MCCORMICK, J. A., MUTIG, K., NELSON, J. H., SARITAS, T., HOORN, E. J., YANG, C.-L., ROGERS, S., CURRY, J., DELPIRE, E. & BACHMANN, S. 2011. A SPAK isoform switch modulates renal salt transport and blood pressure. *Cell metabolism*, 14, 352-364.
- MCMANUS, R. J. & MANT, J. 2018. Hypertension: New US blood-pressure guidelines—who asked the patients? *Nature Reviews Cardiology*.
- MEYER, J. W., FLAGELLA, M., SUTLIFF, R. L., LORENZ, J. N., NIEMAN, M. L., WEBER, C. S., PAUL, R. J. & SHULL, G. E. 2002. Decreased blood pressure and vascular smooth muscle tone in mice lacking basolateral Na⁺-K⁺-2Cl⁻ cotransporter. *American Journal of Physiology-Heart and Circulatory Physiology*, 283, H1846-H1855.
- MIN, X., LEE, B.-H., COBB, M. H. & GOLDSMITH, E. J. 2004. Crystal structure of the kinase domain of WNK1, a kinase that causes a hereditary form of hypertension. *Structure*, 12, 1303-1311.
- MOES, A. D., VAN DER LUBBE, N., ZIETSE, R., LOFFING, J. & HOORN, E. J. 2014. The sodium chloride cotransporter SLC12A3: new roles in sodium, potassium, and blood pressure regulation. *Pflügers Archiv-European Journal of Physiology*, 466, 107-118.
- MONDAL, M., GROOTHUIS, D. E. & HIRSCH, A. K. 2015. Fragment growing exploiting dynamic combinatorial chemistry of inhibitors of the aspartic protease endothiapepsin. *MedChemComm*, 6, 1267-1271.
- MORI, T., KIKUCHI, E., WATANABE, Y., FUJII, S., ISHIGAMI-YUASA, M., KAGECHIKA, H., SOHARA, E., RAI, T., SASAKI, S. & UCHIDA, S. 2013. Chemical library screening for WNK signalling inhibitors using fluorescence correlation spectroscopy. *Biochemical Journal*, 455, 339-345.

- MORIGUCHI, T., URUSHIYAMA, S., HISAMOTO, N., IEMURA, S.-I., UCHIDA, S., NATSUME, T., MATSUMOTO, K. & SHIBUYA, H. 2005. WNK1 regulates phosphorylation of cation-chloride-coupled cotransporters via the STE20-related kinases, SPAK and OSR1. *Journal of Biological Chemistry*, 280, 42685-42693.
- MURTHY, M., KURZ, T. & O'SHAUGHNESSY, K. M. 2017. WNK signalling pathways in blood pressure regulation. *Cellular and Molecular Life Sciences*, 74, 1261-1280.
- MUSTONEN, M. V., PYRHÖNEN, S. & KELLOKUMPU-LEHTINEN, P.-L. 2014. Toremifene in the treatment of breast cancer. *World Journal of Clinical Oncology*, 5, 393.
- NAGAR, B., BORNMANN, W. G., PELLICENA, P., SCHINDLER, T., VEACH, D. R., MILLER, W. T., CLARKSON, B. & KURIYAN, J. 2002. Crystal structures of the kinase domain of c-Abl in complex with the small molecule inhibitors PD173955 and imatinib (STI-571). *Cancer research*, 62, 4236-4243.
- NGUYEN, H. H., PARK, J., KANG, S. & KIM, M. 2015. Surface plasmon resonance: a versatile technique for biosensor applications. *Sensors*, 15, 10481-10510.
- NISHIDA, H., SOHARA, E., NOMURA, N., CHIGA, M., ALESSI, D. R., RAI, T., SASAKI, S. & UCHIDA, S. 2012. Phosphatidylinositol 3-kinase/Akt signaling pathway activates the WNK-OSR1/SPAK-NCC phosphorylation cascade in hyperinsulinemic db/db mice. *Hypertension*, HYPERTENSIONAHA.112.201509.
- OHTA, A., SCHUMACHER, F.-R., MEHELLOU, Y., JOHNSON, C., KNEBEL, A., MACARTNEY, T. J., WOOD, N. T., ALESSI, D. R. & KURZ, T. 2013. The CUL3–KLHL3 E3 ligase complex mutated in Gordon's hypertension syndrome interacts with and ubiquitylates WNK isoforms: disease-causing mutations in KLHL3 and WNK4 disrupt interaction. *Biochemical Journal*, 451, 111-122.
- OKADA, H., UEZU, A., MASON, F. M., SODERBLOM, E. J., MOSELEY, M. A. & SODERLING, S. H. 2011. SH3 Domain–Based Phototrapping in Living Cells Reveals Rho Family GAP Signaling Complexes. *Science Signaling*, 4, rs13-rs13.
- OKAMOTO, K., IKEMORI-KAWADA, M., JESTEL, A., VON KÖNIG, K., FUNAHASHI, Y., MATSUSHIMA, T., TSURUOKA, A., INOUE, A. & MATSUI, J. 2014. Distinct binding mode of multikinase inhibitor lenvatinib revealed by biochemical characterization. *ACS medicinal chemistry letters*, 6, 89-94.
- OLIVER, A. W., PAUL, A., BOXALL, K. J., BARRIE, S. E., AHERNE, G. W., GARRETT, M. D., MITTNACHT, S. & PEARL, L. H. 2006. Trans-activation of the DNA-damage signalling protein kinase Chk2 by T-loop exchange. *The European Molecular Biology Organization journal*, 25, 3179-3190.

- ORGANIZATION, W. H. 2013. A global brief on hypertension: silent killer, global public health crisis: World Health Day 2013.
- PARTICIPANTS, V. R. 2005. Guidelines for using verteporfin (Visudyne) in photodynamic therapy for choroidal neovascularization due to age-related macular degeneration and other causes: update. *Retina*, 25, 119-134.
- PATCHING, S. G. 2014. Surface plasmon resonance spectroscopy for characterisation of membrane protein–ligand interactions and its potential for drug discovery. *Biochimica et Biophysica Acta (BBA)-Biomembranes*, 1838, 43-55.
- PATTERSON, H., NIBBS, R., MCINNES, I. & SIEBERT, S. 2014. Protein kinase inhibitors in the treatment of inflammatory and autoimmune diseases. *Clinical & Experimental Immunology*, 176, 1-10.
- PAVER, W. & PAULINE, G. 1964. Hypertension and hyperpotassaemia without renal disease in a young male. *The Medical journal of Australia*, 2, 305-306.
- PEARCE, L. R., KOMANDER, D. & ALESSI, D. R. 2010. The nuts and bolts of AGC protein kinases. *Nature reviews Molecular cell biology*, 11, 9.
- PIALA, A. T., MOON, T. M., AKELLA, R., HE, H., COBB, M. H. & GOLDSMITH, E. J. 2014. Chloride sensing by WNK1 involves inhibition of autophosphorylation. *Science Signaling*, 7, ra41-ra41.
- PIKE, A. C., RELLOS, P., NIESEN, F. H., TURNBULL, A., OLIVER, A. W., PARKER, S. A., TURK, B. E., PEARL, L. H. & KNAPP, S. 2008. Activation segment dimerization: a mechanism for kinase autophosphorylation of non-consensus sites. *The European Molecular Biology Organization journal*, 27, 704-714.
- PONCE-CORIA, J., SAN-CRISTOBAL, P., KAHLE, K. T., VAZQUEZ, N., PACHECO-ALVAREZ, D., DE LOS HEROS, P., JUÁREZ, P., MUÑOZ, E., MICHEL, G. & BOBADILLA, N. A. 2008. Regulation of NKCC2 by a chloride-sensing mechanism involving the WNK3 and SPAK kinases. *Proceedings of the National Academy of Sciences*, 105, 8458-8463.
- POWERS, R. 2007. Functional genomics and NMR spectroscopy. *Combinatorial chemistry & high throughput screening*, 10, 676-697.
- RADIVOJAC, P., BAENZIGER, P. H., KANN, M. G., MORT, M. E., HAHN, M. W. & MOONEY, S. D. 2008. Gain and loss of phosphorylation sites in human cancer. *Bioinformatics*, 24, i241-i247.
- RAFIQI, F. H., ZUBER, A. M., GLOVER, M., RICHARDSON, C., FLEMING, S., JOVANOVIĆ, S., JOVANOVIĆ, A., O'SHAUGHNESSY, K. M. & ALESSI, D. R. 2010. Role of the WNK-activated SPAK kinase in regulating blood pressure. *EMBO molecular medicine*, 2, 63-75.

- REVA, B., ANTIPIN, Y. & SANDER, C. 2011. Predicting the functional impact of protein mutations: application to cancer genomics. *Nucleic acids research*, 39, e118-e118.
- RICHARDSON, C. & ALESSI, D. R. 2008. The regulation of salt transport and blood pressure by the WNK-SPAK/OSR1 signalling pathway. *Journal of cell science*, 121, 3293-3304.
- RICHARDSON, C., RAFIQI, F. H., KARLSSON, H. K., MOLELEKI, N., VANDEWALLE, A., CAMPBELL, D. G., MORRICE, N. A. & ALESSI, D. R. 2008. Activation of the thiazide-sensitive Na⁺-Cl⁻-cotransporter by the WNK-regulated kinases SPAK and OSR1. *Journal of Cell Science*, 121, 675-684.
- RINEHART, J., KAHLE, K. T., DE LOS HEROS, P., VAZQUEZ, N., MEADE, P., WILSON, F. H., HEBERT, S. C., GIMENEZ, I., GAMBA, G. & LIFTON, R. P. 2005. WNK3 kinase is a positive regulator of NKCC2 and NCC, renal cation-Cl⁻-cotransporters required for normal blood pressure homeostasis. *Proceedings of the National Academy of Sciences of the United States of America*, 102, 16777-16782.
- ROSKOSKI JR, R. 2016. Classification of small molecule protein kinase inhibitors based upon the structures of their drug-enzyme complexes. *Pharmacological research*, 103, 26-48.
- ROSKOSKI, R. 2012. MEK1/2 dual-specificity protein kinases: structure and regulation. *Biochemical and biophysical research communications*, 417, 5-10.
- ROY, A., R MCDONALD, P., SITTAMPALAM, S. & CHAGUTURU, R. 2010. Open access high throughput drug discovery in the public domain: a Mount Everest in the making. *Current pharmaceutical biotechnology*, 11, 764-778.
- SANNER, M. F. 1999. Python: a programming language for software integration and development. *Journal of Molecular Graphics and Modelling*, 17, 57-61.
- SARDANA, D., ZHU, C., ZHANG, M., GUDIVADA, R. C., YANG, L. & JEGGA, A. G. 2011. Drug repositioning for orphan diseases. *Briefings in bioinformatics*, 12, 346-356.
- SCHUMACHER, F. R., SIEW, K., ZHANG, J., JOHNSON, C., WOOD, N., CLEARY, S. E., AL MASKARI, R. S., FERRYMAN, J. T., HARDEGE, I. & FIGG, N. L. 2015. Characterisation of the Cullin-3 mutation that causes a severe form of familial hypertension and hyperkalaemia. *EMBO molecular medicine*, e201505444.
- SHAHARABANY, M., HOLTZMAN, E. J., MAYAN, H., HIRSCHBERG, K., SEGER, R. & FARFEL, Z. 2008. Distinct pathways for the involvement of WNK4 in the signaling of hypertonicity and EGF. *The Federation of European Biochemical Societies journal*, 275, 1631-1642.

- SHEKARABI, M., ZHANG, J., KHANNA, A. R., ELLISON, D. H., DELPIRE, E. & KAHLE, K. T. 2017. WNK kinase signaling in ion homeostasis and human disease. *Cell metabolism*, 25, 285-299.
- SHEN, Y., DELAGLIO, F., CORNILESCU, G. & BAX, A. 2009a. TALOS+: a hybrid method for predicting protein backbone torsion angles from NMR chemical shifts. *Journal of biomolecular NMR*, 44, 213-223.
- SHEN, Y., LANGE, O., DELAGLIO, F., ROSSI, P., ARAMINI, J. M., LIU, G., ELETISKY, A., WU, Y., SINGARAPU, K. K. & LEMAK, A. 2008. Consistent blind protein structure generation from NMR chemical shift data. *Proceedings of the National Academy of Sciences*, 105, 4685-4690.
- SHEN, Y., VERNON, R., BAKER, D. & BAX, A. 2009b. De novo protein structure generation from incomplete chemical shift assignments. *Journal of biomolecular NMR*, 43, 63-78.
- SHIBATA, S., ZHANG, J., PUTHUMANA, J., STONE, K. L. & LIFTON, R. P. 2013. Kelch-like 3 and Cullin 3 regulate electrolyte homeostasis via ubiquitination and degradation of WNK4. *Proceedings of the National Academy of Sciences*, 110, 7838-7843.
- SIM, C. H., GABRIEL, K., MILLS, R. D., CULVENOR, J. G. & CHENG, H. C. 2012. Analysis of the regulatory and catalytic domains of PTEN-induced kinase-1 (PINK1). *Human mutation*, 33, 1408-1422.
- SIMON, D. B., KARET, F. E., HAMDAN, J. M., DI PIETRO, A., SANJAD, S. A. & LIFTON, R. P. 1996a. Bartter's syndrome, hypokalaemic alkalosis with hypercalciuria, is caused by mutations in the Na-K-2Cl cotransporter NKCC2. *Nature genetics*, 13, 183.
- SIMON, D. B., NELSON-WILLIAMS, C., BIA, M. J., ELLISON, D., KARET, F. E., MOLINA, A. M., VAARA, I., IWATA, F., CUSHNER, H. M. & KOOLEN, M. 1996b. Gitelman's variant of Barter's syndrome, inherited hypokalaemic alkalosis, is caused by mutations in the thiazide-sensitive Na-Cl cotransporter. *Nature genetics*, 12, 24.
- SIRTORI, C. R. 2001. Aescin: pharmacology, pharmacokinetics and therapeutic profile. *Pharmacological Research*, 44, 183-193.
- SMYTH, L. A. & COLLINS, I. 2009. Measuring and interpreting the selectivity of protein kinase inhibitors. *Journal of chemical biology*, 2, 131-151.
- SOLCA, F., DAHL, G., ZOEPHEL, A., BADER, G., SANDERSON, M., KLEIN, C., KRAEMER, O., HIMMELSBACH, F., HAAKSMA, E. & ADOLF, G. R. 2012. Target binding properties and cellular activity of afatinib (BIBW 2992), an irreversible ErbB family blocker. *Journal of Pharmacology and Experimental Therapeutics*, 343, 342-350.

- SRIVASTAVA, S., PANDA, S., LI, Z., FUHS, S. R., HUNTER, T., THIELE, D. J., HUBBARD, S. R. & SKOLNIK, E. Y. 2016. Histidine phosphorylation relieves copper inhibition in the mammalian potassium channel KCa3. 1. *Elife*, 5.
- SUGIKI, T., FURUITA, K., FUJIWARA, T. & KOJIMA, C. 2018. Current NMR Techniques for Structure-Based Drug Discovery. *Molecules*, 23, 148.
- SUSA, K., SOHARA, E., RAI, T., ZENIYA, M., MORI, Y., MORI, T., CHIGA, M., NOMURA, N., NISHIDA, H. & TAKAHASHI, D. 2014. Impaired degradation of WNK1 and WNK4 kinases causes PHAII in mutant KLHL3 knock-in mice. *Human molecular genetics*, 23, 5052-5060.
- SWAN, G. 1999. The pharmacology of halogenated salicylanilides and their anthelmintic use in animals. *Journal of the South African Veterinary Association*, 70, 61-70.
- SWEIS, R. F. 2015. Target (in) validation: a critical, sometimes unheralded, role of modern medicinal chemistry. ACS Publications.
- SZYMAŃSKI, P., MARKOWICZ, M. & MIKICIUK-OLASIK, E. 2011. Adaptation of high-throughput screening in drug discovery—toxicological screening tests. *International journal of molecular sciences*, 13, 427-452.
- TAMARI, M., DAIGO, Y. & NAKAMURA, Y. 1999. Isolation and characterization of a novel serine threonine kinase gene on chromosome 3p22-21.3. *Journal of human genetics*, 44, 116-120.
- TAYLOR IV, C. A., JUANG, Y.-C., EARNEST, S., SENGUPTA, S., GOLDSMITH, E. J. & COBB, M. H. 2015. Domain-swapping switch point in Ste20 protein kinase SPAK. *Biochemistry*, 54, 5063-5071.
- TAYLOR, S. S. & KORNEV, A. P. 2017. PKA and the Structural Kinome. *Periodicum biologorum*, 118.
- TERKER, A. S., ZHANG, C., ERSPAMER, K. J., GAMBA, G., YANG, C.-L. & ELLISON, D. H. 2016. Unique chloride-sensing properties of WNK4 permit the distal nephron to modulate potassium homeostasis. *Kidney international*, 89, 127-134.
- TORKAMANI, A., KANNAN, N., TAYLOR, S. S. & SCHORK, N. J. 2008. Congenital disease SNPs target lineage specific structural elements in protein kinases. *Proceedings of the National Academy of Sciences*, 105, 9011-9016.
- TROTT, O. & OLSON, A. J. 2010. AutoDock Vina: improving the speed and accuracy of docking with a new scoring function, efficient optimization, and multithreading. *Journal of computational chemistry*, 31, 455-461.
- UBERSAX, J. A. & FERRELL JR, J. E. 2007. Mechanisms of specificity in protein phosphorylation. *Nature reviews Molecular cell biology*, 8, 530.

- UCHIDA, S., SOHARA, E., RAI, T. & SASAKI, S. 2014. Regulation of with-no-lysine kinase signaling by Kelch-like proteins. *Biology of the Cell*, 106, 45-56.
- USHIRO, H., TSUTSUMI, T., SUZUKI, K., KAYAHARA, T. & NAKANO, K. 1998. Molecular cloning and characterization of a novel Ste20-related protein kinase enriched in neurons and transporting epithelia. *Archives of biochemistry and biophysics*, 355, 233-240.
- VENKITAKRISHNAN, R. P., BENARD, O., MAX, M., MARKLEY, J. L. & ASSADI-PORTER, F. M. 2012. Use of NMR saturation transfer difference spectroscopy to study ligand binding to membrane proteins. *Membrane Protein Structure and Dynamics*. Springer.
- VERISSIMO, F. & JORDAN, P. 2001. WNK kinases, a novel protein kinase subfamily in multi-cellular organisms. *Oncogene*, 20, 5562.
- VERKHIVKER, G. 2016. Molecular dynamics simulations and modelling of the residue interaction networks in the BRAF kinase complexes with small molecule inhibitors: probing the allosteric effects of ligand-induced kinase dimerization and paradoxical activation. *Molecular BioSystems*, 12, 3146-3165.
- VIDAL-PETIOT, E., ELVIRA-MATELOT, E., MUTIG, K., SOUKASEUM, C., BAUDRIE, V., WU, S., CHEVAL, L., HUC, E., CAMBILLAU, M. & BACHMANN, S. 2013. WNK1-related familial hyperkalemic hypertension results from an increased expression of L-WNK1 specifically in the distal nephron. *Proceedings of the National Academy of Sciences*, 110, 14366-14371.
- VIEGAS, A., MANSO, J., NOBREGA, F. L. & CABRITA, E. J. 2011. Saturation-transfer difference (STD) NMR: a simple and fast method for ligand screening and characterization of protein binding. *Journal of chemical Education*, 88, 990-994.
- VILLA, F., DEAK, M., ALESSI, D. R. & VAN AALTEN, D. M. 2008. Structure of the OSR1 kinase, a hypertension drug target. *Proteins: Structure, Function, and Bioinformatics*, 73, 1082-1087.
- VILLA, F., GOEBEL, J., RAFIQI, F. H., DEAK, M., THASTRUP, J., ALESSI, D. R. & VAN AALTEN, D. M. 2007. Structural insights into the recognition of substrates and activators by the OSR1 kinase. *European Molecular Biology Organization Reports*, 8, 839-845.
- VITARI, A. C., DEAK, M., MORRICE, N. A. & ALESSI, D. R. 2005. The WNK1 and WNK4 protein kinases that are mutated in Gordon's hypertension syndrome phosphorylate and activate SPAK and OSR1 protein kinases. *Biochemical Journal*, 391, 17-24.
- VITARI, A. C., THASTRUP, J., RAFIQI, F. H., DEAK, M., MORRICE, N. A., KARLSSON, H. K. & ALESSI, D. R. 2006. Functional interactions of the

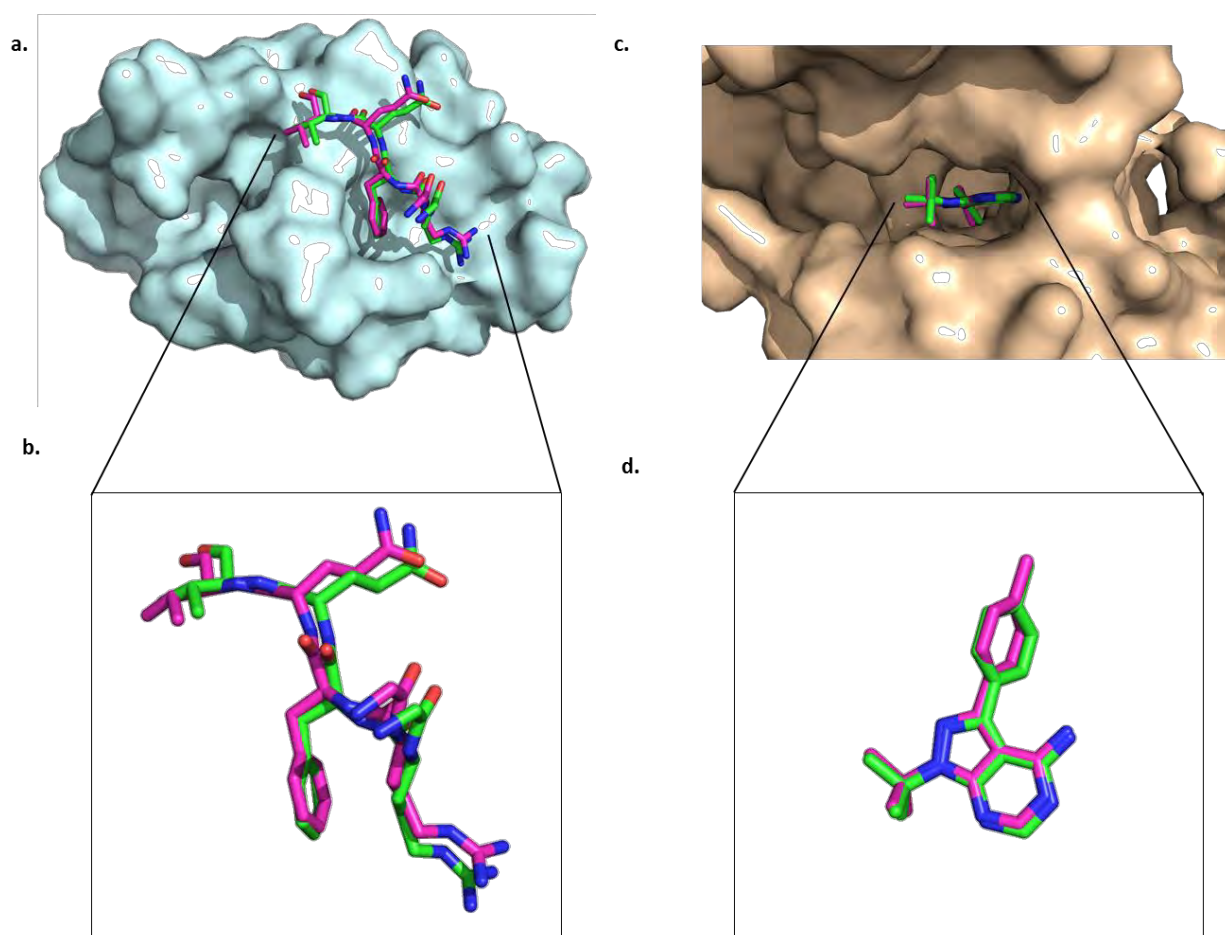
- SPAK/OSR1 kinases with their upstream activator WNK1 and downstream substrate NKCC1. *Biochemical Journal*, 397, 223-231.
- VRANKEN, W. F., BOUCHER, W., STEVENS, T. J., FOGH, R. H., PAJON, A., LLINAS, M., ULRICH, E. L., MARKLEY, J. L., IONIDES, J. & LAUE, E. D. 2005. The CCPN data model for NMR spectroscopy: development of a software pipeline. *Proteins: Structure, Function, and Bioinformatics*, 59, 687-696.
- VULPETTI, A. & BOSOTTI, R. 2004. Sequence and structural analysis of kinase ATP pocket residues. *Il farmaco*, 59, 759-765.
- WADEI, H. M. & TEXTOR, S. C. 2012. The role of the kidney in regulating arterial blood pressure. *Nature Reviews Nephrology*, 8, 602.
- WAKABAYASHI, M., MORI, T., ISOBE, K., SOHARA, E., SUSAKI, K., ARAKI, Y., CHIGA, M., KIKUCHI, E., NOMURA, N. & MORI, Y. 2013. Impaired KLHL3-mediated ubiquitination of WNK4 causes human hypertension. *Cell reports*, 3, 858-868.
- WALSH, D. A., PERKINS, J. P. & KREBS, E. G. 1968. An adenosine 3',5'-monophosphate-dependant protein kinase from rabbit skeletal muscle. *J Biol Chem*, 243, 3763-5.
- WANG, Y., O'CONNELL, J. R., MCARDLE, P. F., WADE, J. B., DORFF, S. E., SHAH, S. J., SHI, X., PAN, L., RAMPERSAUD, E. & SHEN, H. 2009. Whole-genome association study identifies STK39 as a hypertension susceptibility gene. *Proceedings of the National Academy of Sciences*, 106, 226-231.
- WILLIAMSON, M. P. 2013. Using chemical shift perturbation to characterise ligand binding. *Progress in nuclear magnetic resonance spectroscopy*, 73, 1-16.
- WILSON, F. H., DISSE-NICODEME, S., CHOATE, K. A., ISHIKAWA, K., NELSON-WILLIAMS, C., DESITTER, I., GUNEL, M., MILFORD, D. V., LIPKIN, G. W. & ACHARD, J.-M. 2001. Human hypertension caused by mutations in WNK kinases. *Science*, 293, 1107-1112.
- WISHART, D. S. & SYKES, B. D. 1994. The ¹³C chemical-shift index: a simple method for the identification of protein secondary structure using ¹³C chemical-shift data. *Journal of biomolecular NMR*, 4, 171-180.
- WU, P., CLAUSEN, M. H. & NIELSEN, T. E. 2015. Allosteric small-molecule kinase inhibitors. *Pharmacology & therapeutics*, 156, 59-68.
- WU, P., NIELSEN, T. E. & CLAUSEN, M. H. 2016. Small-molecule kinase inhibitors: an analysis of FDA-approved drugs. *Drug Discovery Today*, 21, 5-10.
- XIE, J., YOON, J., YANG, S.-S., LIN, S.-H. & HUANG, C.-L. 2013. WNK1 protein kinase regulates embryonic cardiovascular development through the OSR1 signaling cascade. *Journal of Biological Chemistry*, 288, 8566-8574.

- XU, B.-E., ENGLISH, J. M., WILSBACHER, J. L., STIPPEC, S., GOLDSMITH, E. J. & COBB, M. H. 2000. WNK1, a novel mammalian serine/threonine protein kinase lacking the catalytic lysine in subdomain II. *Journal of Biological Chemistry*, 275, 16795-16801.
- XU, Q., MODREK, B. & LEE, C. 2002. Genome-wide detection of tissue-specific alternative splicing in the human transcriptome. *Nucleic acids research*, 30, 3754-3766.
- YAISH, P., GAZIT, A., GILON, C. & LEVITZKI, A. 1988. Blocking of EGF-dependent cell proliferation by EGF receptor kinase inhibitors. *Science*, 242, 933-935.
- YAMADA, K., LEVELL, J., YOON, T., KOHLS, D., YOWE, D., RIGEL, D. F., IMASE, H., YUAN, J., YASOSHIMA, K. & DIPETRILLO, K. 2017. Optimization of Allosteric With-No-Lysine (WNK) Kinase Inhibitors and Efficacy in Rodent Hypertension Models. *Journal of Medicinal Chemistry*, 60, 7099-7107.
- YAMADA, K., PARK, H.-M., RIGEL, D. F., DIPETRILLO, K., WHALEN, E. J., ANISOWICZ, A., BEIL, M., BERSTLER, J., BROCKLEHURST, C. E. & BURDICK, D. A. 2016a. Small-molecule WNK inhibition regulates cardiovascular and renal function. *Nature chemical biology*, 12, 896.
- YAMADA, K., ZHANG, J.-H., XIE, X., REINHARDT, J., XIE, A. Q., LASALA, D., KOHLS, D., YOWE, D., BURDICK, D. & YOSHISUE, H. 2016b. Discovery and characterization of allosteric WNK kinase inhibitors. *ACS chemical biology*, 11, 3338-3346.
- YANG, S.-S., LO, Y.-F., WU, C.-C., LIN, S.-W., YEH, C.-J., CHU, P., SYTWU, H.-K., UCHIDA, S., SASAKI, S. & LIN, S.-H. 2010. SPAK-knockout mice manifest Gitelman syndrome and impaired vasoconstriction. *Journal of the American Society of nephrology*, 21, 1868-1877.
- YANG, S.-S., MORIMOTO, T., RAI, T., CHIGA, M., SOHARA, E., OHNO, M., UCHIDA, K., LIN, S.-H., MORIGUCHI, T. & SHIBUYA, H. 2007. Molecular pathogenesis of pseudohypoaldosteronism type II: generation and analysis of a Wnk4D561A/+ knockin mouse model. *Cell metabolism*, 5, 331-344.
- YUN, C.-H., BOGGON, T. J., LI, Y., WOO, M. S., GREULICH, H., MEYERSON, M. & ECK, M. J. 2007. Structures of lung cancer-derived EGFR mutants and inhibitor complexes: mechanism of activation and insights into differential inhibitor sensitivity. *Cancer cell*, 11, 217-227.
- ZAGÓRSKA, A., POZO-GUISADO, E., BOUDEAU, J., VITARI, A. C., RAFIQI, F. H., THASTRUP, J., DEAK, M., CAMPBELL, D. G., MORRICE, N. A. & PRESCOTT, A. R. 2007. Regulation of activity and localization of the WNK1 protein kinase by hyperosmotic stress. *The Journal of cell biology*, 176, 89-100.

- ZAMBROWICZ, B. P., ABUIN, A., RAMIREZ-SOLIS, R., RICHTER, L. J., PIGGOTT, J., BELTRANDELRIO, H., BUXTON, E. C., EDWARDS, J., FINCH, R. A. & FRIDDLE, C. J. 2003. Wnk1 kinase deficiency lowers blood pressure in mice: a gene-trap screen to identify potential targets for therapeutic intervention. *Proceedings of the National Academy of Sciences*, 100, 14109-14114.
- ZEGZOUTI, H., ZDANOVSKAIA, M., HSIAO, K. & GOUELI, S. A. 2009. ADP-Glo: a bioluminescent and homogeneous ADP monitoring assay for kinases. *Assay and drug development technologies*, 7, 560-572.
- ZHANG, J.-H., CHUNG, T. D. & OLDENBURG, K. R. 1999. A simple statistical parameter for use in evaluation and validation of high throughput screening assays. *Journal of biomolecular screening*, 4, 67-73.
- ZHANG, J., ADRIÁN, F. J., JAHNKE, W., COWAN-JACOB, S. W., LI, A. G., IACOB, R. E., SIM, T., POWERS, J., DIERKS, C. & SUN, F. 2010. Targeting Bcr–Abl by combining allosteric with ATP-binding-site inhibitors. *Nature*, 463, 501.
- ZHANG, J., SIEW, K., MACARTNEY, T., O'SHAUGHNESSY, K. M. & ALESSI, D. R. 2015. Critical role of the SPAK protein kinase CCT domain in controlling blood pressure. *Human Molecular Genetics*, 24, 4545-4558.
- ZHAO, X., WANG, X., FANG, L., LAN, C., ZHENG, X., WANG, Y., ZHANG, Y., HAN, X., LIU, S. & CHENG, K. 2017. A combinatorial strategy using YAP and pan-RAF inhibitors for treating KRAS-mutant pancreatic cancer. *Cancer letters*, 402, 61-70.

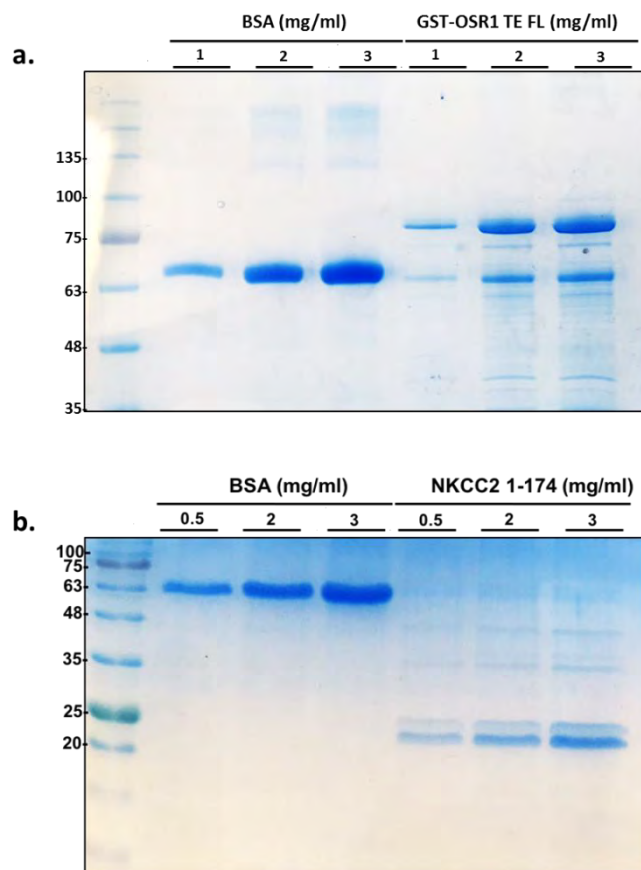
APPENDICES

Appendix 3.1.



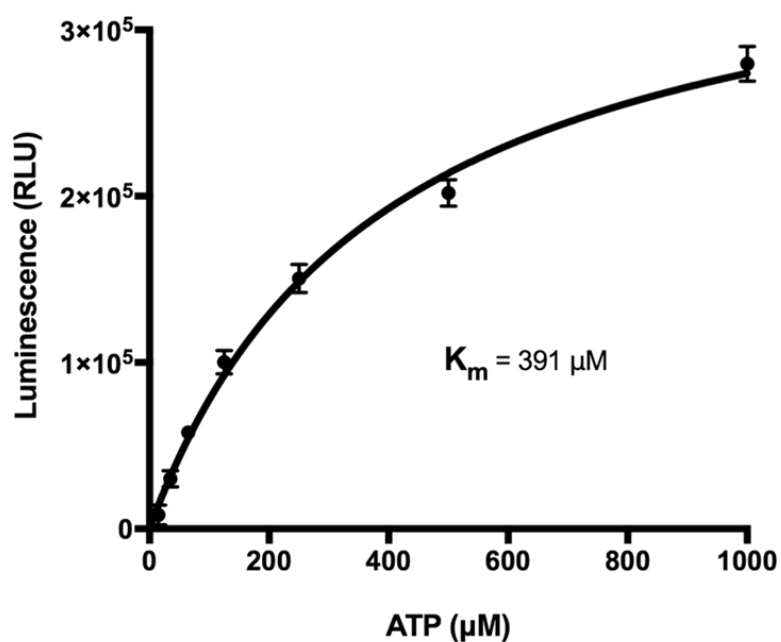
Optimisation of the docking approach using AutoDock Vina software. (a) and (b) Overlap of the docked pose (AutoDock vina) of RFQV peptide (pink) with the corresponding pose of RFQV peptide (green) in the original crystal structure of OSR1 CCT (PDB ID: 2V3S). (c) and (d) Overlap of the docked pose (AutoDock vina) of PP1 Src inhibitor (pink) with the corresponding pose of PP1 Src inhibitor (green) in the original crystal structure of Hck (PDB ID: 1QCF).

Appendix 3.2.



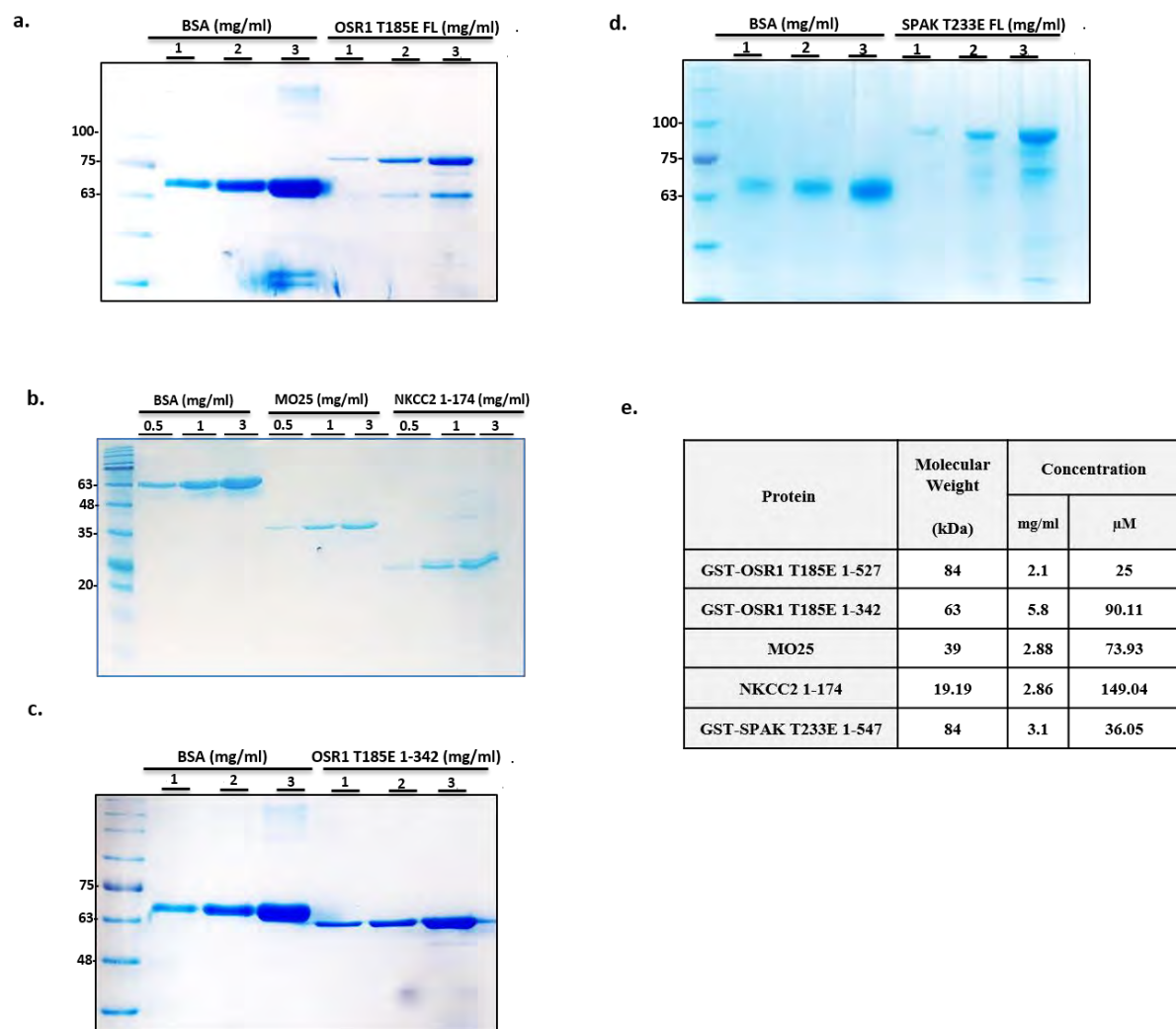
SDS-PAGE analysis of protein purifications using Coomassie blue stain. (a) Human GST-OSR1 T185E FL, (b) human NKCC2 1-174 was purified were expressed in *E.coli* and purified with a good yield of 1.68 and 2.99 mg per liter of culture, respectively and purity of > 95%. (BSA) Bovine serum albumin (Sigma Aldrich, cat# A2153, purity \geq 96% determined by agarose gel electrophoresis) was used at different concentrations as standards for determinations of proteins yield and purity.

Appendix 3.3.



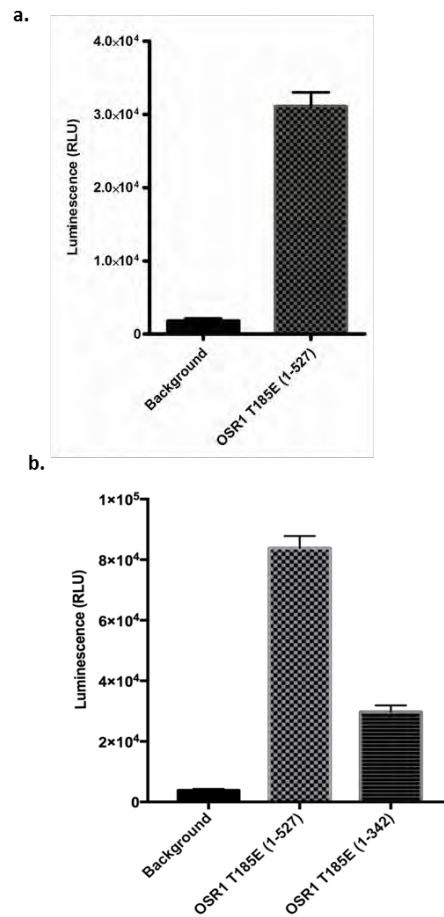
Michaelis–Menten saturation curve for determination of the K_m (Michaelis constant) value of OSR1 T185E (the concentration of ATP required to produce 50% of the V_{\max} value). Kinase assay was performed by titration of serial ATP concentrations (1000- 0.05 μM) into a reaction mixture containing 0.2 μM OSR1 T185E and 5 μM NKCC2 1-174 at 30°C for 30 minutes. Data represent the average signals ($n=4$, $\pm\text{SEM}$).

Appendix 4.1



SDS-PAGE analysis of (a) GST-OSR1 T185E FL, (b) NKCC2 1-174 and MO25, (c) GST-OSR1 T185E 1-342 and (d) GST-SPAK T233E purifications using Coomassie blue stain. BSA (Sigma Aldrich, cat#A2153, purity $\geq 96\%$ (agarose gel electrophoresis)) was used at different concentrations as standards for proteins yield and purity determination. (e) A table illustrates proteins yield and concentration.

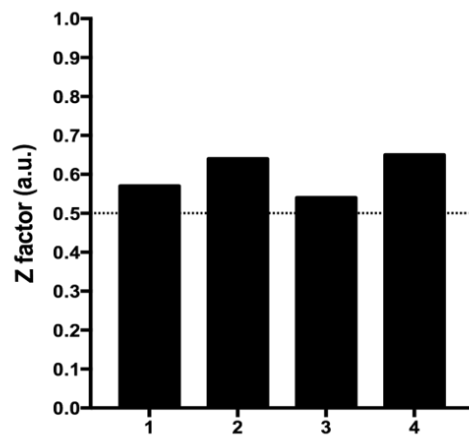
Appendix 4.2



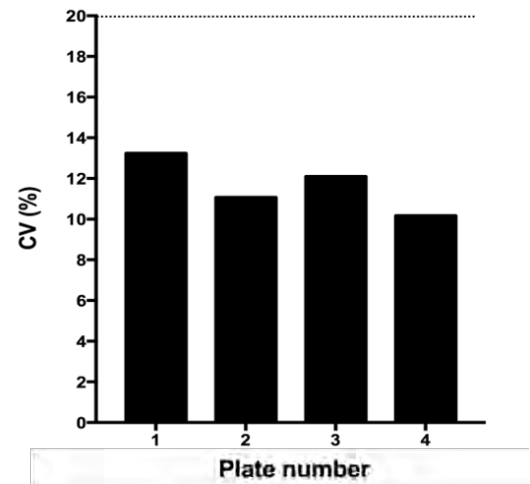
Optimisation of ADP-GLO™ kinase assay as a HTS assay. Assay was performed in 384 well-plates by incubating (a) 0.2 μ M OSR1 T185E FL with 5 μ M NKCC2 1-174 substrate or (b) 0.2 μ M OSR1 T185E FL or truncated OSR1 T185E 1-342 with 250 μ M CATCHtide in 5 μ l kinase reaction buffer.

Appendix 4.3

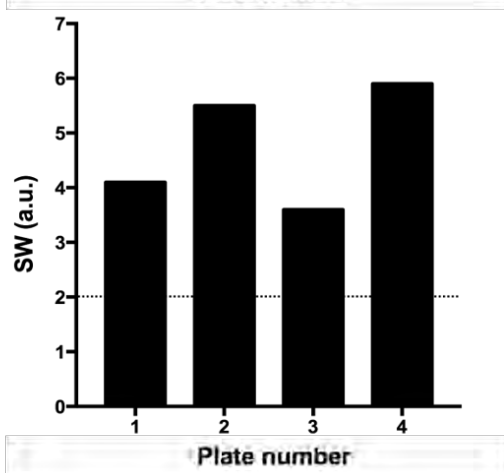
a.



c.



b.



Post screening assay parameters. (a) The z' factor, (b) signal window (SW), and (c) coefficient of variation (CV) of each plate were calculated and then compared with the minimum pass criteria. Dashed lines show the minimum pass criteria ($z' > 0.5$, $SW > 2$, $CV < 20\%$).

Appendix 4.4

a. FDA chemical library

Drug Name	Well	Runnmuber	Molecular Formula	Molecular Weight
Azaguanine-8	A02	RN000205	C ₄ H ₄ N ₆ O	152.12
Sulfaguanidine	A11	RN000205	C ₇ H ₁₀ N ₄ O ₂ S	214.25
Nocodazole	B11	RN000206	C ₁₄ H ₁₁ N ₃ O ₃ S	301.33
Lymecycline	D11	RN000217	C ₂₉ H ₃₈ N ₄ O ₁₀	602.65
Alfadolone acetate	E02	RN000217	C ₂₃ H ₃₄ O ₅	390.52
Alfaxalone	E03	RN000217	C ₂₁ H ₃₂ O ₃	332.49
Azapropazone	E04	RN000217	C ₁₆ H ₂₀ N ₄ O ₂	300.36
Meptazinol hydrochloride	E05	RN000217	C ₁₅ H ₂₃ NO.HCl	269.82
Apramycin	E06	RN000217	C ₂₁ H ₄₁ N ₅ O ₁₁	539.59
Epitiostanol	E07	RN000217	C ₁₉ H ₃₀ O ₅	306.51
Fursultiamine Hydrochloride	E08	RN000217	C ₁₇ H ₂₆ N ₄ O ₃ S ₂ .HCl	435.01
Gabexate mesilate	E09	RN000217	C ₁₆ H ₂₃ N ₃ O ₄ .CH ₄ O ₃ S	417.49
Pivampicillin	E10	RN000217	C ₂₂ H ₂₉ N ₃ O ₆ S	463.56
R(-) Apomorphine hydrochloride hemihydrate	C02	RN000206	2C ₁₇ H ₁₇ N ₂ O ₂ .2HCl.H ₂ O	312.8
Talampicillin hydrochloride	E11	RN000217	C ₂₄ H ₂₃ N ₃ O ₆ S.HCl	517.99
Flucloxacillin sodium	F02	RN000217	C ₁₉ H ₁₆ ClFN ₃ O ₅ S.Na	475.86
Trapidil	F03	RN000217	C ₁₀ H ₁₅ N ₅	205.26
Deptropine citrate	F04	RN000217	C ₂₃ H ₂₇ NO.C ₆ H ₈ O ₇	525.61
Sertraline	F05	RN000217	C ₁₇ H ₁₇ Cl ₂ N	306.24
Ethamsylate	F06	RN000217	C ₆ H ₆ O ₅ S.C ₄ H ₁₁ N	263.32
Moxonidine	F07	RN000217	C ₉ H ₁₂ CIN ₅ O	241.68
Etilefrine hydrochloride	F08	RN000217	C ₁₀ H ₁₅ NO ₂ .HCl	217.7
Alprostadil	F09	RN000217	C ₂₀ H ₃₄ O ₅	354.49
Tribenoside	F10	RN000217	C ₂₉ H ₃₄ O ₆	478.59
Amoxapine	C03	RN000206	C ₁₇ H ₁₆ CIN ₃ O	313.79
Rimexolone	F11	RN000217	C ₂₄ H ₃₄ O ₃	370.54
Isradipine	G02	RN000217	C ₁₉ H ₂₁ N ₃ O ₅	371.4
Tiletamine hydrochloride	G03	RN000217	C ₁₂ H ₁₇ NOS.HCl	259.8
Isometheptene mucate	G04	RN000217	2C ₉ H ₁₉ N.C ₆ H ₁₀ O ₈	246.33
Nifurtimox	G05	RN000217	C ₁₀ H ₁₃ N ₃ O ₅ S	287.3
Letrozole	G06	RN000217	C ₁₇ H ₁₁ N ₅	285.31
Arbutin	G07	RN000217	C ₁₂ H ₁₆ O ₇	272.26
Tocainide hydrochloride	G08	RN000217	C ₁₁ H ₁₆ N ₂ O.HCl	228.72
Benzathine benzylpenicillin	G09	RN000217	2C ₁₆ H ₁₈ N ₂ O ₅ S.C ₁₆ H ₂₀ N ₂	470.58

Risperidone	G10	RN000217	C23H27FN4O2	410.5
Cyproheptadine hydrochloride	C04	RN000206	C21H21N.HCl	323.87
Torsemide	G11	RN000217	C16H20N4O3S	348.43
Halofantrine hydrochloride	H02	RN000217	C26H30Cl2F3NO.HCl	536.9
Articaine hydrochloride	H03	RN000217	C13H20N2O3S.HCl	320.84
Nomegestrol acetate	H04	RN000217	C23H30O4	370.49
Pancuronium bromide	H05	RN000217	C35H60N2O4.2Br	732.69
Molindone hydrochloride	H06	RN000217	C16H24N2O2.HCl	312.84
Alcuronium chloride	H07	RN000217	C44H50N4O2.2Cl	737.82
Zalcitabine	H08	RN000217	C9H13N3O3	211.22
Methyldopate hydrochloride	H09	RN000217	C12H17NO4.HCl	275.73
Levocabastine hydrochloride	H10	RN000217	C26H29FN2O2.HCl	456.99
Famotidine	C05	RN000206	C8H15N7O2S3	337.45
Pyrvinium pamoate	H11	RN000217	2C26H28N3.C23H14O6	575.71
Rafoxanide	A02	RN000204	C19H11Cl2I2NO3	626.01
Etomidate	A02	RN000218	C14H16N2O2	244.3
Tridihexethyl chloride	A03	RN000218	C21H36NO.Cl	353.98
Penbutolol sulfate	A04	RN000218	2C18H29NO2.H2O4S	340.48
Prednicarbate	A05	RN000218	C27H36O8	488.58
Sertaconazole nitrate	A06	RN000218	C20H15Cl3N2OS.HNO3	500.79
Repaglinide	A07	RN000218	C27H36N2O4	452.6
Piretanide	A08	RN000218	C17H18N2O5S	362.41
Piperacetazine	A09	RN000218	C24H30N2O2S	410.58
Oxyphenbutazone	A10	RN000218	C19H20N2O3	324.38
Danazol	C06	RN000206	C22H27NO2	337.47
Quinethazone	A11	RN000218	C10H12ClN3O3S	289.74
Moricizine hydrochloride	B02	RN000218	C22H25N3O4S.HCl	463.99
Iopanoic acid	B03	RN000218	C11H12I3NO2	570.94
Pivmecillinam hydrochloride	B04	RN000218	C21H33N3O5S.HCl	476.04
Levopropoxyphene napsylate	B05	RN000218	C22H29NO2.C10H8O3S	547.72
Piperidolate hydrochloride	B06	RN000218	C21H25NO2.HCl	359.9
Trifluridine	B07	RN000218	C10H11F3N2O5	296.2
Oxprenolol hydrochloride	B08	RN000218	C15H23NO3.HCl	301.82
Ondansetron Hydrochloride	B09	RN000218	C18H19N3O.HCl	329.83
Propoxycaine hydrochloride	B10	RN000218	C16H26N2O3.HCl	330.86

Nicorandil	C07	RN000206	C8H9N3O4	211.18
Oxaprozin	B11	RN000218	C18H15NO3	293.33
Phensuximide	C02	RN000218	C11H11NO2	189.22
Ioxaglic acid	C03	RN000218	C24H21I6N5O8	1268.89
Naftifine hydrochloride	C04	RN000218	C21H21N.HCl	323.87
Meprylcaine hydrochloride	C05	RN000218	C14H21NO2.HCl	271.79
Milrinone	C06	RN000218	C12H9N3O	211.23
Methantheline bromide	C07	RN000218	C21H26NO3.Br	420.35
Ticarcillin sodium	C08	RN000218	C15H15N2O6S2.Na	406.41
Thiethylperazine dimalate	C09	RN000218	C22H29N3S2.2C4H6O5	667.8
Mesalamine	C10	RN000218	C7H7NO3	153.14
Imidurea	D02	RN000218	C11H16N8O8	388.3
Lansoprazole	D03	RN000218	C16H14F3N3O2S	369.37
Bethanechol chloride	D04	RN000218	C7H17N2O2.Cl	196.68
Cyproterone acetate	D05	RN000218	C24H29ClO4	416.95
(R)-Propranolol hydrochloride	D06	RN000218	C16H21NO2.HCl	295.81
Ciprofibrate	D07	RN000218	C13H14Cl2O3	289.16
Benzylpenicillin sodium	D09	RN000218	C16H17N2O4S.Na	356.38
Chlorambucil	D10	RN000218	C14H19Cl2NO2	304.22
Nomifensine maleate	C09	RN000206	C16H18N2.C4H4O4	354.41
Methiazole	D11	RN000218	C12H15N3O2S	265.34
(S)-propranolol hydrochloride	E02	RN000218	C16H21NO2.HCl	295.81
(-)-Eseroline fumarate salt	E03	RN000218	C13H18N2O.C4H4O4	334.37
D-cycloserine	E07	RN000218	C3H6N2O2	102.09
2-Chloropyrazine	E08	RN000218	C4H3ClN2	114.53
(+,-)-Synephrine	E09	RN000218	C9H13NO2	167.21
(S)-(-)-Cycloserine	E10	RN000218	C3H6N2O2	102.09
Dizocilpine maleate	C10	RN000206	C16H15N.C4H4O4	337.37
Homosalate	E11	RN000218	C16H22O3	262.35
Spaglumic acid	F02	RN000218	C11H16N2O8	304.26
Ranolazine	F03	RN000218	C24H33N3O4	427.55
Sulfadoxine	F05	RN000218	C12H14N4O4S	310.33
Cyclopentolate hydrochloride	F06	RN000218	C17H25NO3.HCl	327.85
Estriol	F07	RN000218	C18H24O3	288.39

(-)-Isoproterenol hydrochloride	F08	RN000218	C11H17NO3.HCl	247.72
Nialamide	F10	RN000218	C16H18N4O2	298.35
Meticrane	B02	RN000205	C10H13NO4S2	275.35
Acenocoumarol	C09	RN000211	C19H15NO6	353.33
Perindopril	G02	RN000218	C19H32N2O5	368.48
Fexofenadine HCl	G03	RN000218	C32H39NO4.HCl	538.13
Clonixin Lysinate	G05	RN000218	C13H11CIN2O2.C6H14N2O2	408.89
Verteporfin	G06	RN000218	C41H42N4O8	718.81
Meropenem	G07	RN000218	C17H25N3O5S	383.47
Ramipril	G08	RN000218	C23H32N2O5	416.52
Mephenytoin	G09	RN000218	C12H14N2O2	218.26
Rifabutin	G10	RN000218	C46H62N4O11	847.03
Naloxone hydrochloride	D02	RN000206	C19H21NO4.HCl	363.84
Parbendazole	G11	RN000218	C13H17N3O2	247.3
Mecamylamine hydrochloride	H02	RN000218	C11H21N.HCl	203.76
Procarbazine hydrochloride	H03	RN000218	C12H19N3O.HCl	257.76
Viomycin sulfate	H04	RN000218	C25H43N13O10.H2O4S	783.78
Saquinavir mesylate	H05	RN000218	C38H50N6O5.CH4O3S	766.97
Ronidazole	H06	RN000218	C6H8N4O4	200.16
Dorzolamide hydrochloride	H07	RN000218	C10H16N2O4S3.HCl	360.9
Azaperone	H08	RN000218	C19H22FN3O	327.41
Cefepime hydrochloride	H09	RN000218	C19H25N6O5S2.Cl	517.03
Clocortolone pivalate	H10	RN000218	C27H36ClFO5	495.04
Metolazone	D03	RN000206	C16H16CIN3O3S	365.84
Nadifloxacin	H11	RN000218	C19H21FN2O4	360.39
Carbadox	E06	RN000212	C11H10N4O4	262.23
Oxiconazole Nitrate	A07	RN000213	C18H13Cl4N3O.HNO3	492.15
Acipimox	F09	RN000212	C6H6N2O3	154.13
Benazepril HCl	G09	RN000212	C24H28N2O5.HCl	460.96
Ciprofloxacin hydrochloride monohydrate	D04	RN000206	C17H18FN3O3.HCl.H2O	385.83
Azelastine HCl	C10	RN000212	C22H24CIN3O.HCl	418.37
Celiprolol HCl	D10	RN000212	C20H33N3O4.HCl	415.96
Cytarabine	G06	RN000212	C9H13N3O5	243.22
Doxofylline	G11	RN000213	C11H14N4O4	266.26

Esmolol hydrochloride	A11	RN000216	C16H25NO4.HCl	331.84
Itraconazole	A08	RN000212	C35H38Cl2N8O4	705.65
Ampicillin trihydrate	D05	RN000206	C16H19N3O4S.3H2O	403.46
Liranaftate	A08	RN000214	C18H20N2O2S	328.44
Mirtazapine	H07	RN000211	C17H19N3	265.36
Modafinil	B06	RN000210	C15H15NO2S	273.36
Haloperidol	D06	RN000206	C21H23ClFNO2	375.87
Nefazodone HCl	F10	RN000209	C25H32ClN5O2.HCl	506.48
Nilvadipine	A09	RN000213	C19H19N3O6	385.38
Oxcarbazepine	E05	RN000210	C15H12N2O2	252.28
Rifapentine	G08	RN000210	C47H64N4O12	877.05
Ropinirole HCl	B09	RN000212	C16H24N2O.HCl	296.84
Sibutramine HCl	C08	RN000211	C17H26ClN.HCl	316.32
Naltrexone hydrochloride dihydrate	D07	RN000206	C20H23NO4.HCl.2H2O	413.9
Stanozolol	F03	RN000210	C21H32N2O	328.5
Zonisamide	C10	RN000213	C8H8N2O3S	212.23
Acitretin	C09	RN000213	C21H26O3	326.44
Rebamipide	A08	RN000213	C19H15ClN2O4	370.8
Diacerein	A10	RN000216	C19H12O8	368.3
Miglitol	E04	RN000211	C8H17NO5	207.23
Chlorpheniramine maleate	D08	RN000206	C16H19ClN2.C4H4O4	390.87
Venlafaxine	F06	RN000213	C17H27NO2	277.41
Irsogladine maleate	C11	RN000213	C9H7Cl2N5.C4H4O4	372.17
Acarbose	A09	RN000212	C25H43NO18	645.62
Carbidopa	F05	RN000212	C10H14N2O4	226.23
Aniracetam	G10	RN000212	C12H13NO3	219.24
Busulfan	A10	RN000206	C6H14O6S2	246.3
Nalbuphine hydrochloride	D09	RN000206	C21H27NO4.HCl	393.91
Docetaxel	G08	RN000219	C43H53NO14	807.9
Tibolone	E08	RN000207	C21H28O2	312.46
Tizanidine HCl	E03	RN000212	C9H8ClN5S.HCl	290.17
Temozolomide	D08	RN000212	C6H6N6O2	194.15
Tioconazole	E05	RN000206	C16H13Cl3N2OS	387.72
Granisetron	D09	RN000219	C18H24N4O	312.42
Ziprasidone Hydrochloride	A02	RN000212	C21H21ClN4OS.HCl	449.4

Montelukast	G07	RN000219	C35H36ClNO3S	586.2
Picotamide monohydrate	D10	RN000206	C21H20N4O3.H2O	394.44
Olmesartan	G05	RN000219	C29H30N6O6	558.6
Oxandrolone	C11	RN000206	C19H30O3	306.45
Thimerosal	E07	RN000213	C9H9HgO2S.Na	404.81
Toltrazuril	F11	RN000218	C18H14F3N3O4S	425.39
Topotecan	F02	RN000219	C23H23N3O5	421.46
Toremifene	H03	RN000216	C26H28ClNO	405.97
Tranilast	E02	RN000212	C18H17NO5	327.34
Tripelennamine hydrochloride	E10	RN000219	C16H21N3.HCl	291.83
Benzonate	B03	RN000205	C30H53NO11	603.76
Triamcinolone	D11	RN000206	C21H27FO6	394.44
4-aminosalicylic acid	G04	RN000218	C7H7NO3	153.14
5-fluorouracil	D02	RN000219	C4H3FN2O2	130.08
Acetylcysteine	B02	RN000219	C5H9NO3S	163.2
Acetylsalicylic acid	H10	RN000219	C9H8O4	180.16
Bromocryptine mesylate	E02	RN000206	C32H40BrN5O5.CH4O3S	750.72
Alendronate sodium	H02	RN000212	C4H12NO7P2.Na	271.08
Alfacalcidol	C07	RN000212	C27H44O2	400.65
Allopurinol	F11	RN000216	C5H4N4O	136.11
Amisulpride	G03	RN000212	C17H27N3O4S	369.49
Amlodipine	B05	RN000210	C20H25ClN2O5	408.89
Anastrozole	A03	RN000219	C17H19N5	293.37
Anethole-trithione	B05	RN000219	C10H8OS3	240.37
Anthralin	D10	RN000219	C14H10O3	226.23
Argatroban	B11	RN000212	C23H36N6O5S	508.64
Aripiprazole	E04	RN000219	C23H27Cl2N3O2	448.4
Dehydrocholic acid	E04	RN000206	C24H34O5	402.54
Asenapine maleate	D06	RN000207	C17H16ClNO.C4H4O4	401.85
Atorvastatin	F03	RN000219	C33H35FN2O5	558.66
Auranofin	B02	RN000215	C20H34AuO9PS	678.49
Azithromycin	F04	RN000219	C38H72N2O12	749
Benztropine mesylate	F07	RN000219	C21H25NO.CH4O3S	403.55
Bicalutamide	H07	RN000215	C18H14F4N2O4S	430.38
Bifonazole	F11	RN000219	C22H18N2	310.4

Erlotinib	B11	RN000210	C22H23N3O4	393.45
Bosentan	G03	RN000219	C27H29N5O6S	551.63
Bromhexine hydrochloride	B04	RN000219	C14H20Br2N2.HCl	412.6
Famciclovir	C02	RN000219	C14H19N5O4	321.34
Perphenazine	E06	RN000206	C21H26ClN3OS	403.98
Butalbital	F10	RN000210	C11H16N2O3	224.26
Butenafine Hydrochloride	E05	RN000212	C23H27N.HCl	353.94
Butylscopolammonium (n-) bromide	E10	RN000213	C21H30NO4.Br	440.38
Fentiazac	H05	RN000210	C17H12ClNO2S	329.81
Caffeine	B07	RN000219	C8H10N4O2	194.19
Calcipotriene	F04	RN000210	C27H40O3	412.62
Candesartan	C07	RN000219	C24H20N6O3	440.47
Canrenone	A03	RN000217	C22H28O3	340.47
Mefloquine hydrochloride	E07	RN000206	C17H16F6N2O.HCl	414.78
Carprofen	C05	RN000219	C15H12ClNO2	273.72
Carvedilol	B08	RN000219	C24H26N2O4	406.49
Cefdinir	C04	RN000219	C14H13N5O5S2	395.42
Gatifloxacin	G02	RN000219	C19H22FN3O4	375.4
Gemcitabine	G04	RN000219	C9H11F2N3O4	263.2
Gestrinone	A08	RN000217	C21H24O2	308.42
Guaiacol	C06	RN000217	C7H8O2	124.14
Haloproglin	A03	RN000210	C9H4Cl3IO	361.4
Isoconazole	E08	RN000206	C18H14Cl4N2O	416.14
Gefitinib	A03	RN000213	C22H24ClFN4O3	446.91
Escitalopram	B08	RN000212	C20H21FN2O.C2H2O4	414.44
Emedastine	D02	RN000212	C17H26N4O.2C4H4O4	534.57
Stavudine	G11	RN000216	C10H12N2O4	224.22
Spironolactone	E09	RN000206	C24H32O4S	416.58
Mepivacaine hydrochloride	A09	RN000219	C15H22N2O.HCl	282.82
Methenamine	B09	RN000219	C6H12N4	140.19
Buspirone hydrochloride	A02	RN000219	C21H31N5O2.HCl	421.97
Hydroxychloroquine sulfate	E11	RN000212	C18H26ClN3O.H2O4S	433.96
Ibandronate sodium	D10	RN000213	C9H22NO7P2.Na	341.22
Ibudilast	F05	RN000219	C14H18N2O	230.31
Idebenone	A05	RN000210	C19H30O5	338.45

Pirenzepine dihydrochloride	E10	RN000206	C19H21N5O2.2HCl	424.33
Imatinib	H02	RN000219	C29H31N7O	493.62
Imiquimod	G10	RN000219	C14H16N4	240.31
Ipsapirone	E10	RN000212	C19H23N5O3S	401.49
Isosorbide mononitrate	E04	RN000218	C6H9NO6	191.14
Itopride	H03	RN000210	C20H26N2O4	358.44
Lacidipine	B10	RN000212	C26H33NO6	455.56
Lamivudine	B08	RN000210	C8H11N3O3S	229.26
Hydroflumethiazide	B04	RN000205	C8H8F3N3O4S2	331.29
Dexamethasone acetate	E11	RN000206	C24H31FO6	434.51
Pefloxacin	D02	RN000210	C17H20FN3O3	333.37
Olopatadine hydrochloride	D08	RN000219	C21H23NO3.HCl	373.88
Phentermine hydrochloride	B10	RN000219	C10H15N.HCl	185.7
Glipizide	F02	RN000206	C21H27N5O4S	445.54
Phenylbutazone	C11	RN000217	C19H20N2O2	308.38
Pioglitazone	C08	RN000206	C19H20N2O3S	356.45
Clavulanate potassium salt	A07	RN000219	C8H8NO5.K	237.26
Pramipexole	C08	RN000217	C10H17N3S	211.33
Pranlukast	C02	RN000213	C27H23N5O4	481.52
Pranoprofen	E02	RN000213	C15H13NO3	255.28
Pravastatin	H06	RN000219	C23H36O7	424.54
Loxapine succinate	F03	RN000206	C18H18ClN3O.C4H6O4	445.91
Prothionamide	D07	RN000217	C9H12N2S	180.27
Pyridostigmine iodide	A04	RN000212	C9H13N2O2.I	308.12
Quetiapine hemifumarate	G05	RN000210	2C21H25N3O2S.C4H4O4	441.56
Raclopride	H10	RN000210	C15H20Cl2N2O3	347.24
Reboxetine mesylate	C02	RN000212	C19H23NO3.CH4O3S	409.51
Hydroxyzine dihydrochloride	F04	RN000206	C21H27ClN2O2.2HCl	447.83
Rimantadine Hydrochloride	E07	RN000212	C12H21N.HCl	215.77
Rivastigmine	H08	RN000219	C14H22N2O2	250.34
Rofecoxib	A04	RN000211	C17H14O4S	314.36
Rosiglitazone Hydrochloride	H07	RN000219	C18H19N3O3S.HCl	393.89
Rufloxacin	H05	RN000219	C17H18FN3O3S	363.41
Sarafloxacin	F09	RN000218	C20H17F2N3O3	385.37
Diltiazem hydrochloride	F05	RN000206	C22H26N2O4S.HCl	450.99

Secnidazole	E03	RN000213	C7H11N3O3	185.18
Sertindole	H11	RN000212	C24H26ClFN4O	440.95
Sildenafil	H09	RN000219	C22H30N6O4S	474.59
Sparfloxacin	E07	RN000219	C19H22F2N4O3	392.41
Sulbactam	A05	RN000219	C8H11NO5S	233.24
Sumatriptan succinate	D03	RN000213	C14H21N3O2S.C4H6O4	413.5
Tazobactam	D09	RN000213	C10H12N4O5S	300.29
Methotrexate	F06	RN000206	C20H22N8O5	454.45
Telmisartan	F09	RN000219	C33H30N4O2	514.63
Tenatoprazole	B06	RN000212	C16H18N4O3S	346.41
Tulobuterol	E11	RN000219	C12H18ClNO	227.74
Tylosin	F02	RN000213	C46H77NO17	916.12
Vardenafil	C10	RN000219	C23H32N6O4S	488.61
Vatalanib	H02	RN000210	C20H15ClN4	346.82
Vecuronium bromide	F08	RN000219	C34H57N2O4.Br	637.74
Astemizole	F07	RN000206	C28H31FN4O	458.58
Viloxazine hydrochloride	C09	RN000215	C13H19NO3.HCl	273.76
Vorinostat	C11	RN000218	C14H20N2O3	264.33
Warfarin	D11	RN000213	C19H16O4	308.34
Zafirlukast	E04	RN000212	C31H33N3O6S	575.69
Zileuton	C04	RN000213	C11H12N2O2S	236.29
Zopiclone	D11	RN000212	C17H17ClN6O3	388.82
Zotepine	C03	RN000210	C18H18ClNOS	331.87
Zaleplon	D04	RN000212	C17H15N5O	305.34
Clindamycin hydrochloride	F08	RN000206	C18H33ClN2O5S.HCl	461.45
Celecoxib	C06	RN000219	C17H14F3N3O2S	381.38
Chlormadinone acetate	C10	RN000217	C23H29ClO4	404.94
Cilnidipine	G09	RN000219	C27H28N2O7	492.53
Clarithromycin	E09	RN000219	C38H69NO13	747.97
Clinafloxacin	E10	RN000215	C17H17ClFN3O3	365.79
Terfenadine	F09	RN000206	C32H41NO2	471.69
Clobutinol hydrochloride	E03	RN000210	C14H22ClNO.HCl	292.25
Clodronate	E05	RN000213	CH2Cl2O6P2.2Na	288.86
Clofibrate	E02	RN000219	C12H15ClO3	242.7
Closantel	H11	RN000210	C22H14Cl2I2N2O2	663.08

Tetraethylenepentamine pentahydrochloride	C06	RN000213	C8H23N5.5HCl	371.61
Cefotaxime sodium salt	F10	RN000206	C16H16N5O7S2.Na	477.45
Desloratadine	E08	RN000219	C19H19ClN2	310.83
Dexfenfluramine hydrochloride	H09	RN000212	C12H16F3N.HCl	267.72
Dibenzepine hydrochloride	C08	RN000210	C18H21N3O.HCl	331.85
Diclazuril	B11	RN000219	C17H9Cl3N4O2	407.65
Dopamine hydrochloride	C03	RN000219	C8H11NO2.HCl	189.64
Doxycycline hydrochloride	A04	RN000219	C22H24N2O8.HCl	480.91
Sulfacetamide sodic hydrate	B05	RN000205	C8H9N2O3S.Na.H2O	254.25
Tetracycline hydrochloride	F11	RN000206	C22H24N2O8.HCl	480.91
Efavirenz	G07	RN000210	C14H9ClF3NO2	315.68
Enoxacin	D07	RN000219	C15H17FN4O3	320.33
Entacapone	A10	RN000212	C14H15N3O5	305.29
Ethinylestradiol	E05	RN000219	C20H24O2	296.41
Etofenamate	D03	RN000212	C18H18F3NO4	369.34
Etoricoxib	H10	RN000212	C18H15ClN2O2S	358.85
Etretinate	C11	RN000212	C23H30O3	354.49
Verapamil hydrochloride	G02	RN000206	C27H38N2O4.HCl	491.07
Exemestane	D06	RN000212	C20H24O2	296.41
Fleroxacin	A06	RN000219	C17H18F3N3O3	369.35
Floxuridine	A06	RN000217	C9H11FN2O5	246.2
Flubendazol	B03	RN000216	C16H12FN3O3	313.29
Fluconazole	C11	RN000219	C13H12F2N6O	306.28
Fluocinolone acetonide	E06	RN000219	C24H30F2O6	452.5
Dipyridamole	G03	RN000206	C24H40N8O4	504.64
Formestane	D08	RN000218	C19H26O3	302.42
Formoterol fumarate	H04	RN000219	2C19H24N2O4.C4H4O4	402.45
Fosinopril	G11	RN000219	C30H46NO7P	563.68
Fulvestrant	A03	RN000206	C32H47F5O3S	606.79
Levetiracetam	H08	RN000212	C8H14N2O2	170.21
Linezolid	F05	RN000210	C16H20FN3O4	337.35
Chlorhexidine	G04	RN000206	C22H30Cl2N10	505.46
Lofexidine	E02	RN000211	C11H12Cl2N2O	259.14
Loracarbef	F02	RN000212	C16H16ClN3O4	349.78

Loratadine	C05	RN000213	C22H23ClN2O2	382.89
Losartan	F06	RN000219	C22H23ClN6O	422.92
Melengestrol acetate	B03	RN000219	C25H32O4	396.53
Loperamide hydrochloride	G05	RN000206	C29H33ClN2O2.HCl	513.51
Mevastatin	A03	RN000212	C23H34O5	390.52
Misoprostol	F04	RN000218	C22H38O5	382.55
Mitotane	D04	RN000219	C14H10Cl4	320.05
Moxifloxacin	H03	RN000219	C21H24FN3O4	401.44
Nalidixic acid sodium salt	D05	RN000213	C12H11N2O3.Na	254.22
Nicotinamide	A11	RN000212	C6H6N2O	122.13
Chlortetracycline hydrochloride	G06	RN000206	C22H23ClN2O8.HCl	515.35
Norgestimate	C09	RN000217	C23H31NO3	369.51
Nylidrin	F03	RN000215	C19H25NO2	299.42
Olanzapine	E02	RN000215	C17H20N4S	312.44
Opipramol dihydrochloride	D04	RN000213	C23H29N3O.2HCl	436.43
Oxfendazol	C05	RN000217	C15H13N3O3S	315.35
Tamoxifen citrate	G07	RN000206	C26H29NO.C6H8O7	563.66
Oxibendazol	E09	RN000212	C12H15N3O3	249.27
Tomoxetine hydrochloride	H05	RN000212	C17H21NO.HCl	291.82
Tosufloxacin hydrochloride	G06	RN000210	C19H15F3N4O3.HCl	440.81
Tramadol hydrochloride	E08	RN000213	C16H25NO2.HCl	299.84
Troglitazone	B04	RN000212	C24H27NO5S	441.55
Mercaptopurine	G05	RN000212	C5H4N4S	152.18
Nicergoline	G08	RN000206	C24H26BrN3O3	484.4
Amfepramone hydrochloride	E03	RN000206	C13H19NO.HCl	241.76
Hexachlorophene	H11	RN000219	C13H6Cl6O2	406.91
Estradiol Valerate	A11	RN000219	C23H32O3	356.51
Chloroxine	H03	RN000206	C9H5Cl2NO	214.05
Oxacillin sodium	D06	RN000213	C19H18N3O5S.Na	423.43
Amcinonide	B06	RN000219	C28H35FO7	502.59
Penicillamine	C03	RN000213	C5H11NO2S	149.21
Rifaximin	A10	RN000219	C43H51N3O11	785.9
Triclosan	D06	RN000219	C12H7Cl3O2	289.55
Canrenoic acid potassium salt	G09	RN000206	C22H29O4.K	396.57
Racepinephrine HCl	G06	RN000219	C9H13NO3.HCl	219.67

Cyclophosphamide	E03	RN000219	C7H15Cl2N2O2P	261.09
Valproic acid	A08	RN000219	C8H16O2	144.22
Fludarabine	C08	RN000219	C10H12FN5O4	285.24
Cladribine	C09	RN000219	C10H12ClN5O3	285.69
Cortisol acetate	B02	RN000216	C23H32O6	404.51
Mesna	D03	RN000219	C2H5O3S2.Na	164.18
Penciclovir	H07	RN000212	C10H15N5O3	253.26
Amifostine	B03	RN000210	C5H15N2O3PS	214.22
Thiopropazine dimesylate	G10	RN000206	C22H30N4O2S2.2CH4O3S	638.85
Nalmefene hydrochloride	F10	RN000219	C21H25NO3.HCl	375.9
Pentobarbital	A05	RN000212	C11H18N2O3	226.28
Lamotrigine	D11	RN000219	C9H7Cl2N5	256.1
Topiramate	E06	RN000218	C12H21NO8S	339.37
Irinotecan hydrochloride trihydrate	E11	RN000213	C33H38N4O6.HCl.3H2O	677.2
Rabeprazole Sodium salt	H10	RN000215	C18H21N3O3S.Na	382.44
Ambrisentan	D05	RN000219	C22H22N2O4	378.43
Camylofine chlorhydrate	C03	RN000212	C19H32N2O2.2HCl	393.4
Fomepizole	D07	RN000212	C4H6N2	82.11
Heptaminol hydrochloride	B06	RN000205	C8H19NO.HCl	181.71
Dihydroergotamine tartrate	G11	RN000206	2C33H37N5O5.C4H6O6	658.73
Voriconazole	C06	RN000212	C16H14F3N5O	349.32
Fenipentol	F03	RN000212	C11H16O	164.25
Acamprosate calcium	F11	RN000212	2C5H10NO4S.Ca	200.24
Diosmin	F04	RN000212	C28H32O15	608.56
Valacyclovir hydrochloride	C10	RN000210	C13H20N6O4.HCl	360.8
Mizolastine	G02	RN000212	C24H25FN6O	432.5
Acefylline	C08	RN000213	C9H10N4O4	238.2
Ibutilide fumarate	E06	RN000213	2C20H36N2O3S.C4H4O4	442.63
Deflazacort	B08	RN000215	C25H31NO6	441.53
Erythromycin	H02	RN000206	C37H67NO13	733.95
Dolasetron mesilate	A06	RN000216	C19H20N2O3.CH6O4S.H2O	438.5
Aceclidine Hydrochloride	H06	RN000212	C9H15NO2.HCl	205.69
Abacavir Sulfate	C03	RN000216	2C14H18N6O.H2O4S	335.38
Darifenacin hydrobromide	A10	RN000217	C28H30N2O2.HBr	507.47
Fadrozole hydrochloride	H06	RN000207	C14H13N3.HCl	259.74

Levalbuterol hydrochloride	E05	RN000218	C13H21NO3.HCl	275.78
Didanosine	H04	RN000206	C10H12N4O3	236.23
Josamycin	H05	RN000206	C42H69NO15	828.02
Paclitaxel	H06	RN000206	C47H51NO14	853.93
Ivermectin	H07	RN000206	C48H74O14	875.12
Gallamine triethiodide	H08	RN000206	C30H60N3O3.3I	891.54
Neomycin sulfate	H09	RN000206	C23H46N6O13.H2O4S	712.74
Dihydrostreptomycin sulfate	H10	RN000206	2C21H41N7O12.3H2O4S	730.72
Sulfathiazole	B07	RN000205	C9H9N3O2S2	255.32
Gentamicine sulfate	H11	RN000206	C21H43N5O7.C20H41N5O7.C19H39N5O7.H2O4S	1488.82
Aprepitant	C08	RN000214	C23H21F7N4O3	534.44
Pinaverium bromide	A11	RN000213	C26H41BrNO4.Br	591.42
Indatraline hydrochloride	A11	RN000217	C16H15Cl2N.HCl	328.67
Pemirolast potassium	D09	RN000209	C10H7N6O.K	266.31
(-)-Emtricitabine	F06	RN000212	C8H10FN3O3S	247.25
Isoniazid	A02	RN000207	C6H7N3O	137.14
Pentylene tetrazole	A03	RN000207	C6H10N4	138.17
Chlorzoxazone	A04	RN000207	C7H4ClNO2	169.57
Ornidazole	A05	RN000207	C7H10ClN3O3	219.63
Ethosuximide	A06	RN000207	C7H11NO2	141.17
Mafenide hydrochloride	A07	RN000207	C7H10N2O2S.HCl	222.69
Riluzole hydrochloride	A08	RN000207	C8H5F3N2OS.HCl	270.66
Nitrofurantoin	A09	RN000207	C8H6N4O5	238.16
Hydralazine hydrochloride	A10	RN000207	C8H8N4.HCl	196.64
Levodopa	B08	RN000205	C9H11NO4	197.19
Phenelzine sulfate	A11	RN000207	C8H12N2.H2O4S	234.28
Tranexamic acid	B02	RN000207	C8H15NO2	157.21
Etofilline	B03	RN000207	C9H12N4O3	224.22
Tranlycypromine hydrochloride	B04	RN000207	C9H11N.HCl	169.65
Alverine citrate salt	B05	RN000207	C20H27N.C6H8O7	473.57
Aceclofenac	B06	RN000207	C16H13Cl2NO4	354.19
Iproniazide phosphate	B07	RN000207	C9H13N3O.H3O4P	277.22
Sulfamethoxazole	B08	RN000207	C10H11N3O3S	253.28
Mephenesin	B09	RN000207	C10H14O3	182.22
Phenformin hydrochloride	B10	RN000207	C10H15N5.HCl	241.72

Idoxuridine	B09	RN000205	C9H11N2O5	354.1
Flutamide	B11	RN000207	C11H11F3N2O3	276.22
Ampyrone	C02	RN000207	C11H13N3O	203.25
Levamisole hydrochloride	C03	RN000207	C11H12N2S.HCl	240.76
Pargyline hydrochloride	C04	RN000207	C11H13N.HCl	195.69
Methocarbamol	C05	RN000207	C11H15NO5	241.25
Aztreonam	C06	RN000207	C13H17N5O8S2	435.44
Cloxacillin sodium salt	C07	RN000207	C19H17ClN3O5S.Na	457.87
Catharanthine	C08	RN000207	C21H24N2O2	336.44
Pentolinium bitartrate	C09	RN000207	C15H32N2.2C4H4O6	536.59
Aminopurine, 6-benzyl	C10	RN000207	C12H11N5	225.25
Captopril	B10	RN000205	C9H15NO3S	217.29
Tolbutamide	C11	RN000207	C12H18N2O3S	270.35
Midodrine hydrochloride	D02	RN000207	C12H18N2O4.HCl	290.75
Thalidomide	D03	RN000207	C13H10N2O4	258.24
Oxolinic acid	D04	RN000207	C13H11NO5	261.24
Nimesulide	D05	RN000207	C13H12N2O5S	308.31
Pentoxifylline	D07	RN000207	C13H18N4O3	278.31
Metaraminol bitartrate	D08	RN000207	C9H13NO2.2C4H6O6	467.39
Salbutamol	D09	RN000207	C13H21NO3	239.32
Prilocaine hydrochloride	D10	RN000207	C13H20N2O.HCl	256.78
Allantoin	A03	RN000205	C4H6N4O3	158.12
Minoxidil	B11	RN000205	C9H15N5O	209.25
Camptothecin (S,+)	D11	RN000207	C20H16N2O4	348.36
Ranitidine hydrochloride	E02	RN000207	C13H22N4O3S.HCl	350.87
Tiratricol, 3,3',5-triiodothyroacetic acid	E03	RN000207	C14H9I3O4	621.94
Flufenamic acid	E04	RN000207	C14H10F3NO2	281.24
Flumequine	E05	RN000207	C14H12FNO3	261.26
Tolfenamic acid	E06	RN000207	C14H12ClNO2	261.71
Meclofenamic acid sodium salt monohydrate	E07	RN000207	C14H10Cl2NO2.Na.H2O	336.16
Trimethoprim	E09	RN000207	C14H18N4O3	290.32
Metoclopramide monohydrochloride	E10	RN000207	C14H22ClN3O2.HCl	336.26
Sulfaphenazole	C02	RN000205	C15H14N4O2S	314.37
Fenbendazole	E11	RN000207	C15H13N3O2S	299.35

Piroxicam	F02	RN000207	C15H13N3O4S	331.35
Pyrantel tartrate	F03	RN000207	C11H14N2S.C4H6O6	356.4
Fenspiride hydrochloride	F04	RN000207	C15H20N2O2.HCl	296.8
Gemfibrozil	F05	RN000207	C15H22O3	250.34
Mefexamide hydrochloride	F06	RN000207	C15H24N2O3.HCl	316.83
Tiapride hydrochloride	F07	RN000207	C15H24N2O4S.HCl	364.89
Mebendazole	F08	RN000207	C16H13N3O3	295.3
Fenbufen	F09	RN000207	C16H14O3	254.29
Ketoprofen	F10	RN000207	C16H14O3	254.29
Panthenol (D)	C03	RN000205	C9H19NO4	205.26
Indapamide	F11	RN000207	C16H16ClN3O3S	365.84
Norfloxacin	G02	RN000207	C16H18FN3O3	319.34
Antimycin A	G03	RN000207	C28H40N2O9	548.64
Xylometazoline hydrochloride	G04	RN000207	C16H24N2.HCl	280.84
Oxymetazoline hydrochloride	G05	RN000207	C16H24N2O.HCl	296.84
Nifenazone	G06	RN000207	C17H16N4O2	308.34
Griseofulvin	G07	RN000207	C17H17ClO6	352.77
Clemizole hydrochloride	G08	RN000207	C19H20ClN3.HCl	362.3
Tropicamide	G09	RN000207	C17H20N2O2	284.36
Nefopam hydrochloride	G10	RN000207	C17H19NO.HCl	289.81
Sulfadiazine	C04	RN000205	C10H10N4O2S	250.28
Phentolamine hydrochloride	G11	RN000207	C17H19N3O.HCl	317.82
Etodolac	H02	RN000207	C17H21NO3	287.36
Scopolamin-N-oxide hydrobromide	H03	RN000207	C17H21NO5.HBr	400.27
Hyoscyamine (L)	H04	RN000207	C17H23NO3	289.38
Chlorphensin carbamate	H05	RN000207	C10H12ClNO4	245.66
Dilazep dihydrochloride	H07	RN000207	C31H44N2O10.2HCl	677.62
Ofloxacin	H08	RN000207	C18H20FN3O4	361.38
Lomefloxacin hydrochloride	H09	RN000207	C17H19F2N3O3.HCl	387.82
Orphenadrine hydrochloride	H10	RN000207	C18H23NO.HCl	305.85
Norethynodrel	C05	RN000205	C20H26O2	298.43
Proglumide	H11	RN000207	C18H26N2O4	334.42
Mexiletine hydrochloride	A02	RN000208	C11H17NO.HCl	215.72
Flavoxate hydrochloride	A03	RN000208	C24H25NO4.HCl	427.93

Bufexamac	A04	RN000208	C12H17NO3	223.27
Glutethimide, para-amino	A05	RN000208	C13H16N2O2	232.28
Dropropizine (R,S)	A06	RN000208	C13H20N2O2	236.32
Pinacidil	A07	RN000208	C13H19N5	245.33
Albendazole	A08	RN000208	C12H15N3O2S	265.34
Clonidine hydrochloride	A09	RN000208	C9H9Cl2N3.HCl	266.56
Bupropion hydrochloride	A10	RN000208	C13H18ClNO.HCl	276.21
Thiamphenicol	C06	RN000205	C12H15Cl2NO5S	356.23
Alprenolol hydrochloride	A11	RN000208	C15H23NO2.HCl	285.82
Chlorothiazide	B02	RN000208	C7H6ClN3O4S2	295.72
Diphenidol hydrochloride	B03	RN000208	C21H27NO.HCl	345.92
Norethindrone	B04	RN000208	C20H26O2	298.43
Nortriptyline hydrochloride	B05	RN000208	C19H21N.HCl	299.85
Niflumic acid	B06	RN000208	C13H9F3N2O2	282.22
Isotretinoin	B07	RN000208	C20H28O2	300.44
Retinoic acid	B08	RN000208	C20H28O2	300.44
Antazoline hydrochloride	B09	RN000208	C17H19N3.HCl	301.82
Ethacrynic acid	B10	RN000208	C13H12Cl2O4	303.14
Cimetidine	C07	RN000205	C10H16N6S	252.34
Praziquantel	B11	RN000208	C19H24N2O2	312.42
Ethisterone	C02	RN000208	C21H28O2	312.46
Triprolidine hydrochloride	C03	RN000208	C19H22N2.HCl	314.86
Doxepin hydrochloride	C04	RN000208	C19H21NO.HCl	315.85
Dyclonine hydrochloride	C05	RN000208	C18H27NO2.HCl	325.88
Dimenhydrinate	C06	RN000208	C17H21NO.C7H7ClN4O2	469.98
Disopyramide	C07	RN000208	C21H29N3O	339.48
Clotrimazole	C08	RN000208	C22H17ClN2	344.85
Vinpocetine	C09	RN000208	C22H26N2O2	350.46
Clomipramine hydrochloride	C10	RN000208	C19H23ClN2.HCl	351.32
Doxylamine succinate	C08	RN000205	C17H22N2O.C4H6O4	388.47
Fendiline hydrochloride	C11	RN000208	C23H25N.HCl	351.92
Vincamine	D02	RN000208	C21H26N2O3	354.45
Indomethacin	D03	RN000208	C19H16ClNO4	357.8
Cortisone	D04	RN000208	C21H28O5	360.45
Prednisolone	D05	RN000208	C21H28O5	360.45

Fenofibrate	D06	RN000208	C20H21ClO4	360.84
Bumetanide	D07	RN000208	C17H20N2O5S	364.42
Labetalol hydrochloride	D08	RN000208	C19H24N2O3.HCl	364.87
Cinnarizine	D09	RN000208	C26H28N2	368.53
Methylprednisolone, 6-alpha	D10	RN000208	C22H30O5	374.48
Ethambutol dihydrochloride	C09	RN000205	C10H24N2O2.2HCl	277.23
Quinidine hydrochloride monohydrate	D11	RN000208	C20H24N2O2.HCl.H2O	378.91
Fludrocortisone acetate	E02	RN000208	C23H31FO6	422.5
Fenoterol hydrobromide	E03	RN000208	C17H21NO4.HBr	384.27
Homochlorcyclizine dihydrochloride	E04	RN000208	C19H23ClN2.2HCl	387.78
Diethylcarbamazine citrate	E05	RN000208	C10H21N3O.C6H8O7	391.43
Chenodiol	E06	RN000208	C24H40O4	392.58
Perhexiline maleate	E07	RN000208	C19H35N.C4H4O4	393.57
Oxybutynin chloride	E08	RN000208	C22H31NO3.HCl	393.96
Spiperone	E09	RN000208	C23H26FN3O2	395.48
Pyrimidine maleate	E10	RN000208	C17H23N3O.C4H4O4	401.46
Antipyrine	C10	RN000205	C11H12N2O	188.23
Sulfinpyrazone	E11	RN000208	C23H20N2O3S	404.49
Dantrolene sodium salt	F02	RN000208	C14H9N4O5.Na	336.24
Trazodone hydrochloride	F03	RN000208	C19H22ClN5O.HCl	408.33
Glaufenine hydrochloride	F04	RN000208	C19H17ClN2O4.HCl	409.27
Pimethixene maleate	F05	RN000208	C19H19NS.C4H4O4	409.5
Pergolide mesylate	F06	RN000208	C19H26N2S.CH4O3S	410.61
Acemetacin	F07	RN000208	C21H18ClNO6	415.83
Benzylamine hydrochloride	F08	RN000208	C19H23N3O.HCl	345.87
Fipexide hydrochloride	F09	RN000208	C20H21ClN2O4.HCl	425.31
Mifepristone	F10	RN000208	C29H35NO2	429.61
Acetazolamide	A04	RN000205	C4H6N4O3S2	222.25
Antipyrine, 4-hydroxy	C11	RN000205	C11H12N2O2	204.23
Diperodon hydrochloride	F11	RN000208	C22H27N3O4.HCl	433.94
Lisinopril	G02	RN000208	C21H31N3O5.2H2O	441.53
Lincomycin hydrochloride	G03	RN000208	C18H34N2O6S.HCl	443.01
Telenzepine dihydrochloride	G04	RN000208	C19H22N4O2S.2HCl	443.4
Econazole nitrate	G05	RN000208	C18H15Cl3N2O.HNO3	444.7

Bupivacaine hydrochloride	G06	RN000208	C18H28N2O.HCl	324.9
Clemastine fumarate	G07	RN000208	C21H26ClNO.C4H4O4	459.97
Oxytetracycline dihydrate	G08	RN000208	C22H24N2O9.2H2O	496.47
Pimozide	G09	RN000208	C28H29F2N3O	461.56
Amodiaquin dihydrochloride dihydrate	G10	RN000208	C20H22ClN3O.2HCl.2H2O	551.71
Chloramphenicol	D02	RN000205	C11H12Cl2N2O5	323.13
Mebeverine hydrochloride	G11	RN000208	C25H35NO5.HCl	466.02
Ifenprodil tartrate	H02	RN000208	C21H27NO2.C4H6O6	475.54
Flunarizine dihydrochloride	H03	RN000208	C26H26F2N2.2HCl	477.43
Trifluoperazine dihydrochloride	H04	RN000208	C21H24F3N3S.2HCl	480.42
Enalapril maleate	H05	RN000208	C20H28N2O5.C4H4O4	492.53
Minocycline hydrochloride	H06	RN000208	C23H27N3O7.HCl	493.95
Glibenclamide	H07	RN000208	C23H28ClN3O5S	494.01
Guanethidine sulfate	H08	RN000208	2C10H22N4.H2O4S	247.35
Quinacrine dihydrochloride dihydrate	H09	RN000208	C23H30ClN3O.2HCl.2H2O	595.81
Clofilium tosylate	H10	RN000208	C21H37ClN.C7H7O3S	510.19
Epirizole	D03	RN000205	C11H14N4O2	234.26
Fluphenazine dihydrochloride	H11	RN000208	C22H26F3N3OS.2HCl	510.45
Streptomycin sulfate	A02	RN000209	2C21H39N7O12.3H2O4S	728.7
Alfuzosin hydrochloride	A03	RN000209	C19H27N5O4.HCl	425.92
Chlorpropamide	A04	RN000209	C10H13ClN2O3S	276.74
Phenylpropanolamine hydrochloride	A05	RN000209	C9H13NO.HCl	187.67
Ascorbic acid	A06	RN000209	C6H8O6	176.13
Methyl dopa (L,-)	A07	RN000209	C10H13NO4	211.22
Cefoperazone dihydrate	A08	RN000209	C25H27N9O8S2.2H2O	681.71
Zoxazolamine	A09	RN000209	C7H5ClN2O	168.58
Tacrine hydrochloride	A10	RN000209	C13H14N2.HCl	234.73
Diprophylline	D04	RN000205	C10H14N4O4	254.25
Bisoprolol fumarate	A11	RN000209	2C18H31NO4.C4H4O4	383.49
Tremorine dihydrochloride	B02	RN000209	C12H20N2.2HCl	265.23
Practolol	B03	RN000209	C14H22N2O3	266.34
Zidovudine, AZT	B04	RN000209	C10H13N5O4	267.25
Sulfisoxazole	B05	RN000209	C11H13N3O3S	267.31

Zaprinast	B06	RN000209	C13H13N5O2	271.28
Chlormezanone	B07	RN000209	C11H12ClNO3S	273.74
Procainamide hydrochloride	B08	RN000209	C13H21N3O.HCl	271.79
N6-methyladenosine	B09	RN000209	C11H15N5O4	281.27
Guanfacine hydrochloride	B10	RN000209	C9H9Cl2N3O.HCl	282.56
Triamterene	D05	RN000205	C12H11N7	253.27
Domperidone	B11	RN000209	C22H24ClN5O2	425.92
Furosemide	C02	RN000209	C12H11ClN2O5S	330.75
Methapyrilene hydrochloride	C03	RN000209	C14H19N3S.HCl	297.85
Desipramine hydrochloride	C04	RN000209	C18H22N2.HCl	302.85
Clorgyline hydrochloride	C05	RN000209	C13H15Cl2NO.HCl	308.64
Clenbuterol hydrochloride	C06	RN000209	C12H18Cl2N2O.HCl	313.66
Maprotiline hydrochloride	C07	RN000209	C20H23N.HCl	313.87
Thioguanosine	C08	RN000209	C10H13N5O4S	299.31
Chlorprothixene hydrochloride	C09	RN000209	C18H18ClNS.HCl	352.33
Ritodrine hydrochloride	C10	RN000209	C17H21NO3.HCl	323.82
Dapsone	D06	RN000205	C12H12N2O2S	248.31
Clozapine	C11	RN000209	C18H19ClN4	326.83
Chlorthalidone	D02	RN000209	C14H11ClN2O4S	338.77
Dobutamine hydrochloride	D03	RN000209	C18H23NO3.HCl	337.85
Moclobemide	D04	RN000209	C13H17ClN2O2	268.75
Clopamide	D05	RN000209	C14H20ClN3O3S	345.85
Hycanthone	D06	RN000209	C20H24N2O2S	356.49
Adenosine 5'-monophosphate monohydrate	D07	RN000209	C10H14N5O7P.H2O	365.25
Amoxicillin	D08	RN000209	C16H19N3O5S	365.41
Dextromethorphan hydrobromide monohydrate	D10	RN000209	C18H25NO.HBr.H2O	370.34
Troleandomycin	D07	RN000205	C41H67NO15	813.99
Droperidol	D11	RN000209	C22H22FN3O2	379.44
Bambuterol hydrochloride	E02	RN000209	C18H29N3O5.HCl	403.91
Betamethasone	E03	RN000209	C22H29FO5	392.47
Colchicine	E04	RN000209	C22H25NO6	399.45
Metergoline	E05	RN000209	C25H29N3O2	403.53
Brinzolamide	E06	RN000209	C12H21N3O5S3	383.51
Ambroxol hydrochloride	E07	RN000209	C13H18Br2N2O.HCl	414.57

Benfluorex hydrochloride	E08	RN000209	C19H20F3NO2.HCl	387.83
Bepidil hydrochloride	E09	RN000209	C24H34N2O.HCl	403.01
Meloxicam	E10	RN000209	C14H13N3O4S2	351.41
Pyrimethamine	D08	RN000205	C12H13ClN4	248.72
Benzbromarone	E11	RN000209	C17H12Br2O3	424.09
Ketotifen fumarate	F02	RN000209	C19H19NOS.C4H4O4	425.5
Debrisoquin sulfate	F03	RN000209	2C10H13N3.H2O4S	224.28
Amethopterin (R,S)	F04	RN000209	C20H22N8O5	454.45
Methylethergometrine maleate	F05	RN000209	C20H25N3O2.C4H4O4	455.51
Methiothepin maleate	F06	RN000209	C20H24N2S2.C4H4O4	472.63
Clofazimine	F07	RN000209	C27H22Cl2N4	473.41
Nafronyl oxalate	F08	RN000209	C24H33NO3.C2H2O4	473.58
Bezafibrate	F09	RN000209	C19H20ClNO4	361.83
Hexamethonium dibromide dihydrate	D09	RN000205	C12H30N2.2Br.2H2O	398.23
Clebopride maleate	F11	RN000209	C20H24ClN3O2.C4H4O4	489.96
Lidoflazine	G02	RN000209	C30H35F2N3O	491.63
Betaxolol hydrochloride	G03	RN000209	C18H29NO3.HCl	343.9
Nicardipine hydrochloride	G04	RN000209	C26H29N3O6.HCl	516
Probucol	G05	RN000209	C31H48O2S2	516.86
Mitoxantrone dihydrochloride	G06	RN000209	C22H28N4O6.2HCl	517.41
GBR 12909 dihydrochloride	G07	RN000209	C28H32F2N2O.2HCl	523.5
Carbetapentane citrate	G08	RN000209	C20H31NO3.C6H8O7	525.6
Dequalinium dichloride	G09	RN000209	C30H40N4.2Cl	527.59
Ketoconazole	G10	RN000209	C26H28Cl2N4O4	531.44
Diflunisal	D10	RN000205	C13H8F2O3	250.2
Fusidic acid sodium salt	G11	RN000209	C31H47O6.Na	538.71
Terbutaline hemisulfate	H02	RN000209	2C12H19NO3.H2O4S	274.33
Ketanserin tartrate hydrate	H03	RN000209	C22H22FN3O3.C4H8O7.H2O	563.54
Hemicholinium bromide	H04	RN000209	C24H34N2O4.2Br	574.36
Kanamycin A sulfate	H05	RN000209	C18H36N4O11.H2O4S	582.59
Amikacin hydrate	H06	RN000209	C22H43N5O13.2H2O	621.64
Etoposide	H07	RN000209	C29H32O13	588.57
Clomiphene citrate (Z,E)	H08	RN000209	C26H28ClNO.C6H8O7	598.1
Oxantel pamoate	H09	RN000209	2C13H16N2O.C23H16O6	410.48
Prochlorperazine dimaleate	H10	RN000209	C20H24ClN3S.2C4H4O4	606.1

Metformin hydrochloride	A05	RN000205	C4H11N5.HCl	165.63
Niclosamide	D11	RN000205	C13H8Cl2N2O4	327.13
Hesperidin	H11	RN000209	C28H34O15	610.57
Testosterone propionate	A02	RN000210	C22H32O3	344.5
Thyroxine (L)	A04	RN000210	C15H11I4NO4	776.88
Pepstatin A	A06	RN000210	C34H63N5O9	685.91
Morpholinoethylamino-3-benzocyclohepta-(5,6-c)-pyridazine dihydrochloride	A07	RN000210	C19H24N4O.2HCl	397.35
Adamantamine fumarate	A08	RN000210	2C10H17N.C4H4O4	209.29
Butoconazole nitrate	A09	RN000210	C19H17Cl3N2S.HNO3	474.79
Amiodarone hydrochloride	A10	RN000210	C25H29I2NO3.HCl	681.78
Procaine hydrochloride	E02	RN000205	C13H20N2O2.HCl	272.78
Amphotericin B	A11	RN000210	C47H73NO17	924.1
Androsterone	B02	RN000210	C19H30O2	290.45
Carbarsone	B04	RN000210	C7H9AsN2O4	260.08
Bacampicillin hydrochloride	B07	RN000210	C21H27N3O7S.HCl	501.99
Biotin	B09	RN000210	C10H16N2O3S	244.31
Bisacodyl	B10	RN000210	C22H19NO4	361.4
Moxisylyte hydrochloride	E03	RN000205	C16H25NO3.HCl	315.84
Suloctidil	C02	RN000210	C20H35NOS	337.57
Carisoprodol	C04	RN000210	C12H24N2O4	260.34
Cephalosporanic acid, 7-amino	C05	RN000210	C10H12N2O5S	272.28
Chicago sky blue 6B	C06	RN000210	C34H24N6O16S4.4Na	992.82
Buflomedil hydrochloride	C07	RN000210	C17H25NO4.HCl	343.85
Roxatidine Acetate HCl	C09	RN000210	C19H28N2O4.HCl	384.91
Betazole hydrochloride	E04	RN000205	C5H9N3.2HCl	184.07
Cisapride	C11	RN000210	C23H29ClFN3O4	465.96
Corticosterone	D03	RN000210	C21H30O4	346.47
Cyanocobalamin	D04	RN000210	C63H88CoN14O14P	1355.4
Cefadroxil	D05	RN000210	C16H17N3O5S	363.39
Cyclosporin A	D06	RN000210	C62H111N11O12	1202.64
Digitoxigenin	D07	RN000210	C23H34O4	374.53
Digoxin	D08	RN000210	C41H64O14	780.96
Doxorubicin hydrochloride	D09	RN000210	C27H29NO11.HCl	579.99
Carbimazole	D10	RN000210	C7H10N2O2S	186.23

Isoxicam	E05	RN000205	C14H13N3O5S	335.34
Epiandrosterone	D11	RN000210	C19H30O2	290.45
Estradiol-17 beta	E02	RN000210	C18H24O2	272.39
Gabazine bromide	E04	RN000210	C15H18N3O3.Br	368.23
Cyclobenzaprine hydrochloride	E06	RN000210	C20H21N.HCl	311.86
Carteolol hydrochloride	E07	RN000210	C16H24N2O3.HCl	328.84
Hydrocortisone base	E08	RN000210	C21H30O5	362.47
Hydroxytetracycline maleate (R,S)	E09	RN000210	C13H14N2O.C4H4O4	330.34
Pilocarpine nitrate	E10	RN000210	C11H16N2O2.HNO3	271.27
Naproxen	E06	RN000205	C14H14O3	230.27
Dicloxacin sodium salt hydrate	E11	RN000210	C19H16Cl2N3O5S.Na.H2O	510.34
Alizapride HCl	F02	RN000210	C16H21N5O2.HCl	351.84
Mebhydroline 1,5-naphthalenedisulfonate	F06	RN000210	C19H20N2.C10H8O6S2	420.53
Meclocycline sulfosalicylate	F07	RN000210	C22H21ClN2O8.C7H6O6S	695.06
Meclozine dihydrochloride	F08	RN000210	C25H27ClN2.2HCl	463.88
Melatonin	F09	RN000210	C13H16N2O2	232.28
Naphazoline hydrochloride	E07	RN000205	C14H14N2.HCl	246.74
Dinoprost trometamol	F11	RN000210	C20H34O5.C4H11NO3	475.63
Tropisetron HCl	G02	RN000210	C17H20N2O2.HCl	320.82
Cefixime	G03	RN000210	C16H15N5O7S2	453.46
Metrizamide	G04	RN000210	C18H22I3N3O8	789.1
Neostigmine bromide	G09	RN000210	C12H19N2O2.Br	303.2
Niridazole	G10	RN000210	C6H6N4O3S	214.2
Ticlopidine hydrochloride	E08	RN000205	C14H14ClNS.HCl	300.25
Ceforanide	G11	RN000210	C20H21N7O6S2	519.56
Cefotetan	H04	RN000210	C17H17N7O8S4	575.62
Brompheniramine maleate	H06	RN000210	C16H19BrN2.C4H4O4	435.32
Primaquine diphosphate	H07	RN000210	C15H21N3O.2H3O4P	455.34
Progesterone	H08	RN000210	C21H30O2	314.47
Felodipine	H09	RN000210	C18H19Cl2NO4	384.26
Dicyclomine hydrochloride	E09	RN000205	C19H35NO2.HCl	345.96
Serotonin hydrochloride	A02	RN000211	C10H12N2O.HCl	212.68
Cefotiam hydrochloride	A03	RN000211	C18H23N9O4S3.HCl	562.09
Benperidol	A05	RN000211	C22H24FN3O2	381.45

Cefaclor hydrate	A06	RN000211	C15H14ClN3O4S.H2O	385.83
Colistin sulfate	A07	RN000211	C52H98N16O13.H2O4S	1253.54
Daunorubicin hydrochloride	A08	RN000211	C27H29NO10.HCl	563.99
Dosulepin hydrochloride	A09	RN000211	C19H21NS.HCl	331.91
Ceftazidime pentahydrate	A10	RN000211	C22H22N6O7S2.5H2O	636.66
Amyleine hydrochloride	E10	RN000205	C14H21NO2.HCl	271.79
Iobenguane sulfate	A11	RN000211	C8H10IN3.H2O4S	373.17
Metixene hydrochloride	B02	RN000211	C20H23NS.HCl	345.94
Nitrofurantoin	B03	RN000211	C6H6N4O4	198.14
Omeprazole	B04	RN000211	C17H19N3O3S	345.42
Propylthiouracil	B05	RN000211	C7H10N2OS	170.23
Terconazole	B06	RN000211	C26H31ClN5O3	532.47
Tiaprofenic acid	B07	RN000211	C14H12O3S	260.31
Vancomycin hydrochloride	B08	RN000211	C66H75Cl2N9O24.HCl	1485.75
Artemisinin	B09	RN000211	C15H22O5	282.34
Propafenone hydrochloride	B10	RN000211	C21H27NO3.HCl	377.91
Atracurium besylate	A06	RN000205	C53H72N2O12.2C6H5O3S	1243.51
Lidocaine hydrochloride	E11	RN000205	C14H22N2O.HCl	270.8
Ethamivan	B11	RN000211	C12H17NO3	223.27
Vigabatrin	C02	RN000211	C6H11NO2	129.16
Biperiden hydrochloride	C03	RN000211	C21H29NO.HCl	347.93
Cetirizine dihydrochloride	C04	RN000211	C21H25ClN2O3.2HCl	461.82
Etifenin	C05	RN000211	C16H22N2O5	322.36
Metaproterenol sulfate, orciprenaline sulfate	C06	RN000211	2C11H17NO3.H2O4S	260.3
Sisomicin sulfate	C07	RN000211	C19H37N5O7.H2O4S	545.62
Bromperidol	C10	RN000211	C21H23BrFNO2	420.33
Trichlorfon	F02	RN000205	C4H8Cl3O4P	257.44
Cyclizine hydrochloride	C11	RN000211	C18H22N2.HCl	302.85
Fluoxetine hydrochloride	D02	RN000211	C17H18F3NO.HCl	345.79
Iohexol	D03	RN000211	C19H26I3N3O9	821.15
Norcyclobenzaprine	D04	RN000211	C19H19N	261.37
Pyrazinamide	D05	RN000211	C5H5N3O	123.12
Trimethadione	D06	RN000211	C6H9NO3	143.14
Lovastatin	D07	RN000211	C24H36O5	404.55
Nystatine	D08	RN000211	C47H75NO17	926.12

Budesonide	D09	RN000211	C25H34O6	430.55
Imipenem	D10	RN000211	C12H17N3O4S	299.35
Carbamazepine	F03	RN000205	C15H12N2O	236.28
Sulfasalazine	D11	RN000211	C18H14N4O5S	398.4
Thiostrepton	E03	RN000211	C72H85N19O18S5	1664.92
Tiabendazole	E05	RN000211	C10H7N3S	201.25
Rifampicin	E06	RN000211	C43H58N4O12	822.96
Ethionamide	E07	RN000211	C8H10N2S	166.25
Tenoxicam	E08	RN000211	C13H11N3O4S2	337.38
Triflusal	E09	RN000211	C10H7F3O4	248.16
Mesoridazine besylate	E10	RN000211	C21H26N2OS2.C6H6O3S	544.76
Triflupromazine hydrochloride	F04	RN000205	C18H19F3N2S.HCl	388.88
Trolox	E11	RN000211	C14H18O4	250.3
Pirenperone	F02	RN000211	C23H24FN3O2	393.47
Isoquinoline, 6,7-dimethoxy-1-methyl-1,2,3,4-tetrahydro, hydrochloride	F03	RN000211	C12H17NO2.HCl	243.73
Phenacetin	F04	RN000211	C10H13NO2	179.22
Atovaquone	F05	RN000211	C22H19ClO3	366.85
Methoxamine hydrochloride	F06	RN000211	C11H17NO3.HCl	247.72
(R)-(+)-Atenolol	H04	RN000216	C14H22N2O3	266.34
Piracetam	F08	RN000211	C6H10N2O2	142.16
Phenindione	F09	RN000211	C15H10O2	222.25
Thiocolchicoside	F10	RN000211	C27H33NO10S	563.63
Mefenamic acid	F05	RN000205	C15H15NO2	241.29
Clorsulon	F11	RN000211	C8H8Cl3N3O4S2	380.66
Ciclopixox ethanolamine	G02	RN000211	C12H17NO2.C2H7NO	268.35
Probenecid	G03	RN000211	C13H19NO4S	285.36
Betahistine mesylate	G04	RN000211	C8H12N2.2CH4O3S	328.41
Tobramycin	G05	RN000211	C18H37N5O9	467.52
Tetramisole hydrochloride	G06	RN000211	C11H12N2S.HCl	240.76
Pregnenolone	G07	RN000211	C21H32O2	316.49
Molsidomine	G08	RN000211	C9H14N4O4	242.24
Chloroquine diphosphate	G09	RN000211	C18H26ClN3.2H3O4P	515.87
Trimetazidine dihydrochloride	G10	RN000211	C14H22N2O3.2HCl	339.26

Acetohexamide	F06	RN000205	C15H20N2O4S	324.4
Parthenolide	G11	RN000211	C15H20O3	248.32
Hexetidine	H02	RN000211	C21H45N3	339.61
Selegiline hydrochloride	H03	RN000211	C13H17N.HCl	223.75
Pentamidine isethionate	H04	RN000211	C19H24N4O2.2C2H6O4S	592.69
Tolazamide	H05	RN000211	C14H21N3O3S	311.41
Nifuroxazide	H06	RN000211	C12H9N3O5	275.22
Dirithromycin	H08	RN000211	C42H78N2O14	835.09
Gliclazide	H09	RN000211	C15H21N3O3S	323.42
DO 897/99	H10	RN000211	C26H31N3O2.2HCl	490.48
Sulpiride	F07	RN000205	C15H23N3O4S	341.43
Prenylamine lactate	H11	RN000211	C24H27N.C3H6O3	419.57
Atropine sulfate monohydrate	A06	RN000212	2C17H23NO3.H2O4S.H2O	347.43
Eserine hemisulfate salt	A07	RN000212	2C15H21N3O2.H2O4S	324.39
Benoxinate hydrochloride	F08	RN000205	C17H28N2O3.HCl	344.88
Tetracaine hydrochloride	B02	RN000212	C15H24N2O2.HCl	300.83
Mometasone furoate	B03	RN000212	C27H30Cl2O6	521.44
Dacarbazine	B05	RN000212	C6H10N6O	182.19
Acetopromazine maleate salt	B07	RN000212	C19H22N2OS.C4H4O4	442.53
Oxethazaine	F09	RN000205	C28H41N3O3	467.66
Papaverine hydrochloride	C04	RN000212	C20H21NO4.HCl	375.85
Yohimbine hydrochloride	C05	RN000212	C21H26N2O3.HCl	390.91
Cilostazol	C08	RN000212	C20H27N5O2	369.47
Galanthamine hydrobromide	C09	RN000212	C17H21NO3.HBr	368.27
Pheniramine maleate	F10	RN000205	C16H20N2.C4H4O4	356.42
Diclofenac sodium	D05	RN000212	C14H10Cl2NO2.Na	318.14
Xylazine	D09	RN000212	C12H16N2S	220.34
Isoflupredone acetate	A07	RN000205	C23H29FO6	420.48
Tolazoline hydrochloride	F11	RN000205	C10H12N2.HCl	196.68
Eburnamonine (-)	E08	RN000212	C19H22N2O	294.4
Morantel tartrate	G02	RN000205	C12H16N2S.C4H6O6	370.43
Demecarium bromide	F07	RN000212	C32H52N4O4.2Br	716.61
Quipazine dimaleate salt	F08	RN000212	C13H15N3.2C4H4O4	445.43
Diflorasone Diacetate	F10	RN000212	C26H32F2O7	494.54
Homatropine hydrobromide (R,S)	G03	RN000205	C16H21NO3.HBr	356.26

Pyridoxine hydrochloride	G04	RN000212	C8H11NO3.HCl	205.64
Racecadotril	G07	RN000212	C21H23NO4S	385.49
Folic acid	G08	RN000212	C19H19N7O6	441.41
Nifedipine	G04	RN000205	C17H18N2O6	346.34
Dimethisoquin hydrochloride	G11	RN000212	C17H24N2O.HCl	308.85
Thiamine hydrochloride	D08	RN000213	C12H17N4OS.HCl2	337.27
Dipivefrin hydrochloride	H03	RN000212	C19H29NO5.HCl	387.91
Thiorphan	H04	RN000212	C12H15NO3S	253.32
Chlorpromazine hydrochloride	G05	RN000205	C17H19ClN2S.HCl	355.33
Sulmazole	A02	RN000213	C14H13N3O2S	287.34
Flunisolide	A04	RN000213	C24H31FO6	434.51
N-Acetyl-DL-homocysteine Thiolactone	A05	RN000213	C6H9NO2S	159.21
Flurandrenolide	A06	RN000213	C24H33FO6	436.53
Etanidazole	A10	RN000213	C7H10N4O4	214.18
Diphenhydramine hydrochloride	G06	RN000205	C17H21NO.HCl	291.82
Glimepiride	B02	RN000213	C24H34N4O5S	490.63
Picrotoxinin	B03	RN000213	C15H16O6	292.29
Mepenzolate bromide	B04	RN000213	C21H26NO3.Br	420.35
Benfotiamine	B05	RN000213	C19H23N4O6PS	466.46
Halcinonide	B06	RN000213	C24H32ClFO5	454.97
Lanatoside C	B07	RN000213	C49H76O20	985.14
Benzamil hydrochloride	B08	RN000213	C13H14ClN7O.HCl	356.22
Suxibuzone	B09	RN000213	C24H26N2O6	438.48
6-Furfurylaminopurine	B10	RN000213	C10H9N5O	215.22
Minaprine dihydrochloride	G07	RN000205	C17H22N4O.2HCl	371.31
Avermectin B1a	B11	RN000213	C48H72O14	873.1
Nisoldipine	C07	RN000213	C20H24N2O6	388.42
Miconazole	G08	RN000205	C18H14Cl4N2O	416.14
Dydrogesterone	D02	RN000213	C21H28O2	312.46
Beta-Escin	D07	RN000213	C54H84O25	1133.26
Isoxsuprine hydrochloride	G09	RN000205	C18H23NO3.HCl	337.85
Pempidine tartrate	E04	RN000213	C10H21N.C4H6O6	305.38
Estropiate	E09	RN000213	C18H22O5S.C4H10N2	436.58
Acebutolol hydrochloride	G10	RN000205	C18H28N2O4.HCl	372.89

Citalopram Hydrobromide	F03	RN000213	C20H21FN2O.HBr	405.31
Promazine hydrochloride	F04	RN000213	C17H20N2S.HCl	320.89
Sulfamerazine	F05	RN000213	C11H12N4O2S	264.31
Ethotoin	F07	RN000213	C11H12N2O2	204.23
3-alpha-Hydroxy-5-beta-androstan-17-one	F08	RN000213	C19H30O2	290.45
Tetrahydrozoline hydrochloride	F09	RN000213	C13H16N2.HCl	236.75
Hexestrol	F10	RN000213	C18H22O2	270.37
Amiloride hydrochloride dihydrate	A08	RN000205	C6H8ClN7O.HCl.2H2O	302.12
Tolnaftate	G11	RN000205	C19H17NOS	307.42
Cefmetazole sodium salt	F11	RN000213	C15H16N7O5S3.Na	493.52
Trihexyphenidyl-D,L Hydrochloride	G02	RN000213	C20H31NO.HCl	337.94
Succinylsulfathiazole	G03	RN000213	C13H13N3O5S2	355.39
Famprofazone	G04	RN000213	C24H31N3O	377.53
Bromopride	G05	RN000213	C14H22BrN3O2	344.25
Methyl benzethonium chloride	G06	RN000213	C28H44NO2.Cl	462.12
Chlorcyclizine hydrochloride	G07	RN000213	C18H21ClN2.HCl	337.29
Diphenylpyraline hydrochloride	G08	RN000213	C19H23NO.HCl	317.86
Benzethonium chloride	G09	RN000213	C27H42NO2.Cl	448.09
Trioxsalen	G10	RN000213	C14H12O3	228.25
Todralazine hydrochloride	H02	RN000205	C11H12N4O2.HCl	268.7
Sulfabenzamide	H02	RN000213	C13H12N2O3S	276.32
Benzocaine	H03	RN000213	C9H11NO2	165.19
Dipyrone	H04	RN000213	C13H16N3O4S.Na	333.34
Isosorbide dinitrate	H05	RN000213	C6H8N2O8	236.14
Sulfachloropyridazine	H06	RN000213	C10H9ClN4O2S	284.73
Pramoxine hydrochloride	H07	RN000213	C17H27NO3.HCl	329.87
Finasteride	H08	RN000213	C23H36N2O2	372.56
Fluorometholone	H09	RN000213	C22H29FO4	376.47
Cephalothin sodium salt	H10	RN000213	C16H15N2O6S2.Na	418.43
Imipramine hydrochloride	H03	RN000205	C19H24N2.HCl	316.88
Cefuroxime sodium salt	H11	RN000213	C16H15N4O8S.Na	446.37
Althiazide	A02	RN000214	C11H14ClN3O4S3	383.9

Isopyrin hydrochloride	A03	RN000214	C14H19N3O.HCl	281.79
Phenethicillin potassium salt	A04	RN000214	C17H19N2O5S.K	402.52
Sulfamethoxypyridazine	A05	RN000214	C11H12N4O3S	280.31
Deferoxamine mesylate	A06	RN000214	C25H48N6O8.CH4O3S	656.81
Mephentermine hemisulfate	A07	RN000214	2C11H17N.H2O4S	212.3
Sulfadimethoxine	A09	RN000214	C12H14N4O4S	310.33
Sulfanilamide	A10	RN000214	C6H8N2O2S	172.21
Sulindac	H04	RN000205	C20H17FO3S	356.42
Balsalazide Sodium	A11	RN000214	C17H13N3O6.2Na	401.29
Sulfaquinoxaline sodium salt	B02	RN000214	C14H11N4O2S.Na	322.32
Streptozotocin	B03	RN000214	C8H15N3O7	265.22
Metoprolol-(+,-) (+)-tartrate salt	B04	RN000214	2C15H25NO3.C4H6O6	342.41
Flumethasone	B05	RN000214	C22H28F2O5	410.46
Flecainide acetate	B06	RN000214	C17H20F6N2O3.C2H4O2	474.4
Cefazolin sodium salt	B07	RN000214	C14H13N8O4S3.Na	476.49
Atractyloside potassium salt	B08	RN000214	C30H44O16S2.2K	803
Folinic acid calcium salt	B09	RN000214	C20H21N7O7.Ca	511.51
Levonordefrin	B10	RN000214	C9H13NO3	183.21
Amitriptyline hydrochloride	H05	RN000205	C20H23N.HCl	313.87
Ebselen	B11	RN000214	C13H9NOSe	274.18
Nadide	C02	RN000214	C21H27N7O14P2	663.44
Sulfamethizole	C03	RN000214	C9H10N4O2S2	270.33
Medrysone	C04	RN000214	C22H32O3	344.5
Flunixin meglumine	C05	RN000214	C14H11F3N2O2.C7H17NO5	491.47
Spiramycin	C06	RN000214	C43H73N2O14R	842.07
Glycopyrrolate	C07	RN000214	C19H28NO3.Br	398.34
Monensin sodium salt	C09	RN000214	C36H61O11.Na	692.87
Isoetharine mesylate salt	C10	RN000214	C13H21NO3.CH4O3S	335.43
Adiphenine hydrochloride	H06	RN000205	C20H25NO2.HCl	347.89
Mevalonic-D, L acid lactone	C11	RN000214	C6H10O3	130.14
Terazosin hydrochloride	D02	RN000214	C19H25N5O4.HCl	423.9
Phenazopyridine hydrochloride	D03	RN000214	C11H11N5.HCl	249.7
Demeclocycline hydrochloride	D04	RN000214	C21H21ClN2O8.HCl	501.32

Fenoprofen calcium salt dihydrate	D05	RN000214	2C15H13O3.Ca.2H2O	279.33
Piperacillin sodium salt	D06	RN000214	C23H26N5O7S.Na	539.55
Diethylstilbestrol	D07	RN000214	C18H20O2	268.36
Chlorotrianisene	D08	RN000214	C23H21ClO3	380.88
Ribostamycin sulfate salt	D09	RN000214	C17H34N4O10.H2O4S	552.56
Methacholine chloride	D10	RN000214	C8H18NO2.Cl	195.69
Dibucaine	H07	RN000205	C20H29N3O2	343.47
Pipenzolate bromide	D11	RN000214	C22H28NO3.Br	434.37
Butamben	E02	RN000214	C11H15NO2	193.25
Sulfapyridine	E03	RN000214	C11H11N3O2S	249.29
Meclofenoxate hydrochloride	E04	RN000214	C12H16ClNO3.HCl	294.18
Furaltadone hydrochloride	E05	RN000214	C13H16N4O6.HCl	360.76
Ethoxyquin	E06	RN000214	C14H19NO	217.31
Tinidazole	E07	RN000214	C8H13N3O4S	247.27
Guanadrel sulfate	E08	RN000214	2C10H19N3O2.H2O4S	262.32
Vidarabine	E09	RN000214	C10H13N5O4	267.25
Sulfameter	E10	RN000214	C11H12N4O3S	280.31
Prednisone	H08	RN000205	C21H26O5	358.44
Isopropamide iodide	E11	RN000214	C23H33N2O.I	480.43
Alclometasone dipropionate	F02	RN000214	C28H37ClO7	521.06
Leflunomide	F03	RN000214	C12H9F3N2O2	270.21
Norgestrel(-)-D	F04	RN000214	C21H28O2	312.46
Fluocinonide	F05	RN000214	C26H32F2O7	494.54
Sulfamethazine sodium salt	F06	RN000214	C12H13N4O2S.Na	300.32
Guaifenesin	F07	RN000214	C10H14O4	198.22
Alexidine dihydrochloride	F08	RN000214	C26H56N10.2HCl	581.72
Proadifen hydrochloride	F09	RN000214	C23H31NO2.HCl	389.97
Zomepirac sodium salt	F10	RN000214	C15H13ClNO3.Na	313.72
Thioridazine hydrochloride	H09	RN000205	C21H26N2S2.HCl	407.04
Cinoxacin	F11	RN000214	C12H10N2O5	262.22
Clobetasol propionate	G02	RN000214	C25H32ClFO5	466.98
Podophyllotoxin	G03	RN000214	C22H22O8	414.42
Clofibric acid	G04	RN000214	C10H11ClO3	214.65
Bendroflumethiazide	G05	RN000214	C15H14F3N3O4S2	421.42
Dicumarol	G06	RN000214	C19H12O6	336.3

Methimazole	G07	RN000214	C4H6N2S	114.17
Merbromin	G08	RN000214	C20H8Br2HgO6.2Na	750.66
Hexylcaine hydrochloride	G09	RN000214	C16H23NO2.HCl	297.83
Drofenine hydrochloride	G10	RN000214	C20H31NO2.HCl	353.94
Diphenamil methylsulfate	H10	RN000205	C20H24N.CH3O4S	389.52
Cycloheximide	G11	RN000214	C15H23NO4	281.35
(R) -Naproxen sodium salt	H02	RN000214	C14H13O3.Na	252.25
Propidium iodide	H03	RN000214	C27H34N4.2I	668.41
Cloperastine hydrochloride	H04	RN000214	C20H24ClNO.HCl	366.33
Eucatropine hydrochloride	H05	RN000214	C17H25NO3.HCl	327.85
Isocarboxazid	H06	RN000214	C12H13N3O2	231.26
Lithocholic acid	H07	RN000214	C24H40O3	376.58
Methotrimoprazine maleat salt	H08	RN000214	C19H24N2O5.C4H4O4	444.55
Dienestrol	H09	RN000214	C18H18O2	266.34
Pridinol methanesulfonate salt	H10	RN000214	C20H25NO.CH4O3S	391.54
Amprolium hydrochloride	A09	RN000205	C14H19N4.Cl.HCl	315.24
Trimethobenzamide hydrochloride	H11	RN000205	C21H28N2O5.HCl	424.93
Amrinone	H11	RN000214	C10H9N3O	187.2
Carbinoxamine maleate salt	A02	RN000215	C16H19ClN2O.C4H4O4	406.87
Methazolamide	A03	RN000215	C5H8N4O3S2	236.27
Pyridylidone	A04	RN000215	C9H13NO2	167.21
Spectinomycin dihydrochloride	A05	RN000215	C14H24N2O7.2HCl	405.28
Piromidic acid	A06	RN000215	C14H16N4O3	288.31
Trimipramine maleate salt	A07	RN000215	C20H26N2.C4H4O4	410.51
Chloropyramine hydrochloride	A08	RN000215	C16H20ClN3.HCl	326.27
Furazolidone	A09	RN000215	C8H7N3O5	225.16
Dichlorphenamide	A10	RN000215	C6H6Cl2N2O4S2	305.16
Metronidazole	A02	RN000206	C6H9N3O3	171.16
Sulconazole nitrate	A11	RN000215	C18H15Cl3N2S.HNO3	460.77
Cromolyn disodium salt	B03	RN000215	C23H14O11.2Na	512.34
Bucladesine sodium salt	B04	RN000215	C18H23N5O8P.Na	491.38
Cefsulodin sodium salt	B05	RN000215	C22H19N4O8S2.Na	554.54
Fosfosal	B06	RN000215	C7H7O6P	218.1

Suprofen	B07	RN000215	C14H12O3S	260.31
Nadolol	B09	RN000215	C17H27NO4	309.41
Moxalactam disodium salt	B10	RN000215	C20H18N6O9S.2Na	564.45
Aminophylline	B11	RN000215	2C7H8N4O2.C2H8N2	210.22
Azlocillin sodium salt	C02	RN000215	C20H22N5O6S.Na	483.48
Clidinium bromide	C03	RN000215	C22H26NO3.Br	432.36
Sulfamonomethoxine	C04	RN000215	C11H12N4O3S	280.31
Benzthiazide	C05	RN000215	C15H14CIN3O4S3	431.94
Trichlormethiazide	C06	RN000215	C8H8Cl3N3O4S2	380.66
Oxalamine citrate salt	C07	RN000215	C14H19N3O.C6H8O7	437.46
Propantheline bromide	C08	RN000215	C23H30NO3.Br	448.4
Dimethadione	C10	RN000215	C5H7NO3	129.12
Edrophonium chloride	A04	RN000206	C10H16NO.Cl	201.7
Ethaverine hydrochloride	C11	RN000215	C24H29NO4.HCl	431.96
Butacaine	D02	RN000215	C18H30N2O2	306.45
Cefoxitin sodium salt	D03	RN000215	C16H16N3O7S2.Na	449.44
Ifosfamide	D04	RN000215	C7H15Cl2N2O2P	261.09
Novobiocin sodium salt	D05	RN000215	C31H35N2O11.Na	634.62
Tetrahydroxy-1,4-quinone monohydrate	D06	RN000215	C6H4O6.H2O	190.12
Indoprofen	D07	RN000215	C17H15NO3	281.31
Carbenoxolone disodium salt	D08	RN000215	C34H48O7.2Na	614.74
Iocetamic acid	D09	RN000215	C12H13I3N2O3	613.96
Ganciclovir	D10	RN000215	C9H13N5O4	255.24
Moroxidine hydrochloride	A05	RN000206	C6H13N5O.HCl	207.66
Ethopropazine hydrochloride	D11	RN000215	C19H24N2S.HCl	348.94
Trimeprazine tartrate	E03	RN000215	2C18H22N2S.C4H6O6	373.49
Nafcillin sodium salt monohydrate	E04	RN000215	C21H21N2O5S.Na.H2O	454.49
Procyclidine hydrochloride	E05	RN000215	C19H29NO.HCl	323.91
Amiprilose hydrochloride	E06	RN000215	C14H27NO6.HCl	341.83
Ethynylestradiol 3-methyl ether	E07	RN000215	C21H26O2	310.44
(-) -Levobunolol hydrochloride	E08	RN000215	C17H25NO3.HCl	327.85
Iodixanol	E09	RN000215	C35H44I6N6O15	1550.2
Baclofen (R,S)	A06	RN000206	C10H12ClNO2	213.67

Equilin	E11	RN000215	C18H20O2	268.36
Paroxetine Hydrochloride	F02	RN000215	C19H20FNO3.HCl	365.83
Liothyronine	F04	RN000215	C15H12I3NO4	650.98
Roxithromycin	F05	RN000215	C41H76N2O15	837.07
Beclomethasone dipropionate	F06	RN000215	C28H37ClO7	521.06
Tolmetin sodium salt dihydrate	F07	RN000215	C15H14NO3.Na.2H2O	315.3
(+) -Levobunolol hydrochloride	F08	RN000215	C17H25NO3.HCl	327.85
Doxazosin mesylate	F09	RN000215	C23H25N5O5.CH4O3S	547.6
Fluvastatin sodium salt	F10	RN000215	C24H25FNO4.Na	433.46
Acyclovir	A07	RN000206	C8H11N5O3	225.21
Methylhydantoin-5-(L)	F11	RN000215	C4H6N2O2	114.1
Gabapentin	G02	RN000215	C9H17NO2	171.24
Raloxifene hydrochloride	G03	RN000215	C28H27NO4S.HCl	510.06
Etidronic acid, disodium salt	G04	RN000215	C2H6O7P2.2Na	249.99
Methylhydantoin-5-(D)	G05	RN000215	C4H6N2O2	114.1
Simvastatin	G06	RN000215	C25H38O5	418.58
Azacytidine-5	G07	RN000215	C8H12N4O5	244.21
Paromomycin sulfate	G08	RN000215	C23H45N5O14.H2O4S	713.72
Acetaminophen	G09	RN000215	C8H9NO2	151.17
Phthalylsulfathiazole	G10	RN000215	C17H13N3O5S2	403.44
Diazoxide	A08	RN000206	C8H7ClN2O2S	230.67
Luteolin	G11	RN000215	C15H10O6	286.24
Iopamidol	H02	RN000215	C17H22I3N3O8	777.09
Iopromide	H03	RN000215	C18H24I3N3O8	791.12
Theophylline monohydrate	H04	RN000215	C7H8N4O2.H2O	198.19
Theobromine	H05	RN000215	C7H8N4O2	180.17
Reserpine	H06	RN000215	C33H40N2O9	608.69
Scopolamine hydrochloride	H08	RN000215	C17H21NO4.HCl	339.82
Ioversol	H09	RN000215	C18H24I3N3O9	807.12
Amidopyrine	A09	RN000206	C13H17N3O	231.3
Carbachol	H11	RN000215	C6H15N2O2.Cl	182.65
Niacin	A02	RN000216	C6H5NO2	123.11
Bemegride	A03	RN000216	C8H13NO2	155.2
Digoxigenin	A04	RN000216	C23H34O5	390.52

Meglumine	A05	RN000216	C7H17NO5	195.22
Clioquinol	A07	RN000216	C9H5ClINO	305.5
Oxybenzone	A08	RN000216	C14H12O3	228.25
Promethazine hydrochloride	A09	RN000216	C17H20N2S.HCl	320.89
Felbinac	B04	RN000216	C14H12O2	212.25
Butylparaben	B05	RN000216	C11H14O3	194.23
Aminohippuric acid	B06	RN000216	C9H10N2O3	194.19
N-Acetyl-L-leucine	B07	RN000216	C8H15NO3	173.21
Pipemidic acid	B08	RN000216	C14H17N5O3	303.32
Dioxybenzone	B09	RN000216	C14H12O4	244.25
Adrenosterone	B10	RN000216	C19H24O3	300.4
Hydrochlorothiazide	A10	RN000205	C7H8ClN3O4S2	297.74
Pindolol	A11	RN000206	C14H20N2O2	248.33
Methylatropine nitrate	B11	RN000216	C18H26NO3.NO3	366.41
Hymecromone	C02	RN000216	C10H8O3	176.17
Diloxanide furoate	C04	RN000216	C14H11Cl2NO4	328.15
Metyrapone	C05	RN000216	C14H14N2O	226.28
Urapidil hydrochloride	C06	RN000216	C20H29N5O3.HCl	423.95
Fluspirilen	C07	RN000216	C29H31F2N3O	475.59
S-(+)-ibuprofen	C08	RN000216	C13H18O2	206.29
Ethinodiol diacetate	C09	RN000216	C24H32O4	384.52
Nabumetone	C10	RN000216	C15H16O2	228.29
Khellin	B02	RN000206	C14H12O5	260.25
Nisoxetine hydrochloride	C11	RN000216	C17H21NO2.HCl	307.82
(+)-Isoproterenol (+)-bitartrate salt	D02	RN000216	C11H17NO3.C4H6O6	361.35
Monobenzone	D03	RN000216	C13H12O2	200.24
2-Aminobenzenesulfonamide	D04	RN000216	C6H8N2O2S	172.21
Estrone	D05	RN000216	C18H22O2	270.37
Lorglumide sodium salt	D06	RN000216	C22H31Cl2N2O4.Na	481.4
Nitrendipine	D07	RN000216	C18H20N2O6	360.37
Flurbiprofen	D08	RN000216	C15H13FO2	244.27
Nimodipine	D09	RN000216	C21H26N2O7	418.45
Bacitracin	D10	RN000216	C66H103N17O16S	1422.73
Zimelidine dihydrochloride monohydrate	B03	RN000206	C16H17BrN2.2HCl.H2O	408.17

L(-)-vesamicol hydrochloride	D11	RN000216	C17H25NO.HCl	295.85
Nizatidine	E02	RN000216	C12H21N5O2S2	331.46
Thiopramide maleate	E03	RN000216	C15H24N4S.C4H4O4	408.52
Xamoterol hemifumarate	E04	RN000216	C16H25N3O5.C4H4O4	455.46
Rolipram	E05	RN000216	C16H21NO3	275.35
Thonzonium bromide	E06	RN000216	C32H55N4O.Br	591.72
Idazoxan hydrochloride	E07	RN000216	C11H12N2O2.HCl	240.69
Quinapril HCl	E08	RN000216	C25H30N2O5.HCl	474.99
Nilutamide	E09	RN000216	C12H10F3N3O4	317.23
Ketorolac tromethamine	E10	RN000216	C15H13NO3.C4H11NO3	376.42
Azacyclonol	B04	RN000206	C18H21NO	267.37
Protriptyline hydrochloride	E11	RN000216	C19H21N.HCl	299.85
Propofol	F02	RN000216	C12H18O	178.28
S(-)Eticlopride hydrochloride	F03	RN000216	C17H25ClN2O3.HCl	377.31
Primidone	F04	RN000216	C12H14N2O2	218.26
Flucytosine	F05	RN000216	C4H4FN3O	129.09
(-)-MK 801 hydrogen maleate	F06	RN000216	C16H15N.C4H4O4	337.37
Bephenium hydroxynaphthoate	F07	RN000216	C17H22NO.C11H7O3	443.55
Dehydroisoandrosterone 3-acetate	F08	RN000216	C21H30O3	330.47
Benserazide hydrochloride	F09	RN000216	C10H15N3O5.HCl	293.71
Iodipamide	F10	RN000216	C20H14I6N2O6	1139.77
Azathioprine	B05	RN000206	C9H7N7O2S	277.27
Pentetic acid	G02	RN000216	C14H23N3O10	393.35
Bretylum tosylate	G03	RN000216	C11H17BrN.C7H7O3S	414.37
Pralidoxime chloride	G04	RN000216	C7H9N2O.Cl	172.61
Phenoxybenzamine hydrochloride	G05	RN000216	C18H22ClNO.HCl	340.3
Salmeterol	G06	RN000216	C25H37NO4	415.58
Altretamine	G07	RN000216	C9H18N6	210.28
Prazosin hydrochloride	G08	RN000216	C19H21N5O4.HCl	419.87
Timolol maleate salt	G09	RN000216	C13H24N4O3S.C4H4O4	432.5
(+,-)-Octopamine hydrochloride	G10	RN000216	C8H11NO2.HCl	189.64
Lynestrenol	B06	RN000206	C20H28O	284.45
Crotamiton	H02	RN000216	C13H17NO	203.29

(S)-(-)-Atenolol	F07	RN000211	C14H22N2O3	266.34
Tyloxapol	H05	RN000216	C59H96O12	997.42
Florfenicol	H06	RN000216	C12H14Cl2FNO4S	358.22
Megestrol acetate	H07	RN000216	C24H32O4	384.52
Deoxycorticosterone	H08	RN000216	C21H30O3	330.47
Urosiol	H09	RN000216	C24H40O4	392.58
Proparacaine hydrochloride	H10	RN000216	C16H26N2O3.HCl	330.86
Guanabenz acetate	B07	RN000206	C8H8Cl2N4.C2H4O2	291.14
Aminocaproic acid	H11	RN000216	C6H13NO2	131.18
Denatonium benzoate	A02	RN000217	C21H29N2O.C7H5O2	446.6
Enilconazole	A04	RN000217	C14H14Cl2N2O	297.19
Methacycline hydrochloride	A05	RN000217	C22H22N2O8.HCl	478.89
Sotalol hydrochloride	A07	RN000217	C12H20N2O3S.HCl	308.83
Decamethonium bromide	A09	RN000217	C16H38N2.2Br	418.3
Disulfiram	B08	RN000206	C10H20N2S4	296.54
Remoxipride Hydrochloride	B02	RN000217	C16H23BrN2O3.HCl	407.74
THIP Hydrochloride	B03	RN000217	C6H8N2O2.HCl	176.6
Pirlindole mesylate	B04	RN000217	C15H18N2.CH4O3S	322.43
Pronethalol hydrochloride	B05	RN000217	C15H19NO.HCl	265.78
Naftopidil dihydrochloride	B06	RN000217	C24H28N2O3.2HCl	465.42
Tracazolate hydrochloride	B07	RN000217	C16H24N4O2.HCl	340.86
Zardaverine	B08	RN000217	C12H10F2N2O3	268.22
Memantine Hydrochloride	B09	RN000217	C12H21N.HCl	215.77
Ozagrel hydrochloride	B10	RN000217	C13H12N2O2.HCl	264.71
Acetylsalicylsalicylic acid	B09	RN000206	C16H12O6	300.27
Piribedil hydrochloride	B11	RN000217	C16H18N4O2.HCl	334.81
Nitrocaramiphen hydrochloride	C02	RN000217	C18H26N2O4.HCl	370.88
Nandrolone	C03	RN000217	C18H26O2	274.41
Dimaprit dihydrochloride	C04	RN000217	C6H15N3S.2HCl	234.19
Proscillaridin A	C07	RN000217	C30H42O8	530.66
Mianserine hydrochloride	B10	RN000206	C18H20N2.HCl	300.83
Gliquidone	D02	RN000217	C27H33N3O6S	527.64
Pizotifen malate	D03	RN000217	C19H21NS.C4H6O5	429.54
Ribavirin	D04	RN000217	C8H12N4O5	244.21
Cyclopenthiiazide	D05	RN000217	C13H18ClN3O4S2	379.89

Fluvoxamine maleate	D06	RN000217	C15H21F3N2O2.C4H4O4	434.41
Fluticasone propionate	D08	RN000217	C25H31F3O5S	500.58
Zuclopenthixol dihydrochloride	D09	RN000217	C22H25ClN2OS.2HCl	473.89
Proguanil hydrochloride	D10	RN000217	C11H16ClN5.HCl	290.2

b. Diverse chemical library

Chemical Name	ID Number	Well	Runnmuber	Molecular Weight
4-propylbicyclo[2.2.2]octan-1-ol	AA-516/30035004	B08	RW036141	168.3
3-chloro-1-benzothiophene-2-carboxamide	AA-516/31407040	A02	RW036141	211.7
2-nitroso-3-phenylimidazo[1,2-a]pyridine	AA-516/31409049	B09	RW036141	223.2
N-[4-(trifluoromethyl)-1,3-thiazol-2-yl]acetamide	AB-601/30915037	A05	RW036141	210.2
methyl 4-morpholinylcarbothioylcarbamate	AB-601/30963030	A04	RW036141	204.2
4-methyl-N-(1,3-thiazol-2-yl)benzenesulfonamide	AB-601/30965020	A07	RW036141	254.3
N-methyl-4-phenyl-1,3-thiazol-2-amine	AB-601/30965024	A06	RW036141	190.3
4-phenyl-2-quinazolinol	AC-907/34110024	G04	RW036141	222.2
ethyl 2,3,6-tribromo-4-pyridinyl ether	AC-907/34114019	G05	RW036141	359.8
3-amino-N-isopropyl-6-phenyl-2-pyrazinecarboxamide 4-oxide	AC-907/34124015	G02	RW036141	272.3
5,5'-bis[2-ethoxypyridine]	AC-907/34130029	H06	RW036141	244.3
diethyl 3,3'-bipyridine-2,2'-dicarboxylate	AC-907/34130052	H08	RW036141	300.3
4-ethoxy-5-phenoxy-2-phenylpyrimidine	AC-907/34131011	G09	RW036141	292.3
N-[2-(dimethylamino)ethyl]-N-(3-methoxy-5,6-dihydrobenzo[c]acridin-7-yl)amine	AE-641/11516886	F02	RW036141	509.3
2-phenyl-1,10b-dihydropyrazolo[1,5-c][1,3]benzoxazine	AE-848/10301053	D09	RW036141	250.3
3-[(1-phenyl-1H-tetrazol-5-yl)sulfanyl]-2,4-pentanedione	AF-615/11251004	H09	RW036141	276.3
2-(1H-benzimidazol-1-yl)ethanethioamide	AF-615/31154061	E03	RW036141	191.3
4-[(1,1,3,3-tetramethylbutyl)amino]-1-oxaspiro[4.5]dec-3-en-2-one	AG-205/11234138	G08	RW036141	279.4
N-(4-chloro-5H-1,2,3-dithiazol-5-ylidene)-N-(5-methyl-3-isoxazolyl)amine	AG-205/11317031	C04	RW036141	233.7
2-(1-azepanylethyl)-5-(1,3-benzodioxol-5-yl)-7-(trifluoromethyl)pyrazolo[1,5-a]pyrimidine	AG-219/37149070	F07	RW036141	432.4
N~1~[3-(4-chlorophenyl)-6-phenyl-1,2,4-triazin-5-yl]-1,2-ethanediamine	AG-227/37195035	F09	RW036141	325.8
2-chloro-3-(4-methyl-1-piperidinyl)naphthoquinone	AG-670/14311008	H02	RW036141	289.8
2-[4-(4-methoxyphenyl)-1,3-thiazol-2-yl]-5-phenyl-2,4-dihydro-3H-pyrazol-3-one	AH-628/31526003	E07	RW036141	349.4
4-amino-1-cinnamylpyridinium	AI-204/31679025	B03	RW036141	291.2
S-ethyl 2-oxotetrahydro-3-thienylthiocarbamate	AI-204/31691006	B05	RW036141	205.3
6-chloro-2-(4-fluorophenyl)-1-methyl-1H-imidazo[1,2-a]pyridin-4-ium	AI-204/31692024	B04	RW036141	388.6
N-(3,5-dichloro-2-pyridinyl)-N'-(4-fluorophenyl)urea	AI-204/31694057	H07	RW036141	300.1
ethyl 2-({[(5-chloro-2-pyridinyl)sulfanyl]acetyl}amino)-4,5,6,7-tetrahydro-1-benzothiophene-3-carboxylate	AI-204/31760030	A09	RW036141	410.9

2-[anilino(phenyl)methyl]-2,4-dimethyl-3-morpholinone	AI-555/32073018	B06	RW036141	310.4
2-acetyl-5-phenyl-1,3-cyclohexanedione	AI-559/11192003	E06	RW036141	230.3
1-(1,3-benzodioxol-5-yl)-1,4-dihydrobenzo[f]quinolin-3(2H)-one	AI-559/11192017	G07	RW036141	317.3
N-(3,4-dibromo-5-oxo-2,5-dihydro-2-furanyl)acetamide	AI-559/11193086	A08	RW036141	298.9
2-{{3-(2,2-dimethyltetrahydro-2H-pyran-4-yl)-4-oxo-3,4,5,6-tetrahydrospiro(benzo[h]quinazoline-5,1'-cyclohexane)-2-yl}sulfanyl}acetamide	AJ-292/12640010	E02	RW036141	467.6
N-{4-[(dipropylamino)sulfonyl]phenyl}-2-methoxyacetamide	AJ-292/41695099	A03	RW036141	328.4
1-[2-(2-tert-butylphenoxy)ethyl]pyrrolidine	AJ-292/41722298	C02	RW036141	247.4
1-(1,3-benzothiazol-2-yl)-3-methyl-4-(4-oxo-1,4-dihydro-2-quinolinyl)-1H-pyrazol-5-olate	AJ-292/42034615	F04	RW036141	396.4
N-(2,5-dimethylphenyl)-N'-[2-(4-fluorophenyl)ethyl]thiourea	AJ-292/42034967	E05	RW036141	302.4
N-(4-butylphenyl)-4-hydroxy-1-piperidinecarbothioamide	AJ-292/42035002	E08	RW036141	292.4
ethyl 4-(2-furoyl)-1-(4-methylphenyl)-1H-pyrazole-3-carboxylate	AJ-916/13004033	H03	RW036141	324.3
6-amino-8-(2-chlorophenyl)-8,8a-dihydro-1H-isothiochromene-5,7,7(3H)-tricarbonitrile	AK-777/10805016	G06	RW036141	352.8
2-amino-8-(4,5-dibromo-2-furyl)-7,9-dioxo-1-thia-3-azaspiro[4.5]dec-2-en-4-one	AK-778/37151003	F06	RW036141	412.1
5-methyl-N-{4-methyl-2-[(5-methyl-2-furoyl)amino]phenyl}-2-furamide	AK-968/12572216	C05	RW036141	338.4
3-cyclohexyl-N-(2,3-dihydro-1,4-benzodioxin-6-yl)propanamide	AK-968/12686065	C06	RW036141	289.4
2,6-bis(3,4-dimethoxyphenyl)-3,5-dimethyl-4-piperidinone	AM-760/12199004	F08	RW036141	399.5
2-amino-4-[4-(cyclopentyloxy)-3-methoxyphenyl]-5-oxo-4H,5H-thiochromeno[4,3-b]pyran-3-carbonitrile	AM-807/43303324	G10	RW036141	446.5
N-{1-benzyl-2-oxo-2-[(2-pyridinylmethyl)amino]ethyl}benzamide	AN-023/42183986	E11	RW036141	359.4
(2-isobutoxy-1-naphthyl)acetonitrile	AN-056/25005720	E04	RW036141	239.3
2-(6-methyl-1H-benzimidazol-2-yl)phenol	AN-353/12702010	B07	RW036141	224.3
ethyl 4-(5-{1-[4-(acetylamino)anilino]cyclohexyl}-1H-tetraazol-1-yl)benzoate	AN-512/12674123	C08	RW036141	448.5
ethyl 7-oxo-5,7,9,10-tetrahydrospiro(6H-benzo[h][1,3]thiazolo[2,3-b]quinazoline-6,1'-cyclohexane)-10-carboxylate	AN-512/12674278	C07	RW036141	396.5
N-(3,4-dimethylphenyl)-3-methylbenzamide	AN-652/11165279	A10	RW036141	239.3
3,4,5-triethoxy-N-(2-methylcyclohexyl)benzamide	AN-652/43339972	D11	RW036141	349.5
8-methoxy-1-[(4-methylphenyl)sulfonyl]-1,2,3,4-tetrahydro-5H-1-benzazepin-5-one	AN-975/13811034	H04	RW036141	345.4
4-bromo-1-[(4-methylphenyl)sulfonyl]-1,2,3,4-tetrahydro-5H-1-benzazepin-5-one	AN-975/13811041	H05	RW036141	394.3
2-{{1-(3,4-dimethylphenyl)-1H-tetraazol-5-yl}sulfanyl}-N-(2-fluorophenyl)acetamide	AN-989/40660209	B10	RW036141	357.4
2-[2-fluoro(phenylsulfonyl)anilino]-N-[2-(4-methoxyphenyl)ethyl]acetamide	AN-989/42063810	D03	RW036141	442.5

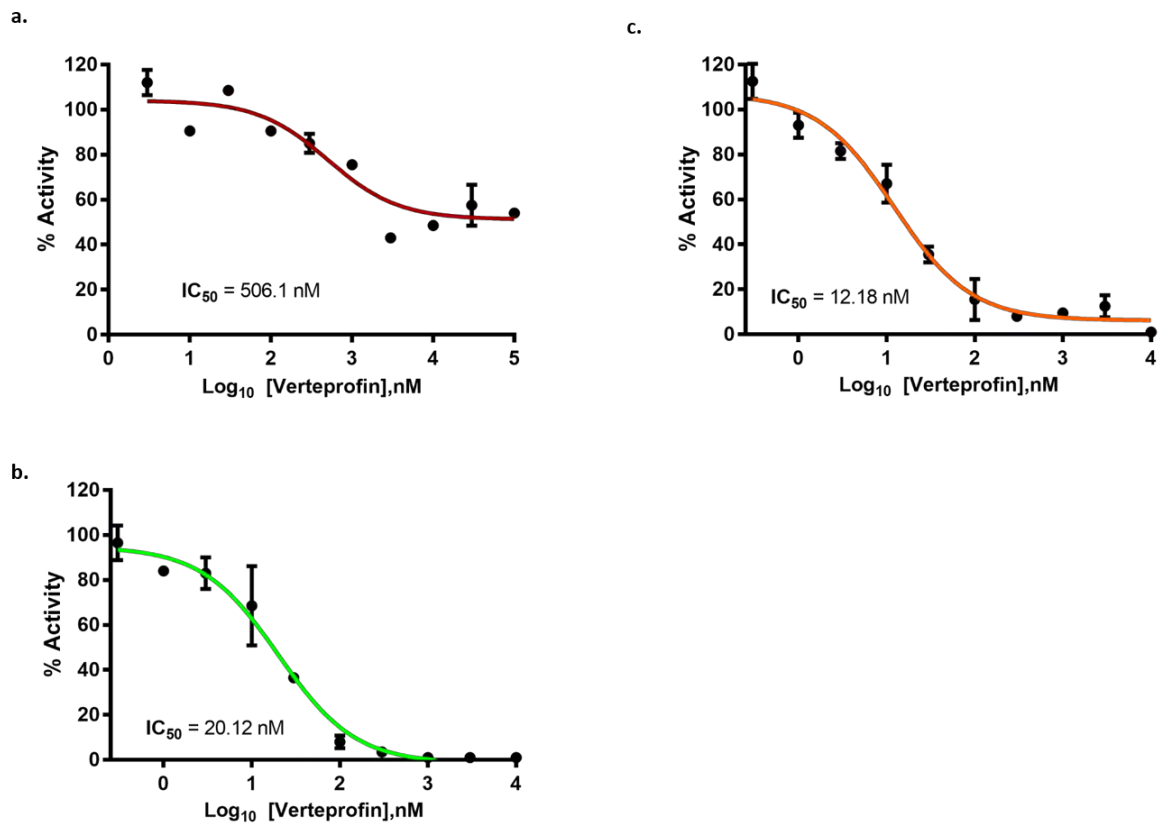
N-{2-[(3-chlorobenzyl)sulfonyl]ethyl}-2-[4-fluoro(methylsulfonyl)anilino]acetamide	AN-989/42063881	D07	RW036141	431
N-(3-chloro-4-methoxyphenyl)-2-[4-fluoro(methylsulfonyl)anilino]acetamide	AN-989/42063890	D05	RW036141	386.8
2-[4-fluoro(methylsulfonyl)anilino]-N-(4-methylbenzyl)acetamide	AN-989/42063891	D04	RW036141	350.4
N-(3-chloro-2-methylphenyl)-2-[2,4-dimethoxy(methylsulfonyl)anilino]acetamide	AN-989/42064093	D02	RW036141	412.9
2-[3-chloro-2-methyl(methylsulfonyl)anilino]-N-(3-pyridinyl)acetamide	AN-989/42064246	D06	RW036141	353.8
4-{[(2-methylphenoxy)acetyl]amino}-N-(tetrahydro-2-furanylmethyl)benzamide	AO-080/41819744	H11	RW036141	368.4
N-methyl-2-{[4-phenyl-5-(2-phenylethyl)-4H-1,2,4-triazol-3-yl]sulfonyl}acetamide	AO-080/41821110	E10	RW036141	352.5
17-methyl-9-oxo-12-oxa-8-aza-17-azoniaheptacyclo[15.5.2.0~1,18~.0~2,7~.0~8,22~.0~11,21~.0~15,20~]tetracos-2,4,6,14-tetraene	AO-080/43342692	H10	RW036141	460.6
3-isopropyl-6-(3,4,5-trimethoxyphenyl)[1,2,4]triazolo[3,4-b][1,3,4]thiadiazole	AO-365/43263933	G11	RW036141	334.4
N-{2-[(2-iodobenzoyl)amino]ethyl}nicotinamide	AO-365/43264566	F11	RW036141	395.2
N-{2-[(3,4-dichlorobenzoyl)amino]ethyl}nicotinamide	AO-365/43264596	F10	RW036141	338.2
2-(4-chlorobenzoyl)-N-(4-methoxybenzyl)benzamide	AO-548/43279624	D10	RW036141	379.8
[5-benzoyl-1-(3-chlorobenzyl)-1H-1,2,3-triazol-4-yl](phenyl)methanone	AP-006/41057238	A11	RW036141	401.9
2,5-dichloro-N,N-diethyl-4-methoxybenzenesulfonamide	AP-263/40917848	E09	RW036141	312.2
N-(1,3-benzodioxol-5-ylmethyl)[1,1'-biphenyl]-4-sulfonamide	AP-263/41417989	F03	RW036141	367.4
1-[(2-methoxy-4-methylphenyl)sulfonyl]pyrrolidine	AP-263/42173190	F05	RW036141	255.3
ethyl 4-[(4-bromo-3-ethoxyphenyl)sulfonyl]-1-piperazinecarboxylate	AP-263/42610805	D08	RW036141	421.3
2-[1-(4-phenyl-1,3-thiazol-2-yl)-5-(trifluoromethyl)-1H-pyrazol-4-yl]-6-(trifluoromethyl)[1,2,4]triazolo[5,1-b][1,3,4]thiadiazole	AP-501/43295675	B11	RW036141	487.4
4-(1-azepanylsulfonyl)-N-(4-methoxyphenyl)benzamide	AP-866/42031495	C03	RW036141	388.5
ethyl 4-{[4-(1-azepanylsulfonyl)benzoyl]amino}benzoate	AP-866/42031497	C09	RW036141	430.5
2-[methyl(phenylsulfonyl)amino]-N-(1,3,4-thiadiazol-2-yl)benzamide	AP-866/42031637	B02	RW036141	374.4
4-[2-(4-bromophenyl)-4-hydroxy-3-(4-methylbenzoyl)-5-oxo-2,5-dihydro-1H-pyrrol-1-yl]butanoic acid	AQ-149/13890128	G03	RW036141	458.3
7-benzyl-2-{[(4-methylphenyl)sulfonyl]methyl}-5,6,7,8-tetrahydropyrido[4',3':4,5]thieno[2,3-d]pyrimidin-4(3H)-one	AR-434/42807199	C11	RW036141	465.6
5-phenyl-2-(2-toluidinomethyl)thieno[2,3-d]pyrimidin-4(3H)-one	AR-434/42808088	C10	RW036141	347.4
(4-phenyl-3-buten-1-ynyl)benzene	AB-016/30004032	A04	RW036145	204.3
4,5-dimethyl-2-(4-methylphenyl)-1-oxido-3,6-dihydro-2H-thiopyran-2-yl methyl sulfide	AB-131/15501123	B09	RW036145	280.5
propyl 4-[(propoxycarbonyl)amino]benzoate	AE-641/12753553	G03	RW036145	265.3
isopentyl 4-[(propoxycarbonyl)amino]benzoate	AE-641/12753563	G02	RW036145	293.4

N-(1,1-dioxidotetrahydro-3-thienyl)-3-methoxy-N-(4-methoxybenzyl)benzamide	AF-399/42093129	B07	RW036145	389.5
4-tert-butyl-N-(1,1-dioxidotetrahydro-3-thienyl)-N-(2-thienylmethyl)benzamide	AF-399/42093398	B08	RW036145	391.6
N-(3,4-dimethoxybenzyl)-N-(1,1-dioxidotetrahydro-3-thienyl)-2-(mesityloxy)acetamide	AF-399/42093523	A09	RW036145	461.6
3-methyl-N-{4-[4-(4-morpholinylsulfonyl)phenyl]-1,3-thiazol-2-yl}butanamide	AF-399/42217175	A06	RW036145	409.5
3-(4-methoxyphenoxy)-2-methyl-4-oxo-4H-chromen-7-yl dimethylcarbamate	AF-399/42316017	A05	RW036145	369.4
8-(1-azepanylmethyl)-3-(2,3-dihydro-1,4-benzodioxin-6-yl)-7-hydroxy-4H-chromen-4-one	AF-399/42316251	A08	RW036145	407.5
4-[1-(4-fluorobenzyl)-1H-benzimidazol-2-yl]-1-phenyl-2-pyrrolidinone	AF-399/42322455	A07	RW036145	385.4
N-[1-isobutyl-6,6-dimethyl-2,4-dioxo-3-(trifluoromethyl)-2,3,4,5,6,7-hexahydro-1H-indol-3-yl]cyclopropanecarboxamide	AG-389/42159307	A02	RW036145	386.4
N-(4-fluorophenyl)-2-(4-[(2-phenylethyl)amino]sulfonyl)phenoxyacetamide	AH-487/41947170	H02	RW036145	428.5
methyl 4-methyl-3-({4-[(2-methylbenzyl)(methylsulfonyl)amino]benzoyl}amino)benzoate	AH-487/42143108	H07	RW036145	466.6
methyl 2-({4-[methyl(methylsulfonyl)amino]benzoyl}amino)-4,5,6,7-tetrahydro-1-benzothiophene-3-carboxylate	AH-487/42144850	D09	RW036145	422.5
2-[2,3-dichloro(phenylsulfonyl)anilino]-N-(4-pyridinylmethyl)acetamide	AH-487/42200101	G09	RW036145	450.3
methyl 2-({[(4-ethyl-5-phenyl-4H-1,2,4-triazol-3-yl)thio]acetyl}amino)benzoate	AH-487/42276492	C09	RW036145	396.5
N-(4-chlorobenzyl)-3-{4-[(cyclohexylamino)sulfonyl]phenyl}propanamide	AH-487/42307105	H06	RW036145	435
2-[4-(3-methoxyphenyl)-1-piperazinyl]-N-(6-methyl-4,5,6,7-tetrahydro-1,3-benzothiazol-2-yl)acetamide	AJ-292/42032127	C06	RW036145	400.5
N-(4-butylphenyl)-N'-(2,2-dimethoxyethyl)thiourea	AJ-292/42035021	C04	RW036145	296.4
N-isobutyl-N'-(2-methoxyphenyl)thiourea	AJ-292/42035166	C05	RW036145	238.4
4-benzoyl-N-[3-(1-piperidinylsulfonyl)-4-pyridinyl]-1-piperazinamine	AJ-333/09213064	B03	RW036145	429.5
N,N-diethyl-6-(4-methyl-1-piperazinyl)-3-pyridinesulfonamide	AJ-333/09216038	D02	RW036145	312.4
4-[3-(trifluoromethyl)phenoxy]-3-pyridinamine	AJ-333/09217039	C02	RW036145	290.7
6-[4-(2-hydroxyethyl)-1-piperazinyl]-N-isopropyl nicotinamide	AJ-333/13050147	A03	RW036145	310.4
4-[(2-chlorophenyl)sulfanyl]-3-({[(propylamino)carbonyl]amino}sulfonyl)pyridine	AJ-333/25006006	E02	RW036145	385.9
4-[(4-chlorophenyl)sulfanyl]-3-({[(methylamino)carbonyl]amino}sulfonyl)pyridine	AJ-333/25006007	E03	RW036145	357.8
2-(4-aminophenyl)-1-(4-methoxyphenyl)-1-butanone	AJ-333/25006080	D03	RW036145	269.3
N-ethyl-N'-(3-pyridinylcarbonyl)urea	AJ-333/25006147	C03	RW036145	193.2
ethyl benzylsulfonylcarbamate	AJ-333/25006258	B02	RW036145	243.3
6-[5-(2-pyridinyl)-4,5-dihydro-1H-pyrazol-3-yl]-2H-1,4-benzoxazin-3(4H)-one	AK-820/13218079	F02	RW036145	294.3
2-oxo-2-phenylethyl 4-butoxybenzoate	AK-918/40097236	G08	RW036145	312.4

3-(1-adamantyl)-6-amino-4-(2,3,4-trimethoxyphenyl)-2,4-dihydropyrano[2,3-c]pyrazole-5-carbonitrile	AM-807/42005335	G06	RW036145	462.6
2-(4-{{(5-amino-1H-tetraazol-1-yl)amino}methyl}-2-ethoxyphenoxy)-N-(tert-butyl)acetamide	AN-465/41989886	D07	RW036145	363.4
N-benzyl-2-(2,4-dibromophenoxy)propanamide	AN-652/42191143	B04	RW036145	413.1
10-bromo-3-(methylsulfanyl)-6-(3-thienyl)-6,7-dihydro[1,2,4]triazino[5,6-d][3,1]benzoxazepine	AN-655/13534011	F03	RW036145	407.3
N-(4-bromo-2,3-dimethylphenyl)-2-{{5-(3-methylphenyl)-1,3,4-oxadiazol-2-yl}sulfanyl}acetamide	AN-698/42116854	H09	RW036145	432.3
2-{{4-methyl-5-[(3-methylphenoxy)methyl]-4H-1,2,4-triazol-3-yl}sulfanyl)-N-(1-naphthyl)acetamide	AN-698/42147898	H08	RW036145	418.5
N-(4-bromo-3-chlorophenyl)-2-{{4-methyl-5-(1-phenoxyethyl)-4H-1,2,4-triazol-3-yl}sulfanyl}acetamide	AN-698/42147972	E04	RW036145	481.8
2-{{4-amino-5-(phenoxyethyl)-4H-1,2,4-triazol-3-yl}sulfanyl}-N-(2-fluorophenyl)acetamide	AN-698/42147988	D04	RW036145	373.4
N-[2-oxo-2-(4-phenyl-1-piperazinyl)ethyl]-N-(2-phenylethyl)methanesulfonamide	AN-698/42374830	D06	RW036145	401.5
N-(3-chloro-4-fluorophenyl)-2-[cyclohexyl(methylsulfonyl)amino]acetamide	AN-698/42374848	C07	RW036145	362.9
N-[2-chloro-5-(trifluoromethyl)phenyl]-2-[cyclohexyl(methylsulfonyl)amino]acetamide	AN-698/42374853	D05	RW036145	412.9
butyl 5-{{(3-methylbenzyl)sulfanyl}methyl}-1,3,4-thiadiazol-2-ylcarbamate	AN-758/42380777	E09	RW036145	351.5
2-[(4-methylphenyl)sulfanyl]-N-[5-(2-thienyl)-1,3,4-thiadiazol-2-yl]acetamide	AN-758/42380997	E08	RW036145	347.5
2-methyl-N-[5-(2-thienylmethyl)-1,3,4-thiadiazol-2-yl]propanamide	AN-758/42382786	E07	RW036145	267.4
4-(4-methylphenyl)-6-oxo-2-[(2-phenylethyl)sulfanyl]-1,4,5,6-tetrahydro-3-pyridinecarbonitrile	AO-081/41887353	G04	RW036145	348.5
4-chloro-3,5-dimethylphenyl 5-fluoro-2-methoxybenzenesulfonate	AP-263/42173272	G07	RW036145	344.8
4-chloro-2,5-dimethoxy-N-(2-methoxyethyl)benzenesulfonamide	AP-263/42173381	G05	RW036145	309.8
ethyl 5-amino-1-[6-(3,4-dimethylphenoxy)-2-(methylsulfanyl)-4-pyrimidinyl]-1H-pyrazole-4-carboxylate	AP-501/42397551	B05	RW036145	399.5
3-(trifluoromethyl)-6-[2-(trifluoromethyl)phenyl][1,2,4]triazolo[3,4-b][1,3,4]thiadiazole	AP-501/42397576	B06	RW036145	338.2
N-[4-(allyloxy)-3-methoxybenzyl]-N-benzylamine	AP-970/42167964	E05	RW036145	319.8
1-(3-methylphenyl)-5-oxo-N,7-diphenyl-1,5-dihydro[1,2,4]triazolo[4,3-a]pyrimidine-3-carboxamide	AP-982/41979599	C08	RW036145	421.5
2-methoxyethyl 5-{{(4-chlorophenyl)sulfonyl}amino}-2-methyl-1-benzofuran-3-carboxylate	AQ-390/40720495	E06	RW036145	423.9
1-[1-(2-methoxyethyl)-2,5-dimethyl-1H-pyrrol-3-yl]-2-(2-quinolinylsulfanyl)ethanone	AQ-750/42050665	F08	RW036145	354.5
4-fluoro-N-(3-{{[4-(2-furoyl)-1-piperazinyl]methyl}-4,5-dimethyl-2-thienyl}benzamide	AQ-750/42051186	F06	RW036145	441.5

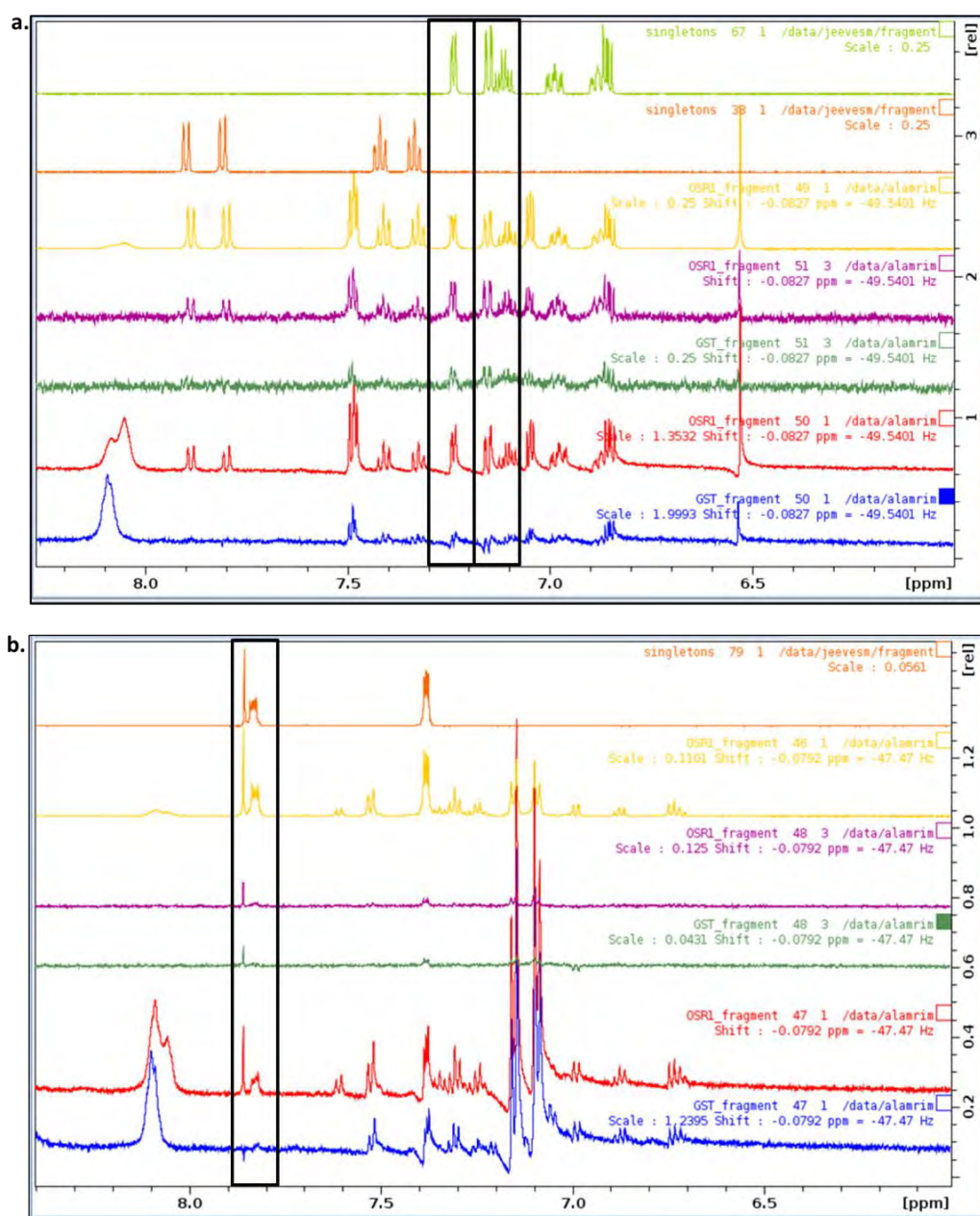
N-{4,5-dimethyl-3-[(2-methyl-1-piperidiny)methyl]-2-thienyl}-2-fluorobenzamide	AQ-750/42051225	F05	RW036145	360.5
N-(4-methoxyphenyl)-2-[(4-oxo-5-phenyl-4,5-dihydro-1H-pyrazolo[3,4-d]pyrimidin-6-yl)sulfanyl]acetamide	AQ-750/42052696	F09	RW036145	407.5
2-[(4-oxo-5-phenyl-4,5-dihydro-1H-pyrazolo[3,4-d]pyrimidin-6-yl)thio]-N-[3-(trifluoromethyl)phenyl]acetamide	AQ-750/42052714	F04	RW036145	445.4
6-{[2-(3,4-dichlorophenyl)-2-oxoethyl]sulfanyl}-5-phenyl-1,5-dihydro-4H-pyrazolo[3,4-d]pyrimidin-4-one	AQ-750/42052744	F07	RW036145	431.3
2,5-dimethyl-N-[2-oxo-2-(1-pyrrolidinyl)ethyl]benzenesulfonamide	AQ-750/42209273	H05	RW036145	296.4
2-[(2,5-dimethylphenyl)sulfonyl]amino}-N-(2-fluorophenyl)propanamide	AQ-750/42209638	H04	RW036145	350.4
N-(3-pyridinyl)-4-({[(2,3,5,6-tetramethylphenyl)sulfonyl]amino}methyl)benzamide	AQ-750/42210121	D08	RW036145	423.5
4-[(1,3-dimethyl-3H-benzimidazol-1-ium-2-yl)methoxy]phenyl dimethylcarbamate	AQ-776/42801509	H03	RW036145	375.9

Appendix 4.5



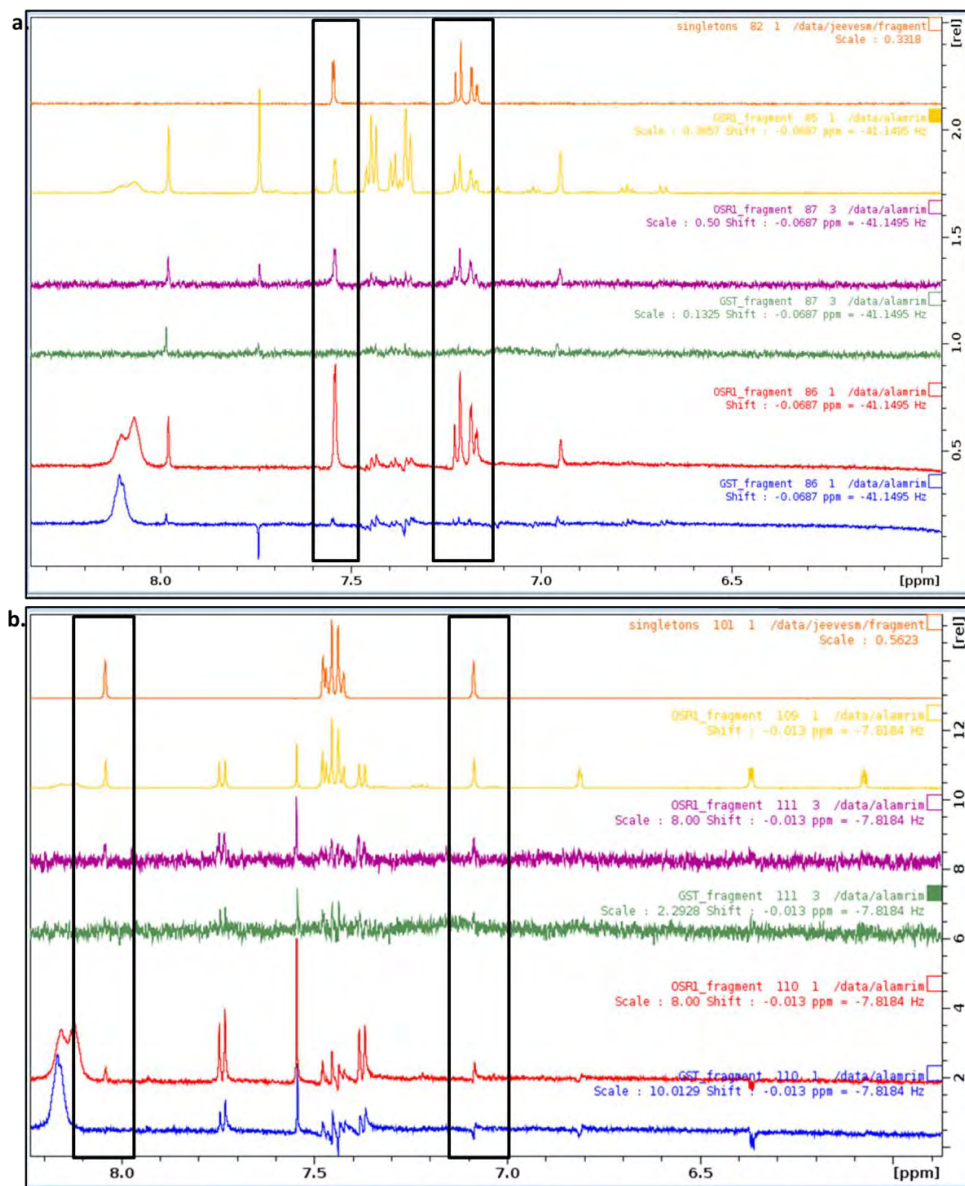
Determination of the inhibitory effect of Verteporfin on (a) OSR1 T185E, (b) Map4k3 and (c) Ikke protein kinases using ³³P-labeled ATP *in vitro* kinase assay. Data presented as a mean ($n=2$, \pm SD).

Appendix 5.1a



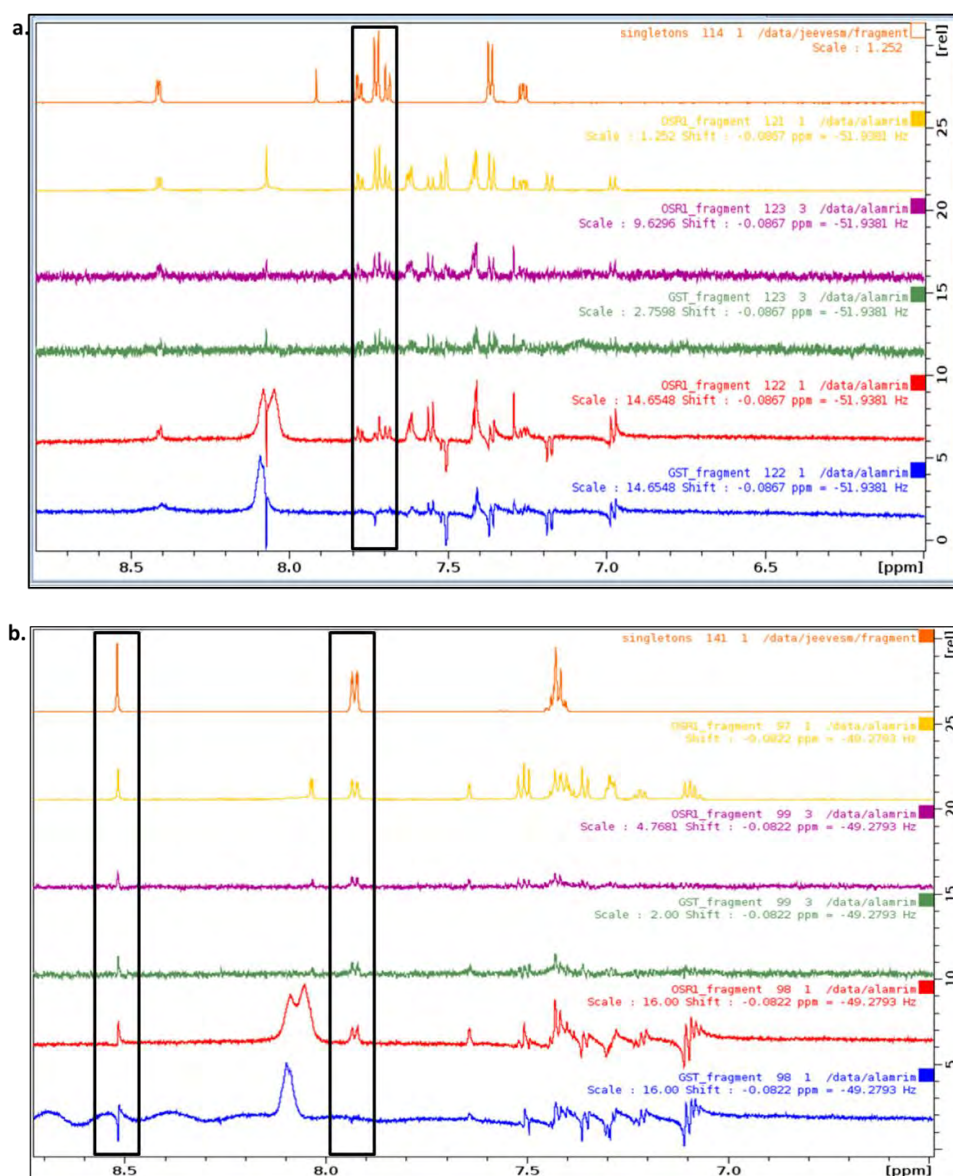
STD-NMR and waterLogsy spectra for fragment hits. Spectra of fragment hits number (a) 67-38 and (b) 79. The green and orange spectra in (a) are for 1HNMR reference spectra for 67 and 38 reference compounds, respectively. The orange spectrum in (b) is for 1HNMR reference spectrum for reference compound. The yellow spectrum is for 1HNMR reference spectrum for the cocktail sample which composed of 4 distinct fragment molecules, violet spectrum is for STD-NMR experiment with GST-OSR1 CCT domain, green spectrum is for STD-NMR experiment with GST-tag protein, red spectrum is for waterLogsy experiment with GST-OSR1 CCT domain and blue spectrum is for waterLogsy experiment with GST-tag protein. The compound peaks that tested positive in both STD-NMR and waterLogsy with GST-OSR1 CCT domain, but not GST-tag protein were highlighted with black rectangle.

Appendix 5.1b



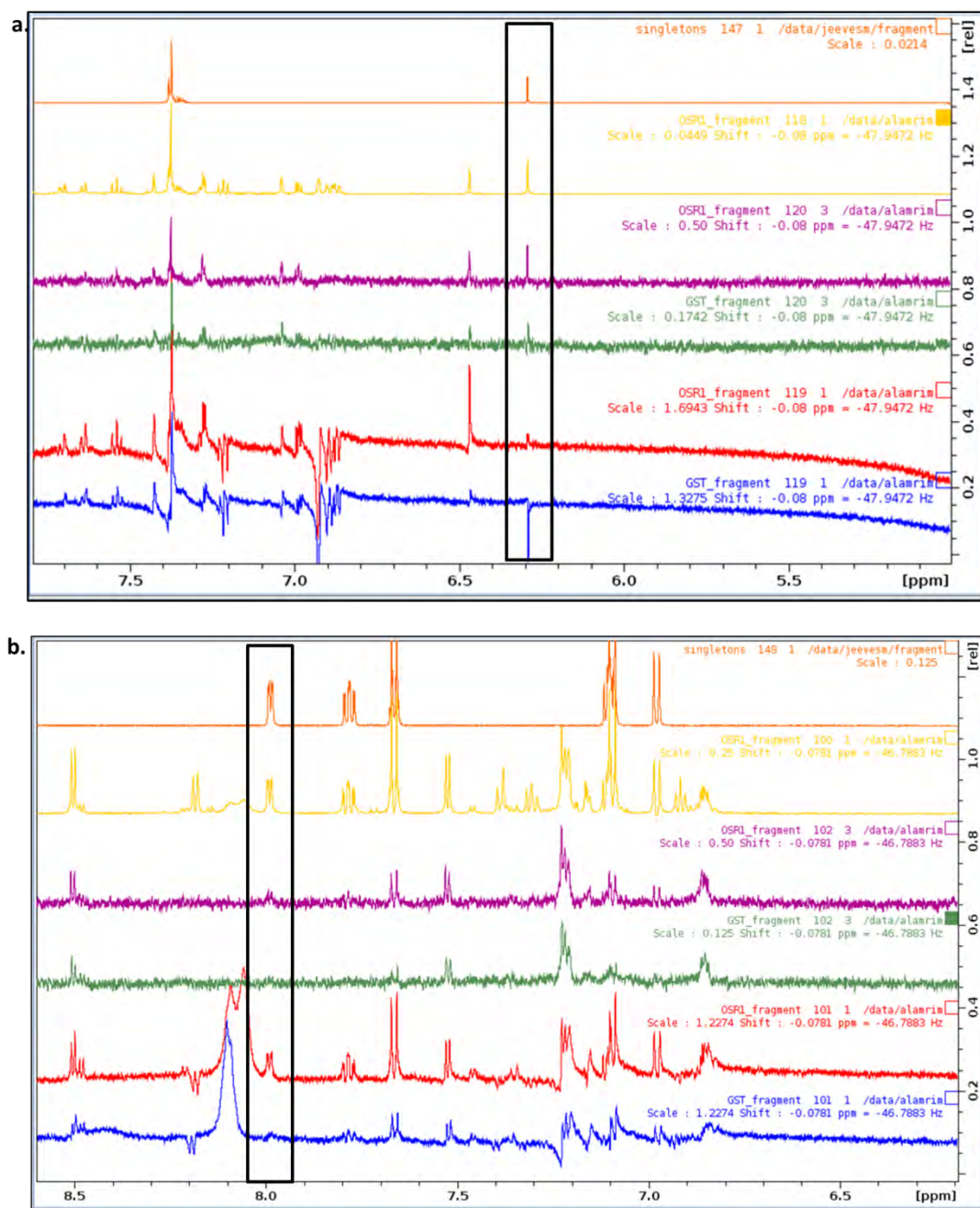
STD-NMR and waterLogsy spectra for fragment hits. Spectra of fragment hits number (a) 82 and (b) 101. The orange spectrum is for ^1H NMR reference spectrum for reference compound, yellow spectrum is for ^1H NMR reference spectrum for the cocktail sample which composed of 4 distinct fragment molecules, violet spectrum is for STD-NMR experiment with GST-OSR1 CCT domain, green spectrum is for STD-NMR experiment with GST-tag protein, red spectrum is for waterLogsy experiment with GST-OSR1 CCT domain and blue spectrum is for waterLogsy experiment with GST-tag protein. The compound peaks that tested positive in both STD-NMR and waterLogsy with GST-OSR1 CCT domain but not GST-tag protein were highlighted with black rectangle.

Appendix 5.1c



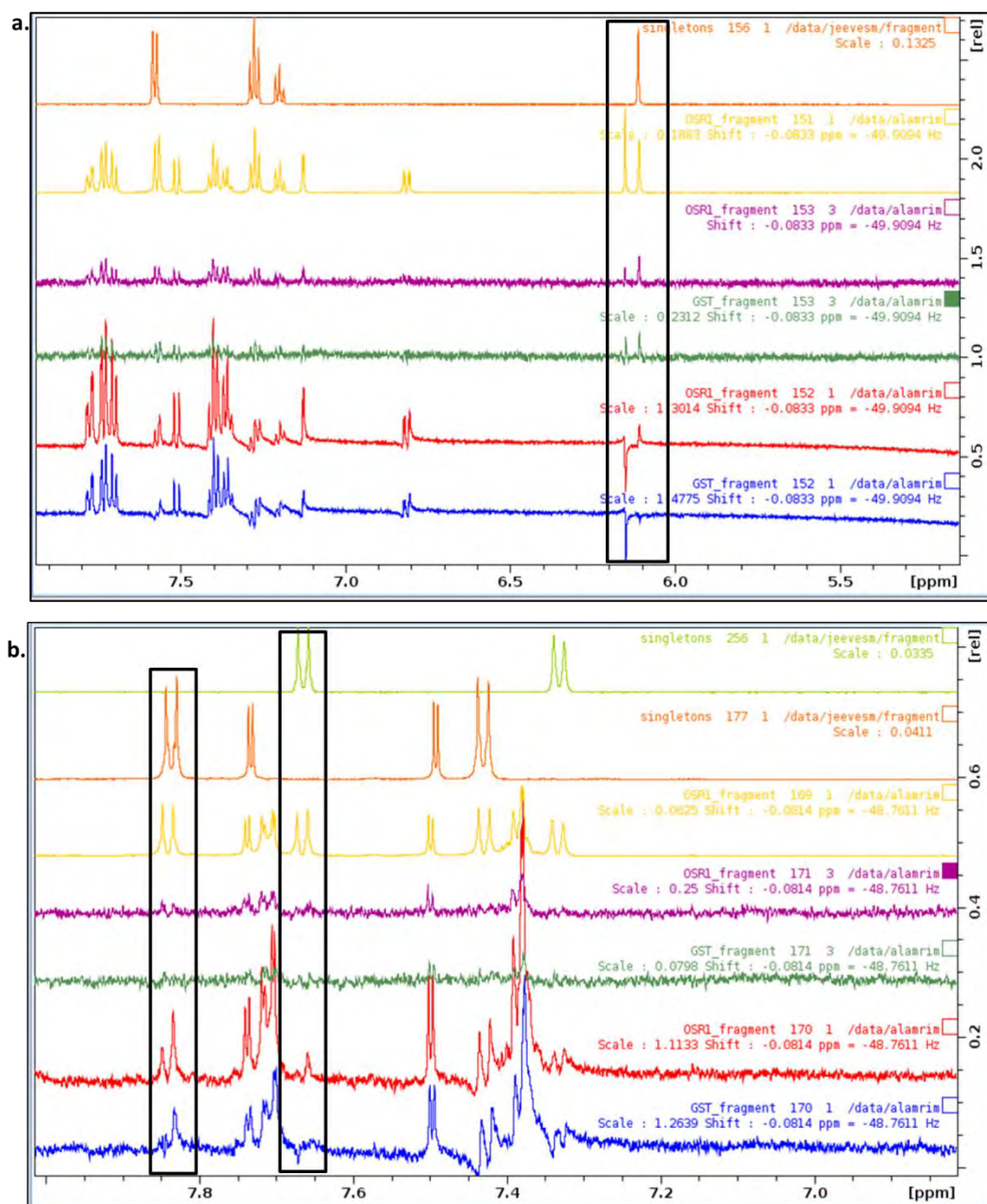
STD-NMR and waterLogsy spectra for fragment hits. Spectra of fragment hits number (a) 114 and (b) 141. The orange spectrum is for 1HNMR reference spectrum for reference compound, yellow spectrum is for 1HNMR reference spectrum for the cocktail sample which composed of 4 distinct fragment molecules, violet spectrum is for STD-NMR experiment with GST-OSR1 CCT domain, green spectrum is for STD-NMR experiment with GST-tag protein, red spectrum is for waterLogsy experiment with GST-OSR1 CCT domain and blue spectrum is for waterLogsy experiment with GST-tag protein. The compound peaks that tested positive in both STD-NMR and waterLogsy with GST-OSR1 CCT domain but not GST-tag protein were highlighted with black rectangle.

Appendix 5.1d



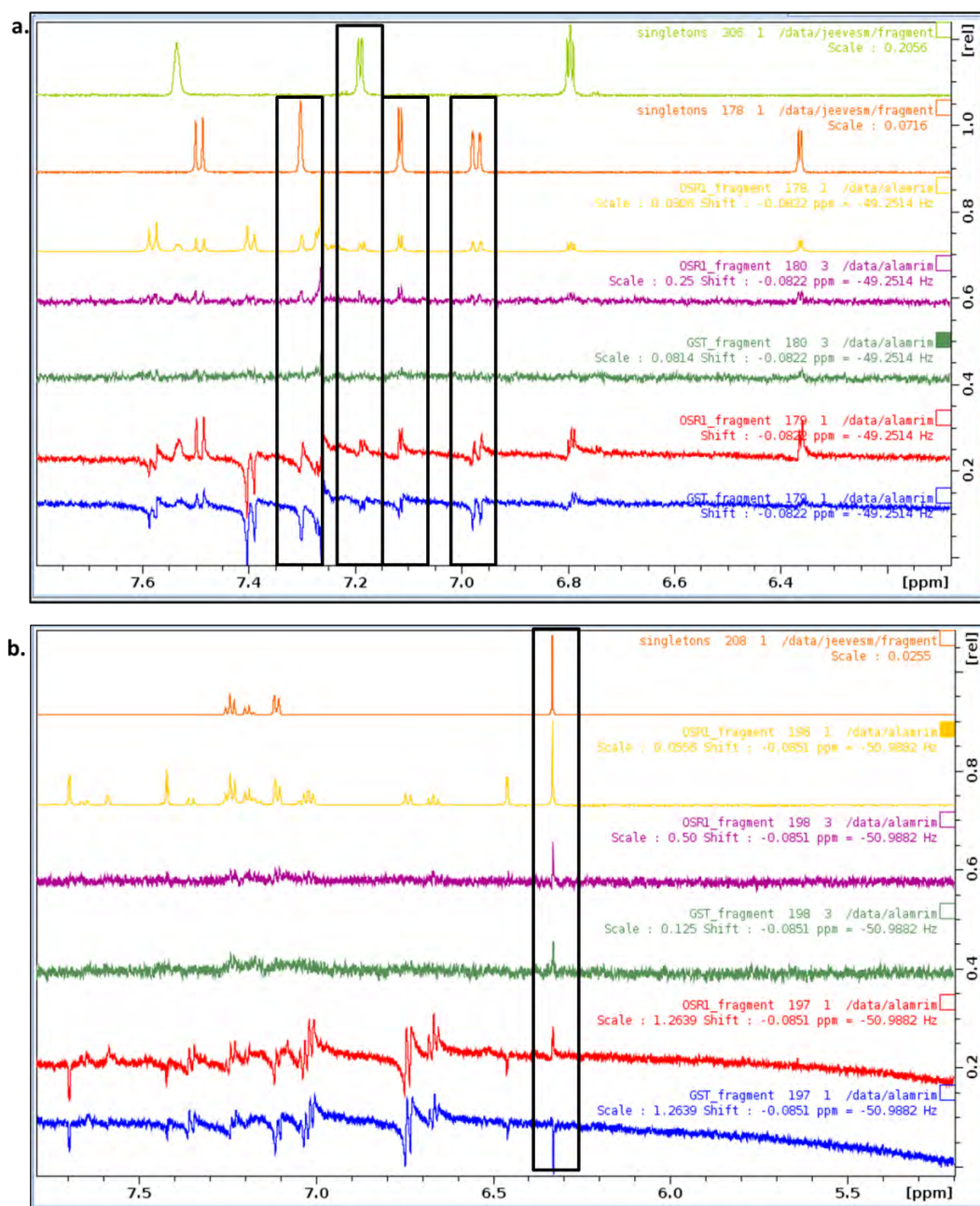
STD-NMR and waterLogsy spectra for fragment hits. Spectra of fragment hits number (a) 147 and (b) 148. The orange spectrum is for 1HNMR reference spectrum for reference compound, yellow spectrum is for 1HNMR reference spectrum for the cocktail sample which composed of 4 distinct fragment molecules, violet spectrum is for STD-NMR experiment with GST-OSR1 CCT domain, green spectrum is for STD-NMR experiment with GST-tag protein, red spectrum is for waterLogsy experiment with GST-OSR1 CCT domain and blue spectrum is for waterLogsy experiment with GST-tag protein. The compound peaks that tested positive in both STD-NMR and waterLogsy with GST-OSR1 CCT domain but not GST-tag protein were highlighted with black rectangle.

Appendix 5.1e



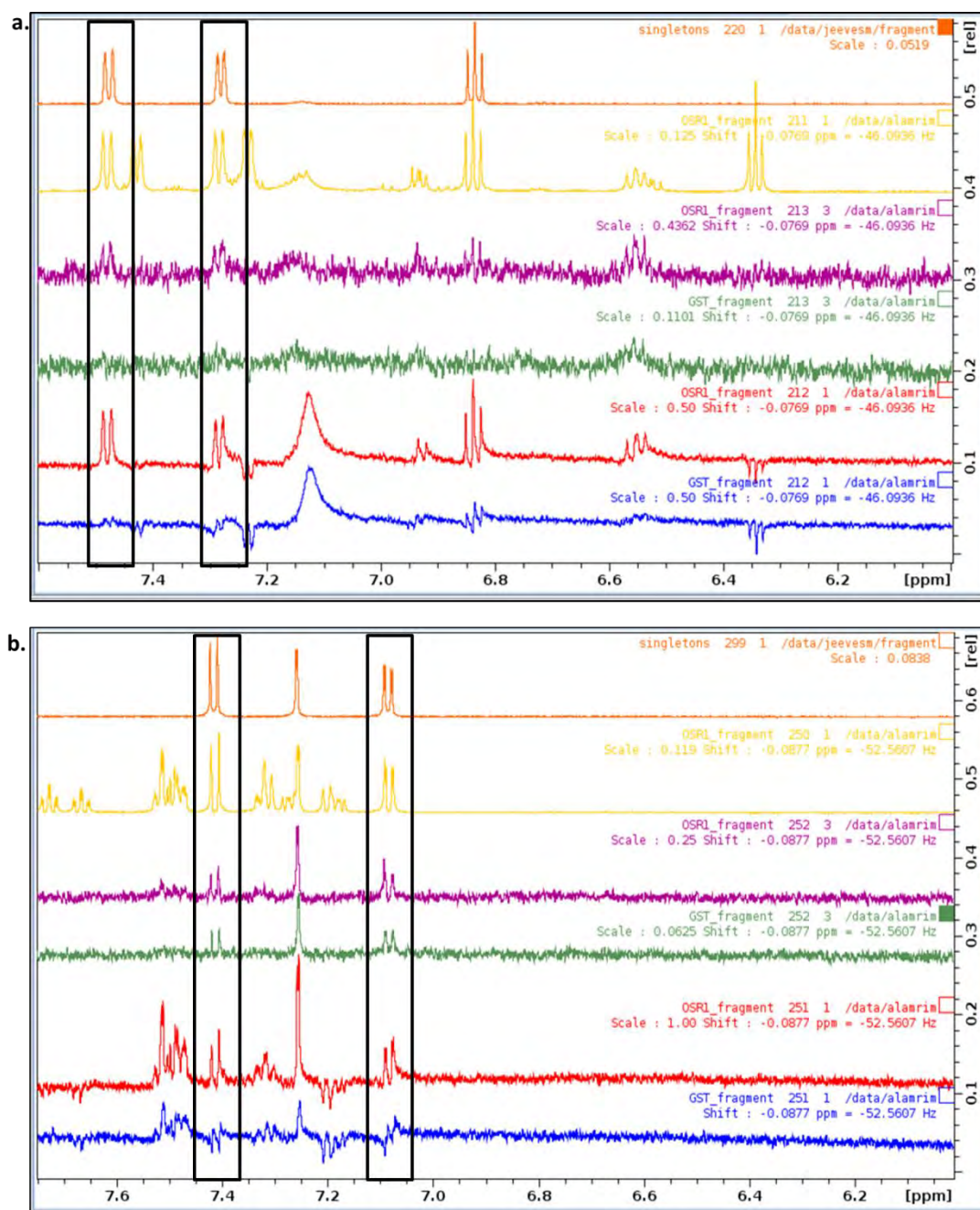
STD-NMR and waterLogsy spectra for fragment hits. Spectra of fragment hits number (a) 156 and (b) 256-177. The orange spectrum in (a) is for ^1H NMR reference spectrum for reference compound. The green and orange spectra in (b) are for ^1H NMR reference spectrum for 256 and 177 reference compounds, respectively. The yellow spectrum is for ^1H NMR reference spectrum for the cocktail sample which composed of 4 distinct fragment molecules, violet spectrum is for STD-NMR experiment with GST-OSR1 CCT domain, green spectrum is for STD-NMR experiment with GST-tag protein, red spectrum is for waterLogsy experiment with GST-OSR1 CCT domain and blue spectrum is for waterLogsy experiment with GST-tag protein. The compound peaks that tested positive in both STD-NMR and waterLogsy with GST-OSR1 CCT domain but not GST-tag protein were highlighted with black rectangle.

Appendix 5.1f



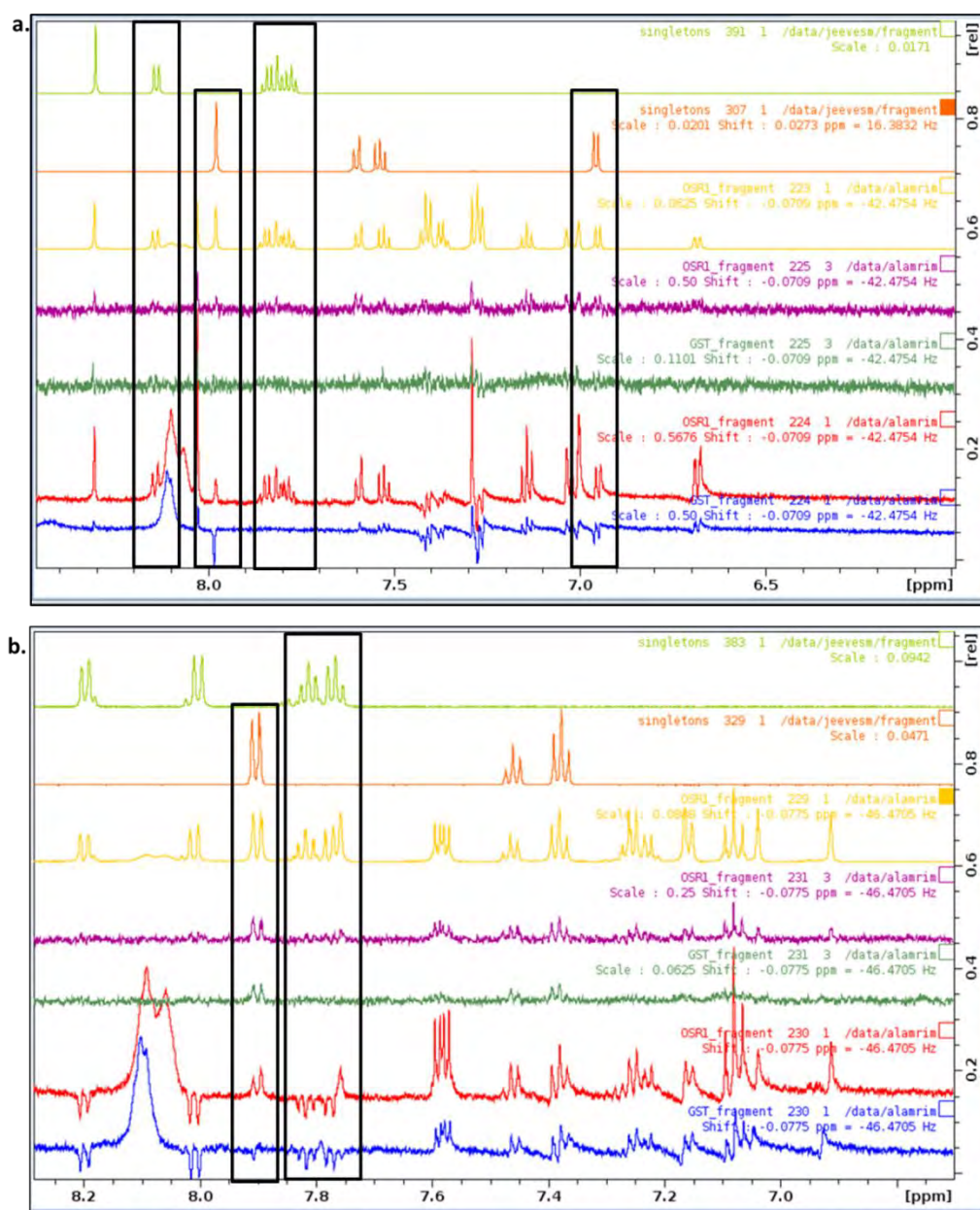
STD-NMR and waterLogsy spectra for fragment hits. Spectra of fragment hits number (a) 306-178 and (b) 208. The green and orange spectra in (a) are for ¹HNMR reference spectrum for 306 and 178 reference compounds, respectively. The orange spectrum in (b) is for ¹HNMR reference spectrum for 208 reference compound. The yellow spectrum is for ¹HNMR reference spectrum for the cocktail sample which composed of 4 distinct fragment molecules, violet spectrum is for STD-NMR experiment with GST-OSR1 CCT domain, green spectrum is for STD-NMR experiment with GST-tag protein, red spectrum is for waterLogsy experiment with GST-OSR1 CCT domain and blue spectrum is for waterLogsy experiment with GST-tag protein. The compound peaks that tested positive in both STD-NMR and waterLogsy with GST-OSR1 CCT domain but not GST-tag protein were highlighted with black rectangle.

Appendix 5.1g



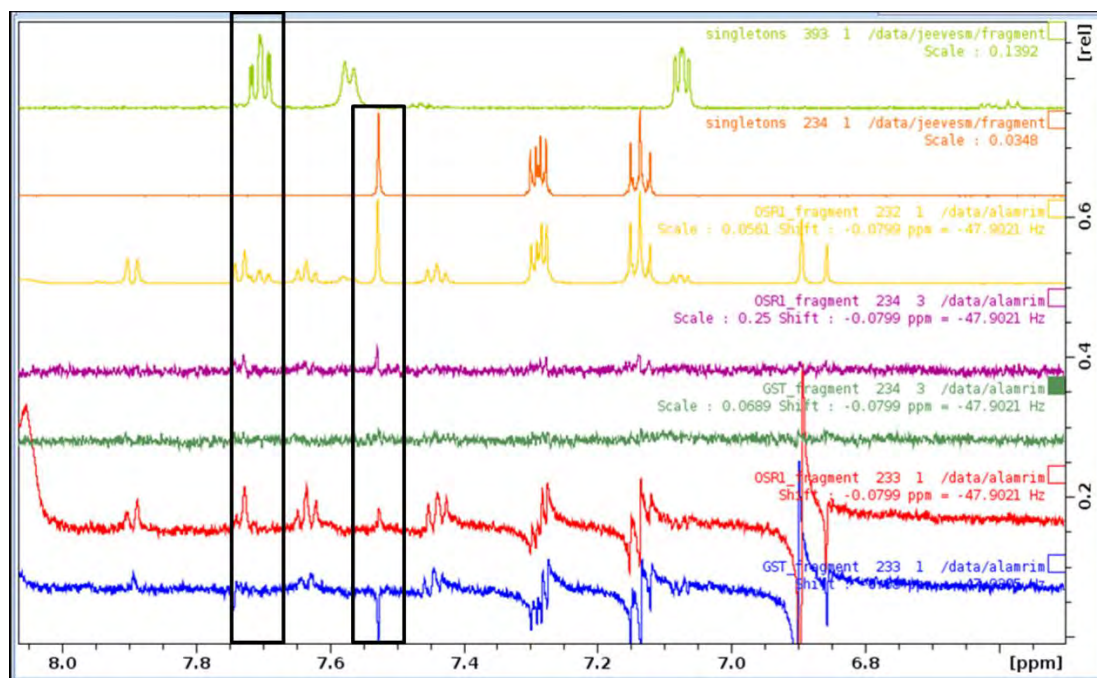
STD-NMR and waterLogsy spectra for fragment hits. Spectra of fragment hits number (a) 220 and (b) 299. The orange spectrum is for ^1H NMR reference spectrum for reference compound, yellow spectrum is for ^1H NMR reference spectrum for the cocktail sample which composed of 4 distinct fragment molecules, violet spectrum is for STD-NMR experiment with GST-OSR1 CCT domain, green spectrum is for STD-NMR experiment with GST-tag protein, red spectrum is for waterLogsy experiment with GST-OSR1 CCT domain and blue spectrum is for waterLogsy experiment with GST-tag protein. The compound peaks that tested positive in both STD-NMR and waterLogsy with GST-OSR1 CCT domain but not GST-tag protein were highlighted with black rectangle.

Appendix 5.1h



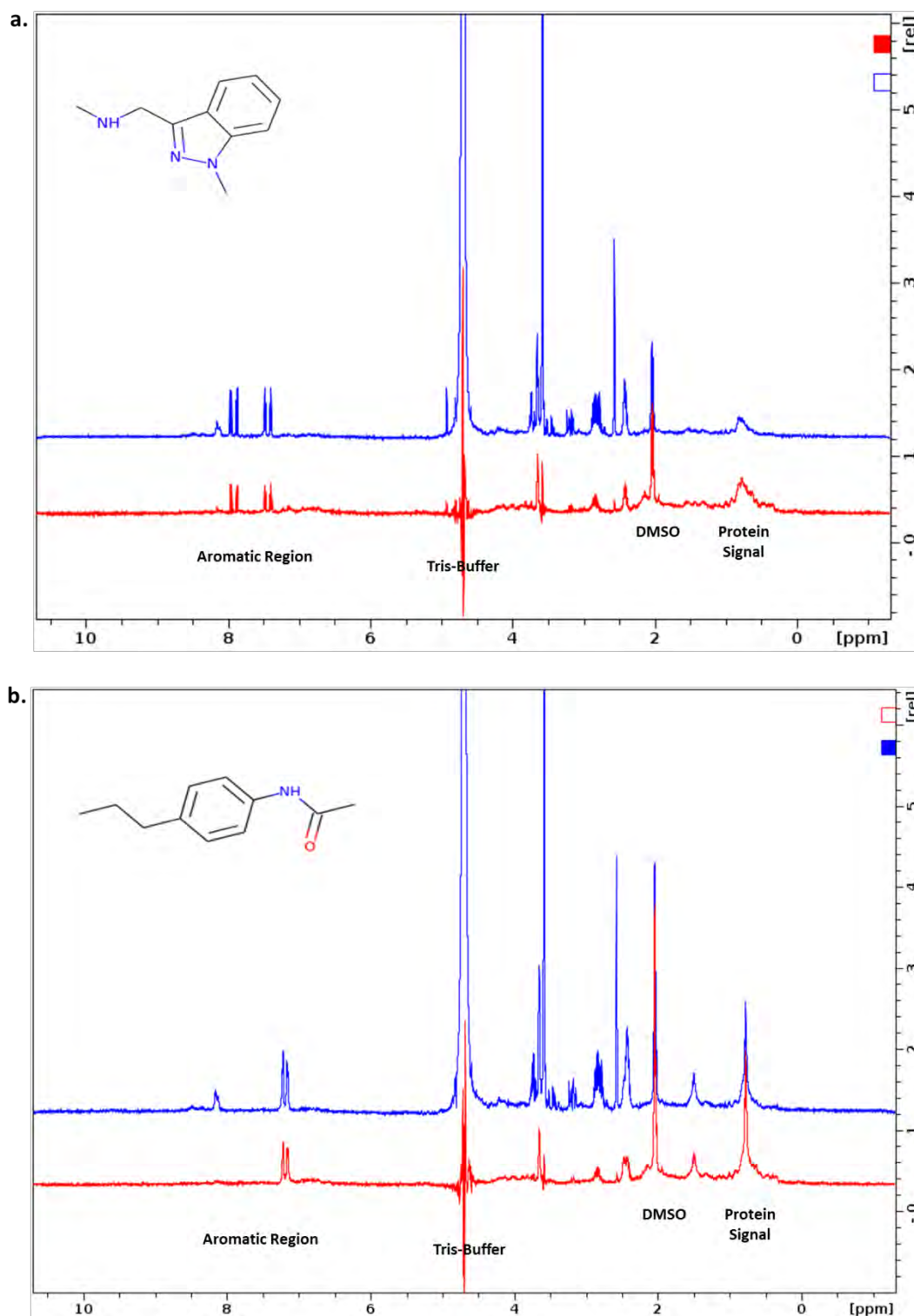
STD-NMR and waterLogsy spectra for fragment hits. Spectra of fragment hits number (a) 391-307 and (b) 383-329. The green and orange spectra in (a) are for 1HNMR reference spectrum for 391 and 307 reference compounds, respectively. The green and orange spectra in (b) are for 1HNMR reference spectrum for 383 and 329 reference compounds, respectively. The yellow spectrum is for 1HNMR reference spectrum for the cocktail sample which composed of 4 distinct fragment molecules, violet spectrum is for STD-NMR experiment with GST-OSR1 CCT domain, green spectrum is for STD-NMR experiment with GST-tag protein, red spectrum is for waterLogsy experiment with GST-OSR1 CCT domain and blue spectrum is for waterLogsy experiment with GST-tag protein. The compound peaks that tested positive in both STD-NMR and waterLogsy with GST-OSR1 CCT domain but not GST-tag protein were highlighted with black rectangle.

Appendix 5.1i



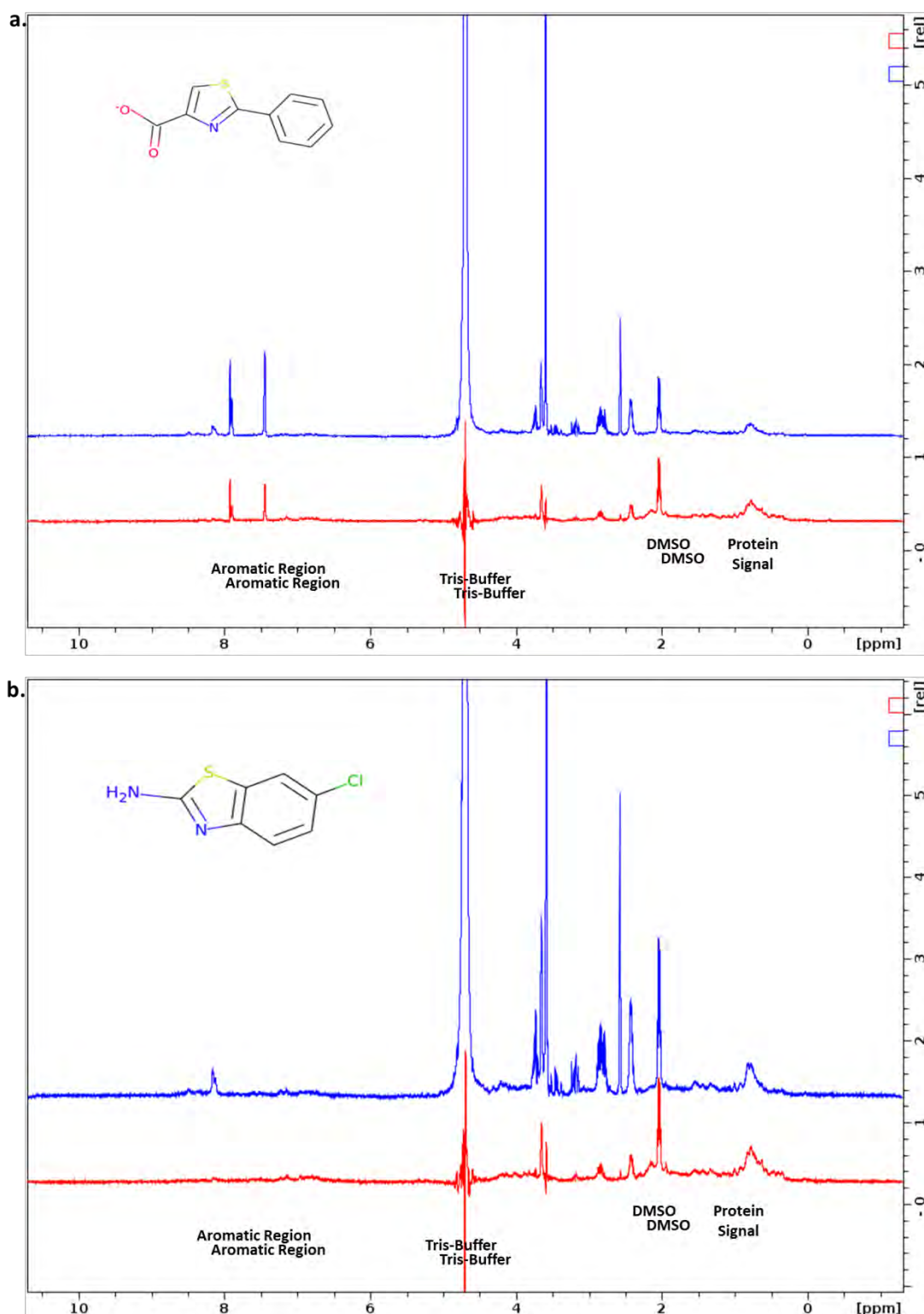
STD-NMR and waterLogsy spectra for fragment hits. Spectra of fragment hits number 393-234. The green and orange spectra are for ¹H NMR reference spectrum for reference compound 393 and 234 respectively. The yellow spectrum is for ¹H NMR reference spectrum for the cocktail sample which composed of 4 distinct fragment molecules, violet spectrum is for STD-NMR experiment with GST-OSR1 CCT domain, green spectrum is for STD-NMR experiment with GST-tag protein, red spectrum is for waterLogsy experiment with GST-OSR1 CCT domain and blue spectrum is for waterLogsy experiment with GST-tag protein. The compound peaks that tested positive in both STD-NMR and waterLogsy with GST-OSR1 CCT domain but not GST-tag protein were highlighted with black rectangle.

Appendix 5.2a



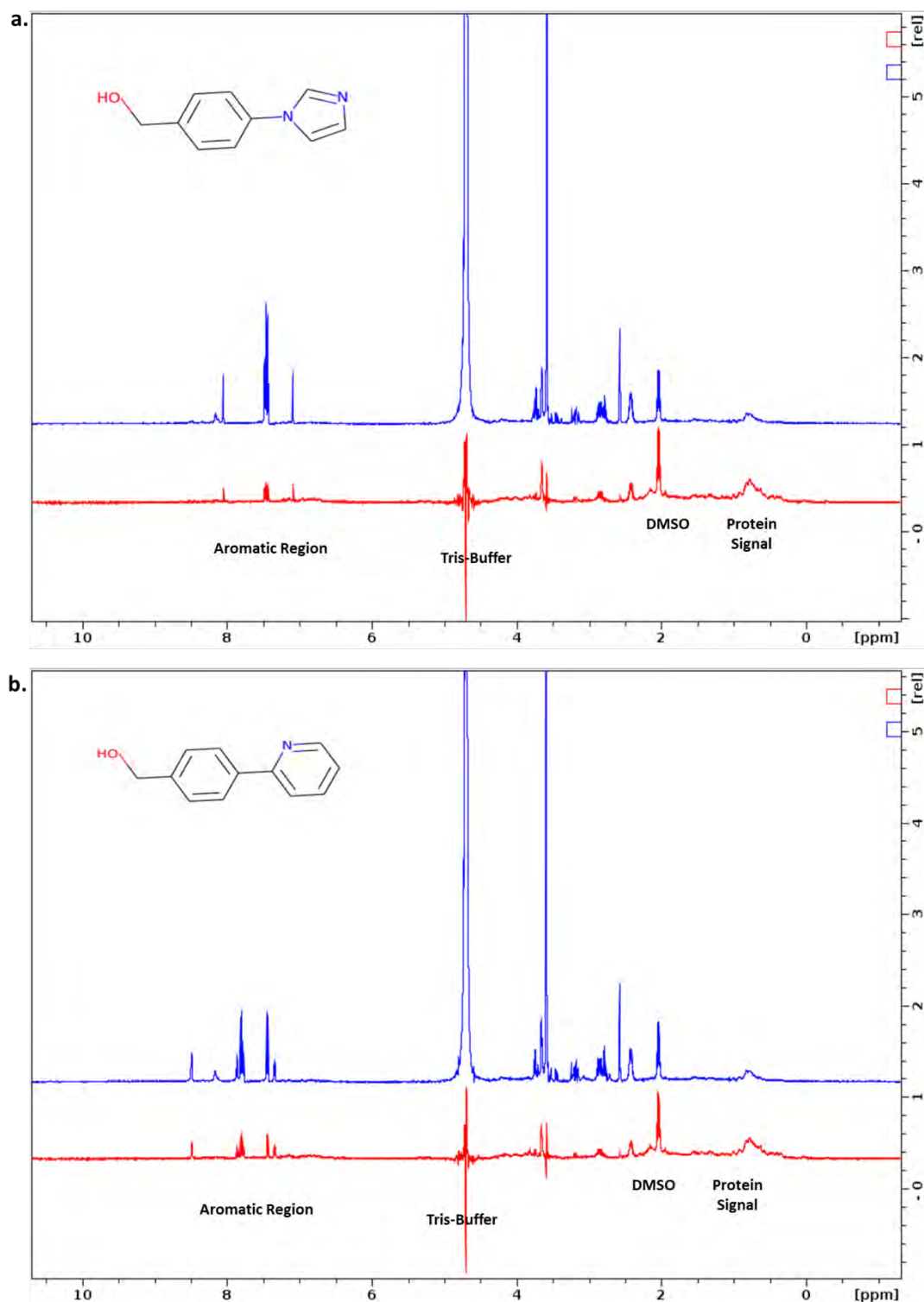
STD-NMR for confirming the binding of fragment number (a) 38 and (b) 67 to OSR1 CCT domain. The blue spectrum is for ^1H NMR reference spectrum for reference compound and red spectrum is for STD-NMR experiment with GST-OSR1 CCT domain. NMR spectrum regions were labelled.

Appendix 5.2b



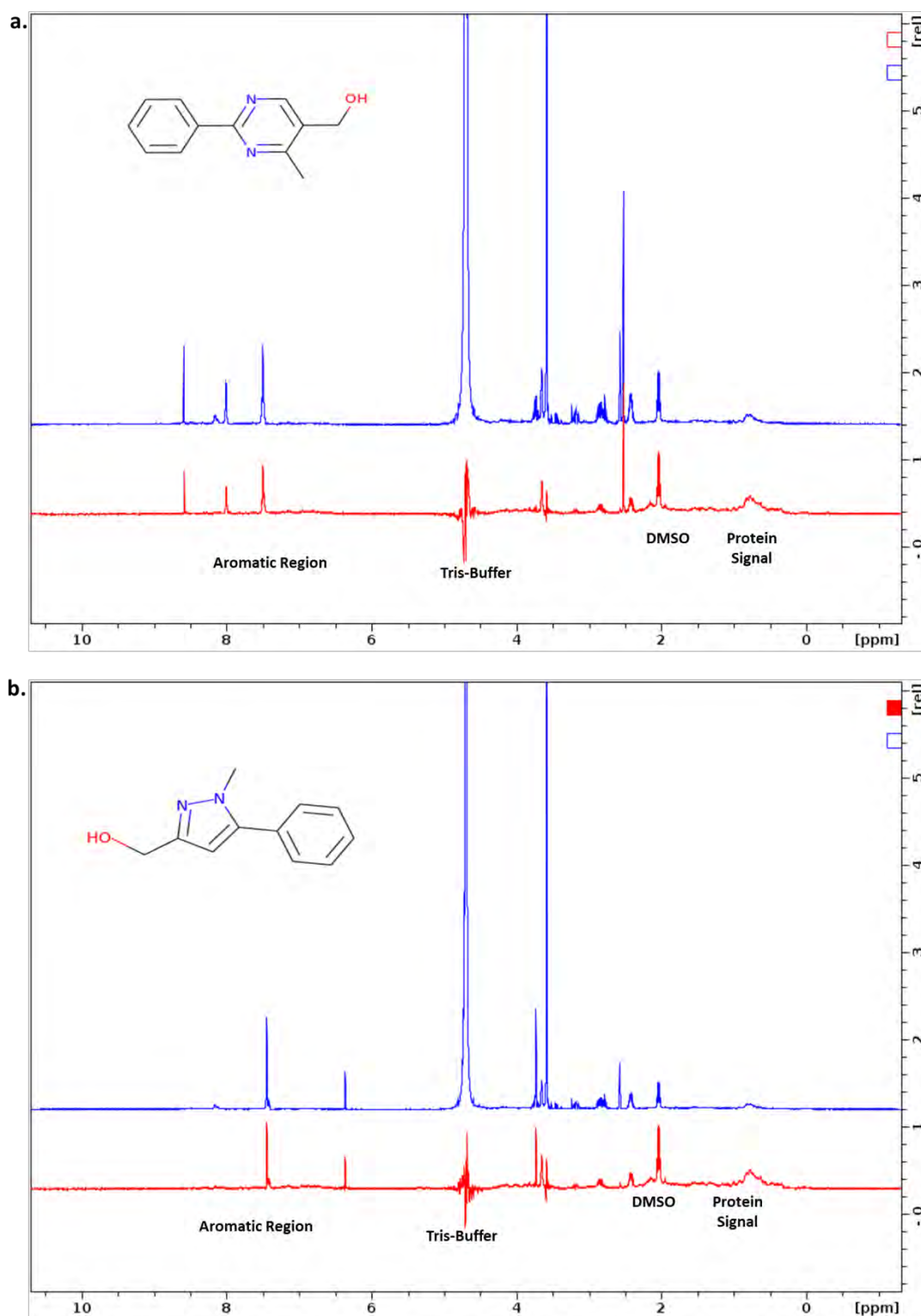
STD-NMR for confirming the binding of fragment number (a) 79 and (b) 82 to OSR1 CCT domain. The blue spectrum is for ^1H NMR reference spectrum for reference compound and red spectrum is for STD-NMR experiment with GST-OSR1 CCT domain. NMR spectrum regions were labelled.

Appendix 5.2c



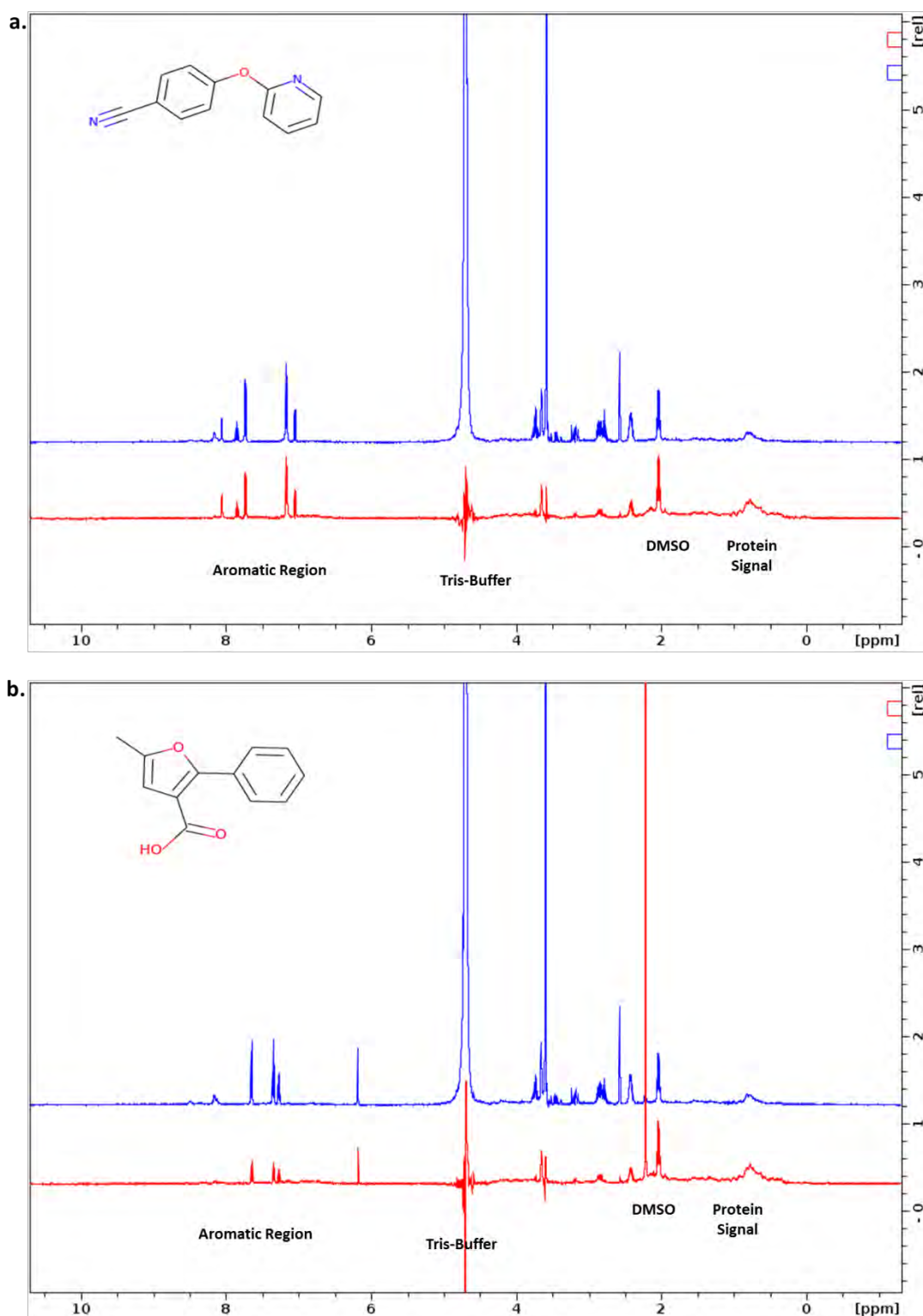
STD-NMR for confirming the binding of fragment number (a) 101 and (b) 114 to OSR1 CCT domain. The blue spectrum is for ^1H NMR reference spectrum for reference compound and red spectrum is for STD-NMR experiment with GST-OSR1 CCT domain. NMR spectrum regions were labelled.

Appendix 5.2d



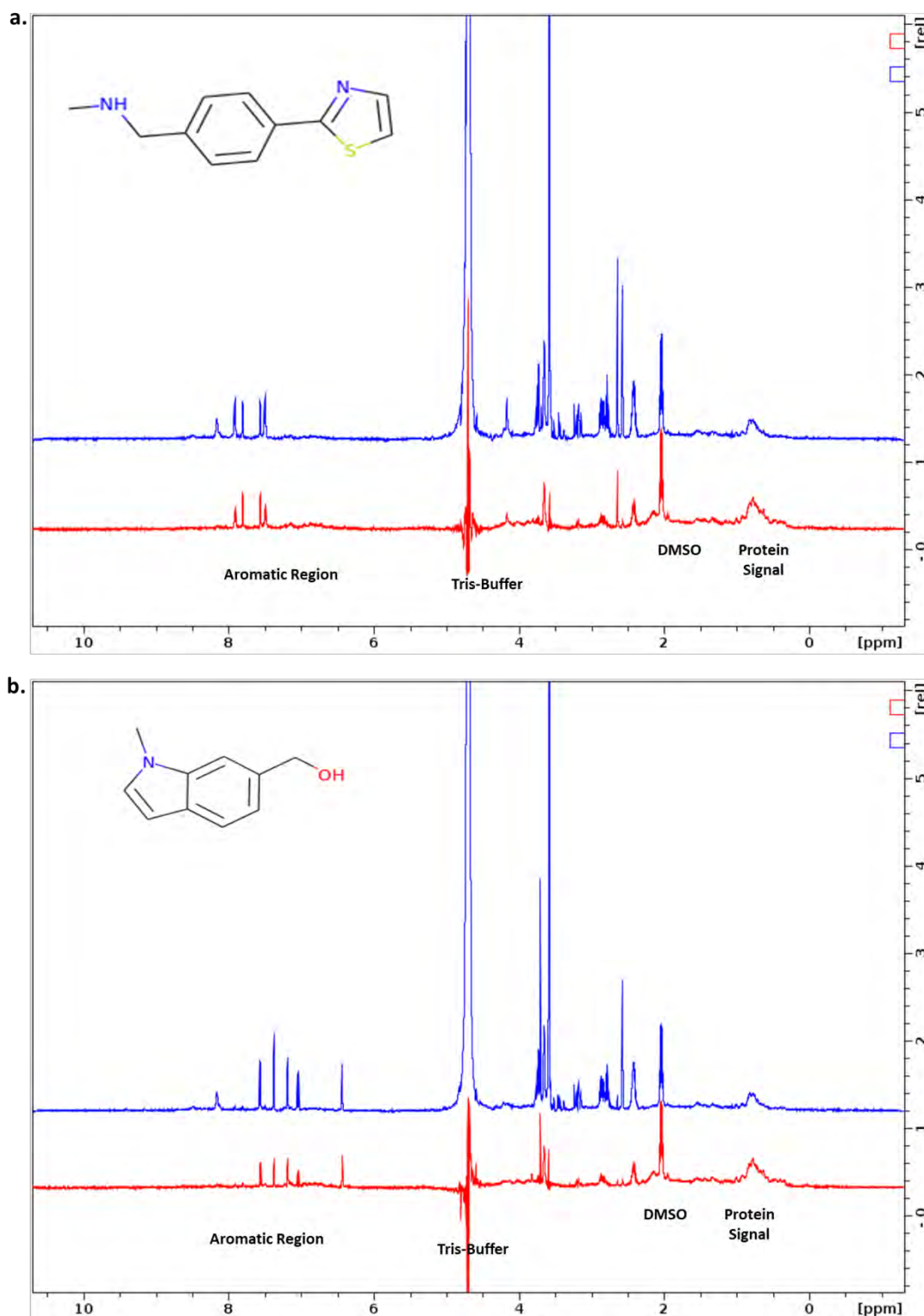
STD-NMR for confirming the binding of fragment number (a) 141 and (b) 147 to OSR1 CCT domain. The blue spectrum is for ^1H NMR reference spectrum for reference compound and red spectrum is for STD-NMR experiment with GST-OSR1 CCT domain. NMR spectrum regions were labelled.

Appendix 5.2e



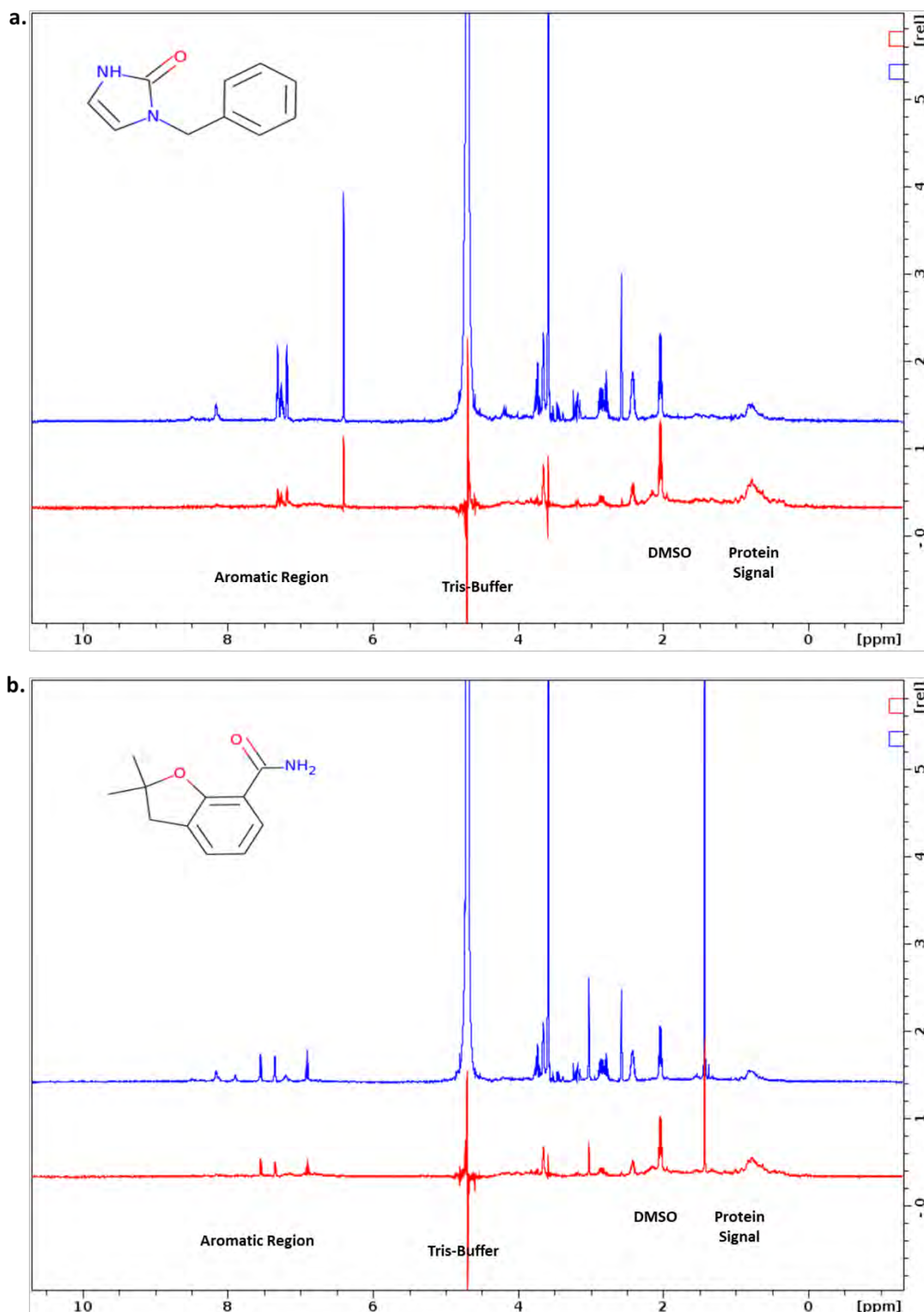
STD-NMR for confirming the binding of fragment number (a) 148 and (b) 156 to OSR1 CCT domain. The blue spectrum is for ^1H NMR reference spectrum for reference compound and red spectrum is for STD-NMR experiment with GST-OSR1 CCT domain. NMR spectrum regions were labelled.

Appendix 5.2f



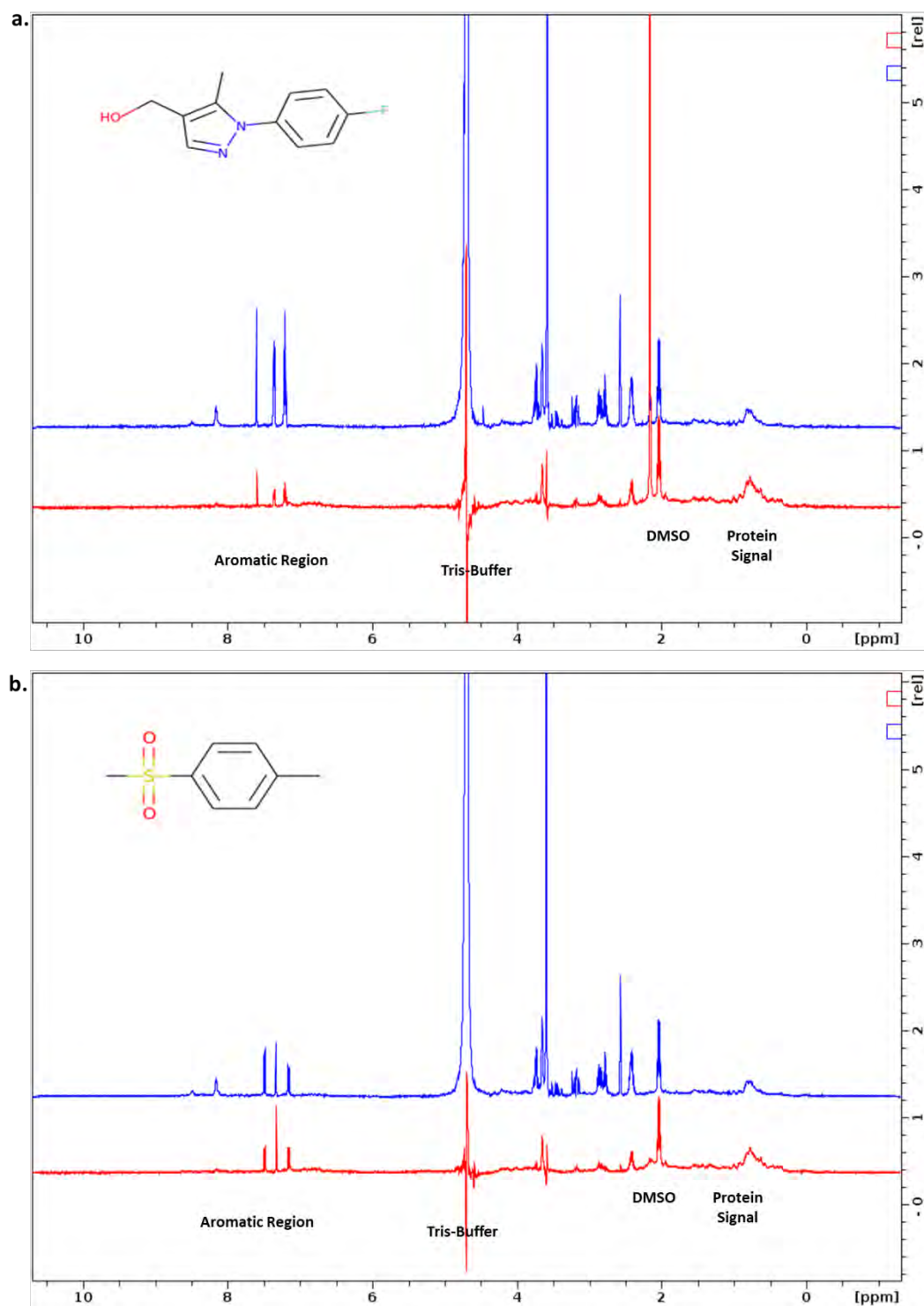
STD-NMR for confirming the binding of fragment number (a) 177 and (b) 178 to OSR1 CCT domain. The blue spectrum is for ^1H NMR reference spectrum for reference compound and red spectrum is for STD-NMR experiment with GST-OSR1 CCT domain. NMR spectrum regions were labelled.

Appendix 5.2g



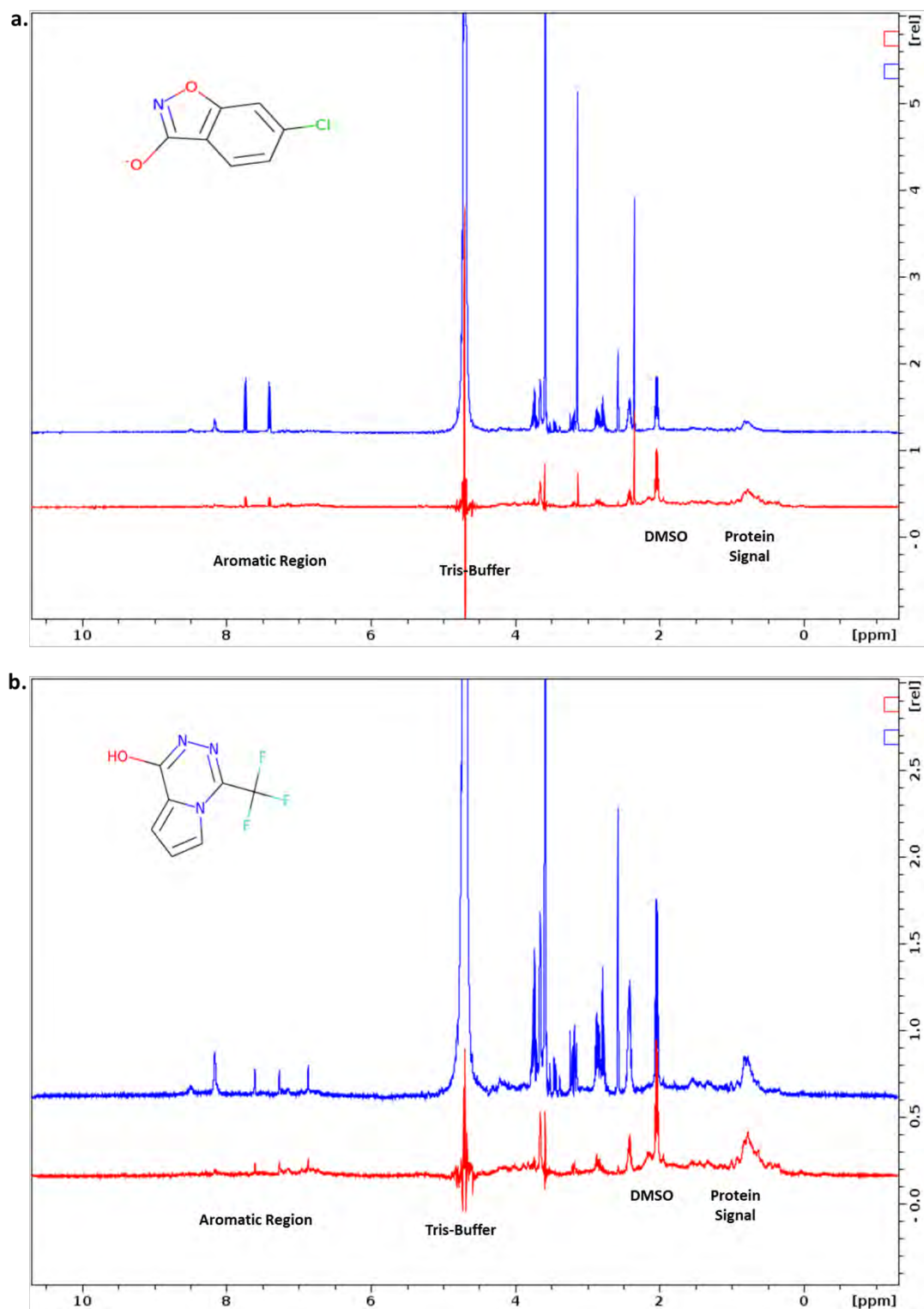
STD-NMR for confirming the binding of fragment number (a) 208 and (b) 220 to OSR1 CCT domain. The blue spectrum is for ^1H NMR reference spectrum for reference compound and red spectrum is for STD-NMR experiment with GST-OSR1 CCT domain. NMR spectrum regions were labelled.

Appendix 5.2h



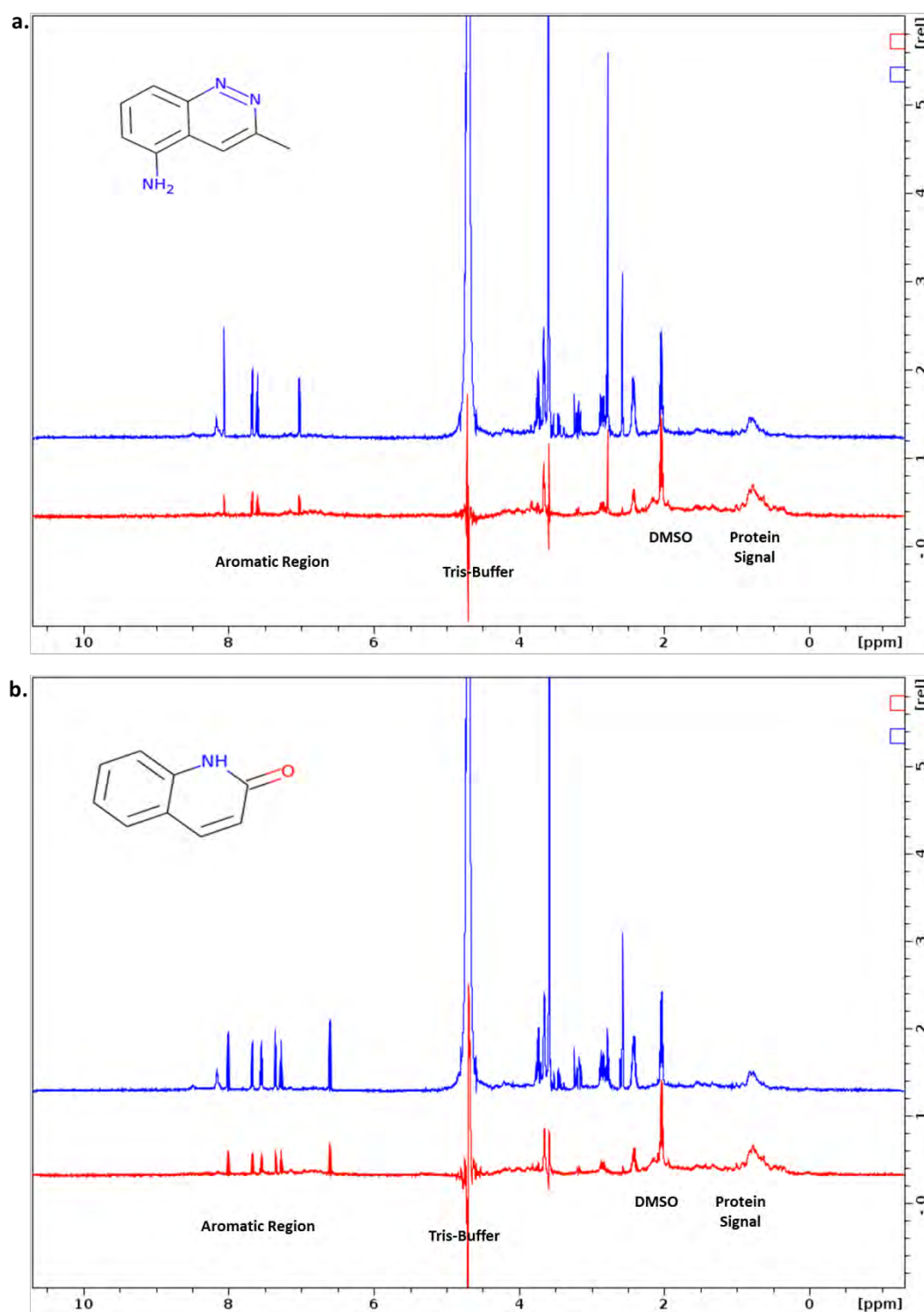
STD-NMR for confirming the binding of fragment number (a) 234 and (b) 256 to OSR1 CCT domain. The blue spectrum is for ^1H NMR reference spectrum for reference compound and red spectrum is for STD-NMR experiment with GST-OSR1 CCT domain. NMR spectrum regions were labelled.

Appendix 5.2i



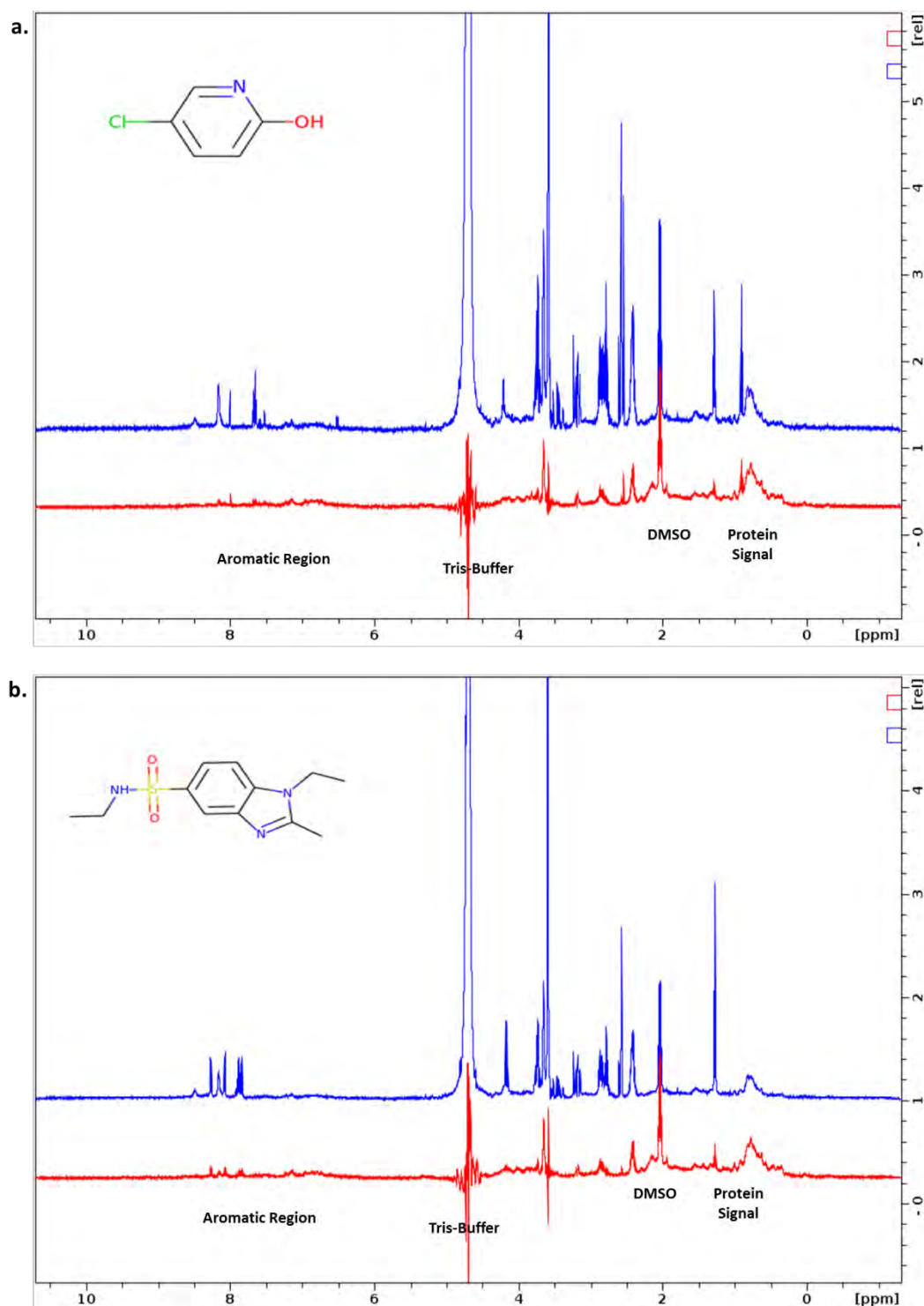
STD-NMR for confirming the binding of fragment number (a) 299 and (b) 306 to OSR1 CCT domain. The blue spectrum is for ^1H NMR reference spectrum for reference compound and red spectrum is for STD-NMR experiment with GST-OSR1 CCT domain. NMR spectrum regions were labelled.

Appendix 5.2j



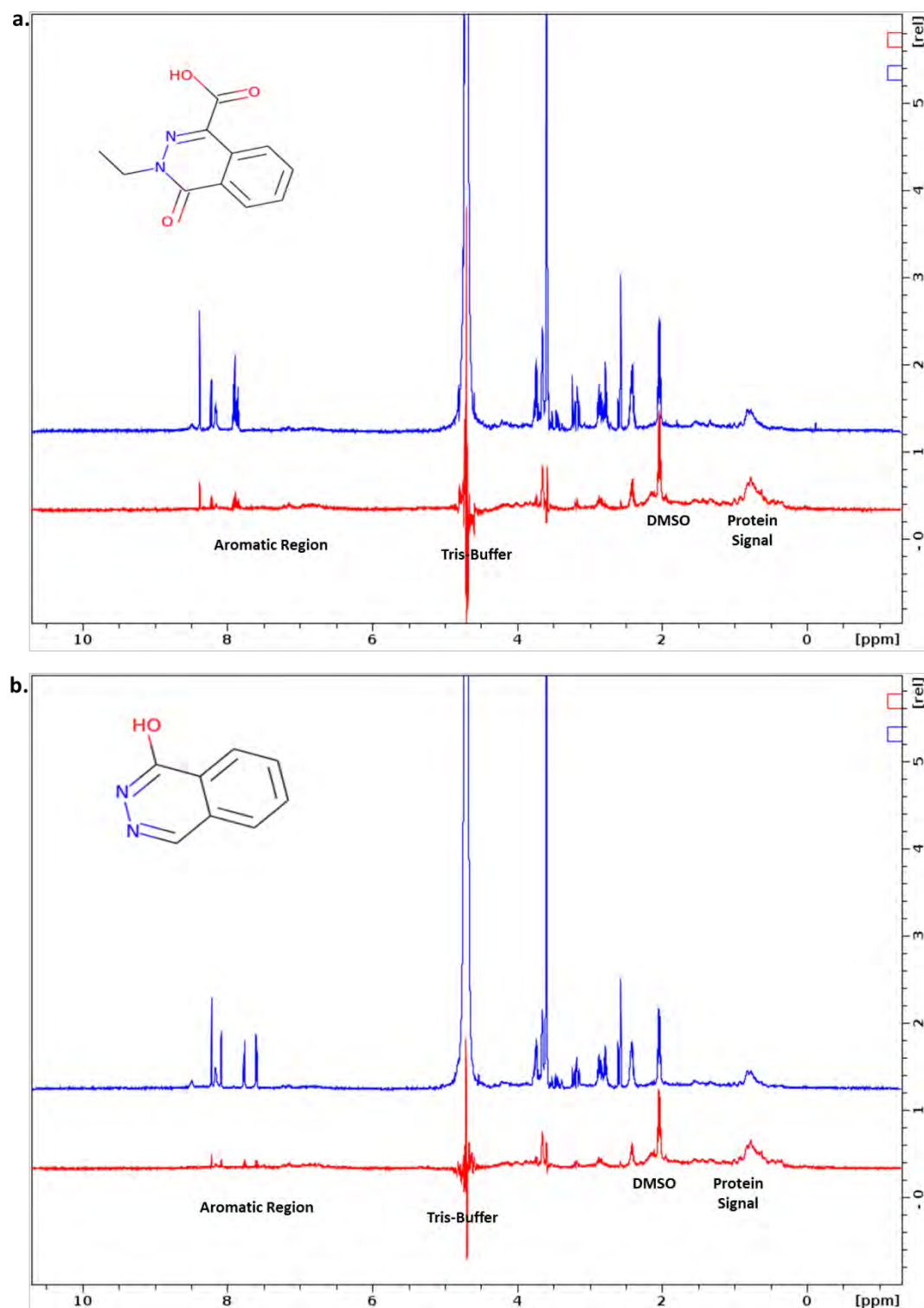
STD-NMR for confirming the binding of fragment number (a) 307 and (b) 329 to OSR1 CCT domain. The blue spectrum is for ^1H NMR reference spectrum for reference compound and red spectrum is for STD-NMR experiment with GST-OSR1 CCT domain. NMR spectrum regions were labelled.

Appendix 5.2k



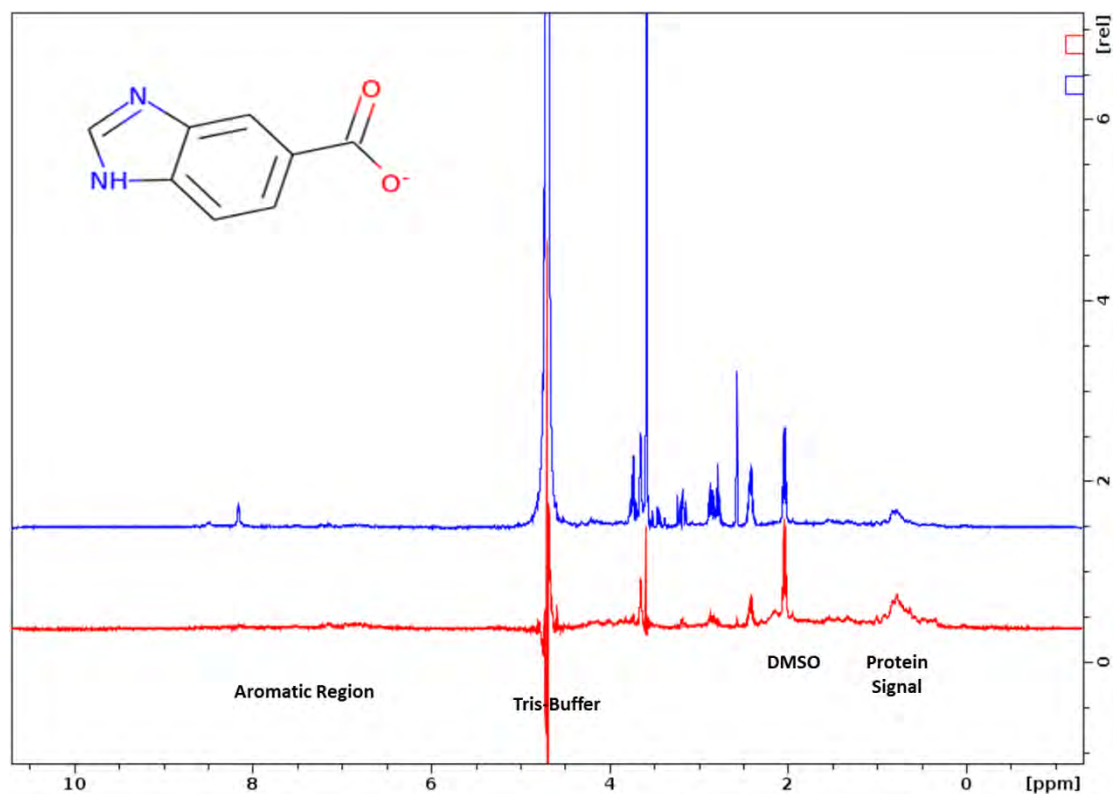
STD-NMR for confirming the binding of fragment number (a) 337 and (b) 343 to OSR1 CCT domain. The blue spectrum is for ^1H NMR reference spectrum for reference compound and red spectrum is for STD-NMR experiment with GST-OSR1 CCT domain. NMR spectrum regions were labelled.

Appendix 5.2I



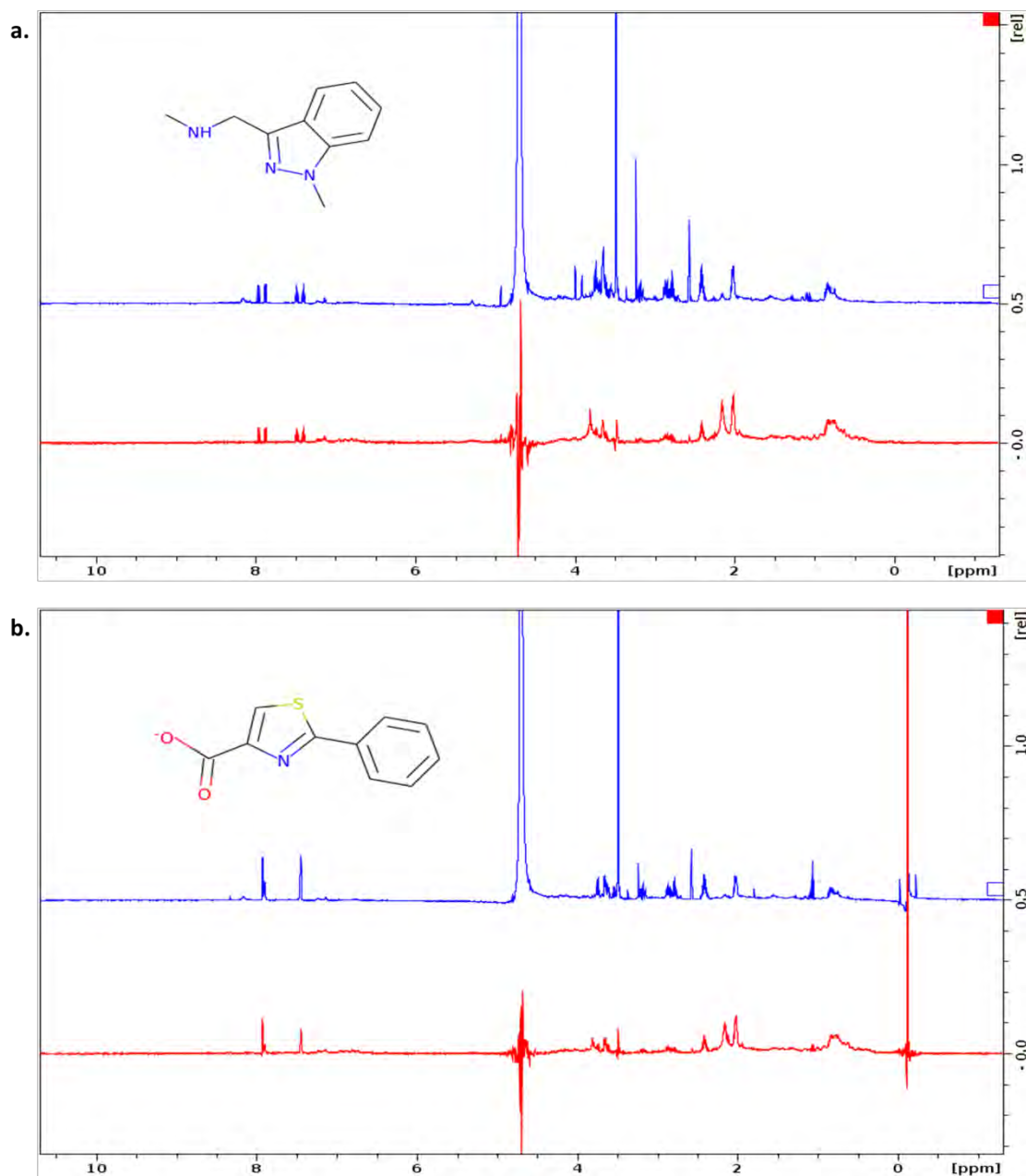
STD-NMR for confirming the binding of fragment number (a) 383 and (b) 391 to OSR1 CCT domain. The blue spectrum is for ¹H NMR reference spectrum for reference compound and red spectrum is for STD-NMR experiment with GST-OSR1 CCT domain. NMR spectrum regions were labelled.

Appendix 5.2m



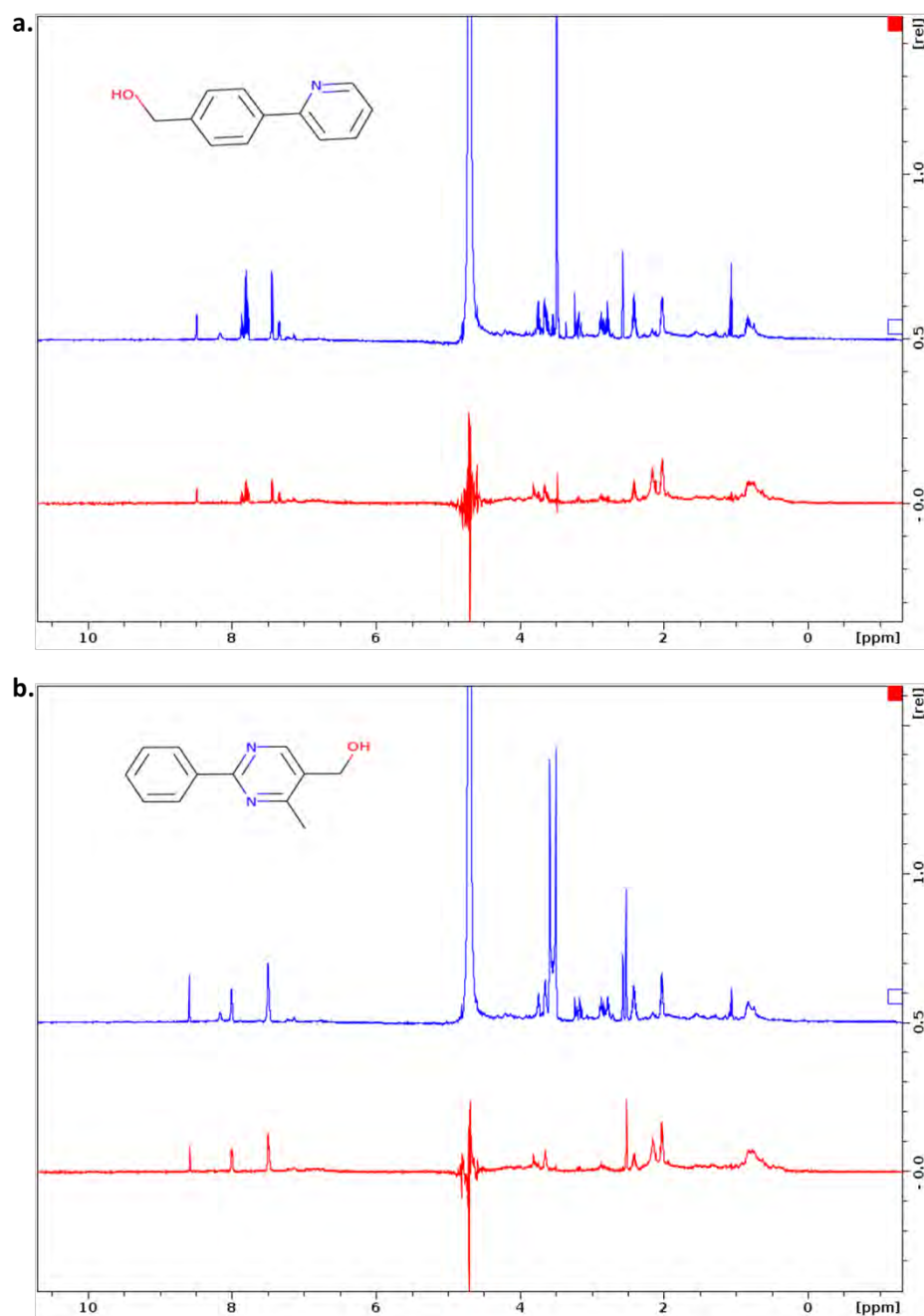
STD-NMR for confirming the binding of fragment number 393 to OSR1 CCT domain. The blue spectrum is for ¹H NMR reference spectrum for reference compound and red spectrum is for STD-NMR experiment with GST-OSR1 CCT domain. NMR spectrum regions were labelled.

Appendix 5.3a



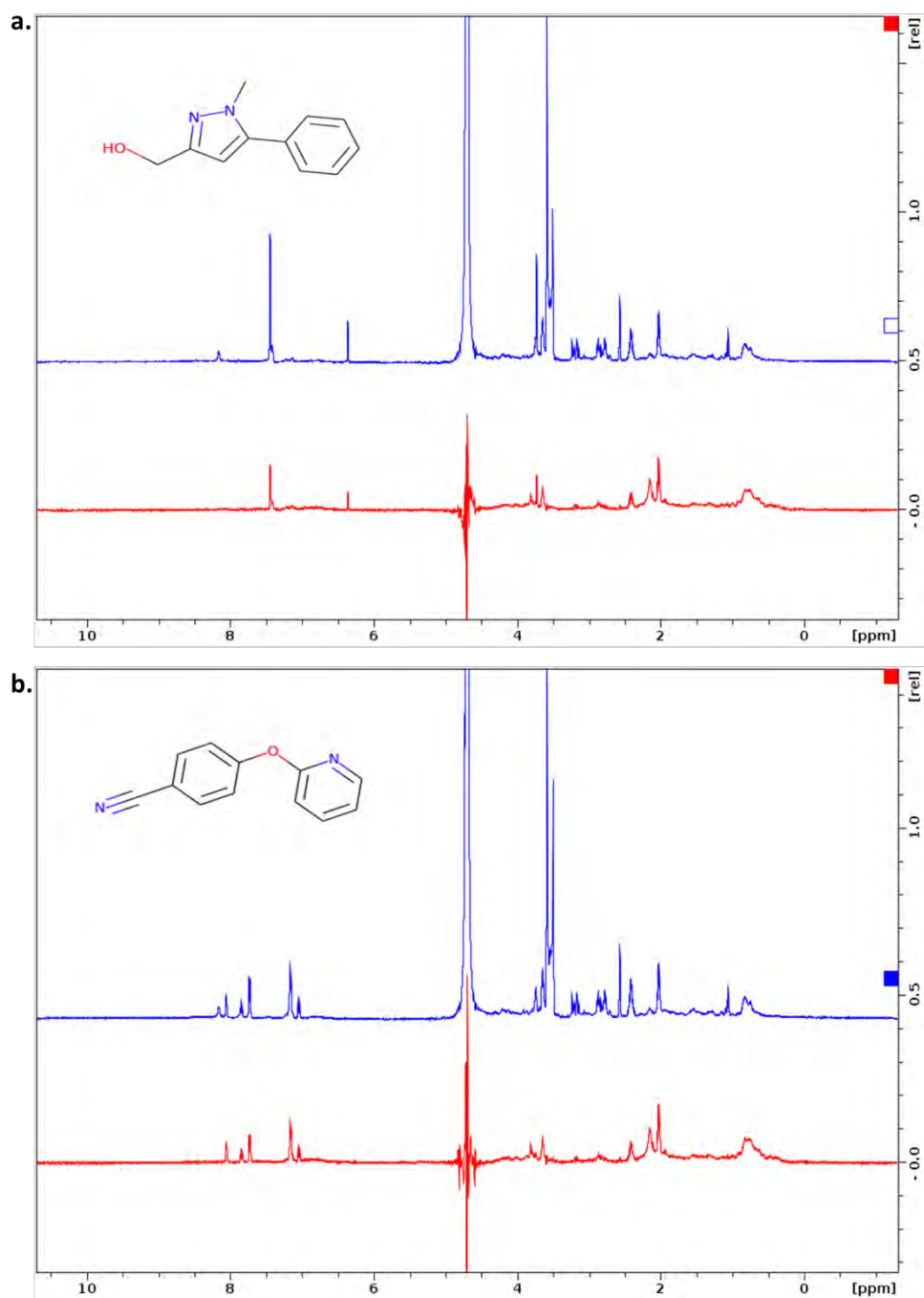
STD-NMR competition assay for ligand binding specificity. Compound (a) 38 and (b) 79 did not compete with 18-mer RFQV peptide derived from WNK4 on the primary pocket as the STD-NMR peaks intensity did not change in presence (red) or absence (blue) of RFQV peptide.

Appendix 5.3b



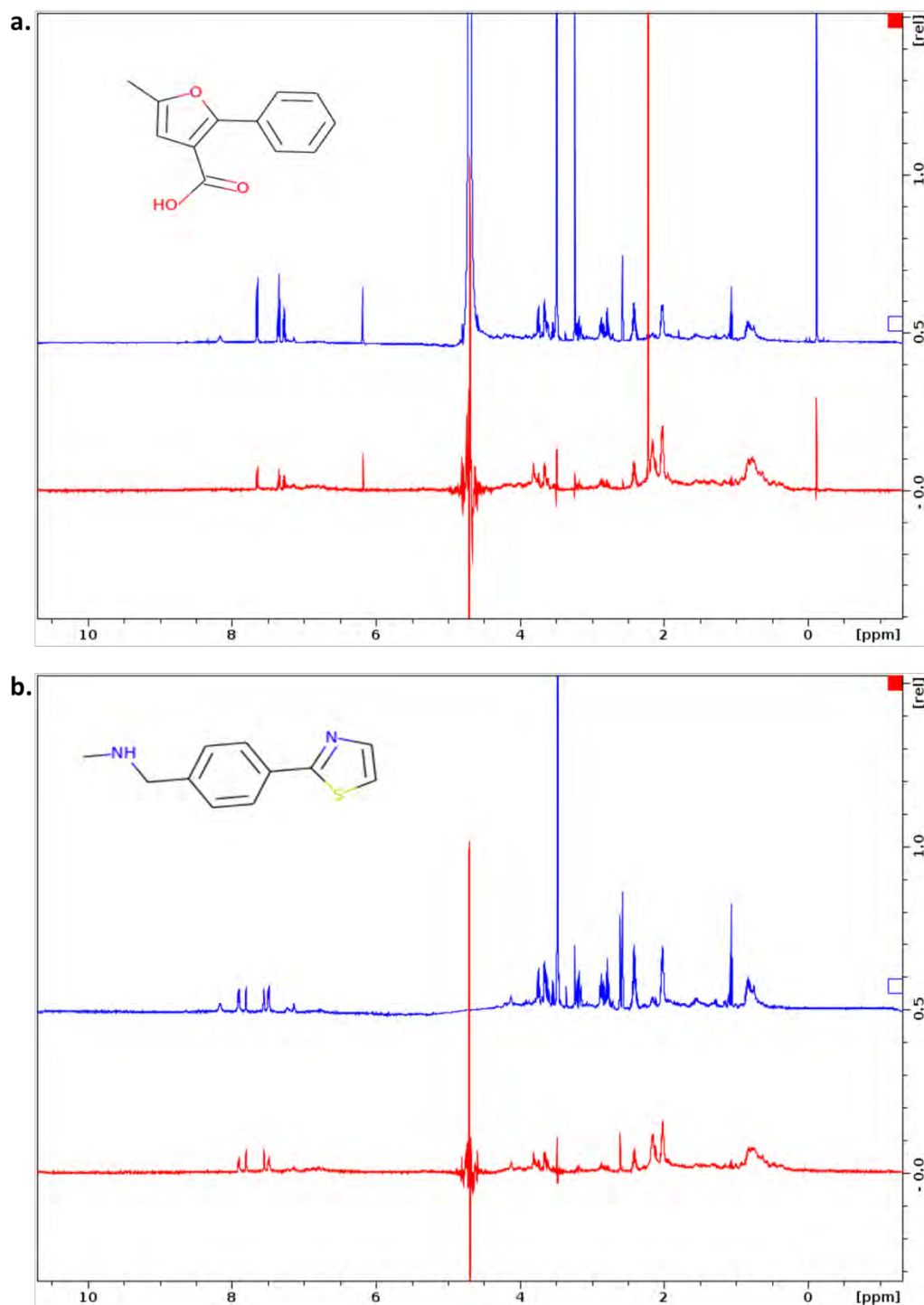
STD-NMR competition assay for ligand binding specificity. Compound (a) 114 and (b) 141 did not compete with 18-mer RFQV peptide derived from WNK4 on the primary pocket as the STD-NMR peaks intensity did not change in presence (red) or absence (blue) of RFQV peptide.

Appendix 5.3c



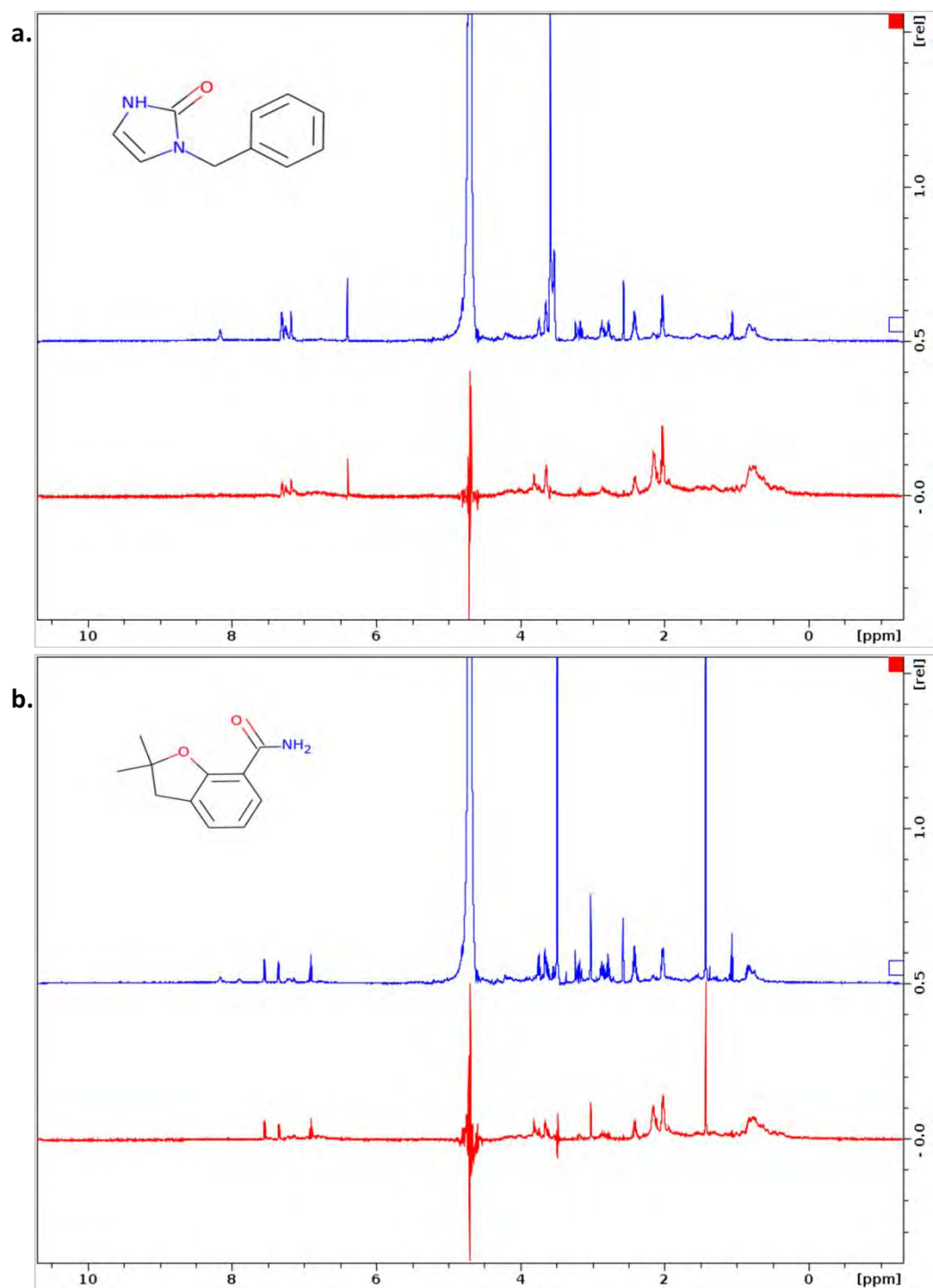
STD-NMR competition assay for ligand binding specificity. Compound (a) 147 and (b) 148 did not compete with 18-mer RFQV peptide derived from WNK4 on the primary pocket as the STD-NMR peaks intensity did not change in presence (red) or absence (blue) of RFQV peptide.

Appendix 5.3d



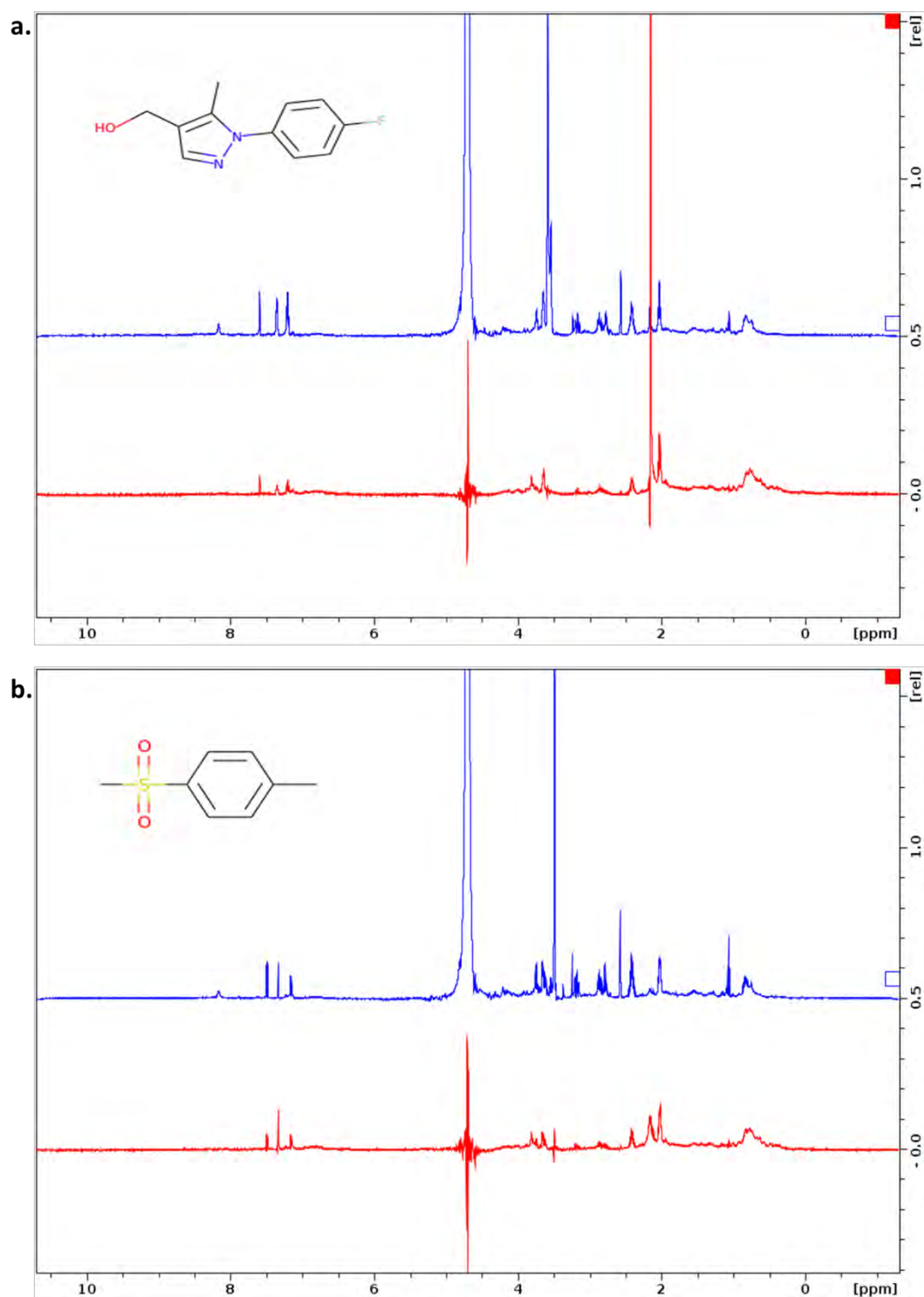
STD-NMR competition assay for ligand binding specificity. Compound (a) 156 and (b) 177 did not compete with 18-mer RFQV peptide derived from WNK4 on the primary pocket as the STD-NMR peaks intensity did not change in presence (red) or absence (blue) of RFQV peptide.

Appendix 5.3e



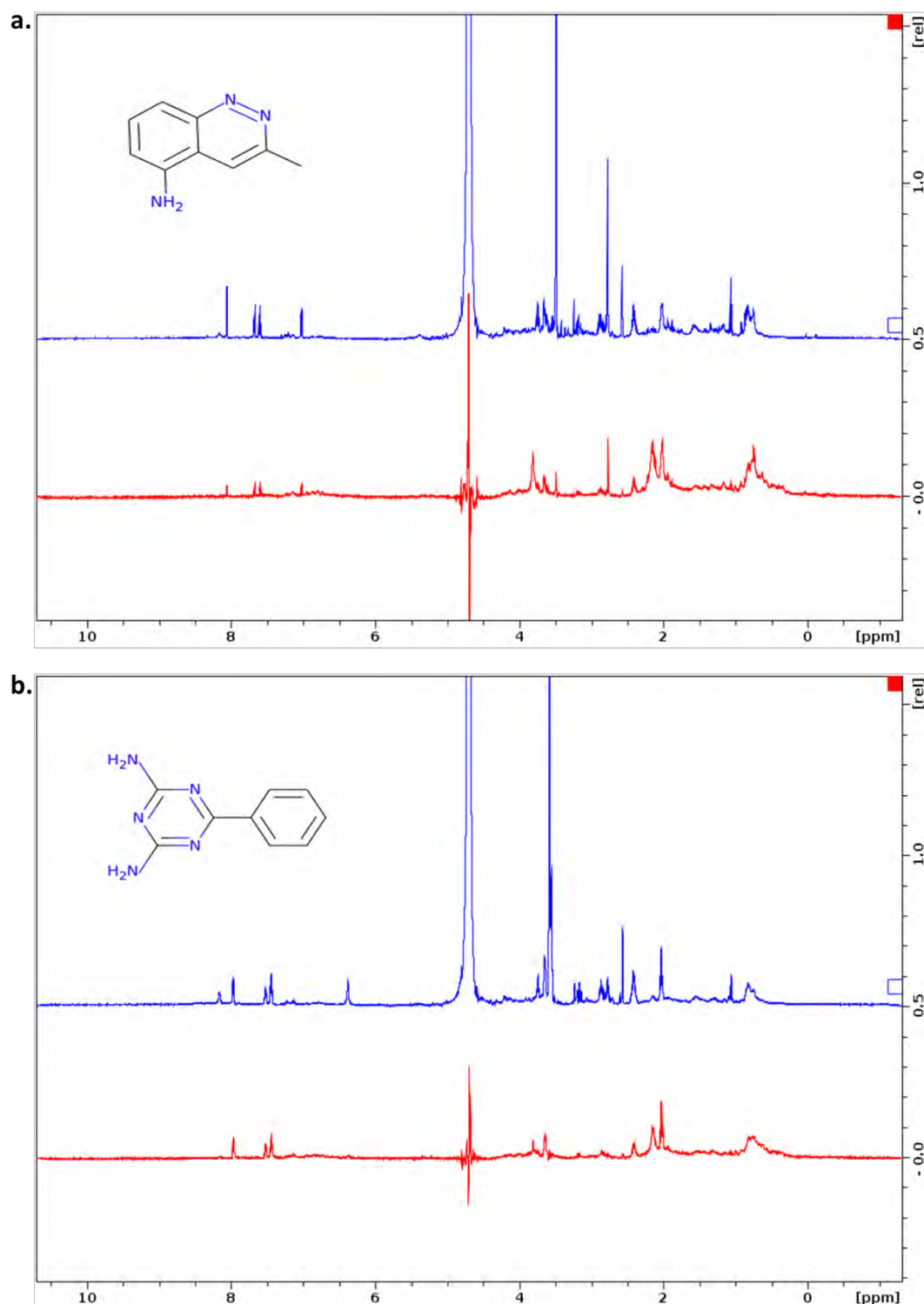
STD-NMR competition assay for ligand binding specificity. Compound (a) 208 and (b) 220 did not compete with 18-mer RFQV peptide derived from WNK4 on the primary pocket as the STD-NMR peaks intensity did not change in presence (red) or absence (blue) of RFQV peptide.

Appendix 5.3f



STD-NMR competition assay for ligand binding specificity. Compound (a) 234 and (b) 256 did not compete with 18-mer RFQV peptide derived from WNK4 on the primary pocket as the STD-NMR peaks intensity did not change in presence (red) or absence (blue) of RFQV peptide.

Appendix 5.3g



STD-NMR competition assay for ligand binding specificity. Compound (a) 307 and (b) 330 did not compete with 18-mer RFQV peptide derived from WNK4 on the primary pocket as the STD-NMR peaks intensity did not change in presence (red) or absence (blue) of RFQV peptide.

Appendix 5.4

Name	Cat#	Supplier
Protoporphyrin IX dimethyl ester	09626	Sigma-Aldrich
2,3,7,8,12,13,17,18-Octaethyl-21H,23H-porphine	252409	Sigma-Aldrich
Protoporphyrin IX	P8293	Sigma-Aldrich
Cp1	MolPort-038-4 13-895	MolPort
Cp2	MolPort-005-707-143	MolPort
Cp3	MolPort-009-146-922	MolPort
Cp4	MolPort-002-006-838	MolPort

List of chemical compounds used in Chapter IV and V.